U.PORTO

FEUP FACULDADE DE ENGENHARIA
UNIVERSIDADE DO PORTO

Analysis of Long-Term Damage of Offshore Wind Turbine Foundations

JOÃO RICARDO DE SÁ CHAMBEL

Dissertation submitted for partial requirements attendance for the degree on

MASTER ON CIVIL ENGINEERING — HYDRAULICS SPECIALIZATION

Supervisor: Professor Doctor Francisco de Almeida Taveira Pinto

Co-Supervisor: Engineer Doctor Tiago João Fazeres Marques Ferradosa

2019, SEPTEMBER

MESTRADO INTEGRADO EM ENGENHARIA CIVIL 2018/2019

DEPARTAMENTO DE ENGENHARIA CIVIL

Tel. +351-22-508 1901

Fax +351-22-508 1446

✉ miec@fe.up.pt

Editado por

FACULDADE DE ENGENHARIA DA UNIVERSIDADE DO PORTO

Rua Dr. Roberto Frias

4200-465 PORTO

Portugal

Tel. +351-22-508 1400

Fax +351-22-508 1440

✉ feup@fe.up.pt

🌍 http://www.fe.up.pt

À minha família e amigos

“You can’t go back and change the beginning,
but you can start where you are and change the ending”
C.S Lewis

ACKNOWLEDGMENTS

Desde já agradecer ao meu orientador, Professor Doutor Francisco de Almeida Taveira Pinto, pelo o acompanhamento, disponibilidade, compreensão e ensinamentos não só ao longo da realização desta dissertação, mas também ao longo do meu percurso académico. Enaltecer também o facto de me ter proporcionado sempre as melhores condições de trabalho sem quaisquer entraves, independentemente das circunstâncias, e por me ter dado a oportunidade de mostrar o meu valor.

Ao meu coorientador, Doutor Engenheiro Tiago João Marques Fazeres Ferradosa, agradecer o acompanhamento diário, motivação, auxílio e transmissão de conhecimentos necessários para a realização desta dissertação. O seu profundo saber relativo às temáticas abordadas foram de um contributo incalculável.

A todos os professores que fizeram parte de todo o meu percurso académico, principalmente aos da Secção de Hidráulica, Recursos Hídricos e Ambiente (SHRHA), o meu obrigado, sem eles não teria chegado e terminado esta etapa.

Porém, um especial agradecimento aos dois professores que mais me influenciaram durante todo o meu percurso académico. À Professora Doutora Elsa Maria da Silva Carvalho e ao Professor Doutor Francisco Manuel de Oliveira Piqueiro, um agradecimento especial pelos ensinamentos, disponibilidade, orientação e aconselhamento em todos os momentos. Obrigado por me ter ajudado sempre que necessário durante este meu percurso.

Não posso esquecer também do papel vital do Sr.Miguel e da D.Esmeralda, pela amizade, apoio e preocupação demonstrados e por fazerem de tudo para proporcionar as melhores condições possíveis aos estudantes da especialidade. São um verdadeiro exemplo.

A Engenheira Ana Bento e ao Engenheiro Mahdi Alemi pela preciosa ajuda e auxílio na realização de todo o processo de fotogrametria.

Aos meus colegas da FEUP, Carneiro, Francisco Carvalho, Francisco Teixeira, Francisco Pereira, Daniel, Diogo, Duarte, Ivan, Júlio, Jorge, Luís Barroso, Luís Barros, Mourão, Nuno, Rafa, Rocha, Tomé, Vinagre e Zé pela amizade, apoio, motivação e longos e bons momentos passados não só à entrada do DEC mas também fora da FEUP. Mas seria injusto não destacar um deles em especial. A ti, Pedro Vinagre, o meu profundo respeito pelas qualidades acima referidas mas também pela enorme pessoa que és e pelo enorme exemplo de perseverança e tenacidade que sempre demonstraste e que, consciente ou inconscientemente, me soubeste transmitir.

A todos aqueles que conheci durante a minha estadia em Brno, na República Checa, e por essa Europa fora, ao abrigo do programa Erasmus+, o meu profundo agradecimento. Foi graças a vocês que esta se tornou na grande aventura da minha vida, e a qual nunca irei esquecer. Um agradecimento especial, obviamente, ao Álvaro Magalhães, ao David Farinha, à Rita Cardoso, ao Dani Yáñez, ao David Garcia, ao Ander Teran, ao Atakan Aydogdu, ao Adérito Almeida, ao Simone Patroncini e à Maria Jesus Roldan

Aos meus amigos de Esmoriz, minha terra natal, André Rosa, André Gomes, Bruno Santiago, Bruna Gradim, Daniel, David, Filipa Sá, Francisco Ferreira, Luís Gomes, Nuno Leite, Nuno Santiago, Pedro Santos, Pedro Silva, Rui Magalhães e Zé Pedro, pela amizade, companheirismo, motivação, auxílio e acima de tudo pela paciência em lidar com todas as minhas particularidades. A vocês devo tudo! Apesar de muitas vezes não ter estado lá para vocês ou convosco, nunca mo cobraram nem nunca me faltaram com nada. Porém gostaria de deixar uma ressalva ao Nuno Santiago, ao Bruno Santiago e ao Francisco Ferreira por terem sido sempre o meu maior apoio, na fase mais difícil da minha vida. Olho para vocês como verdadeiros irmãos.

À família Cunha Rodrigues por durante 7 largos e bons anos me ter tratado como um verdadeiro membro da família. Ao Professor Doutor Carlos Rodrigues pela simpatia, amabilidade e respeito e a ti Ana Isabel pela amizade, carinho, simpatia e pela enorme pessoa que és. O meu muito obrigado a ambos. Mas o meu maior agradecimento não poderia deixar de ir para si, Professora Idalina Cunha, e para ti Inês. Professora, agradeço-lhe tudo o que fez por mim, pela simpatia, carinho e afeto mas principalmente pela bruta honestidade e frontalidade com que sempre lidou comigo desde o ensino Secundário. Será sempre como uma segunda mãe para mim e considero-a como um dos meus maiores ídolos. A ti Inês, obrigado por teres feito parte da grande maioria deste percurso, por teres tornado fáceis os dias mais difíceis, pelas inúmeras conversas e por teres acreditado em mim e no meu valor como poucos. Obrigado pelas grandes viagens, por teres sido uma das pessoas que fez com que acreditasse que este dia chegaria, mas sobretudo por todos os momentos incalculáveis que levarei sempre comigo. Sabes que apesar de tudo, desejo-te sempre a maior sorte do mundo. Sei bem do potencial tremendo que tens e só quero que saibas que estarei sempre feliz se tu também o tiveres.

E finalmente, às pessoas mais importantes da minha vida, a minha família. Sei que não sou a pessoa mais expressiva e emotiva do mundo, mas também sei que sem um bom suporte de base nada era possível. Aos meus avós pela sabedoria transmitida, cada um à sua maneira, aos meus tios, pelo enorme companheirismo que sempre demonstraram, aos meus primos, que apesar de pequenos não deixam de ser mais ou menos importantes, mas acima de tudo aos meus pais, à minha madrasta e aos meus irmãos. Mãe, obrigado pelos incalculáveis sacrifícios pelos quais passaste, muitas vezes em silêncio, para que os teus três filhos pudessem chegar ainda mais longe do que onde tu chegaste. Ao meu pai, pelo exemplo, pela coragem, pela capacidade de sofrimento, pela mentalidade e força de vontade sempre demonstrada não só para com os filhos, mas também quando estiveste fora, destacado em missões. És um herói para mim. À minha madrasta pela calma, simpatia e pela paciência sempre demonstradas. À minha irmã pela capacidade em mudar o rumo dos acontecimentos quando é mais preciso. E como não poderia deixar de ser, ao meu irmão. Ao génio de todos os génios, à pessoa intelectualmente mais desafiante que alguma vez conheci na vida e com uma tenacidade, resiliência e espírito de sacrifício em prol dos outros só ao nível dos melhores dos melhores. A ti, o meu mais profundo obrigado, pelo enorme exemplo que me transmites a cada dia que passa.

Este trabalho é suportado pelo projecto POCI-01_0145-FEDER-032170 (ORACLE project), financiado pelo Fundo Europeu para o Desenvolvimento Regional (FEDER), através do COMPETE2020, do Programa Operacional Competitividade e Internacionalização (POCI) e FCT/METES através de fundos nacionais (PIDDAC),

.

ABSTRACT

Offshore wind farms represent the sector of marine renewable energy with the highest commercial development at present state-of-the-art. However, the margins to optimize offshore wind foundations is still considerable and has been deriving the focus of the scientific and the industrial stakeholders. Due to the uncertainty and complexity of offshore environment, the foundation of an offshore wind turbine corresponds to a large portion of the capital expenditures parcel of the overall investment, that lies between 25 and 34%. An important part of the foundation in marine environment is the scour protection, which avoids the occurrence of scour phenomena, one of the most common causes that leads ultimate and service limit. The optimization of scour protections typically lead to considerable cost savings, while ensuring the structural stability of the system.

One of the most recent focus of scour protections optimization is the concept of dynamic scour protections, which allow for a dynamic armour layer, where the armour units can have a controlled degree of movement. Dynamic scour protections, have been more intensely studied over the last 10 years. However, there are considerable knowledge gaps that need to be the aim of deep research in order to develop a suitable solution for a generalised application in terms of the market's applicability. The design of dynamic protections has a remarkable empirical nature and the uncertainty related to its behaviour that stills need to be understood. In addition, to its complexity these types of protections, applied in offshore environment, deal with the wave- and current-induced loads. Therefore, common approaches mainly developed for bridge piers and fluvial environment are not enough to ensure the viability of this optimisation in offshore windfarms. State-of-the-art literature shows that there is a in physical modelling activities focused on the long-term behaviour of dynamic scour protections for offshore wind foundations. While the majority of the studies encompass scour protection tests under a total of 5000 waves, with very few results being reported for 7000 waves, little no results are available for large duration tests, *e.g.* 9000 waves or more. It is reported that this protections typically present the largest damage rates between until 1000 to 3000 waves, with a potential equilibrium after that. However, tests performed until 5000 and 7000 waves have also shown that sometimes this equilibrium may not endure in larger durations, thus leading to considerable damage. The present dissertation aims to set the preliminary work for a proper a clarification of this gap. This aspect presents an added value when facing new market trends as the turbines re-powering and life-time extension, particularly, within a scenario of Climate Change, where sea-state conditions can be harsher and structures are expected to operate for longer periods.

The present research has two key objectives. Firstly, it contributes with a deep work of adaptation of laboratorial facilities, in order to convert a current flume into a wave and current flume, suitable for the physical modelling of offshore wind turbine protections. Secondly, it provides the preliminary results of long-duration tests, where damage is monitored and analysed. These tests are an important contribution to open the way for more accurate testing of long-term damage. Results show that the facilities were successfully adapted for the intended research goal. However, particular, but crucial, aspects still require further work and calibration, namely in terms of dissipation to avoid reflection effects. Still a successful setup was achieved and used for the physical modelling activities. The results on the long-term damage developments showed a filter exposure after 5000 waves, thus emphasizing the importance of further research on the present topic. It was also concluded that new granulometry should be used in order to achieve a more dynamic behaviour of the armour layer.

KEYWORDS: Offshore Foundation, Offshore Wind Turbine, Scour, Dynamic Scour Protections, Laboratory Facility Adaptations

RESUMO

Os parques eólicos offshore representam o setor de energia renovável marinha com o maior desenvolvimento comercial no presente estado-da-arte. No entanto, as margens para otimizar as fundações eólicas offshore ainda são consideráveis e têm obtido o foco das stakeholders científicas e industriais. Devido à incerteza e à complexidade das condições offshore, a fundação de uma turbina eólica offshore representa uma grande parcela do investimento alocado para este tipo de estruturas, representando cerca de 25 a 34% do investimento total. Uma parte importante da fundação, é a proteção contra a erosão, que evita a ocorrência de fenómenos de erosão localizada, uma das causas mais comuns para que o estado limite último e de serviço seja atingido. A otimização deste tipo de protecções leva a consideráveis reduções de custos, ao mesmo tempo que garantem a estabilidade estrutural do sistema.

Um dos conceitos mais recentes de optimização de protecções contra a erosão é o conceito de protecção dinâmica, onde é permitido um determinado grau de movimento aos elementos da camada resistente. As protecções dinâmicas têm sido alvo de um estudo mais exaustivo nos últimos 10 anos. No entanto, existem ainda algumas lacunas que ainda necessitam de ser analisadas, de forma a que seja desenvolvida uma solução generalizada e mais adequada ao mercado. O dimensionamento de protecções dinâmicas possui uma natureza empírica notável e um grau de incerteza associado ao seu comportamento e estabilidade. Adicionalmente, este tipo de protecções, aplicadas em ambiente offshore, precisam de lidar com cargas induzidas por ondas e correntes, que fazem aumentar a sua complexidade. Assim, abordagens genéricas maioritariamente desenvolvidas para pilar de pontes e para ambientes fluviais não são suficientes viáveis para torres eólicas offshore. A literatura mostra que também existem lacunas no que diz respeito à modelação física deste tipo de protecções, nomeadamente o seu comportamento a agitação de longo prazo. A maioria dos estudos é realizada para valores inferiores a 5000 ondas, com poucos resultados a serem reportados para 7000 ondas, sendo que pouco ou nenhum resultado está disponível para testes de longa duração (9000 ou mais ondas). Existem referências de que protecções dinâmicas normalmente apresentam elevadas taxas de dano entre 1000 a 3000 ondas, com a tendência para o equilíbrio. No entanto, testes realizados até 5000 e 7000 ondas demonstraram que esse equilíbrio às vezes pode não permanecer para durações mais longas, levando a um dano considerável. A presente dissertação tem como objectivo criar um trabalho preliminar que possibilite a clarificação de algumas lacunas. Este aspecto é de grande importância, não só devido a novas tendências que vão surgindo todos os dias no mercado, o aparecimento de turbinas mais potentes e com maior tempo de vida útil, mas também num cenário de alterações climáticas (com condições de agitação marítima mais severas e onde este tipo de estruturas precisarão de trabalhar durante longos períodos).

Esta tese apresenta dois objectivos principais: contribuir para um trabalho profundo de adaptação de instalações laboratoriais, a fim de converter um canal de correntes para um canal de ondas e correntes (adequado para modelação física de protecções de turbinas offshore), mas também fornecer resultados preliminares de testes de longa duração, onde o dano é monitorizado e analisado. Estes testes são uma contribuição importante para o desenvolvimento de futuros testes cada vez mais precisos em protecções dinâmicas. Os resultados demonstram que as adaptações foram realizadas com sucesso. No entanto, alguns aspectos cruciais necessitam ainda de melhorias futuras, nomeadamente ao nível da dissipação. Os testes realizados mostraram uma exposição de filtro depois de 5000 ondas, enfatizando a importância de futuras analises referentes a este tópico. Conclui-se também, que uma nova granulometria deverá ser usada de maneira a obter uma protecção com um comportamento dinâmico mais relevante.

PALAVRAS-CHAVE: Fundações Offshore, Turbina Eólica Offshore, Erosão Localizada, Protecções Dinâmicas, Adaptações Instalações Laboratoriais

TABLE OF CONTENTS

FIGURES INDEX

TABLES INDEX

NOMENCLATURE AND ABBREVIATION

In this section a list of symbols and abbreviations used in the realization of this dissertations is presented. In some cases, the same symbol may have different meanings due to the extensive number of formulas, variables and parameters that were used. However, each symbol is usually associated with a particular subject and it is easy to distinguish its meaning, given the context in which it is presented.

NOMENCLATURE

A [m] – Amplitude of the wave orbital motion

A [-] – Constant

A^* [m^2] – Projected area of the grain in the horizontal plane

A_{av} [m^2] – Surface available area

A_o [m^2] – Surface occupied area

A_{sub} [m^2] – Area of a sub-area of the scour protection

a [m] – Wave amplitude

a0 [-] – Coefficient for hydrodynamic conditions

a1, a2, a3, a4 [-] – Regression fitting coefficient

B [-] – Constant

b0 [-] – Regression fitting coefficient

b1 [-] – Constant

C [-] – Constant

Ca [-] – Cauchy Number

Ch [$m^{1/2}/s$] – Chézy constant

D [m] – Diameter

D^* [-] – Dimensionless grain size

D_{cr} [m] – Critical diameter

D_n [m] – Nominal diameter

D_{50} [m] – Mean stone diameter of the scour protection

D_{n50} [m] – Nominal stone diameter of the scour protection

D_s [m] – Diameter of a sphere

D_p [m] – Pile diameter

d [m] – Water depth

d_{50} [m] – Mean diameter of bed sediments

d_s [m] – Diameter of the sediment grain

Eu [-] – Euler Number

e [-] – Nepper's Number

F_D [N] – Horizontal drag force

F_L [N] – Vertical lift force

Fr [-] – Froude Number

F_S [N] – Frictional forces between grains

f [s^{-1}] – Wave frequency

f_c [-] – Current friction factor

f_i [s^{-1}] – Wave frequency, $1/T_i$

f_n [s^{-1}] – Natural frequency

f_p [s^{-1}] – Peak frequency

f_w [-] – Wave friction factor

g [m/s^2] – Gravitational acceleration

H [m] – Wave height

$\overline{H}_{1/3}$ - average of the highest 1/3 of all waves

$\overline{H}_{1/10}$ - average of the highest 1/10 of all waves

$\overline{H}_{1/100}$ - average of the highest 1/100 of all waves

H_b [m] – Breaking wave height

H_d [m] – Design wave height

H_i [m] – Individual wave height

H_m [m] – Mean wave height

H_{m0} [m] – Spectral wave height from the 0^{th} order moment of a wave train with N waves

H_{max} [m] – Maximum wave height

H_{rms} [m] – Root-mean-square wave height

H_s [m] – Significant wave height

H_{si} [m] – Significant incident wave height

H_{sr} [m] – Significant reflected wave height

H_r [m] – Ripple's height

KC [-] – Keulegan-Carpenter number

K_α [-] – Pier alignment factor

K_σ [-] – Grain size distribution factor

K_d [-] – Flow depth factor

K_s [-] – Shape factor

K_{si} [-] – Slope factor

k [-] – Wave Number, $2\pi/L$

k [-] – Von Karman constant

k_s [m] – Bottom roughness

L [m] – Wave length

L(f) [m] – Wave length as function of frequency

M [kg] – Mass

m_n [-] – n^{th} order moment

Ma [-] – Mach Number

N [rpm] – Rotations

N [-] – Number of waves

N_{charac} [-] – Characteristic number of waves

n [-] – n^{th} overlapping ring

P [kN] – Power

P_N [Pa] – Nominal pressure

$P(H>H_d)$ [-] – Exceeding probability

Q [m^3/s] - Flow

Re [-] – Reynold Number

$Re_{,p}$ [-] – Pile Reynolds Number

Re* [-] – Grain Reynolds Number

S [m] – Scour depth

S(f) [m^2/s] – Energy spectral density

S_{3D} [-] – Dimensionless damage number

$S_{3D,measured}$ [-] – Measured damage number

$S_{3D,predicted}$ [-] – Predicted damage number

$S_{3D,sub}$ [-] – Damage Number of a sub-area

S_e [m] - Equilibrium scour depth

$S_U(f)$ [m^2/s] – Power spectrum of the bottom velocity

St [-] – Strouhal Number

Stab [-] – Stability parameter

s [-] – specific density, ρ_s/ρ_w

T [s] – Wave Period

T(f) [s] – Wave period as function of frequency

T_0 [s] – Total duration of wave train

T_i [s] – Individual wave Period

T_p [s] – Wave peak Period

T_r [years] – Return Period

$T_{m-1,0}$ [s] – Energy wave Period

$T_{mi,j}$ [s] – Wave Period obtained from the i^{th} order moment and the j^{th} order moment

T_z [s] – Mean up- or down-crossing wave period

t [s] – Time

t_e [s] – Time scale of the equilibrium scour depth

U [m/s] - Velocity

U_c [m/s] – Depth-averaged flow velocity

U_{cr} [m/s] – Critical velocity

U_{cw} [-] – Velocity ratio

U_m [m/s] – Maximum wave orbital velocity

Ur [-] – Ursell number

U_w [m/s] – Horizontal wave orbital velocity

U_δ [m/s] – Peak value of near bed orbital velocity

u [m/s] – Horizontal velocity

u_* [m/s] - Friction velocity

u_{*cr} [m/s] – Critical friction velocity

V [m^3] - Volume

V_e [-] – Eroded Volume

V_s [m^3] – Volume of a solid rock

W [N] – Submerged weight of a grain particle

W_{50} [N] – Mean weight of stones of the armour layer

w [rad/s] – angular frequency

w_s [m/s] – settling velocity

We [-] – Weber Number

x [m] – Horizontal position

z [m] – Vertical distance

z_o [m] – Bed roughness length

α [-] – Amplification factor

ϒ [-] – Peak enhancement factor

δ [m] - Bottom boundary layer

Δ [-] - Relative density

Δf [-] – Frequency band

Θ [-] – Shields parameter

Θ_{cr} [-] – Critical Shields parameter

Θ_{max} [-] – Max Shields parameter

λ [-] – Scale factor

μ [N·s/m^2] – Dynamic viscosity

ρ [kg/m^3] – Fluid density

ρ_d [kg/m^3] – Bulk density

ρ_s [kg/m^3] – Sediment or stone mass density

ρ_w [kg/m^3] – Water mass density

σ_g [-] – Grain size distribution

σ_s [-] – Standard deviation of scour depth

σ_u [-] – Orbital velocity spectrum

σ_u [-] – Uniformity parameter

τ [N/m^2] – Amplified bed shear stress

τ_∞ [N/m^2] – Undisturbed bed shear stress

τ_b [N/m^2] – Bed Shear Stress

$\tau_{b,c}$ [N/m^2] – Undisturbed current-induced bed shear stress

$\tau_{b,w}$ [N/m^2] – Undisturbed wave induced shear stress

τ_c [N/m^2] – Current-induced bed shear stress

τ_{cr} [N/m^2] – Critical bed shear stress

τ_{cw} [N/m^2] – Wave and current induced bed shear stress

τ_m [N/m^2] – Mean combined bed shear stress, current and wave induced

τ_{max} [N/m^2] – Maximum combined bed shear stress, current and wave induced

τ_w [N/m^2] – Wave induced bed shear stress

ν [m^2/s] - Kinematic viscosity of water

Φ [º] – Angle between the propagating direction of waves and currents

Φ_c [º] – Current direction

Φ_w [º] – Wave direction

η [m] – surface water elevation

η [%] – Pump efficiency

χ [-] – Corrective Factor

ψ [rad] – Phase shift

ABBREVIATIONS

ADV – Acoustic Doppler Velocimetry

AC – Alternating Current

ASTM – American Society for Testing and Materials

DTM – Digital Terrain Model

EU – European Union

FEUP – Faculty of Engineering of the University of Porto

FOWT – Floating Offshore Wind Turbine

HRW – HR Wallingford

ISO – International Organization of Standardization

ITTC – International Towing Tank Congress

JONSWAP – Joint North Sea Wave Project

LCoE – Levelized Cost od Energy

LMEC – Construction Materials Testing Laboratory

MDCP – Motor Drive Control Panel

NEMAR – Hydraulic Structures and Marine Energy Group

ORACLE – Offshore Risk Analysis for Climate Changes and Lifetime Extension

OPTI-PILE – Optimisation of Monopile foundations for offshore wind turbines in deep water and North Sea Conditions

OWT – Offshore Wind Turbine

PMMA – *Polymethyl methacrylate*

PM – Pierson-Moskowitz

PP - *Polypropylene*

PVC – *Polyninyk chloride*

ROV – Remotely Operated Vehicles

SBR – *Styrene-butadiene*

SHRHA – Water Resources and Environment Division

SNR – Signal-to-Noise Ratio

SPM – Scour Management Plans

SWL – Still-Water Level

UK – United Kingdom

ULS – Ultimate Limit State

1 INTRODUCTION

1.1. BACKGROUND

The offshore wind energy is one of the largest forms of clean energy and it is a sector that experienced continuous growth over the last decades (Matutano, 2013; Negro *et al.*, 2014; Fazeres-Ferradosa, 2018).

Europe is the leader in installed offshore windfarms (Fazeres-Ferradosa, 2018) and the European Wind Energy Association, now WindEurope, predicts that until 2030 the installed capacity of this type of structures will be around 49 to 99 GW, between 6.5 to 14.9% of the electricity demand of the European Union (EU) (WindEurope, 2017). In 2018, Europe had a total installed offshore wind capacity of 18 499 MW, Figure 1.1, corresponding to 4 543 offshore turbines installed and grid-connected (WindEurope, 2018). In the same year of 2018, the amount invested in new offshore wind was of €10.3 billion, with the refinancing of offshore windfarms hitting a new record of €8.5 billion that brought the total investment, including transmission lines, to €19.6 billion (WindEurope, 2018).

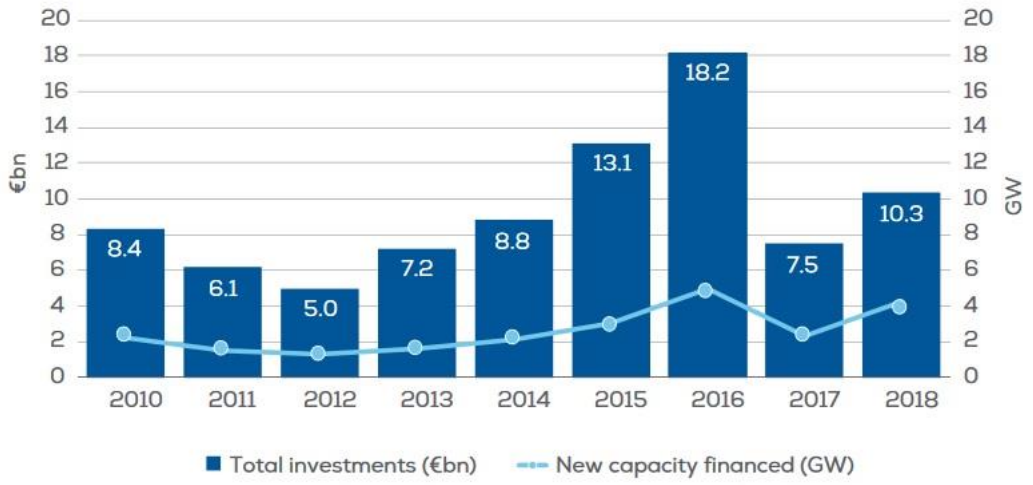

Figure 1.1 - New offshore wind investments and capacity financed: 2010-2018 (billion €) (WindEurope, 2018).

As this type of structures represents a multi-million euro investment, the path is towards the optimization, *i.e.* more energy production with fewer investment expenses. The Levelized Cost of Energy (LCoE) represents the ratio between the lifetime costs and the energy production, giving the total cost of building, operating and maintaining a power plant over an assumed lifetime, and is a key aspect in the optimization achievement. In 2015, the LCoE value for offshore wind was around 130 to

170 €/MWh, and the main goal is to reduce that value to the range of 90 to 60 €/MWh until 2030 (Fazeres-Ferradosa, 2018). Because the foundations' costs may be around 30% of the overall investment of an offshore windfarm (Matutano *et al.*, 2013; Bhattacharya, 2014), they represent an important target for cost reduction. For that reason, it is important to secure the correct protection against scour phenomena. At the same time, if the goal is to reduce the LCoE for this type of structures, that may be obtained through the optimization and reduction of the total cost of the foundations and their protections. If the lowering of the LCoE is achieved, that may lead to an increase of profits.

Focusing on the offshore wind turbine (OWT) foundation itself, the most common configuration is the monopile (WindEurope, 2018), as shown in Figure 1.2, "…representing 81.9% of all installed substructures in Europe." (WindEurope, 2018). Only in 2018, monopiles were the most installed foundation, representing 66% of all the installed foundations in that same year (WindEurope, 2018). Since monopile foundations are fixed-bottom foundations, as such the jacket, tripod, tripile and gravity based foundation, they are the most prone to scour phenomena (Fazeres-Ferradosa, 2018).

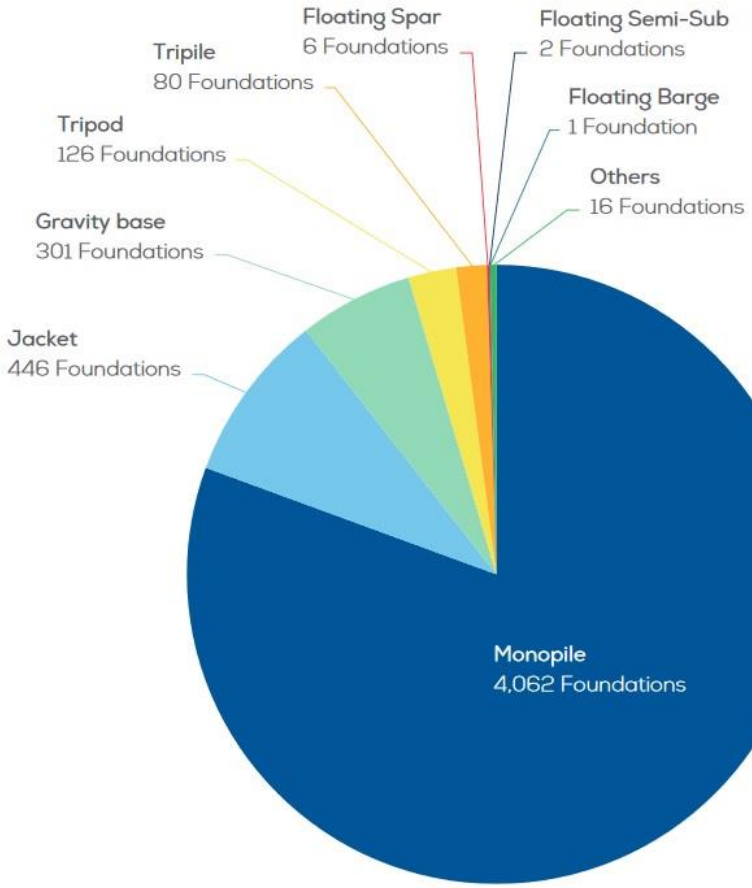

Figure 1.2 - Share of substructures types of grid-connected wind turbines at the end of 2018 (WindEurope, 2018)

This dissertation arises in an effort to contribute to the optimization of scour protections for offshore wind turbine foundations, an important area of research in the offshore wind sector – due to its costs and complexity. A particular focus will be given to scour protections in monopile foundations, the study case of this dissertation.

1.2. CONTEXT AND OBJECTIVES

The offshore wind sector is trending towards cost reduction. That reduction is closely linked to the improvement of the design of the foundation and its scour protection. This dissertation will focus in scour phenomenon induced by long-term sea state on offshore wind turbine foundations and the behaviour of their protections. Although the scour topic is one of the most studied fields of Hydraulic Engineering, the uncertainties related to offshore wind foundation design leads many times to an inaccurate design that may lead to the collapse of the structure, if under designed, or lead to an excessive investment, if overdesigned (Fazeres-Ferradosa, 2018).

Because there are gaps/uncertainties in the literature regarding the design and behaviour of these foundations, and their protections, against long-term sea state (De Vos *et al.*, 2011; Negro *et al.*, 2014; Fazeres-Ferradosa, 2018) the opportunity to discover new solutions is immense. But, to find new solutions, we need to comprehend and reduce the main uncertain factors associated to the scour phenomena. In that regard, the contribution of physical and numerical modeling is vital (De Vos *et al.*, 2011; Fazeres-Ferradosa *et al.*, 2018).

For the design of the protections, most of the studies propose empirical or semi-empirical approaches (Zanke *et al.*, 2011; Matutano, 2013; Petersen *et al.*, 2015). Those same empirical approaches do not consider the long term modeling of environmental variables (Fazeres-Ferradosa, 2018), which are important in today's scenario of climate change.

This dissertation will address the concept of dynamic scour protection introduced by De Vos *et al.* (2012), an economic alternative to static protections. The main objective is to understand if the dynamic scour protections are effective against currents and waves (for long-term sea state), what is their behavior against scour phenomenon, try to understand if there is a specific number of waves for which the dynamic equilibrium is reached and whether they can be as reliable as the static protections.

For that reason, a physical model was constructed and studied at the flume of the Hydraulics Laboratory at the Hydraulics, Water Resources and Environment Division (SHRHA) from the Faculty of Engineering of the University of Porto (FEUP). With a planned series of test for a set of target conditions, a dynamic design approach according to De Vos *et al.* (2012) was carried out, it was tried to define the scour damage and scour depth of the protection models and to fill some gaps regarding the lack of information on the cumulative effects suffered by the protections.

Last but not least, another important aspect of this dissertation is related to the adaptation works made in the Laboratory flume – transforming it from a "current only" flume into a "wave and current" flume. This adaptation played a vital role in the setup of the experimental stage and consequently to the development of this dissertation.

1.3. DISSERTATION OUTLINE

The present dissertation is divided in 5 chapters, presented sequentially, in which all the works performed are described.

Chapter 1 contains a brief introduction to the global wind sector and the importance of offshore scour protections to the sector is given. It is also presented the context and the objectives of this dissertation.

Chapter 2 is dedicated to the research and basic notions regarding the scour phenomena and the design of offshore wind turbine foundations according to a dynamic design approach and it comparison to the static design. In this chapter a brief description of all the parameters necessary to the design of the protections is presented.

Chapter 3 is focused on the experimental installation, the SHRHA laboratory flume at FEUP, and the detailed adaptations regarding the installation of a new wave paddle in order to enable the study of scour protections for the combination of waves and currents. In this chapter it is also mentioned the calibration process of all the necessary equipments, the methods of analysis of the bathymetry and of the assessment of damage in the model and finally explained the construction of the respective model used for the experimental tests.

Chapter 4 is reserved for the presentation of the results obtained and its respective analysis and discussion. Also, a preliminary work regarding the damage number analysis based on a profile obtained using the close-photogrammetry technique is presented. Finally, using the results obtained during the tests, a discussion on the design of protections using the predicted S_{3D} parameter is made, comparing it to the static design of protections.

Chapter 5, reviews and summarizes the conclusions obtained and highlights future research topics that should be addressed, in order to improve the results obtained.

2
STATE-OF-THE-ART

2.1. SCOUR IN OFFSHORE WIND TURBINES

As the offshore term refers to, an offshore wind turbine is a structure located in the marine environment, in the ocean, detached and at a relative distance from the coast (Figure 2.1).

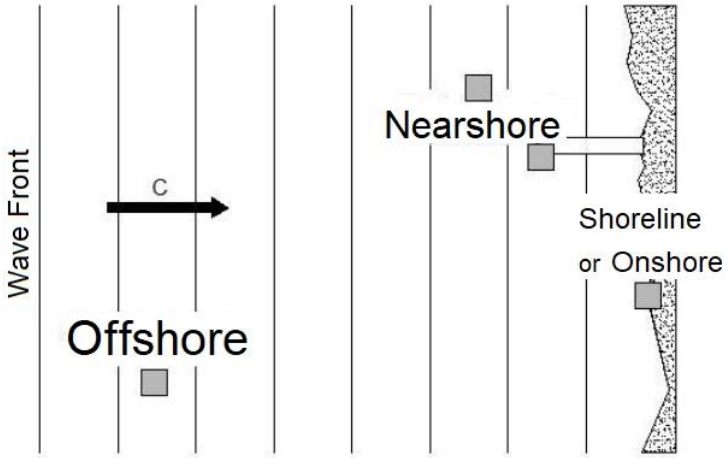

Figure 2.1 - Classification of structures regarding the distance from the coastline (adapted from Teixeira *et al.* (2011)).

As shown in Figure 1.2, Figure 2.2 and Figure 2.3, offshore wind turbines have different foundation configurations. They can be divided into two major groups: the fixed-bottom foundations (Figure 2.2) and the floating offshore wind turbines (FOWT) (Figure 2.3). Because these types of structures are placed in a marine environment, the foundations are normally founded in movable sea-beds, composed by sediments with cohesive - like clays and silts - or non-cohesive - like sand and gravel - properties. The offshore conditions can vary significantly, so the installation of an offshore wind turbine induces substantial changes on the flow. The interaction structure-fluid increases the bed shear stress, that causes the sediment transport, and when the shear stress exceeds a certain value, known as critical shear stress, the sediments start to move away from around the structure, initiating the scour process (Sumer *et al.*, 2001; De Vos *et al.*, 2011; Whitehouse *et al.*, 2011; Sørensen *et al.*, 2013). This dissertation will study scour effects on the most common foundation type, the monopile, founded in non-cohesive sea-beds and protected by a rip-rap scour protection.

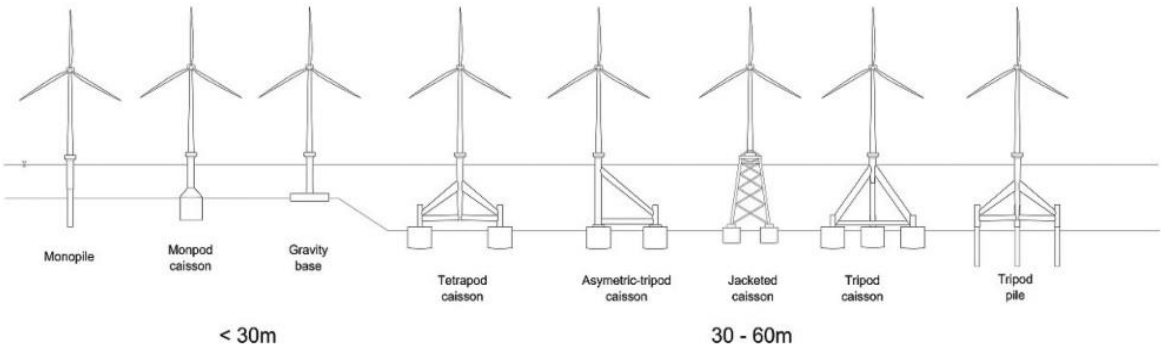

Figure 2.2 - Different types of foundations (Bhattacharya, 2014).

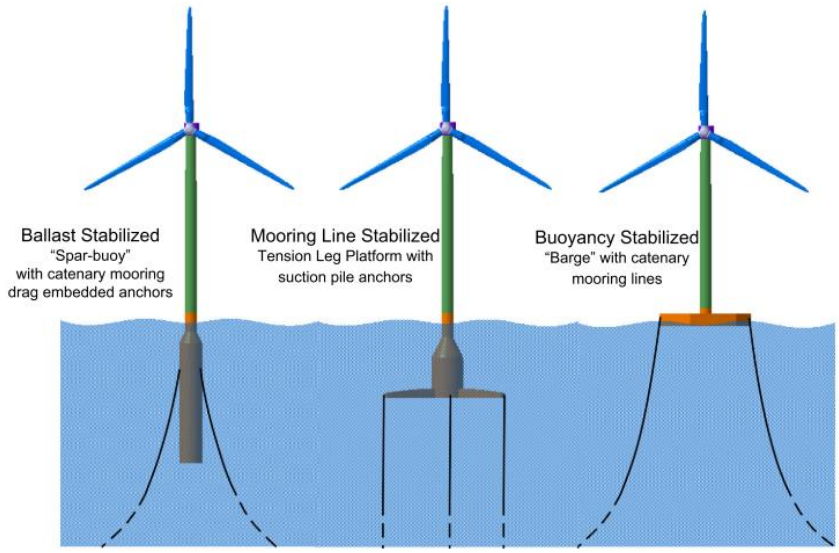

Figure 2.3 - Floating platform concepts for an offshore wind turbine (Tran *et al.*, 2015).

Scour is the erosion of the sea bed in the structures vicinity as a result of the soil-fluid-structure interaction resulting in a generalized sinking of the sea-bed. On the basis of the scour phenomena is the sediment transport. The sediment transport can be of two types (Figure 2.4): bed-load transport, which includes the rolling and saltation mechanisms, and suspended load transport. As aforementioned, when the bed shear stress surpasses the critical shear stress, beginning of the incipient motion, the particle starts to move. Than the saltation occurs when the energy/shear stress increases. Finally, the shear stress increases even further, making the particle to reach the suspended load layer. The particles remains in suspension as much time as the frictional velocity of the particle is bigger than the fall velocity (Collins, 2017).

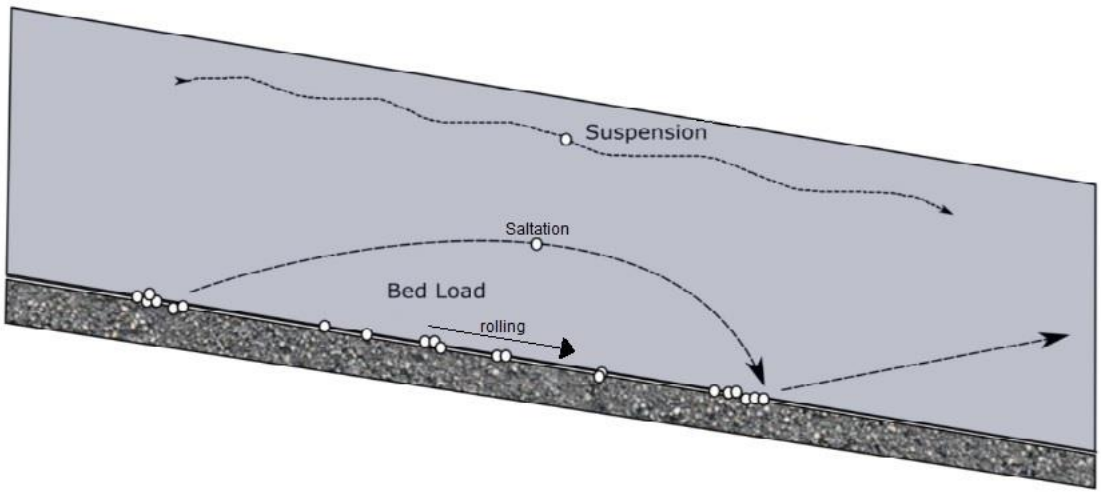

Figure 2.4 - Sediment transport (adapted from Collins (2017)).

As for the scour process, it can be divided into two major categories, that can also be divided into two sub-categories:

- according to their position and influence: global scour or local scour;
- according to the flow regime: clear-water scour or live-bed scour.

Considering the jacket-type foundation example (Figure 2.5) – foundation structure composed by sets of piles – local scour correspond to steep depressions surrounding each one the structure's piles, result of hydrodynamic effects (Fazeres-Ferradosa, 2018). Global scour is expressed by a wider depression formed around the structure, including all the structure footprints. The global scour is the result of a multiplicity of flow effects, detailed in Fazeres-Ferradosa (2018).

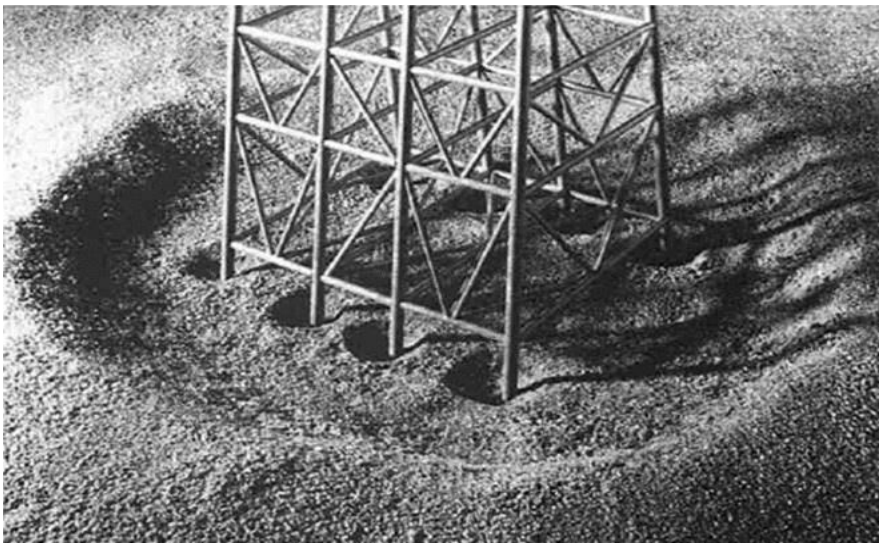

Figure 2.5 - Global and local scour at a jacket type foundation (Whitehouse, 1998).

Clear-water scour happen when the bed shear stress is lower than the critical shear stress. As said before, scour only happens when the bed shear stress is bigger than the critical shear stress but, in the vicinity of the structure, there will be an amplified bed shear stress that induces the sediment motion. This is the clear-water scour principle. As for the live-bed scour, it happens when the bed shear stress is above the critical shear stress, so the sediment transport occurs in the entire sea bed, not only on the structure vicinity. Clear-water scour is defined as occurring when the seabed material upstream of the scouring location remains at rest, whereas live-bed scour conditions exist when there is general sediment transport taking place across the seabed (Harris *et al.*, 2010). Normally, the analysis and comparison of these two forms of scour are made using the Shields parameter (θ) (Fazeres-Ferradosa, 2018).

Much of the effects that scour induces, like the scour depth, on the sea-bed and in the offshore foundations are due to flow patterns resultant from the soil-fluid-structure interaction.

The monopile offshore wind turbine can be considered as a slender pile. The changes in the flow, and the respective flow patterns, induced by vertical slender piles, like the monopile, have been studied for steady currents (Sumer *et al.*, 1997; Nielsen *et al.*, 2013) or waves (Soulsby, 1997; Sumer *et al.*, 1997; Sumer *et al.*, 1997). But, the combination of both effects has some gaps in literature.

The most important flow patterns originated, Figure 2.6, reported by Breusers *et al.* (1991), Sumer (2002) and Petersen *et al.* (2015) are:

- The downflow;
- The horseshoe vortex;
- The lee-wake vortices;
- The contraction of the streamlines.

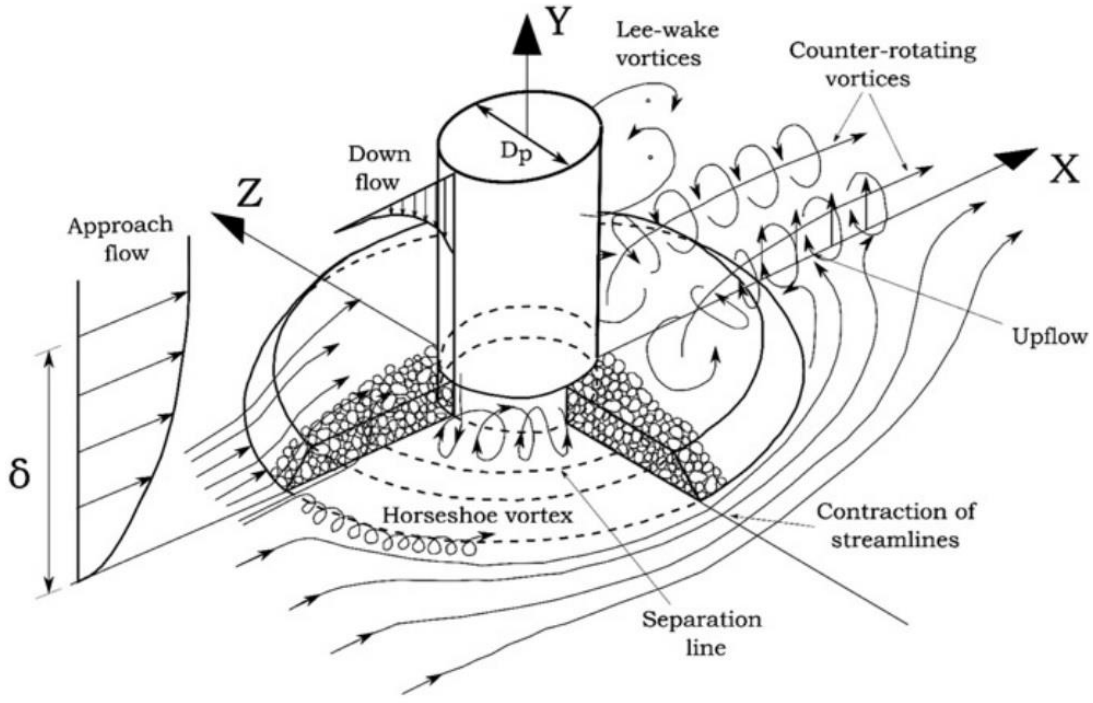

Figure 2.6 - Flow patterns around a monopile foundation and protection (Petersen *et al.*, 2015).

The downflow is caused by the monopile obstruction of the flow. This leads to an abrupt decrease of velocity and to the decrease of stagnation pressure downwards, creating a downward pressure gradient (Fazeres-Ferradosa, 2018).

The horseshoe vortex is the most dominant flow pattern (Petersen *et al.*, 2015) and the major scour mechanism (Whitehouse, 1998). It infiltrates on the scour protection at the pile base and exfiltrating upstream into the main flow, Petersen *et al.* (2015). Due to the downflow in front of the monopile, the flow goes downwards and when it meats the sea-bed it rolls up, generating a vortex. This vortex increases the bed shear stress, leading to scour on the upstream part of the foundation, Figure 2.7.

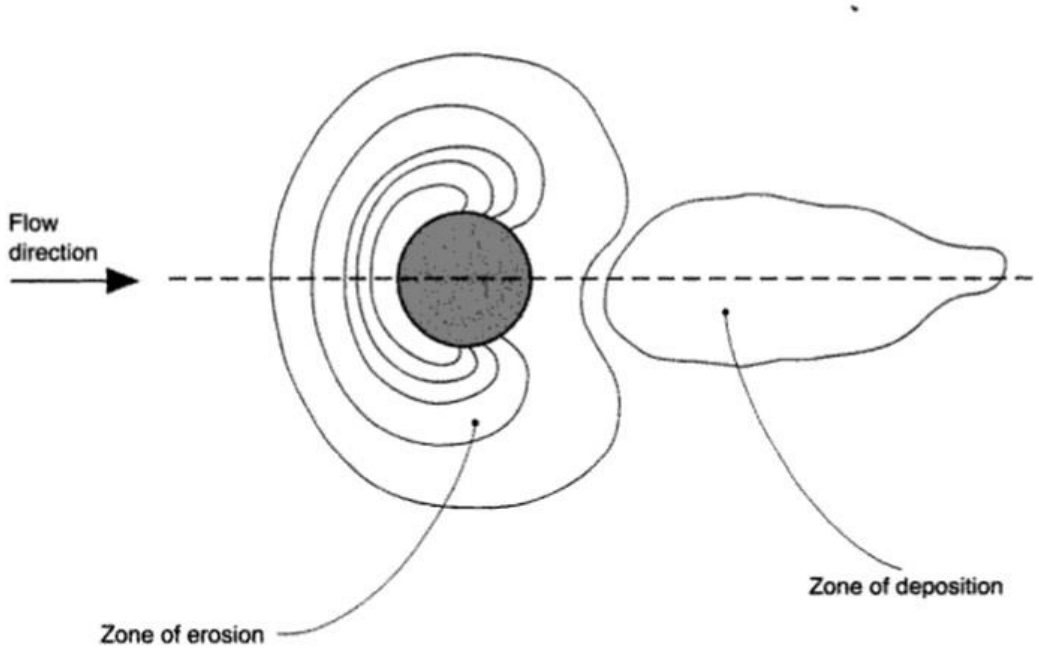

Figure 2.7 - Scour pattern for a vertical cylinder in a steady current (Whitehouse, 1998).

Studies about the horseshoe vortex were performed by Baker (1979), Sumer *et al.* (1992), Sumer *et al.* (1997) and Sumer (2002).

The lee-wake vortices are a flow pattern and a scour mechanism generated on the downstream side of the monopile, due to the separation of the flow. These vortices increase the turbulence levels, due to the flow velocity variation, increasing the bed shear stress on the downstream, arising from the pile edges. So that will lead to scour, on the downstream side of the protection, and respective sediment transport, until its deposition, away from the structure, when the shear stress is no longer enough to cause movement (Fazeres-Ferradosa, 2018).

More information about this topic and the relation of it with the Reynolds number can be found on Sumer (2002) and De Vos (2008). The same relation, but with the Keulegan-Carpenter number, can be found on Sumer *et al.* (1997), Sumer (2002) and De Vos (2008).

The contraction of the streamlines is caused by the separation and bending of the flow around the monopile. When the flow encounters the pile, in the upstream side, the flow deaccelerates to then gain

new acceleration, from the edges to the downstream side. This leads to the increase of shear stress and to scour, near the edges of the monopile (Fazeres-Ferradosa, 2018).

So, why is so important to prevent and protect offshore wind turbines against scour? In the design of this type of structures, the natural frequency of the structure (f_n) has a vital role. The natural frequency of a structure is the frequency at which the structure vibrates freely without any external excitation (Chopra, 2017). In slender structures, as the monopile, the increasing of scour depth leads to the decrease of the relative natural frequency as shown on van der Temple (2006) (Figure 2.8). The change of the natural frequency will produce modifications on the dynamic amplification, leading to an increase of the vibration amplitudes, stresses and to fatigue problems (Bhattacharya, 2014). In that regard, is essential to apply scour protections to the offshore wind turbine foundations in order to prevent scour and its harmful effects to the structure safety. In order to a more extensive development on this subject, the works of van der Temple (2006) and Bhattacharya (2014) are recommended.

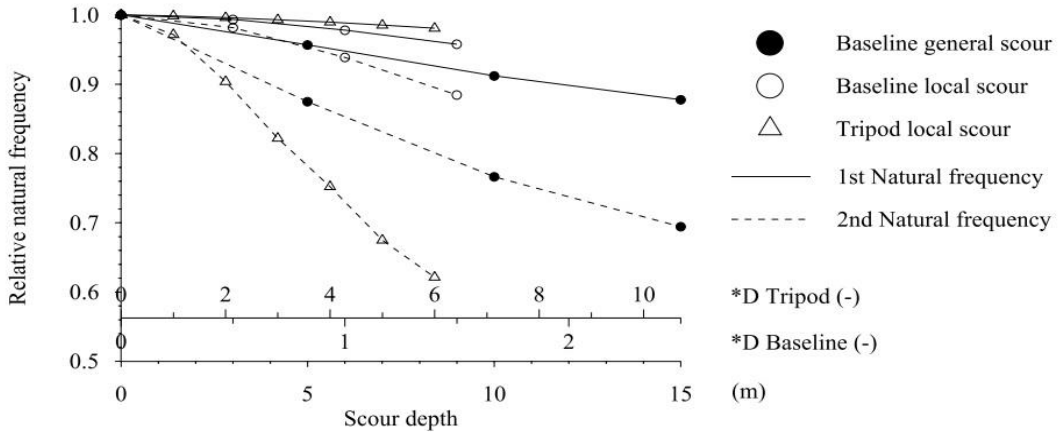

Figure 2.8 – Variation of natural frequency with local an general scour (Zaaijer, 2002).

It is important to understand and define the scour phenomena and all the variables attached to it. This chapter will focus on the basic concepts related to this topic, which are crucial to the development of future chapters.

2.2. BED SHEAR STRESS

The bed shear stress, τ_b (N/m^2), is the frictional force per unit of the sand-bed area responsible for the sediment motion and can be expressed as a function of the friction velocity u_* (m/s) as in Eq. (2.1).

$$\tau_b = \rho_w \cdot (u_*)^2 \tag{2.1}$$

The bed shear stress is mainly induced by waves, steady currents or by the combination of both. There are other variables that influence the bed shear stress, like tides, as described by Fazeres-Ferradosa (2018), but this dissertation will only focus on the effects that waves and currents generate.

There is one concept, regarding the flow, that is crucial for the future topics and for the understanding of the behavior of the fluid in the vicinity of a structure. That concept is the so-called bottom boundary

layer (δ), also known as bed boundary layer. Described as the layer in which the flow is considerably influenced by the sea-bed (Fazeres-Ferradosa, 2018). According to De Vos (2008), the bottom boundary layer, Figure 2.9 and Figure 2.10, is commonly referred as the distance from the boundary surface to the point where the local velocity is equal to 0.995 times the depth-averaged flow velocity (U_c).

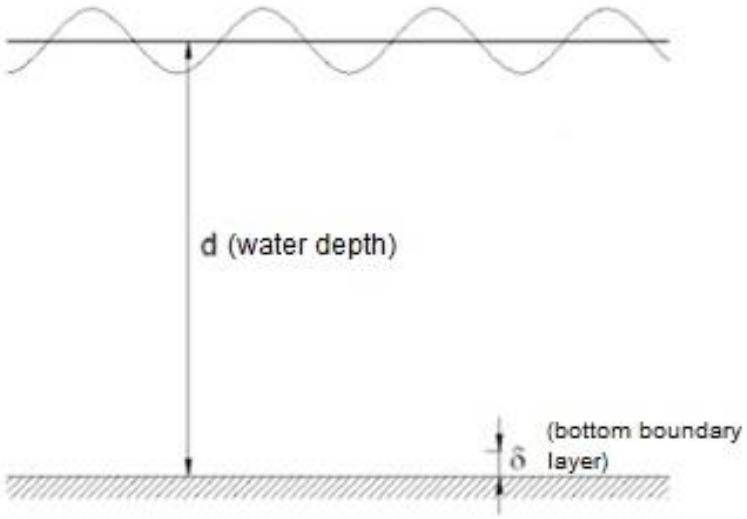

Figure 2.9 - Water depth and boundary layer (adapted from Fredsøe *et al.* (1992)).

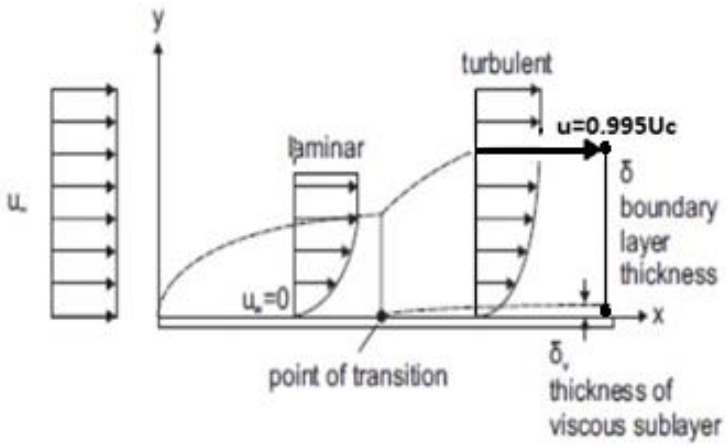

Figure 2.10 - Boundary Layer velocity profile (adapted from Schlichting *et al.* (2013)).

Typically, as smaller the thickness of the boundary layer is, the bigger is the shear stress for the same value of U_c (Fazeres-Ferradosa, 2018). Because waves have a smaller boundary layer thickness than currents, the shear stress induced by waves tends to be higher than the one induced by currents. But De

Vos (2008) states that, due to the oscillatory nature of waves, currents are the leading factor in sediment transport. More detailed information about the boundary layer can be found on Soulsby (1997).

2.2.1. Wave induced Bed Shear Stress

The bed shear stress induced by waves, $\tau_{b,w}$ (N/m^2), is a function of the wave friction factor, f_w, of the wave orbital velocity, U_m (m/s), and can be calculated with the Eq. (2.2).

$$\tau_{b,w} = \frac{1}{2} \cdot \rho_w \cdot f_w \cdot {U_m}^2 \tag{2.2}$$

For waves in shallow conditions (d/L<0.5), the wave orbital velocity generated is an oscillatory horizontal velocity with an amplitude of U_m. For that reason, the bed shear stress induced by waves is also oscillatory, but with an amplitude of $\tau_{b,w}$. This velocity is a function of the wave height H (m), the wave period T (s) and the wave length L (m) and for static scour protections can be expressed from the linear wave theory - Eq. (2.3) - and for dynamic scour protections is obtained from the wave spectrum (Fazeres-Ferradosa, 2018).

$$U_m = \frac{\pi H}{T} \cdot \frac{1}{sinh\left(\frac{2\pi d}{L}\right)} \tag{2.3}$$

As for the wave friction factor, there are a variety of formulas, depending on the authors, as described by De Vos (2008) and De Vos *et al.* (2011). The authors also present different formulations for smooth or rough sea beds. Because the bed shear stress induced by waves depends on this parameter, the option for one specific author' formula of the wave friction factor, instead of a different one, may influence the value obtained. This dissertation will follow past works realized by Soulsby (1997), De Vos *et al.* (2011) and Fazeres-Ferradosa (2018). Summarizing the main formulas in the literature, Fredsøe *et al.* (1992) used the Eq. (2.4) for the wave friction factor and the Eq. (2.6) for the wave boundary layer thickness (δ).

$$f_w = 0.04 \cdot \left(\frac{A}{k_s}\right)^{-0.25}, \frac{A}{k_s} > 50 \tag{2.4}$$

$$f_w = 0.04 \cdot \left(\frac{A}{k_s}\right)^{-0.75}, \frac{A}{k_s} < 50 \tag{2.5}$$

$$\frac{\delta}{k_s} = 0.09 \cdot \left(\frac{A}{k_s}\right)^{0.82} \tag{2.6}$$

where A (m) - Eq.(2.7) - represents the amplitude of the wave orbital motion, that depends on the value of U_m and T, and k_s (m) is the bottom roughness.

$$A = \frac{U_m T}{2\pi} \tag{2.7}$$

The Eq. (2.5) is an approximation suggested by Kamphuis (1975) for small values of the ratio A/k_s. But for small values of the ratio A/k_s, Dixen *et al.* (2008) proposed some changes for the equations Eq. (2.5) and Eq. (2.6), as shown in equations Eq. (2.8) and Eq. (2.9), respectively.

$$f_w = 0.32 \cdot \left(\frac{A}{k_s}\right)^{-0.8}, 0.2 < \frac{A}{k_s} < 10 \tag{2.8}$$

$$\frac{\delta}{k_s} = 0.08 \cdot \left[\left(\frac{A}{k_s}\right)^{0.82} + 1\right] \tag{2.9}$$

Nielsen (1992) proposed another formulation for the f_w factor resulting in the equation Eq. (2.10):

$$f_w = exp\left[5.5 \cdot \left(\frac{A}{k_s}\right)^{0.2} - 6.3\right] \tag{2.10}$$

Finally, the formula that will be used during this dissertation, proposed by Soulsby (1997), is valid for all the values of A/k_s, but with a little difference. Instead of k_s, the author replaced the bed roughness for the bed roughness length z_0 (m), that depends on the mean diameter of the sea-bed sediments d_{50} (m).

$$f_w = 1.39 \cdot \left(\frac{A}{z_0}\right)^{-0.52} \tag{2.11}$$

$$z_0 = \frac{d_{50}}{12} \tag{2.12}$$

The Figure 2.11, regarding a study at a geometric scale of 1/50 realized by De Vos *et al.* (2011), shows the influence of the wave friction factor for the final value of the bed shear stress induced by waves, according to the different authors aforementioned.

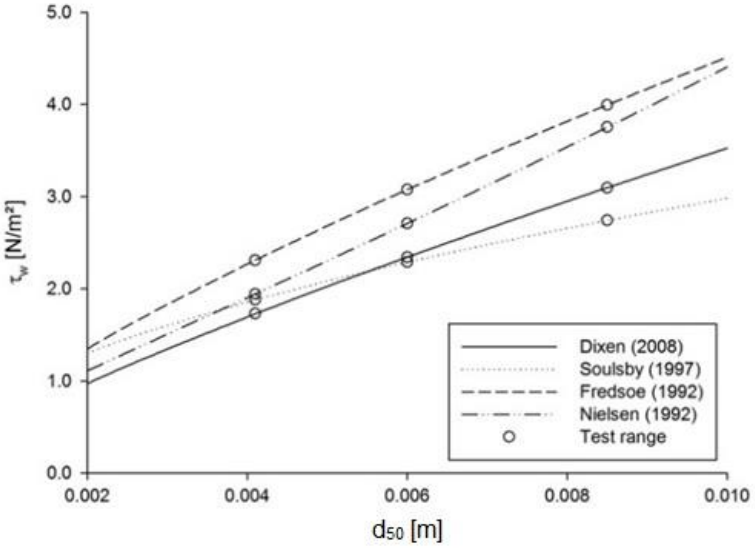

Figure 2.11 - Wave related bed shear stress τw as a function of the stone size d_{50}, for different authors' formulations of the wave friction factor: d=0.4 m; H=0.1 m; T=1.4s (De Vos *et al.*, 2011).

Analyzing Figure 2.11, we can access that the bigger the value of d_{50}, the bigger is the difference between the values of f_w, for different authors. This proves the importance of f_w, for the assessment of $\tau_{b,w}$, especially for larger grains/stone sizes as those used in the scour protections.

2.2.2. Currents induced Bed Shear Stress

The bed shear stress induced by currents, $\tau_{b,c}$ (N/m^2), is a function of the current friction factor, f_c, of the depth average current velocity, U_c (m/s), and can be calculated with the Eq. (2.13).

$$\tau_{b,c} = \frac{1}{2} \cdot \rho_w \cdot f_c \cdot {U_c}^2 \tag{2.13}$$

Like the wave friction factor, there are also various formulations for the current friction factor (De Vos, 2008). For the sake of continuity and coherence with previous works conducted by De Vos (2008) and Fazeres-Ferradosa (2018), this dissertation will use the formulas presented in Liu (1998) - Eq. (2.14).

$$f_c = \frac{2g}{Ch^2} = \frac{2g}{\left[\frac{\sqrt{g}}{k} \cdot \ln\left(\frac{d}{z_0 \cdot e}\right)\right]^2} = \begin{cases} \dfrac{0.06}{\left[\log\left(\dfrac{12d}{3.3 \cdot \frac{\upsilon}{u^*}}\right)\right]^2} & \dfrac{u_* k_s}{\nu} \leq 5 \; - \; smooth\; flow \\ \dfrac{0.06}{\left[\log\left(\dfrac{12d}{k_s}\right)\right]^2} & \dfrac{u_* k_s}{\nu} \geq 70 \; - \; rough\; flow \end{cases} \tag{2.14}$$

In Eq. (2.14) the value of f_c depends on the value of the gravitational acceleration g (m^2/s) and on the Chézy coefficient Ch ($m^{1/2}/s$). The Chézy coefficient can be translated as a function of the square root of the gravitational acceleration, of the Von Karman constant k, in this case equal to 0.4, of the Nepper's number *e*, of the roughness length z_0 (m) and the water depth d (m). The other parameters used on Eq. (2.14) are the kinematic viscosity ν (m^2/s), the bottom roughness k_s (m) and the friction velocity u_* (m/s).

As shown in Eq. (2.14), there is a distinction between smooth flow and rough flow. Smooth and rough flows are two types of turbulent flow regimes. There are two major types of flow regimes:

- Laminar flow;
- Turbulent flow;

Between both, there is an unstable zone that corresponds to the transition regime. So the limits between regimes were made using the so-called Reynolds Number (Re),

$$\mathrm{Re} = \frac{\rho D_p U}{\mu} = \frac{D_p U}{\nu} \tag{2.15}$$

where U (m/s) represents the flow velocity, ρ the fluid density (kg/m^3), D_p the pile diameter (m), μ the dynamic viscosity ($N{\cdot}s/m^2$) and ν the kinematic viscosity (m^2/s).

In the laminar flow (Re<2000), the fluid presents regular trajectories, the fluid particles do not cross each other, the velocity variations are extremely slow in time - or almost non existent - and the flow is dominated by viscosity effects, not being affected by the characteristics of the surface of the rigid layer (Webber, 1971; Quintela, 2005). In the turbulent flow (Re>4000), the fluid particles have abrupt variations in space and time, the velocity field is also variable in space and time and the regime is separated from the boundary surface by a thin layer in which the flow presents laminar behavior (the so-called laminar boundary sub-layer).

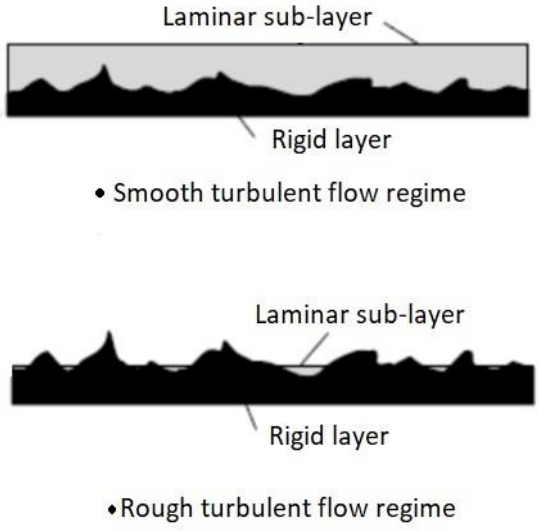

Figure 2.12 - Smooth and Rough turbulent flow (Brkić *et al.*, 2018).

So, the smooth flow regime is ruled by the Reynolds number, as for the rough flow the regime is ruled by the bottom roughness k_s. For a more detailed explanation about this subject, the author suggests the works of Novais-Barbosa (1985).

According to De Vos (2008), the value of k_s can be obtained:

- for the case without ripples: $k_s=2.5d_{50}$;
- for the case with ripples: $ks=(0.5\text{-}1)H_r$.

with d_{50} (m) being the sediment mean diameter and H_r (m) the ripple's height. For d_{50} parameter, should be used D_{50}, when referring to the material of the scour protection (Fazeres-Ferradosa, 2018).

The value of z_0, for the current effect, has a different configuration from the wave effect and can be obtained using the Eq. (2.16), according to the flow type.

$$z_0 = \frac{k_s}{30} + \frac{\upsilon}{9u^*} = \begin{cases} \frac{\upsilon}{9u^*}, & \frac{u^* k_s}{\nu} \leq 5 \quad smooth\ flow \\ \frac{k_s}{30}, & \frac{u^* k_s}{\nu} \geq 70 \quad rough\ flow \end{cases} \tag{2.16}$$

For the steady current effect, the velocity distribution in a steady, uniform, turbulent boundary layers correspond to the logarithmic profile (De Vos, 2008). The velocity equation for a specific depth z (m) is then a function of the friction velocity u_* (m/s), the Von Karman constant k, and the roughness length z_0 (m).

$$U(z) = \frac{u^*}{k} \ln\left(\frac{z}{z_0}\right) \tag{2.17}$$

According to Fazeres-Ferradosa (2018), considering Eq. (2.17) and the rough flow member of Eq. (2.16), we can verify that the value of depth-average current velocity, U_c, is reached, approximately, for a value of 0.4d counting from the sea-bed. That 0.4d reference is also used when measuring the velocities during physical modeling and experimentation phases.

2.2.3. Waves and Currents induced Bed Shear Stress

The simultaneous reproduction of waves and currents and their combined effect is important to replicate offshore and marine conditions as much accurate as possible. But according to several authors, the combination of both effects and both shear stresses do not follow to a linear combination of their separate components (Soulsby, 1997; Soulsby *et al.*, 2005; De Vos *et al.*, 2011; Saruwatari *et al.*, 2014) as shown in Figure 2.14. According to Soulsby (1997), there are different theories that attempt to describe this non-linear interaction between waves and currents. More detailed information about the scour effects due to waves and currents can be found in Sumer *et al.* (2001).

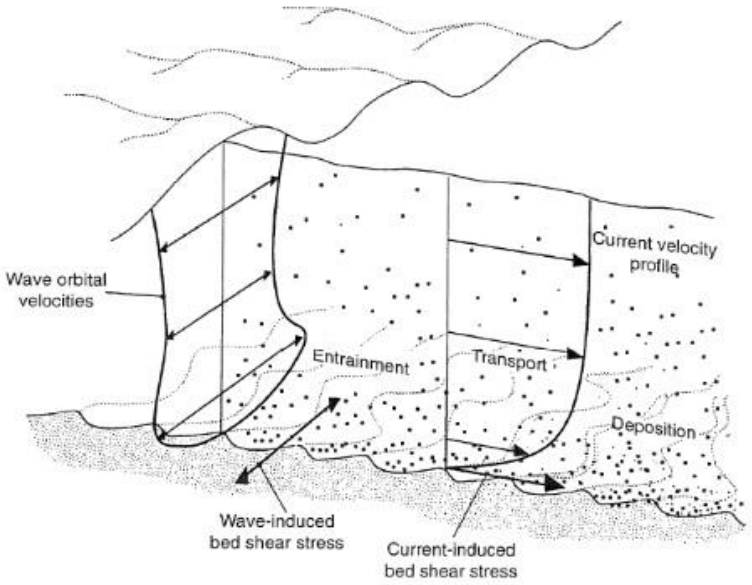

Figure 2.13 - Wave orbital velocity and current velocity profiles (Soulsby, 1997).

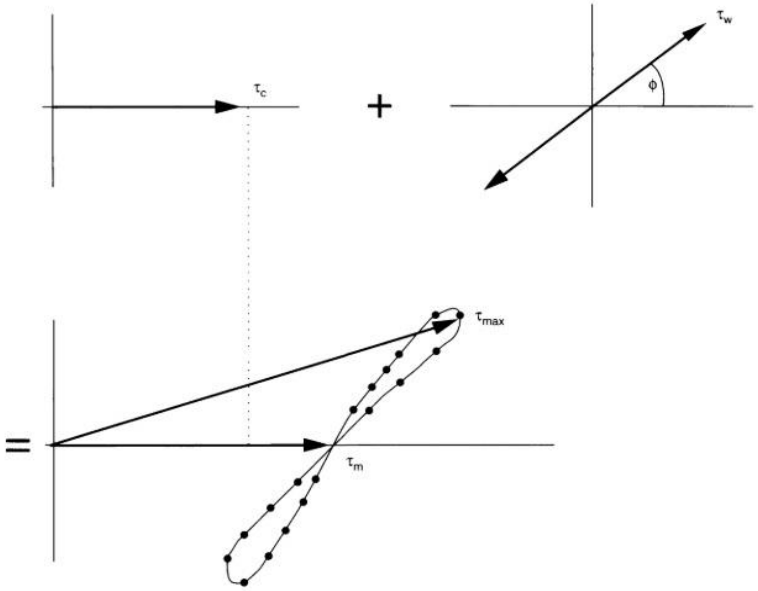

Figure 2.14 - Schematic diagram of non-linear interaction of wave and current bed shear stresses (Soulsby, 1997).

In literature the most common approaches used to describe the interaction between waves and currents, are the ones proposed by Soulsby (1997) and Fredsøe *et al.* (1992).

So, the shear stresses determined by those authors are the combined mean bed shear stress, τ_m (N/m^2), and the maximum bed shear stress, τ_{max} (N/m^2). The first one is important for sediment diffusion while

the second one is important to set the threshold of motion (explained in more detail later), according to Malarkey *et al.* (2012).

According to Soulsby (1997), the formulas for shear stress combinations are:

$$\tau_m = \tau_c \left[1 + 1.2\left(\frac{\tau_w}{\tau_c + \tau_w}\right)^{3.2}\right] \tag{2.18}$$

$$\tau_{max} = [(\tau_m + \tau_w \cos\phi)^2 + (\tau_w \sin\phi)^2]^{1/2} \tag{2.19}$$

Where ϕ (°) is the angle between the currents direction, ϕ_c (°), and the waves direction, ϕ_w (°), Zhu *et al.* (2016). In both Eq. (2.18) and Eq. (2.19), τ_c and τ_w correspond to $\tau_{b,c}$ and $\tau_{b,w}$, respectively.

In Fredsøe *et al.* (1992), the formulas for shear stress combinations are:

$$\tau_m = \frac{2}{\pi}\rho_w f_w U_m U_\delta \tag{2.20}$$

$$\tau_{max} = \frac{2}{\pi}\rho_w f_w (U_m + U_\delta)|U_m + U_\delta| \tag{2.21}$$

U_δ (m/s) represents the peak value of the near-bed orbital velocity that can be computed using Eq. (2.22) - complemented by the use of Eq. (2.23)

$$U_\delta = C - \sqrt{C^2 - {U_c}^2} \tag{2.22}$$

$$\mathrm{C} = U_c + \frac{1}{\pi} f_w U_m \left(6.2 + \frac{1}{k}\ln\left(\frac{d}{30\delta}\right)\right) \tag{2.23}$$

f_w and δ should be calculated according to Eq. (2.4) and Eq. (2.6), respectively.

This dissertation will follow Soulsby (1997) formulas and will only consider the combined effect of waves and currents propagating in the same direction.

2.2.4. AMPLIFICATION FACTOR

The installation of an offshore wind turbine will lead to changes in the flow, increasing the bed-shear stress. For that reason, it is common to use the amplification factor, α, to express the influence of the structure on the modification of flow conditions.

The amplification factor can be described as the ratio between the amplified bed shear stress, τ (N/m^2), and the undisturbed bed shear stress, τ_∞ (N/m^2),

$$\alpha = \frac{\tau}{\tau_\infty} \tag{2.24}$$

Because there is not a consensual value for the amplification factor, the reliability of scour protections could be exposed, since the computation of the acting bed shear stress on scour protections is made by multiplying the undisturbed bed shear stress to the amplification factor (Fazeres-Ferradosa, 2018). An incorrect assessment of the amplification factor value could lead to errors in scour protection design. The amplification factor is assessed through physical modelling.

Table 2.1 - Different values for the amplification factor α, according to some authors.

Reference	Amplification factor α
De Vos (2008)	[2.2 – 2.5] (waves)
Sumer (2002)	3 (waves)
Whitehouse (1998)	4 (steady currents)

The amplification factor is directly related with the scour pattern on the protection and depends on the geometry of the foundation, on the type and velocity of flow, on the distance from the structure and others (Fazeres-Ferradosa, 2018).

2.3. SHIELDS PARAMETER

The Shields parameter (θ) concept was introduced by Shields (1936) and corresponds to the dimensionless form of the shear stress - Eq. (2.25). It gives the ratio between the load on the grain to the gravitational force that resists movement (De Vos, 2008). Normally, it is used to define the threshold of motion and/or the incipient motion of sediments (see section 2.3.1)

$$\theta = \frac{\tau_b}{g(\rho_s - \rho_w)d_s} = \frac{(u_*)^2}{g\Delta d_s} \tag{2.25}$$

$$\Delta = \frac{(\rho_s - \rho_w)}{\rho_w} \tag{2.26}$$

The Shields parameter depends on the bed shear stress (τ_b), gravitational acceleration (g), the water and sediment density (ρ_w and ρ, respectively) and on the diameter of the sediment grain (d_s [m]). But can be simplified by using the friction velocity (u_*) and the relative sediment density (Δ) as shown in Eq. (2.26).

2.3.1. THRESHOLD OF MOTION

The sediment transport occurs due to a different combination of factors and conditions. According to Miller *et al.* (1977):

- Threshold of motion starts when the conditions are slightly less than those necessary to initiate the motion;
- Incipient motion is when a small degree of sediment movement starts due to a slight increase in the velocity and stress of the fluid;

Breusers *et al.* (1991) have a more detailed definition of the threshold, defining it as the moment when the flow forces acting on a particle are enough to surpass the gravity force (main stabilizing force of a non-cohesive particle).

The forces acting on a non-cohesive particle of the sand-bed are shown in Figure 2.15. The forces responsible for the sediment movement are F_D (N) - horizontal drag force - and F_L (N) - vertical lift force – and the main responsible for the particle movement resistance are W (N) – submerge weight and Fs (N) – frictional forces between the grains.

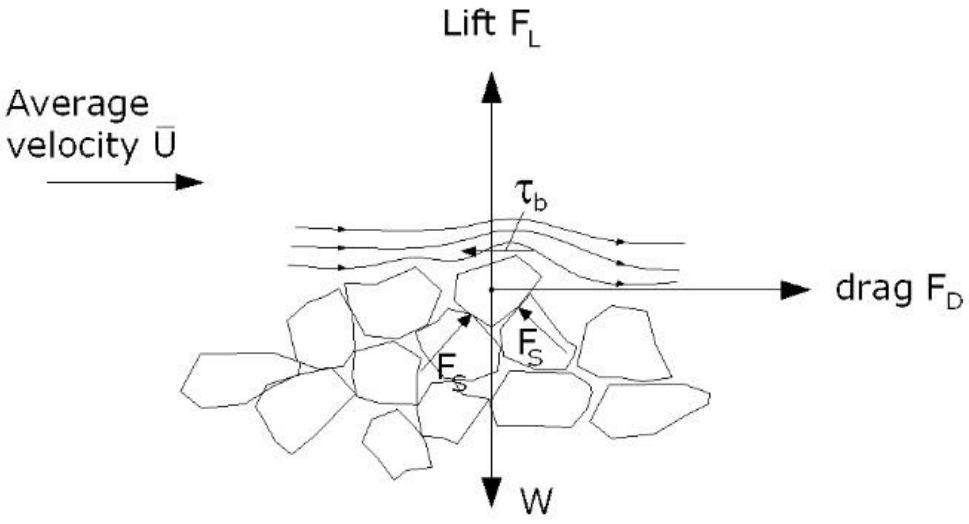

Figure 2.15 - Forces acting on a sediment grain, resting on the bed (De Vos, 2008).

So, the bottom bed shear stress can be expressed as function of the horizontal drag force and of the projected area of the grain on the horizontal plane (A^* [m^2]).

$$\tau_b = \frac{F_D}{A^*} \tag{2.27}$$

The bed shear stress for which the threshold of motion starts is the critical bed shear stress (τ_{cr} [N/m^2]) and represents the minimum shear stress for which the sediments start their motion. Shields (1936)

defined θ_{cr} -Eq. (2.28) - as the non-dimensional parameter for the threshold motion that represents the τ_{cr}.

$$\theta_{cr} = \frac{\tau_{cr}}{g(\rho_s - \rho_w)d_s} = \frac{(u_{cr}^*)^2}{g\Delta d_s} \tag{2.28}$$

Shields (1936) also introduced his concept of the Shields curve (Figure 2.16), that relates the Shields parameter with the Reynolds number of the particle (Re^*) – see Eq. (2.30). With the Shields curve, it is possible to preview, for a certain dimension of sediment and for a certain associated shear stress, if the sediments start to move or not. For large dimensions of a particle, θ_{cr} tends to 0.056. For the scour protections design, De Vos *et al.* (2011) suggests the value of 0.035.

$$Re^* = u_* \frac{d_s}{\upsilon} \tag{2.29}$$

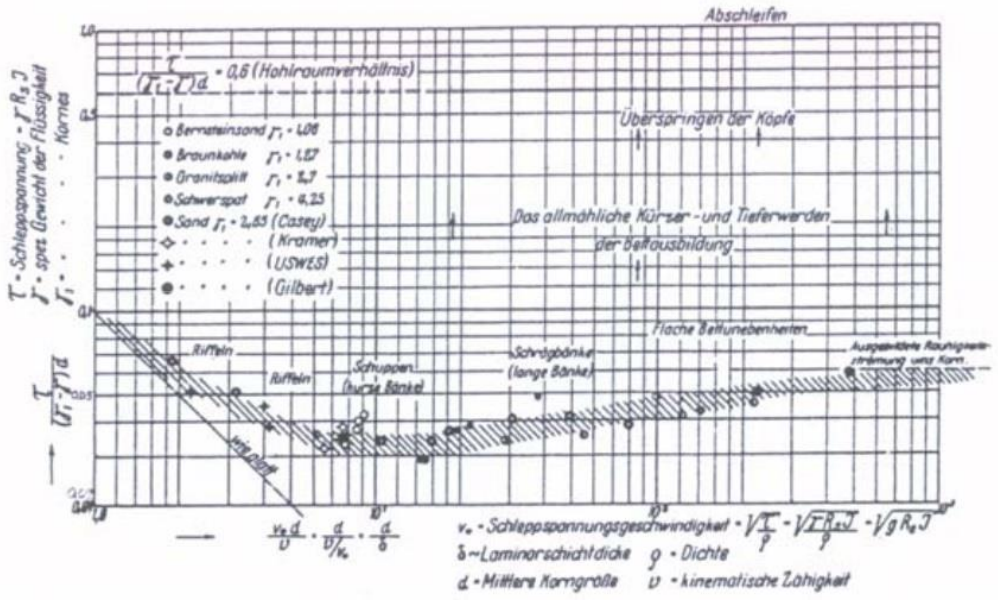

Figure 2.16 - Shields diagram (Shields, 1936).

Because the Shield curve plots a graphic in which both variables are implicit from each another, Soulsby (1997) introduce the notion of the dimensionless grain size (D^*) – Eq. (2.30) - creating an adaption of the Shields curve (Figure 2.17).

$$D^* = \left(\frac{g(s-1)}{v^2}\right)^{1/3} d_s \tag{2.30}$$

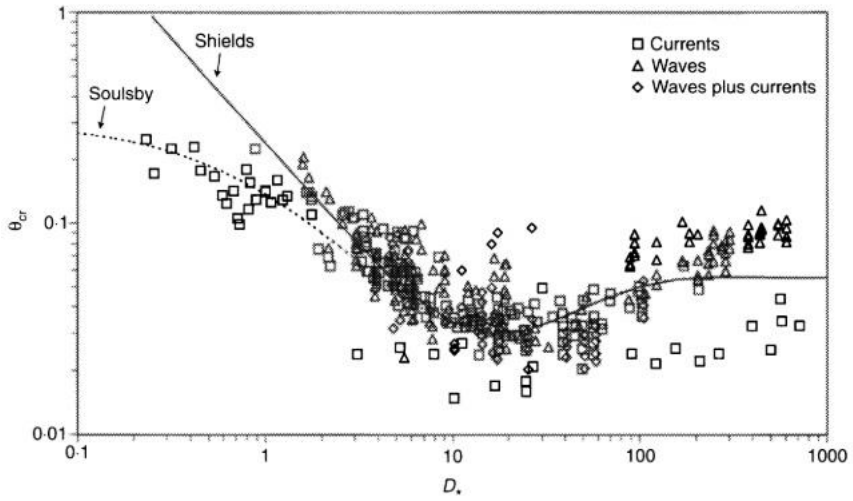

Figure 2.17 - Threshold of motion of sediments beneath waves and/or currents (Soulsby, 1997)

For a more detailed explanation about this subject, the author suggests to the works of Shields (1936), Miller *et al.* (1977), Buffington *et al.* (1997) and Soulsby (1997).

2.4. OTHER PARAMETERS

Shear stress and threshold of motion are two main aspects required to describe the behavior of the sea-bed and the scour protection, under severe offshore conditions. However, for a proper design of a scour protection, other parameters are needed to take into account:

- Environmental parameters: loads acting on the protection due to offshore conditions;
- Structural parameters: associated to the resistance and composition of the scour protection;
- Scour parameters: associate scour effects to the damage or failure of the scour protection;

2.4.1. ENVIRONMENTAL PARAMETERS

The environmental parameters can be described as the properties of the elements that form the offshore environment and that can be related to the loads imposed to the structure.

The most common environmental parameters considered are associated with:

- The water depth;
- The wave characteristics;
- The number of waves;
- The current velocity;
- The sediments properties;
- Storm duration.

2.4.1.1. Water depth

The water depth (d) has a bigger influence on the velocities, both U_c and U_m.

Regarding the steady currents velocities, lower values of water depth lead to higher values of U_c (Fazeres-Ferradosa, 2018). For bottom velocities, higher values of water depth, for the same wave characteristics - height (H) and period (T) -, leads to smaller values of U_m. But because this parameter influences the wave height, the increase of the water depth allows higher waves to occur without breaking and the higher the wave height, the higher the value of U_m (De Vos, 2008).

The effect of certain variables, such as the water depth, is often highly non-linear, thus it is hard to quantify the direct influence of these parameters on the shear stress acting on the scour protection.

2.4.1.2. Wave characteristics

2.4.1.2.1 Linear and non-linear waves

The wave height (H) and period (T), are two of the main characteristics used to define the sea-state conditions, representing an important part of the environmental conditions that affect the offshore structures.

Also noteworthy are the wave amplitude (a), the wave length (L) and the wave frequency (f). The wave amplitude, for linear waves, can be defined as the distance between a wave crest (or trough) and the still-water level (SWL). Its value corresponds to half of the wave height (a=H/2 [m]). The wave length L (m) is the horizontal distance between any two points with the same phase on successive waves. For the linear wave theory, the wavelength is obtained with the Eq. (2.31):

$$L = \frac{gT^2}{2\pi}\tanh\left(\frac{2\pi d}{L}\right) \tag{2.31}$$

The wave frequency f (s^{-1}) can be defined as the number of cycles or the number of occurrences of a repeating event per unit of time. For the linear wave theory, the frequency is commonly defined as the inverse of the wave period.

The linear wave theory, introduced by Airy (1841), also introduces the notion of water surface elevation η (m) - a function of a horizontal position *x* and an instant *t*.

$$\eta(x,t) = a \cdot \cos(k \cdot x - w \cdot t - \Psi) \tag{2.32}$$

where *a* represents the wave amplitude, k is the wave number (k=2π/L), *w* is the angular frequency (*w*=2π/T) and Ψ the phase shift.

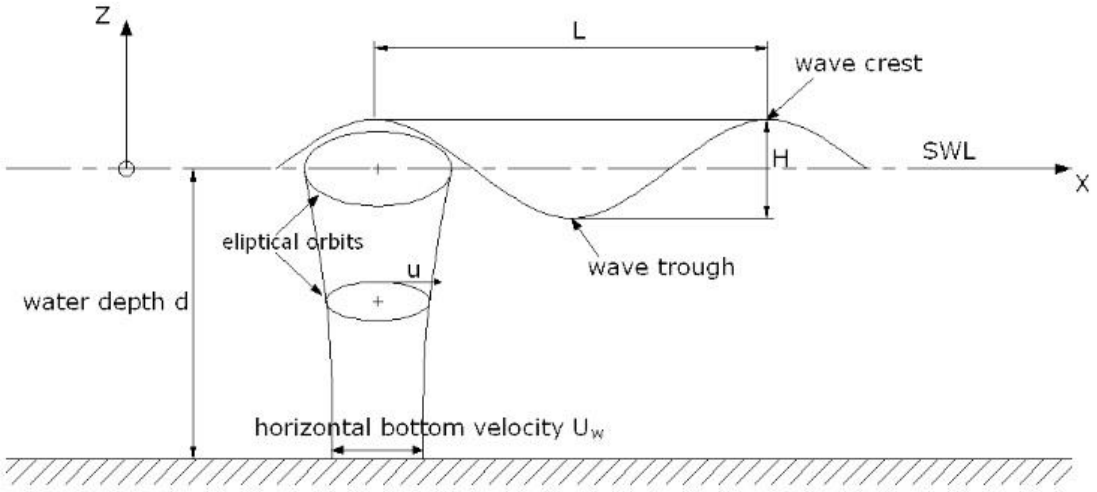

Figure 2.18 - Linear wave theory characteristics (De Vos, 2008)

As shown in Figure 2.18, the motion of a water particle, for a certain water depth d (m), is made according to an elliptical orbit – the velocity of the particle has a vertical and a horizontal component. According to Holthuijsen (2010), when descending towards the bottom, the elliptical orbits tend to be more flattened and only the horizontal velocity component remains. Using the linear wave theory, the amplitude of the horizontal velocity (u) is:

$$u = \frac{H}{2}\frac{gT}{L}\frac{\cosh\left(\frac{2\pi(z+d)}{L}\right)}{\cosh\left(\frac{2\pi d}{L}\right)} \tag{2.33}$$

Because the interest is to determine the bottom velocity, for a depth z=-d the amplitude of the bottom horizontal velocity (U_m) is obtained with the Eq. (2.34).

$$U_m = u(z=-d) = \frac{H}{2}\frac{gT}{L}\frac{1}{\cosh\left(\frac{2\pi d}{L}\right)} = \frac{\pi H}{T}\frac{1}{\sinh\left(\frac{2\pi d}{L}\right)} \tag{2.34}$$

When the wave amplitude is no longer smaller compared with the water depth, non-linear waves start to occur. Thus, the distance between the crest and the SWL is no longer equal to the distance between the trough and the SWL, so the equation a=H/2 is no longer valid for the wave amplitude (De Vos, 2008; Fazeres-Ferradosa, 2018). The non-linear waves troughs become wider and less deep, whereas the crests become steeper and higher (De Vos, 2008). As the water depth becomes small or the wave steepness increases, then higher-order theories must be used – the so-called finite-amplitude wave theories – such as the Stokes or Fenton's Fourier theories (De Vos, 2008; Fazeres-Ferradosa, 2018). A more detailed

explanation about this matter can be found in the works of Fenton (1988), Fenton (1999), De Vos (2008) and US Army Corps of Engineers (2012).

Another important wave characteristic is its height physical limitation by the water depth (d) and the wave length (L). For deep waters, waves break when they are too steep, so the breaking wave height H_b (m) is a function of the wave length - as shown by Michell (1893).

$$\frac{H_b}{L} = 0.142 \tag{2.35}$$

For transitional and shallow waters, waves break when their heights become too high compared to the water depth. So a simplified equation - Eq. (2.36) - was proposed by the US Army Corps of Engineers (2012) for the breaking wave height for this second case.

$$\frac{H_b}{d} = 0.78 \tag{2.36}$$

Since physical model studies performed by the US Army Corps of Engineers (2012) have shown that the Eq. (2.36) gives a good estimation for oscillatory waves this equation will be used during all this dissertation.

2.4.1.2.2 Irregular Waves

In real life, the sea surface is composed of waves with different heights, periods and directions of propagation, producing an irregular wave train.

For the irregular wave's analysis, it is usual to use two different methods:

- Spectral analyses;
- Wave-by-wave analyses.

The first one is based in the Fourier transform of a wave train. Its disadvantage is the distortion of non-linear waves since the spectral analysis is linear. As for the second one, the wave-by-wave – or wave train – analysis is based on the time-history of the sea surface, although it does not take into account the different incident directions of the waves at a certain point (De Vos, 2008).

The wave-by-wave method utilizes the zero down-crossing method, or zero up-crossing method, to identify the individual waves and determine the respective wave height and wave period. Considering the zero down-crossing method, a wave is identified by the downward crossing of the zero-line by the surface elevation (US Army Corps of Engineers, 2012). According to De Vos (2008), each wave identified has an individual wave height H_i (m) – vertical distance between the lowest and highest consecutive point between two zero down-crossings - and an individual wave period T_i (s) – time period between two the two zero-crossings – as shown in Figure 2.19.

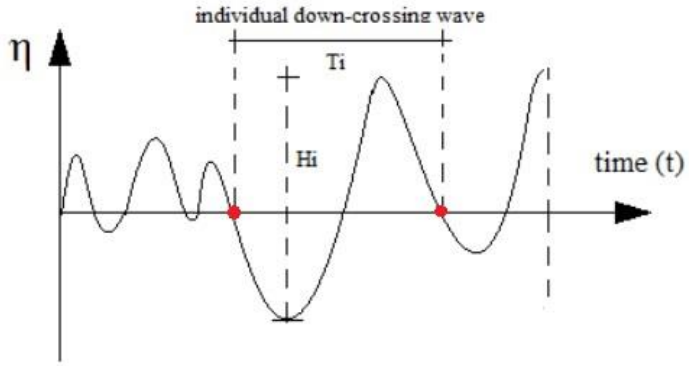

Figure 2.19 - Irregular wave train.

After identifying every wave and their respective heights and periods, the wave-by-wave analysis intends to describe the irregular sea state by means of characteristics values of wave heights – such as the mean wave height (H_m) – and wave periods – such the mean zero-crossing period (T_z). Normally, when designing maritime structures, it is usual to use:

- Significant wave height H_s – average of the highest one-third of all waves ($\overline{H}_{1/3}$);
- Maximum wave height $H_{máx}$ – largest wave recorded;
- Wave height $\overline{H}_{1/10}$ - average of the highest 1/10 of all waves;
- Wave height $\overline{H}_{1/100}$ - average of the highest 1/100 of all waves.

Assuming a Rayleigh distribution – Eq. (2.37) – it is possible to describe these characteristics wave heights as a function of the root-mean-square wave height (H_{rms}):

$$P(H \geq H_d) = e^{\frac{-H_d}{H_{rms}}} \tag{2.37}$$

$$H_{rms} = \sqrt{\frac{1}{N}\sum_{i=1}^{N} H_i^2} \tag{2.38}$$

Leading to the follow values:

$$\begin{aligned} H_m &= 0.886 H_{rms} \\ H_s &= 1.416 H_{rms} \\ \overline{H}_{1/10} &= 1.80 H_{rms} \\ \overline{H}_{1/100} &= 2.359 H_{rms} \\ H_{max} &= 2.63 H_{rms} \end{aligned} \tag{2.39}$$

One of the disadvantages of using the Rayleigh distribution is the fact that it is only applicable no breaking zones and for short-term wave statistic records, as for the reliability of scour protections the long-term wave statistic records have greater importance (Fazeres-Ferradosa, 2018). For long-term wave statistics, it is usual to use Weibull or Fisher-Tippett I distributions.

The spectral analysis considers the irregular sea state as a superposition of a number of regular waves, each one characterized by its own height and period. Typically, the spectral method relies on the water surface elevation expressed in the frequency domain, instead of the time domain (Fazeres-Ferradosa, 2018). By a Fourier transformation, it is possible to define an amplitude or a phase spectrum. According to De Vos (2008) and Fazeres-Ferradosa (2018), only the amplitude spectrum is used – where the wave amplitude (*a*) or wave energy is plotted for each wave frequency f_i ($f_i=1/T_i$). The energy spectral density – or variance spectral density S(f) - is calculated using Eq. (2.40), where $\Delta f=1/T_0$ is the frequency band of the spectrum and T_o (s) is the total duration of the wave train measured.

$$S(f) = \frac{\frac{1}{2}a^2}{\Delta f} \tag{2.40}$$

Since the Fourier transformation yields a double and symmetrical spectrum, only the first half of the spectrum is analyzed – left part of the spectrum in Figure 2.20. Only that part of the frequency spectrum is representative of the actual energy of the wave field.

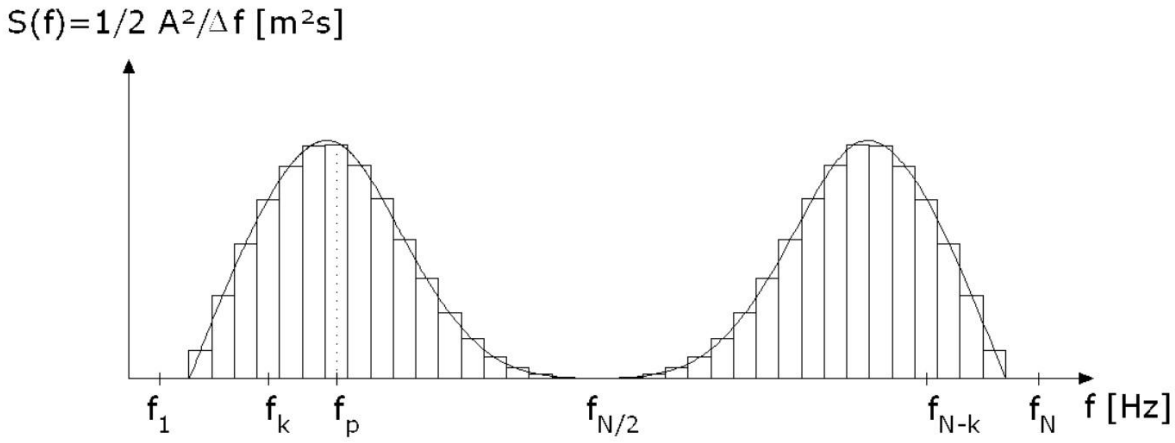

Figure 2.20 - Energy spectral density (De Vos, 2008).

For the different wave characteristics determination its necessary to calculate the moments of spectrum density. Those moments are calculated using Eq. (2.41) for a certain n^{th} moment. The most important moment is the zero moment m_0 - Eq. (2.42) – and represents the energy of the wave spectrum.

$$m_n = \int_0^{+\infty} f^n S(f)\ df \tag{2.41}$$

$$m_0 = \int_0^{+\infty} S(f)\ df \tag{2.42}$$

Other moments needed are the m_1, m_2 and m_{-1}. According to Vogel *et al.* (2001), the m_1 moment can be interpreted as the mean frequency of the spectrum, and the m_2 moment can be interpreted as the standard deviation of an equivalent Gaussian spectrum.

Using the zero moment m_0 it is possible to obtain the significant wave height H_{m0}, often used as a substitute of H_s, but also $H_{1/10}$, $H_{1/100}$ and H_{max} as shown by US Army Corps of Engineers (2012) or De Vos (2008) in Eq. (2.43).

$$\begin{aligned} H_{m_0} &= 4.04\sqrt{m_o} \approx H_s \\ \overline{H}_{1/10} &= 5.091\sqrt{m_o} \\ \overline{H}_{1/100} &= 6.672\sqrt{m_o} \\ H_{max} &= 1.86H_s \approx 7.514\sqrt{m_o} \end{aligned} \tag{2.43}$$

As for the wave periods, the characteristic period that's commonly is the peak period T_p. However, the peak period depends on the frequency band Δf adopted. For that reason other periods, as those presented in Eq. (2.44), are used. The most important for the determination of the S_{3D} damage number, as referred in section 2.4.3.2, is the $T_{m-1,0}$ – also known as the energy wave period (T_e).

$$\begin{aligned} T_{m_{-1,0}} &= T_e = \frac{m_{-1}}{m_0} \\ T_{m_{0,2}} &= \sqrt{\frac{m_0}{m_2}} \\ T_{m_{0,1}} &= T_m = \frac{m_0}{m_1} \end{aligned} \tag{2.44}$$

For irregular waves, the calculation of the orbital bottom velocity (U_m) is from the orbital velocity spectrum (σ_u). According to Whitehouse (1998), and shown in Fazeres-Ferradosa (2018), the calculation of U_m is dependent on Eq. (2.45), Eq. (2.46) and Eq. (2.47).

$$U_m = \sqrt{2}\sigma_u \tag{2.45}$$

$$\sigma_u = \int_0^{+\infty} S_u(f)\ df \tag{2.46}$$

$$S_u(f) = \left[\frac{2\pi}{T(f)\cdot \sinh\left(\frac{2\pi d}{L(f)}\right)}\right]^2 S(f) \tag{2.47}$$

where $S_u(f)$ represents the power spectrum of the bottom velocity, S(f) is the amplitude spectrum, T(f) and L(f) are the wave period and wave length, respectively, as a function of the frequency.

In literature there are two major theoretical spectra, based on wind, used to define the wave spectrum, the:

- Pierson-Moskowitz (PM) spectrum;
- JONSWAP spectrum.

Both use H_{mo} and T_p for parametrization. The JONSWAP extends the PM to include fetch limited seas. Also, the JONSWAP depends on a peak enhancement factor (ϒ), which for North Sea conditions – the same conditions that will be used on the tests – is equal to a mean value of 3.3. For ϒ=1, the PM spectrum and JONSWAP spectrum coincide.

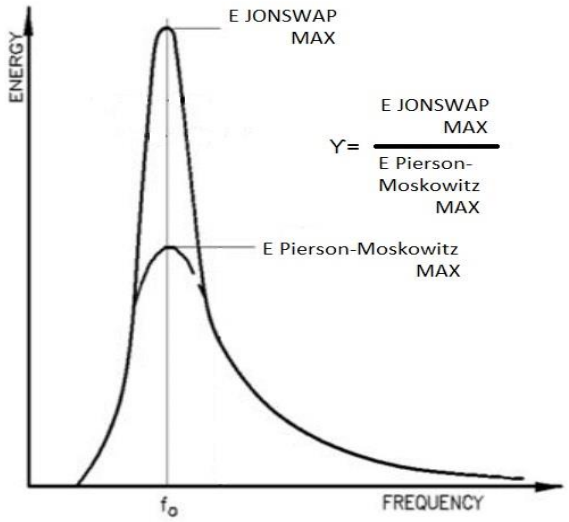

Figure 2.21 - Pierson-Moskowitz and JONSWAP wave spectrum (adapted from Tulsi (2016)).

The Eq. (2.48) was developed by LeBlond *et al.* (1982) for the estimation of the JONSWAP peak enhancement formula.

$$\Upsilon = \left[\frac{S(f_p)}{\frac{5}{16 f_p} {H_{m0}}^2 e^{-5/4}}\right]^{3/2} \tag{2.48}$$

For a JONSWAP spectrum with Υ=3.3, the peak period (T_p) can be related to the moment spectral periods mentioned before.

$$\begin{aligned} T_p &= 1.107 T_{m_{-1,0}} \\ T_p &= 1.386 T_{m_{0,2}} \\ T_p &= 1.1986 T_{m_{0,1}} \end{aligned} \tag{2.49}$$

2.4.1.2.3 Design wave height and period

For the design of offshore structures, the wave height can be described in terms of return period (T_r) and encounter probability. Because the return period for offshore structures normally exceeds the wave height records, there is a need to extrapolate the wave height design value. Monopile foundations for offshore wind turbines normally have a lifespan of 20 to 25 years, but return periods of 50 years, or even 100 years, are chosen to the design of scour protections (De Vos, 2008).

As shown in De Vos (2008) and Fazeres-Ferradosa (2018), when selected a design wave height (H_d) its exceeding probability is obtained with Eq. (2.50).

$$P(H \geq H_d) = \sum_i P(H > H_d)_{Hsi} P(H_{si}) \tag{2.50}$$

where $P(H>H_d)$ represents the exceeding probability of a wave height H_d, $P(H>H_d)_{Hsi}$ the exceeding probability of the wave height H_d in a storm with a certain significant wave height H_{si} and $P(H_{si})$ the encounter probability of H_{si}.

The wave period, for designing proposes, should be conditioned on the value of the wave height selected. According to Soulsby (1997), the up-crossing mean period (T_z) as a function of a known significant wave height H_s is:

$$T_z = 11\sqrt{\frac{H_s}{g}} \tag{2.51}$$

2.4.1.3. Number of waves

The number of waves (N) is one of the parameters that it is taken into account when performing the stability tests for scour protection. This parameter is not considered in design formulas of scour protections, based on the θ_{cr}, but is necessary to calculate the damage number (S_{3D}) of the protection itself (Fazeres-Ferradosa, 2018).

The damage on scour protections is quicker for regular waves, than for irregular waves (De Vos, 2008). This happens because, for regular waves, the same force and shear stress act in the structure protection for each wave, whereas for irregular waves that same force and shear stress, acting on the structure protection, varies with each wave. For that reason, the equilibrium scour takes longer to be reached for irregular waves. So, the number of waves have significant importance since it allows to determine the duration of a storm for which the equilibrium scour is reached.

For physical modeling, the wave characteristics, such as the wave height and period, should be used considering an irregular sea state.

For the scour protections, the exact number of waves for which the protection fails as not been defined. De Vos (2008) and De Vos *et al.* (2012), stated that the damage number increases until 3000 waves and then starts to decrease, although a larger number of waves should be used to reach the equilibrium stage - for 5000 waves the damage was still developing (De Schoesitter *et al.*, 2014).

De Schoesitter *et al.* (2014) and Whitehouse *et al.* (2014) performed some tests for 7000 waves, where it is reported, for a dynamic equilibrium, that some scour holes on the protection were formed and then filled at the same time new holes were formed in other places, to be backfilled also.

So, the main scope of this dissertation will be the behavior of scour protections (and the respective evolution of damage) for N values over the 5000 waves benchmark.

2.4.1.4. Current Velocity

The current velocity at the foundation protection has a slower variation than the loads induced by waves, being considered, for practical and design reasons, constant (Fazeres-Ferradosa, 2018). Its profile is dependent on the boundary layer, as shown in section 2.2.1 and 2.2.1.2. Since, the steady current velocity plays a major role in the combined effect of waves and currents, the depth-averaged flow velocity (U_c), as the current direction and the velocity profiles are the flow characteristics that have the most influence. For a more detailed explanation about the influence of the steady current velocity, the works of Bruserud *et al.* (2019) and Bruserud *et al.* (2018) are suggested for further detail.

2.4.1.5. Sediment characteristics

The sediment characteristics of the seabed, at the offshore wind turbine location, influence the filter and armor layer design. According to Fazeres-Ferradosa (2018), it also influences the extent of scour, the slope of the scour hole – dependent of the sediment's angle of repose Φ (º) - and the settling velocity – that contributes for the damage number determination for dynamic protections.

As aforementioned, this dissertation will focus on structures placed at non-cohesive seabed soil types. For the most common type of seabed soils, the non-cohesive sands, the value of Φ is between 30º and 40º (Fernandes, 2006).

For the sediments characterization, besides the angle of repose, it is also usual to define the sediments size using their mean diameter d_{50} (D_{50} when referring to the armor layer). For non-cohesive soils the diameter varies between 0.062 mm and 2 mm (Fazeres-Ferradosa, 2018) and they can have a narrow or wide gradation, depending on the respective particle size distribution curve (see more in works of Gee *et al.* (2002) and Fernandes (2006)).

For the settling velocity, the formula used it is the one introduced in the works of De Vos *et al.* (2012) that is valid for both values of d_{50} or D_{50}.

$$w_s = 1.1[(s-1) \cdot g \cdot d_s]^{1/2} \tag{2.52}$$

where s represents the ratio between the sediment (ρ_s) and water density (ρ_w), d_s (m) the dimension of the sediment grain (for scour protection should be used the D_{50} value) and g (m/s^2) the value of the gravitational acceleration.

2.4.2. Structural Parameters

The structural parameters are characteristics related to the constituent material of the scour protection, mainly of the armor layer. The main parameters of the protection material analyzed are:

- The density;
- The size, shape and weight;
- The gradation.

The pile diameter and shape are also considered structural parameters since both influence the scour phenomena (Fazeres-Ferradosa, 2018). However, those parameters will not be approached since, according to De Vos (2008), in an offshore environment, the circular shape is the most common shape in order to minimize the influence of the structure on the flow and the diameter is determined according to static and dynamic loads.

2.4.2.1. Density

This parameter has a great influence in the design of scour protections since it determines the gravitational force - stabilizing force - of the armor layer. The mass density ρ_s (kg/m^3) is equal to the ratio between the mass (m [kg]) per unit volume (V_s [m^3]) of the material. The values of ρ_s for the armor layer, for riprap, scour protection type (explained in more detail later), normally range between 2600 kg/m^3 – for granites – and 3100 kg/m^3 – for basalts - (Branch, 2000; De Vos, 2008).

Higher density values can be reached, using artificial blocks, like those used in rubble mound breakwaters. It can also be used the bulk density ρ_d (kg/m^3), that corresponds to the ratio between the mass (m [kg]) per volume of spaces between particles (V_d [m^3]), although being more difficult to determine. But according to De Vos (2008), the bulk density is needed to determine the right weight of riprap material to a certain volume of scour protection required.

2.4.2.2. Size, shape and weight

The size and weight have also a great influence in the scour protection design, since, according to Fazeres-Ferradosa (2018), the weight of the stones, that compose the protections, is the major stabilizing force of scour protections. The stone size affects the resistance of the protection (represented by the critical shear stress) and the acting bed shear stress of scour protection – due to its influence on the bed roughness and f_w and f_c friction factors. Although not so obvious as the other two, the shape of the armor layer stones has an important role on the stability of scour protections due to the entrainment of stones (De Vos, 2008; Fazeres-Ferradosa, 2018).

The majority of riprap scour protections have wide grading curves and are composed of stones with different shapes and sizes. For that reason, it is usual to use the nominal diameter (D_n [m]) – side of a cube with an equivalent volume to the stone considered – or the diameter of a sphere (D_s [m]) – diameter of a sphere with an equivalent volume to the stone considered - when describing stone sizes.

$$D_n = \left(\frac{W}{\rho_s}\right)^{1/3} \tag{2.53}$$

$$D_s = 1.24\left(\frac{W}{\rho_s}\right)^{1/3} \tag{2.54}$$

However, to describe riprap scour protections it is usual to use the mean stone diameter (D_{50} [m]) or the mean stone weight (W_{50} [N]), obtained from the nominal diameter mean value (D_{n50} [m]) using Eq. (2.55).

$$D_{n50} = \left(\frac{W_{50}}{\rho_s}\right)^{1/3} = 0.84D_{50} \tag{2.55}$$

As for the shape, riprap scour protections should use angular and blocky stones (CIRIA *et al.*, 2007; De Vos, 2008; ODOT, 2014; Fazeres-Ferradosa, 2018), preferably with uniform size, instead of rounded ones in order to increase the entrainment and interlock between the stones in order to resist to displacements induced by hydraulic and gravitational forces (ODOT, 2014). For that reason, it is recommended in CIRIA *et al.* (2007), that the largest dimension of the stones should not be three times larger than the shortest dimension.

2.4.2.3. Gradation

As said in sections 2.4.1.5 and 2.4.2.2, the size of the bed sediment and scour protection material, respectively, can have a wide range of sizes and distributions. According to Schendel *et al.* (2014), this parameter has significant importance on the stability of scour protections under waves and currents combination.

De Vos (2008) states that stone distribution is usually done using weight cumulative curves, where W_{50} represents the block weight for which 50% of the total sample material is lighter. So the steepness of weight curves indicates the grading width, like in the granulometric curves (Fazeres-Ferradosa, 2018).

In order to differentiate the stones grading, CIRIA *et al.* (2007) proposed a classification based on the ratio D_{85}/D_{15}:

Table 2.2 - Stone grading classification (adapted from CIRIA *et al.* (2007))

Narrow grading	Wide grading	Very wide grading
$D_{85}/D_{15} \leq 1.5$	$1.5 < D_{85}/D_{15} \leq 2.5$	$2.5 < D_{85}/D_{15} \leq 5$

In the works of De Vos *et al.* (2011), is mentioned that a wide grading stone distribution has a positive effect on the stability of the protection. So, the increment of the ratio D_{85}/D_{15} leads to the increase of the protection reliability (Fazeres-Ferradosa, 2018), since smaller stones tend to be "protected" by larger stones, diminishing the likelihood of being dragged away (De Vos *et al.*, 2011).

2.4.3. Scour Parameters

The scour parameters, as the name indicates, try to explain, measure, quantify and relate the scour effects to the damage and failure of the scour protection and of the offshore wind turbine itself, in the worst case scenario. The most important ones are:

- The scour depth;
- The scour extent;
- The damage number (S_{3D});
- The stability parameter (stab).

Because the objective of this dissertation is the evaluation of damage on offshore wind turbine foundations, the author is focused on the scour depth and mainly on the dimensionless damage number S_{3D} (that is in some way related to the scour depth). Therefore, for the scour extent and the stability parameter, the author suggests an extensive review of the detailed works of De Vos (2008), Matutano (2013) and Fazeres-Ferradosa (2018).

2.4.3.1. Scour Depth

The scour depth, S (m), is maybe one of the most important parameters for the design of protections. It develops according to an asymptotic behavior towards a steady stage, the so-called equilibrium scour depth – S_e (m). Scour depth can be described as the vertical distance between the maximum depth in the scour hole in the equilibrium situation and the surrounding undisturbed bed (Sumer *et al.*, 2001).

The scour depth develops and increases as a function of time, as shown in Figure 2.22. Thus, if the duration of a storm and the time required to reach the equilibrium scour depth are known, then it is possible to define the scour associated to that period of time or the best period of time to install the convenient scour protection.

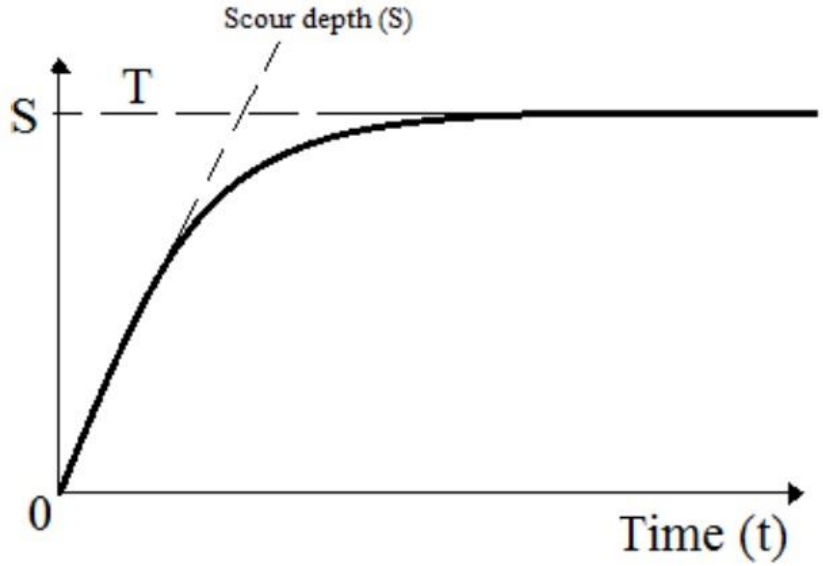

Figure 2.22 - Scour depth development as a function of time (Fazeres-Ferradosa, 2018).

For the scour depth prediction, according to the scour time development, Sumer *et al.* (1992) – Eq. (2.56) - and Melville *et al.* (1999) – Eq. (2.57) – proposed:

$$S(t) = S_e\left(1 - \exp\left(-t/T\right)\right) \tag{2.56}$$

$$\frac{S(t)}{S_e} = exp\left[-0.03\left|\frac{U_{cr}}{U}\ln\left(\frac{t}{t_e}\right)\right|^{1.6}\right] \tag{2.57}$$

$$t_e(days) = \begin{cases} 48.26\dfrac{D_p}{U}\left(\dfrac{U}{U_{cr}} - 0.4\right) & \dfrac{d}{D_p} > 6 \\ 48.26\dfrac{D_p}{U}\left(\dfrac{U}{U_{cr}} - 0.4\right)\left(\dfrac{d}{D_p}\right)^{0.25} & \dfrac{d}{D_p} \leq 6 \end{cases} \tag{2.58}$$

where t (s) is the time variable, T (s) is the time necessary to reach a scour depth around 63% of the S_e value, t_e (s) is the time necessary to reach the S_e value, U_{cr} (m/s) is the critical velocity, U (m/s) is the average velocity, d (m) is the water depth and D_p (m) is the pile diameter.

The scour depth varies with time but also with the type of flow regime. According to Breusers *et al.* (1991) and Sumer (2002), the scour depth and the time scale of the scour process are higher for clear-water scour instead of the live-bed scour. It means that the clear-water regime induces a higher equilibrium scour depth value, in the end, but, for the same time period, before equilibrium stages are reached, scour depth develops at a higher pace for the live-bed regime. For a more detailed explanation regarding the clear-water and live-bed scour effect on the scour depth, the author recommends the works of Zanke *et al.* (2011) and Fazeres-Ferradosa (2018).

2.4.3.1.1 Scour depth for waves

For the wave effects, the scour depth depends largely on the monopile diameter (D_p) and on the Keulegan-Carpenter number (KC). When the ratio $D_p/L>0.2$ and KC>1, diffraction effects have to be taken into account (Fazeres-Ferradosa, 2018).

Sumer *et al.* (1992) proposed a formula for live-bed regimes, where for values of KC lower than 6, scour depth is considered residual or non-existing. For values over 6, the scour depth is given by the Eq. (2.59) where A=1.3, B=0.03, and C=6 for cylindrical piles (Sumer *et al.*, 1992; Fazeres-Ferradosa, 2018).

$$\frac{S_e}{D_p} = A[1 - exp(-B[KC - C])], \qquad KC \geq 6 \tag{2.59}$$

For larger KC values, the scour depth leans towards the scour depth caused by current effects.

2.4.3.1.2 Scour depth for currents

For the current effects, there are several authors and different formulations. Unlike the wave effect do not depend on the KC number. Breusers *et al.* (1991) proposed Eq. (2.60) and Eq. (2.61) for clear-water and live-bed regimes, respectively,

$$\frac{S_e}{D_p} = 2.3K_sK_\sigma K_\alpha K_{si}K_d \tag{2.60}$$

$$\frac{S_e}{D_p} = 2.3K_sK_\alpha K_{si}K_d \tag{2.61}$$

where K_s corresponds to the shape factor, K_σ to a factor dependent of the grain size distribution $\sigma_g=d_{84}/d_{50}$, K_α to the pier alignment factor, K_{si} to the pier size factor and K_d to the flow depth factor. For cylindrical monopiles, K_s and K_α are equal to 1. For values of $d/D_p>3$ K_d is equal to 1 and for high values of D_p/d_{50}, K_{si} is equal to 1. For values of $d/D_p\leq3$, De Vos (2008) refers to the Figure 2.23 for the determination of the K_d value.

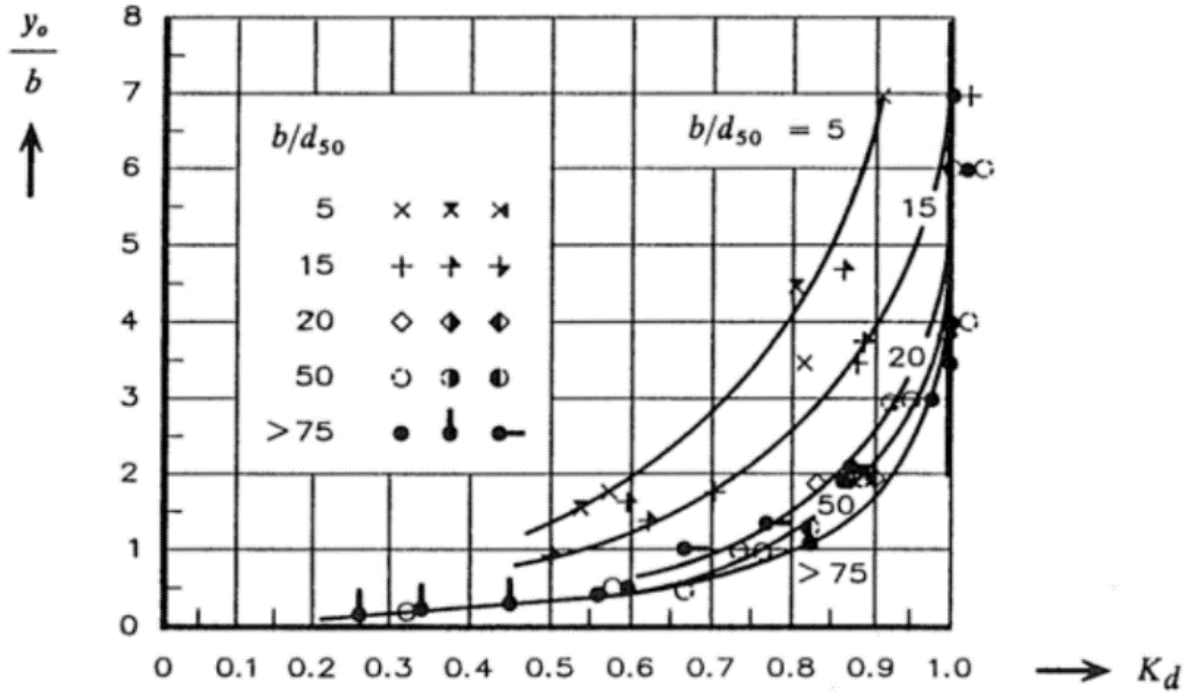

Figure 2.23 - K_d for d/D_p values under 3 (Breusers *et al.*, 1991).

Other authors, like Sumer *et al.* (1992), use Eq. (2.62) for the live-bed regime. As for the clear-water regime, Whitehouse (1998) utilizes Eq. (2.63) that depends on the Shields and critical Shields parameter.

$$\frac{S_e}{D_p} = 1.3 + \sigma_s \tag{2.62}$$

$$\frac{S_e}{D_p} = 1.3\left[2\sqrt{\frac{\theta}{\theta_{cr}}} - 1\right] \tag{2.63}$$

For the value of σ_s (standard deviation of the scour depth), Sumer *et al.* (1992) used the value of 0.7.

2.4.3.1.3 Scour depth for waves and currents combined

Like in the shear stresses topic, the combined effect of waves and currents, on the scour depth, does not translate on the linear sum of the effects of the individual components. This presents a more complex situation.

For the combination of waves and currents, De Vos (2008) states that the effects on the scour depth are lower than for the steady currents. So, normally it is used the dimensionless parameter U_{cw} (velocity ratio) – Eq. (2.64) – that weights the preponderance of both effects in the final effect.

$$U_{cw} = \frac{U_c}{U_c + U_m} \tag{2.64}$$

For high values of U_{cw}, the current effect is bigger than the wave effect so the scour depth tends to Eq. (2.62). For small values of U_{cw}, the wave effect is bigger than the current effect so the scour depth tends to Eq. (2.59).

As said before the main focus of this dissertation is analysis of the long term damage in scour protections and of the evolution of the damage number (S_{3D}) in those protections. Because the S_{3D} is somehow related to the scour depth, for this section 2.4.3.1.3 the most important aspect is the U_{cw} parameter and the weight of each individual effect on the overall effect. So, for the equations of S_e, regarding the waves and currents combination, De Vos (2008), Matutano (2013) and Fazeres-Ferradosa (2018) provide further detail.

2.4.3.2. Damage Number – S_{3D}

The notion of damage number (S_{3D}) was developed by De Vos (2008) and De Vos *et al.* (2012) as an alternative to the stability parameter (stab). The stability parameter emerged on a necessity to define a frontier for the different damage levels proposed by den Boon *et al.* (2004). The damage levels were defined by den Boon *et al.* (2004) in three possible categories:

- No movement (static stability);
- Some movement, but not sufficient to cause failure (dynamic stability);
- Failure.

According to the research developed in the OPTI-PILE project, the failure is reached when the area of exposed filter exceeds the minimum of $4D_{n50}^2$ (E-Connection *et al.*, 2002-2004; den Boon *et al.*, 2004; De Vos, 2008; Fazeres-Ferradosa, 2018). In dynamic protections, the OPTI-PILE project defined failure when the volume of rock that disappears was equal to the volume of rock required to cause failure in static protections (De Vos, 2008; Fazeres-Ferradosa, 2018). A more detailed explanation of static and dynamic protections and their differences is approached in section 2.5.

Using a set of 85 scour tests, with irregular wave conditions, De Vos (2008) tried to develop dynamic design approaches for scour protections.

In these tests, the damage levels were divided into four categories (De Vos, 2008):

- No movement of the stones;
- Very limited movement of the stones;
- Significant movement of the stones, without failure of the protection;
- Failure of the protection.

De Vos *et al.* (2012) stated that the stab parameter had some limitation, failing to predict accurately the damage levels. So, the concept of dimensionless damage number (S_{3D}), for scour protections, was introduced.

To start, De Vos (2008) subjected the scour protection, divided into sub-areas - each one with an area ($A_{sub}=\pi D_p^2/4$) equal to the cross-section area of the monopile - as shown in Figure 2.24, to irregular

waves (3000 or 5000 waves), in different sets of wave trains as shown in Eq. (2.65), combined with a steady current flow.

$$H_{m0,3000} = \frac{1}{3}(H_{m0,1000} + 2H_{m0,2000})$$
$$H_{m0,5000} = \frac{1}{5}(H_{m0,1000} + 2H_{m0,2000} + 2H_{m0,2000}) \quad (2.65)$$

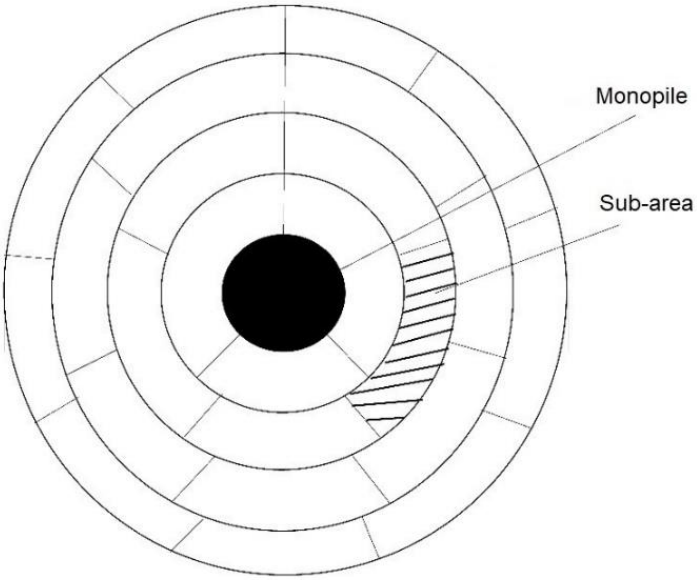

Figure 2.24 - Scour protection division into sub-areas (adapted from Fazeres-Ferradosa et al., 2019).

H_{m0}, $H_{m0,1000}$ and $H_{m0,2000}$ correspond to the spectral wave heights obtained from the zero order moment of a JONSWAP spectrum for an enhance factor Υ=3.3 (see section 2.4.1.2.2).

After each wave train, De Vos (2008) measured the erosion (and accretion) recurring and comparing 3D profiles taken to the protection. Sometimes, for the 5000 wave tests, if at the 3000 waves benchmark the protection failed, then the last 2000 wave train would not be applied. The damage number in each sub-area (S_{3Dsub}) was determined with Eq. (2.66). The final and representative damage number of the entire protection, according to De Vos (2008), corresponds to the highest S_{3D} value registered in all sub-areas (Eq. (2.67)).

$$S_{3Dsub} = \frac{V_e}{D_{n50} \cdot A_{sub}} = \frac{V_e}{D_{n50}\pi\frac{D_p^2}{4}} \quad (2.66)$$

$$S_{3Dmeasured} = \max_{i=1\ to\ n\_sub-area}(S_{3Dsub,i}) \quad (2.67)$$

The V_e (m^3) corresponds to the eroded volume in each sub-area, A_{sub} (m^2) is the sub-area (equal to the cross-section of the monopile). By putting the D_{n50} – nominal mean stone diameter – into the denominator, the value of the S_{3D} gives us the average height of the scour protection that has disappeared in each sub-area, as a function of the D_{n50} (Loosveldt *et al.*, 2012). This equation was inspired by the two-dimensional damage equation of Van Der Meer (1990).

De Vos *et al.* (2012) established limits for the S_{3D} in order to correlate them to a certain damage level. The limits proposed were:

- No movement to very limited movement (static stability): $S_{3D}<0.25$;
- Significant movement, without failure of the protection (dynamic stability): $0.25<S_{3D}<1$;
- Failure: $S_{3D}>1$.

After the extensive set of tests performed, De Vos (2008) proposed an empirical formula to predict and estimate the damage number ($S_{3Dpredicted}$), for dynamic stable design proposes:

$$\frac{S_{3Dpredicted}}{N^{b_0}} = a_0 \cdot \frac{{U_m}^3 \cdot {T_{m-1,0}}^2}{\sqrt{gd} \cdot (s-1)^{\frac{3}{2}} \cdot {D_{n50}}^2} + a_1 \cdot \left(a_2 + a_3 \cdot \frac{\left(\frac{U_c}{w_s}\right)^2 \cdot (U_c + a_4 U_m)^2 \cdot \sqrt{d}}{g {D_{n50}}^{3/2}} \right) \quad (2.68)$$

where N corresponds to the number of waves, U_m (m/s) to the orbital bottom velocity , $T_{m-1,0}$ (s) to the energy spectral wave period, d (m) to the water depth, w_s (m/s) to the settling velocity, U_c (m/s) to the depth-average current velocity, g (m/s^2) to the gravitational acceleration and D_{n50} (m) to the nominal diameter mean value. The U_m and $T_{m-1,0}$ parameters should be obtained with Eq. (2.45) and Eq. (2.44) – or Eq. (2.49) – respectively.

The parameters *a0*, *a2*, *a3* and *b0* were determined through regression and their values are presented in Eq.(2.69). Both *a*1 and *a*4 are dependent on the hydrodynamic conditions and obtained using Eq. (2.70) and Eq.(2.71).

$$\begin{aligned} a_0 &= 0.00076 \\ a_2 &= -0{,}022 \\ a_3 &= 0.0079 \\ b_0 &= 0.243 \end{aligned} \quad (2.69)$$

$$a_1 = \begin{cases} 0 \; for \; \dfrac{U_c}{\sqrt{gD_{n50}}} < 0.92 \; and \; collinear \; waves \; and \; currents \\ 1 \; for \; \dfrac{U_c}{\sqrt{gD_{n50}}} \geq 0.92 \; or \; collinear \; waves \; and \; currents \end{cases} \quad (2.70)$$

$$a_4 = \begin{cases} 1 \ for \ \ collinear \ waves \ and \ currents \\ \dfrac{U_r}{6.4} \ \ for \ opposing \ waves \ and \ currents \end{cases} \tag{2.71}$$

$$U_r = Ursell \ Number = \frac{L^2 H_{m0}}{d} \tag{2.72}$$

As stated by Fazeres-Ferradosa (2018) and Fazeres-Ferradosa *et al.* (2019), this methodology proposed by De Vos (2008) and De Vos *et al.* (2012) does not take into account the cumulative effects of the damage, occurring in different sub-areas, and only considers the maximum damage as the representative of the protection.

In Fazeres-Ferradosa *et al.* (2019) two theoretical examples are presented. The first one, about the consideration of the maximum damage as the representative S_{3D} value of the protection, and the second one, about the cumulative effect of damage in different sub-areas locations. For the first one, and according to De Vos *et al.* (2012), two protections - protection 1 and 2 per say - both with a sub-area with S_{3Dsub}=1 and the remaining ones with S_{3Dsub}=0.25 (protection 1) or S_{3Dsub}=0.8 (protection 2) are classified both as dynamic, even though the scour pattern and severity are different. The second example, alerts to the fact that the eroded height is being average per sub-area, therefore being difficult to understand if several adjacent sub-areas display larger values of S_{3D} than dispersed sub-areas. According to Fazeres-Ferradosa *et al.* (2019), several adjacent sub-areas, and/or at sectors' intersections, with S_{3Dsub}>1 might be more prone to filter exposure than sub-areas with larger S_{3D} values, that are distant from each other.

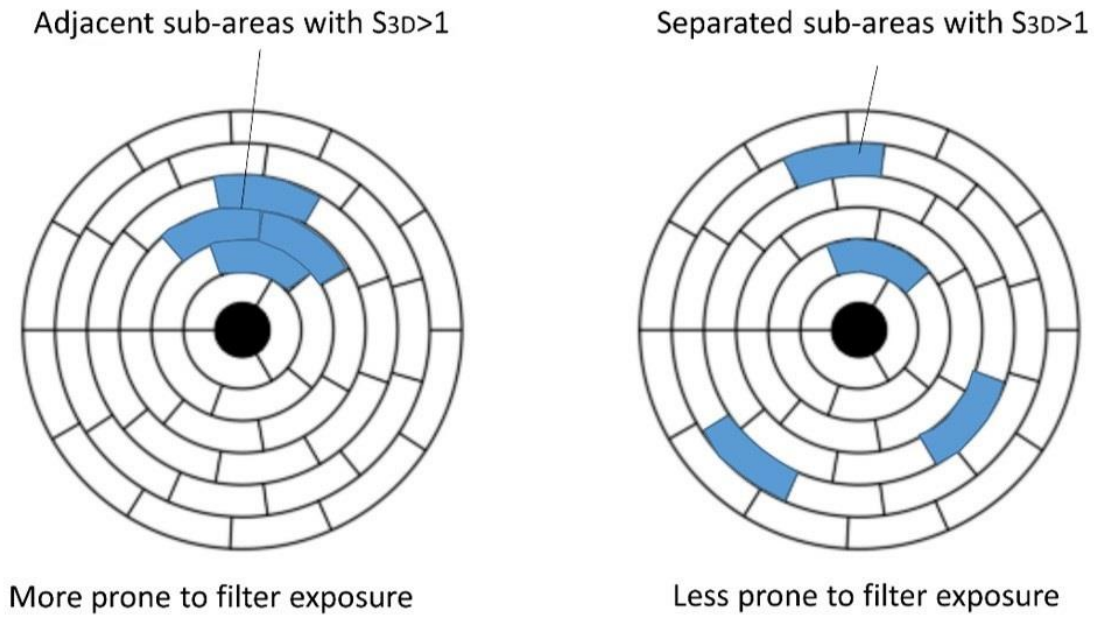

Figure 2.25 – Theoretical example of different scour exposure for the same S_{3D} classification (Fazeres-Ferradosa *et al.*, 2019).

Thus, Fazeres-Ferradosa *et al.* (2019) discusses a potentially different concept in order to cover these aspects. The concept (Figure 2.26) consists in the creation of a mesh of overlapping circles placed in concentric rings - centered at the monopile - with a certain overlapping distance, angle and resolution - according to the accuracy required – in order to cover as much adjacent eroded areas as possible.

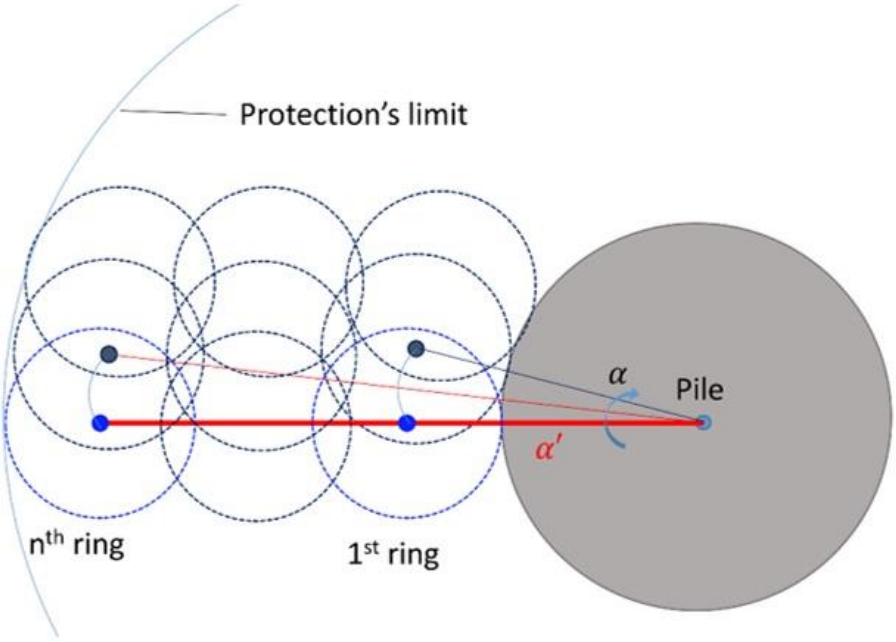

Figure 2.26 - New concept of overlapping circle mesh to determine $S_{3Dmeasured}$ (adapted from Fazeres-Ferradosa *et al.* (2019)).

The alternative equation proposed divides the eroded volume V_e by the area of the overlapping circle (with is radius as a function of the D_{n50}):

$$S_{3Dsub,i} = \frac{V_e}{D_{n50} \cdot \pi \cdot (nD_{n50})^2} \tag{2.73}$$

Fazeres-Ferradosa *et al.* (2019) is suggested for a more detailed explanation of this new concept. Raaijmakers *et al.* (2010) also noted that with Eq. (2.68) the deformation on the protection never reaches an equilibrium stage, unlike other formulas. For that reason, a modification was suggested, for a range between 1000 and 5000 waves, by including the characteristic number of waves N_{charac} – number of waves of a specific design storm.

$$\frac{S_{3Dpredicted}}{N^{b_0}} \approx \frac{S_{3Dpredicted}}{b_1 \cdot \left[1 - exp\left(-\frac{N}{N_{charac}}\right)\right]} \tag{2.74}$$

$$b_1 = 7.6 \tag{2.75}$$

Finally, Loosveldt *et al.* (2012) concluded that by extending the range of some parameters (wave period, water depth, stone sizes, etc) the Eq. (2.68) delivers conservative results out of the tests ranges in De Vos (2008) and De Vos *et al.* (2012).

It is important to note that the limits proposed by De Vos (2008) should be seen more like a transition zone rather than a sharp limit (Fazeres-Ferradosa *et al.*, 2018). As shown in Figure 2.27, static protections (correspondent to damage level 1 and 2) were obtained for an S_{3D} over the 0.25 benchmark and dynamic protections (damage level 3) were obtained for S_{3D} levels close to 1.25, 1.3 (instead of 1).

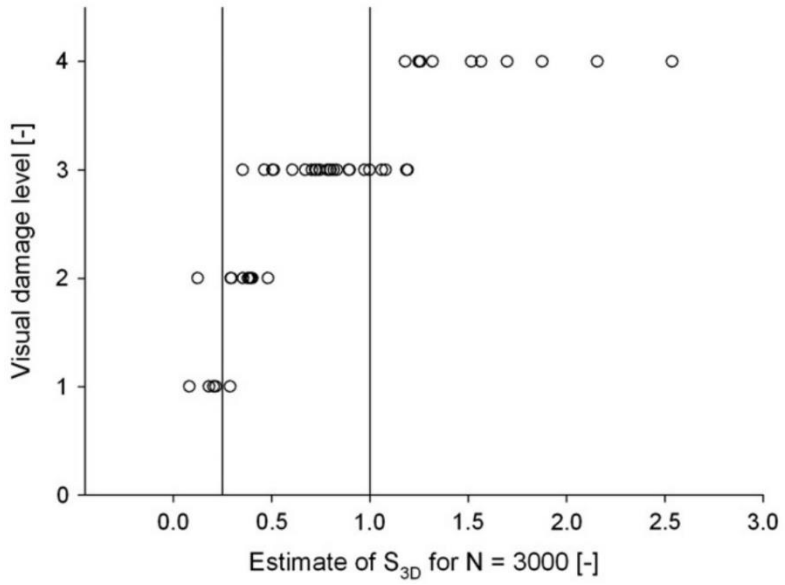

Figure 2.27 - Damage levels vs $S_{3Dpredicted}$ (De Vos *et al.*, 2012)

2.5. SCOUR PROTECTION TYPES

As the main focus of this dissertation, scour protections have an important role in the offshore wind turbine design. Usually, they are applied all around the monopile that supports the turbine. Rip-rap protections are the most common type of protection because of its low cost and availability (De Vos, 2008). Their non-uniform stone size distribution – more susceptible to damage by strong waves and currents - and their non-precise type of installation - by dumping the stones – are some of the disadvantages (De Vos, 2008).

Raaijmakers *et al.* (2010) set a distinction for the different types of riprap protections, according to the movement of the stones, Table 2.3.

Table 2.3 - Types of scour protections (Raaijmakers *et al.*, 2010).

Type of protection	**Definition**
I) Static Protection	Stones movement, in the armour layer, is not allowed.
II) Dynamic Protection	Stones movement is allowed, as long as the structure does not fail.
$II_{a)}$ Fully Dynamic	Movement is allowed without restrictions. During severe conditions, smaller stones are picked in the wave cycle and seabed sediments are washed out before the stones fall back in their place. Scour develops but at a smaller pace and timescale.
$II_{b)}$ Later Installed	Stones are installed after the development of the scour hole and are stable enough to prevent future scour phenomena.
$II_{c)}$ Slightly Dynamic	Stones are installed on the beginning and movement is allowed until the deformations are limited to the top layer.

2.5.1. STATIC PROTECTIONS

den Boon *et al.* (2004) explains that static protections are placed in the seabed right after the monopile installation. They are made of a rock armour layer laid over a finer material filter layer – which prevents sand of being washed-out between the stones of the armour layer, De Schoesitter *et al.* (2014).

In this type of protection, the movement of the stones, in the armour layer, is not allowed. For that reason, the stones' diameter is determined so the wave-and-current induced shear stress is not enough to surpass the critical shear stress of the stones – minimum shear stress necessary to cause stone movement (De Vos *et al.*, 2011). So, static protections are designed according to the threshold of motion concept - as described by the critical shear stress (Fazeres-Ferradosa, 2018).

Some authors, like Breusers *et al.* (1991), propose that the minimum mean stone diameter of the protection - D_{n50} or D_{50} - should be the one that fulfils one of the following equations:

$$\begin{aligned} \tau_{cr} &> 4\tau_{\infty} \\ U_{cr} &> 2U_c \end{aligned} \tag{2.76}$$

Soulsby (1997) proposed the Eq. (2.77), for steady-currents, and Eq. (2.78), for waves, for the critical stone diameter (D_{cr}) value:

$$D_{cr} = \frac{0.25(U_c)^{2.8}}{d^{0.4}[g(s-1)]^{1.4}} \tag{2.77}$$

$$D_{cr} = \frac{0.25(U_w)^{3.08}}{T^{1.08}[g(s-1)]^{2.8}} \tag{2.78}$$

Later on, with the OPTI-PILE project, dedicated to the optimization of the design of scour protections, the stab parameter (stab=θ_{max}/θ_{cr}) was established to classify scour protections according to three levels of damage (see section 2.4.3.2). However, a clear optimization of the static type was not reached. Instead, the conclusion was that dynamic protections could be built using smaller stones.

Then, De Vos *et al.* (2011) proposed the Eq. (2.79), in which τ_{cr} (N/m) is determined as a function of the characteristic diameter $D_{67.5}$ (m) and using a θ_{cr}=0.035 - instead of the usual value of 0.056.

$$\tau_{cr} = \theta_{cr} g(\rho_s - \rho_w) D_{67.5} \tag{2.79}$$

This alternative was proposed since, in the results of its experiments, De Vos *et al.* (2011) noted that the stones in scour protections with narrow graded material tend to move faster than scour protections with wide graded material. Since scour protections with a wide graded material appear to be more stable, calculating τ_{cr} with $D_{67.5}$ will lead to a bigger value of D_{50} for wide graded material than narrow graded (De Vos *et al.*, 2011).

2.5.2. Dynamic Protections

According to den Boon *et al.* (2004), this type of protections allows scour and scour pits to develop until their equilibrium stage. Dynamic protections allow the reshaping of the scour protection keeping the filter layer covered all the time (De Schoesitter *et al.*, 2014). Since static protections have proven to be conservative, by using large stone sizes, the idea that movement, without failure, is allowed meant that smaller diameter stones could be used - thereby reducing the costs of wind turbines. Since smaller stones are used, the increase of the armour layer thickness is possible in order to prevent filter exposure, De Schoesitter *et al.* (2014). Usually, dynamic protections can be constituted by two major layers – an armour and a filter layer – or just by a unique layer of wide-graded material.

Since movement is allowed, the threshold of motion criteria can no longer be applied. Therefore a new design concept is necessary. The OPTI-PILE project, as mentioned, proposed the stab parameter as a design parameter in order to distinguish static from dynamic protections (or even from failure). But since the stab parameter is a function of the critical Shields parameter (θ_{cr}) it is related to the threshold of motion. Values of the stab parameter near the boundary between static and dynamic behaviour (stab=0.460) could fall for each category without an apparent reason (Fazeres-Ferradosa, 2018). That makes the stab parameter a not-so-accurate concept to base the dynamic design in, although it can be used as a good starting point.

Then, in order to surpass the limitations of the stab parameter, De Vos (2008) and De Vos *et al.* (2012) developed a new dynamic design approach based on the damage number S_{3D} – explained in section 2.4.3.2. The failure criteria, equal to the static protections, was the exposure of the filter layer to an area equal to $4D_{n50}^2$. Taking that into consideration, De Vos (2008) proposed a new design equation – Eq. (2.65). De Vos *et al.* (2012) found that dynamic protections fail for an S_{3D}>1.

2.5.3. Failure Modes

The design of scour protections implicate the definition of some key components:

- The armour and filter layer material grading;
- The definition of the armour and filter layer thickness;
- The scour protection extension.

The first one allows to ensure the stability of the armour layer against wave and currents, the second one avoids the washing out of the seabed soil between the layers and the last one ensures that the soil remains stable in the vicinity of the foundation (Fazeres-Ferradosa, 2018).

The incorrect definition of one of these components could lead to the failure of the protection and consequently to the increased risk of collapse of the structure. The failure modes are represented in Table 2.4 and Figure 2.28.

Table 2.4 - Failure Modes.

Failure mode	**Description/Consequences**
Erosion of the top layer	Excess of scour that leads to the exposure of the filter layer; Could lead to the scour of the soil near the structure.
Loss of bed material through the protection	Leads to the sinking of the armour layer.
Edge scour	Reduction of the horizontal size of the scour protection, due to the abrupt change of roughness between the seabed and the riprap.
Flow slide	Steep scour hole, at the edges, that leads to the flow side phenomena damaging the protection edge.
Liquefaction	Leads to the sinking of the scour protection.

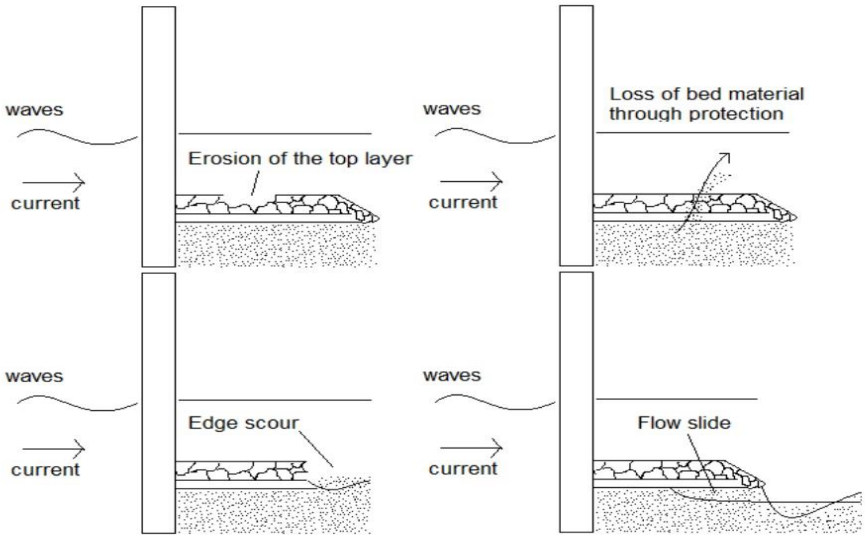

Figure 2.28 - Failure Modes (Fazeres-Ferradosa, 2018).

2.6. LONG-TERM TEST AND MODELS' REVIEW

The offshore wind turbine foundation scour protection theme has been studied, by some authors, for some years now. Many experimental tests and studies were developed, in order to determine and measure damage or just to understand the behaviour of the protections through different and severe conditions. The goal has been the attempt to optimize the scour protections (making them as efficient as possible, while reducing their costs).

Table 2.5 presents a review of the different tests – and their conditions – performed by some authors. Analyzing the table, it is seen that static configurations do not consider the number of waves in their formulations, or only a residual number of waves. As for dynamic configurations, usually the tests were performed for 3000 to 5000 or even 7000 waves. Loosveldt *et al.* (2012) and Schendel *et al.* (2014) reached the 9000 wave benchmark.

As said before, in section 2.4.1.3, the conclusions drawn between different authors research works' could vary. De Vos *et al.* (2012) indicate that the damage increases until 3000 waves and then starts to slow down (although for 5000 waves the damage was still developing). Whitehouse *et al.* (2014) and De Schoesitter *et al.* (2014) performed tests for 7000 waves where scour holes were formed, then filled at the same time other holes started to occur in other locations. But for 9000 waves opinions diverge. Loosveldt *et al.* (2012) concluded that dynamically stable profiles are reached from 5000 waves forward (damage development decreases with 5000 or more waves), as for Schendel *et al.* (2014) an equilibrium scour depth was not achieved for 9000 waves (scour was still developing). One the main reasons for the difference of results between both researches (Table 2.5), could be the fact that Loosveldt *et al.* (2012) used wave and currents – in collinear or opposite directions – during tests and Schendel *et al.* (2014) only used waves.

As for how scour is measured in laboratory and in real life, analyzing the table, it is possible to see that the most reliable tool for the damage assessment, in laboratory, is the use and comparison of Digital Terrain Models (DTM's)– usually taken before each test and after each wave train. But, in real life, according to Whitehouse *et al.* (2011), in order to preserve the structural behaviour of the protections, companies adopt scour management plans (SMP's) that provide frameworks for scour interactions (Figure 2.29). They monitor protections regularly, allowing them to compare locations, depths and extents of scour with data from predictive formulas and physical model tests. The monitoring activities consist in surveys, using datum points or horizontal reference lines, performed by remotely operated vehicles (ROV), by divers or graded scour poles (Whitehouse *et al.*, 2011). Those surveys are made during periods of calm weather, when tidal currents generate most scour, so they can be compared immediately post-storm. Other monitoring systems, like the multibeam echo sounding and the rotating head scanning sonars, have also been used (Whitehouse *et al.*, 2011).

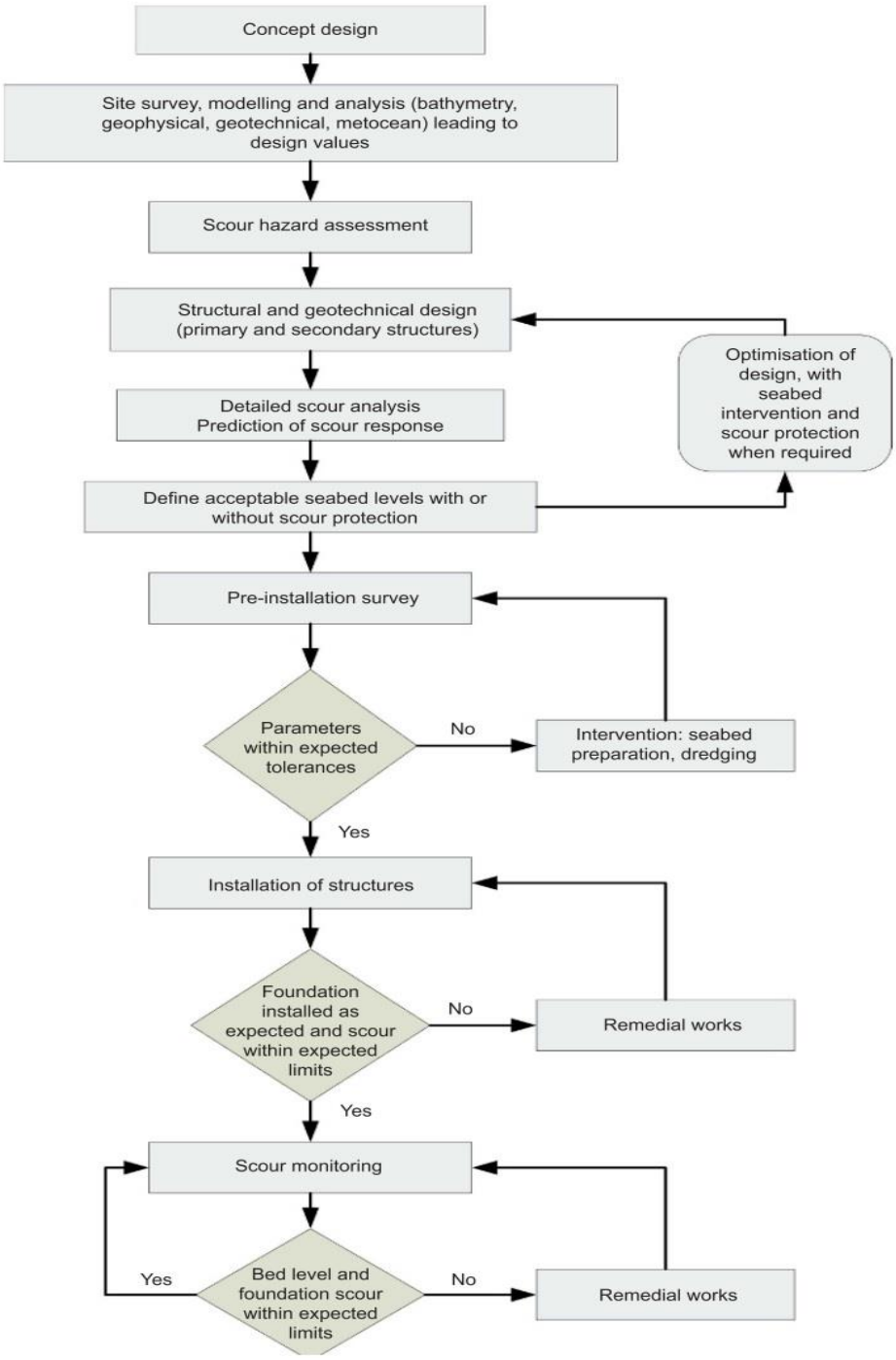

Figure 2.29 - Scour Management Plan chart (Whitehouse *et al.*, 2011).

Table 2.5 - Physical modelling test review.

Authors	den Boon *et al.* (2004)	De Vos *et al.* (2011)	De Vos *et al.* (2012)	Loosveldt *et al.* (2012)	Schendel *et al.* (2014)	De Schoesitter *et al.* (2014)
Type of Protection	Static and Dynamic	Static	Dynamic	Dynamic	-	Dynamic
Scale	1:47.25	1:50	1:50	1:50	1:4	1:50
T_p (s)	1.29 to 1.4	1.13 to 1.7	1.13 to 1.7	1.423 to 2.208	8	1.52 to 1.55
U (m/s)	0.15 to 0.17	0 to 0.3	0 to 0.3	0 to 0.31	0.51 to 0.96	0.15 to 0.23
Wave-current direction	Currents	Collinear Opposite	Waves only Collinear/Opposite	Collinear Opposite	Waves only	Collinear
H (m)	0.14 to 0.18	0.050 to 0.168	0.050 to 0.168	0.057 to 0.160	0.7 to 1.3	0.080 to 0.144
d (m)	0.51	0.2 to 0.4	0.2 to 0.4	0.2 to 0.5	5	0.24 to 0.50
D_p (m)	0.09	0.1	0.1	0.050 to 0.125	1	0.1
Armour $D_{n50 \text{ or } 50}$ (mm)	5 to 600 kg (rock grading)	3.45 to 7.14	3.5 to 7.2	3.5 to 10	12	2.7 to 7.5
ρ_s (kg/m^3)	Not available	2650	2650 to 3200	2650	Not available	2564 to 2600
Armour thickness	$3D_{n50}$	$3D_{n50}$	2.5 to $3D_{n50}$	$2.5D_{n50}$	0.50 m	2 to $8D_{n50}$
Armour extent	$5D_p$	$5D_p$	$5D_p$	$5D_p$	11 m	$5D_p$
Filter layer	Granular	Geotextile	Without, Geotextile or Granular	Geotextile (1 test with Granular)	-	Granular
Type of waves	-	Regular	Irregular	Irregular	Irregular	Irregular
Number of waves (N)	4 model hours	50	1000 to 5000	3000 to 9000	9000 (3 consecutive 3000 wave tests)	1000 to 5000 (one test of 7000)
Total number of tests	11 series 27 tests	1 series 40 tests	1 series 85 tests	1 series 46 tests	1 series 3 tests	3 series 23 tests
Scour Measurement	Radial bed profiles and photographs	-	Visual observation DTM	DTM	Acoustic Backscatter, Echosounders and DTM	Visual observation and DTM

2.7. PHYSICAL MODELLING: SCALE AND MODEL EFFECTS

In order to understand the behaviour and interactions between the maritime conditions and scour protections, researchers support their investigations on:

- Physical modeling;
- Numerical modeling;
- Composite modeling.

The experimental stage of this dissertation will be done using physical modeling. Physical modeling is one of the most conventional techniques used in hydraulic research since it fills the gap between numerical modeling and the real world (Frostick *et al.*, 2011). It allows a good comprehension of the phenomena to which a prototype is subjected, trying to fill the gap of some failures or point out possible optimizations, being one of the most reliable approaches. Physical modelling consists on the reduce scaling of the real prototype conditions and measures, using a scale factor, λ, that relates the respective model variable values with the intended prototype variable values – Eq. (2.76). But maybe its main advantage, comparing it to numeric models, is the fact that there is no need to simplify governing physical processes and suppress non linear terms (De Vos, 2008; Taveira-Pinto, 2011).

To correctly reproduce the prototype characteristics in the physical model, criteria of similitude are used. Similarity is obtained when the model conditions are geometrically, kinematically and dynamically similar to the prototype conditions (Frostick *et al.*, 2011), *i.e.* the ratio between the prototype and the model variables are equal to a constant.

However, the fact that physical models are in fact reduced scale models of the real prototype dimensions, that leads to some discrepancies between the model and the prototype. Those discrepancies are caused by the so-called model and scale effects. According to Frostick *et al.* (2011):

- Scale effects: arise due to force ratios which are not identical between the model and the prototype, resulting in deviations on the observed physical conditions from the prototype at model scale, leading to omissions or oversimplifications;
- Model effects: occur due to the model set-up in the laboratory – and its physical limitations –, introducing on the model non-existing or unreal prototype boundaries and conditions.

Table 2.6 - Scale and model effects examples for physical scour protection models (Fazeres-Ferradosa, 2018).

Effects	Examples
Scale effects	Influence of the Reynolds number on the vortex shedding, sediment scaling, unscaled ripples, different pile roughness between prototype and model, different boundary layers, etc.
Model effects	Generation of long waves, side wall effects, bottom topography, wave reflection, sediment supply, etc.

There are some model effects that must be closely monitored and controlled, mainly the wave reflection, the generation of non-linear effects caused by the combination waves and currents, the side wall effects and the blockage effects. For the wave reflection, the assemble of a reflection structure will be studied. If non-linear effects are detected, generating higher order waves could be a solution. Regarding the side

wall effects, according to De Vos (2008), they can be disregarded when the waves are measured and monitored at the monopile. Regarding, the blockage effects – caused if the pile diameter is considered too large compared to the flume free span – they lead to the constrict of the flow, at the monopile section, increasing the bottom velocities that lead to unrealistic amplified bed shear stresses. In order to avoid those effects, Whitehouse (1998) recommend that the ratio of pile diameter to flume's width should be kept below 1/6.

Regarding the scale effects, one of the most important ones is the sediment scaling. When scaling the seabed sediments, as the diameter decreases, they acquire cohesive properties similar to clays (not corresponding to the prototype non-cohesive properties). In order to maintain the non-cohesive properties of the prototype, it is also used non-cohesive sediments in the model, making the sea bed sediments not being properly scaled. Since the model sediments are not properly scaled, ripples are also not scaled properly (Fazeres-Ferradosa, 2018). So the bed roughness, determined by the ripples' height, is also not correctly scaled contributing to a sediment transport not correspondent to the prototype conditions.

2.7.1. Criteria of Similitude

To achieve a perfect similarity between the model and the prototype, all the geometric, kinematic and dynamic variables relations should be equal to a constant. But in most cases that is not possible, implying to disrespect or neglect some similarities. For hydraulic engineering, and fluid mechanics field, the most suitable one is the dynamic similitude. According to Frostick *et al.* (2011), this similarity applied between two symmetrical geometric and kinematic systems results from Newton's 2nd Law, requiring that:

$$\begin{aligned} m\frac{dU}{dt} = \sum_{n} \overline{F_n} \;\Rightarrow\; \overline{F_i} + \overline{F_{il}} = \; \overline{F_g} + \overline{F_\mu} + \overline{F_e} + \overline{F_p} + \overline{F_\sigma} \\ <=>\; 1 = \frac{(\overline{F_g})}{(\overline{F_i})} + \frac{(\overline{F_\mu})}{(\overline{F_i})} + \frac{(\overline{F_e})}{(\overline{F_i})} + \frac{(\overline{F_p})}{(\overline{F_i})} + \frac{(\overline{F_\sigma})}{(\overline{F_i})} - \frac{(\overline{F_{il}})}{(\overline{F_i})} \end{aligned} \tag{2.75}$$

where $\overline{F_n}$ is the external force acting on the fluid, $\overline{F_i}$ is the inertia force, $\overline{F_{il}}$ is the local inertia force, $\overline{F_g}$ is the gravity force, $\overline{F_\mu}$ is the fluid friction force, $\overline{F_e}$ is the elastic compression force, $\overline{F_p}$ is the pressure force and $\overline{F_\sigma}$ is the surface tension force.

Frostick *et al.* (2011) indicates that the most suitable similitude law is reached by equating the scale factor of inertia force N_{Fi} with other scale factor from other variable from the Eq. (2.75).

The most common similitude laws used are:

- Froude (Fr): ratio between inertia and gravity forces (used for free surface flows or waves);
- Reynolds (Re): ratio between inertia and viscous forces (for viscous driven phenomena, like laminar flows);
- Weber (We): ratio between inertia and surface tension forces (used for overtopping or wave breaking);

- Cauchy (Ca)/Mach (M_a): ratio between inertia and elastic compression forces (used for compressible flows);
- Euler (Eu): ratio between inertia and pressure forces (user for cavitation phenomena);
- Strouhal (St): ratio between local inertia and inertia forces (used for oscillating flows).

For the correct scaling of waves and currents, in the laboratory, the Froude number (F_r) – number that conserves gravity effects - and the Reynolds number (R_e) – number that conserves viscous effects - must be preserved. Though, when preserving the geometric length scale of one, it is not possible to correctly scale both. For scour protection models, to preserve as much as possible the hydrodynamic conditions, the Froude similarity law ($F_{r,prototype}=F_{r,model}$) is adopted in favor of the Reynolds similarity law ($R_{e,prototype}=R_{e,model}$).

$$\lambda = \frac{X_m}{X_p}$$
$$Fr = \sqrt{\frac{F_i}{F_g}} = \frac{U^2}{gL} \tag{2.76}$$
$$Re = \frac{F_i}{F_\mu} = \frac{\rho U L}{\mu}$$

Table 2.7 - Different scale factors between Froude and Reynolds similitudes (adapted from Taveira-Pinto (2011)).

Scale Factor	Froude similitude	Reynolds similitude[1]
Geometric	$\lambda = \lambda_L$	$\lambda = \lambda_L$
Area	$\lambda_A = {\lambda_L}^2$	$\lambda_A = {\lambda_L}^2$
Volume	$\lambda_V = {\lambda_L}^3$	$\lambda_V = {\lambda_L}^3$
Velocity	$\lambda_u = \sqrt{\lambda_L}$	$\lambda_u = \frac{\lambda_\vartheta}{\lambda_L}$
Time	$\lambda_T = \sqrt{\lambda_L}$	$\lambda_T = \frac{{\lambda_L}^2}{\lambda_\vartheta}$
Acceleration	$\lambda_{ac} = 1$	$\lambda_{ac} = \frac{{\lambda_\vartheta}^2}{{\lambda_L}^3}$
Mass	$\lambda_m = \lambda_\rho {\lambda_L}^3$	$\lambda_m = \lambda_\rho {\lambda_L}^3$
Density	$\lambda_\rho = 1$	$\lambda_\rho = 1$
Pressure	$\lambda_p = \lambda_\rho \lambda_L$	$\lambda_p = \lambda_\rho \frac{{\lambda_\vartheta}^2}{{\lambda_L}^2}$
Force	$\lambda_F = \lambda_\rho {\lambda_L}^3$	$\lambda_F = \lambda_\rho {\lambda_\vartheta}^2$
Overtopping (m^3/s)	$\lambda_q = {\lambda_L}^{2.5}$	$\lambda_q = {\lambda_\vartheta}^{5/3}$

[1] In this column, $\lambda_\vartheta$represents the ratio between the kinematic viscosity of the model and of the prototype.

For scour protection models, under waves and currents, the inability to preserve both Froude and Reynolds numbers from the prototype to the model, can be suppressed if $Re \geq 1 \times 10^4$, as flow regime tends to be turbulent and viscous effects can be ignored, (Frostick *et al.*, 2011; Fazeres-Ferradosa, 2018). According to Sumer *et al.* (1992), scale effects, due to the inaccurate scaling of Re, can be restrained for $10^3 < Re < 10^5$.

Other numbers that must be preserved, for scour protections, are:

- The Keulegan-Carpenter number $\left(KC = \frac{U_m \cdot T}{D}\right)$;
- The Shields parameter.

Shields parameter is involved in clear-water scour regime, as for the KC number it represents the way in which the wave flow interacts with the monopile - Frostick *et al.* (2011) - and is involved on live-bed scour regime. The Froude scaling allows that preservation, which conserves the similitude of the equilibrium scour depth (Frostick *et al.*, 2011).

One important scale effect, that is related to the Re and KC number is related to the vortexes. The vortex formation around the monopile, influence the amplification of the bed shear stress (Fazeres-Ferradosa, 2018). According to Sumer (2002), the vortex shedding depend on the pile Reynolds number (Re_p) or on the KC number, for currents or waves respectively. For flow around the monopile, the Re number is important to be kept above 2×10^5 (Sutherland *et al.*, 1998). For the waves, since KC number depends on the U_m, T and D_p - that are scaled geometrically according to the Froude similitude - this number is also preserved in Froude scaling (Fazeres-Ferradosa, 2018). Combining both currents and waves, since the pile roughness is not correctly scaled for Froude scaling, it is important that $Re_p > 2 \times 10^5$ (Fazeres-Ferradosa, 2018). However, when dealing with wave scour modelling, Sumer *et al.* (1992) and Frostick *et al.* (2011) consider that the KC number should be preferably respected, as the Re number and the pile roughness could be considered secondary.

3
EXPERIMENTAL STUDY

3.1. WAVE FLUME AT FEUP

The scour protection tests were performed in the flume of the Hydraulics Laboratory, at SHRHA, FEUP (Figure 3.1 and Figure 3.2). The infrastructure is around 29 m long, 1 m wide and 1 m depth (with a maximum depth of 1.39 m at the two sediment boxes). The flume is fed by a constant head reservoir with the use of two intake pipelines, at 3.02 m above the flume floor. Both pipelines have a regulation valve (with a flowmeter) in order to adjust the flow. One of the flowmeters was damaged, as with the second valve opened the associated flowmeter did not indicate any flow value, thus being impossible to know the exact discharge flow being used when the second valve is open. That leads to an extrapolation of the hypothetic flow using the Continuity equation. The constant head reservoir is fed, in its turn, by an underground reservoir with the use of two pumps – each one with the characteristics presented on Table 3.1. However, as it stands, the two pumps are elevating less water than its max capacity. Instead of the maximum 220 m^3/h, they are only elevating around 134,64 m^3/h (37.4 L/s). The flume is equipped with a gate, in the end, in order to regulate the water depth.

Table 3.1 - Pump characteristics.

Pumps	Nominal Pressure P_N [kPa]	Flow Q [m^3/h]	Static Height H [m]	Rotations N [min^{-1}]	Power P [kN]	Pump Efficiency η [%]
Lowara e-NSCS	1600	25 - 220	22 – 11.4	1470	11	84.1

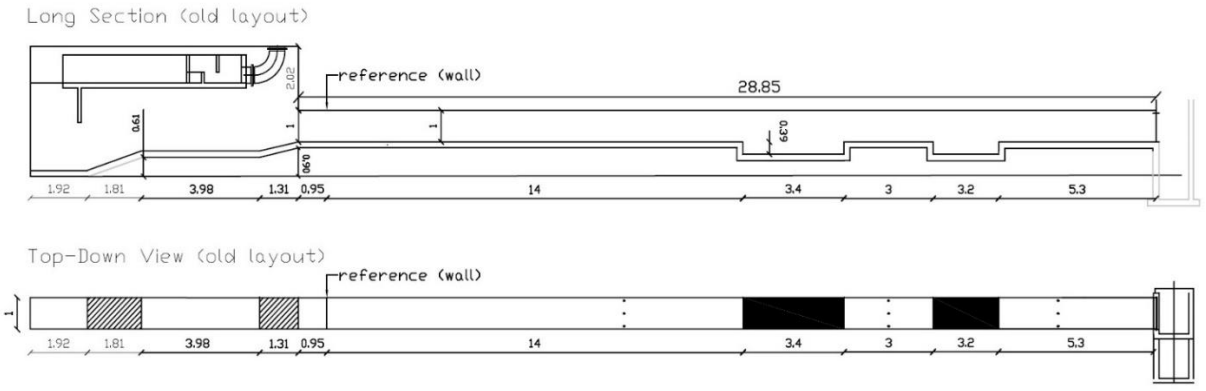

Figure 3.1 - Scheme of the FEUP's flume old layout (distances in meters).

Figure 3.2 - Different views of FEUP's flume old layout.

As it stood, the flume only allowed experimental studies using steady currents. In order to produce and combine waves and currents, conditions needed to perform offshore experimental tests, adaptations and upgrades were made on the flume. The adaptations enabled the installation of a wavemaker - "wet back wave paddle" type with 1m width by 1m height by *HR Wallingford (UK) - HRW – UK*. The paddle allows the reproduction of regular and irregular waves, while a by-pass system beneath it, by means of a metallic plate and a pipeline inlet, allows the water to enter in the flume and reproduce steady current conditions.

So, the adaptation works consisted on:

1. Breaking of the flume floor thickness from 2.26 m behind the reference (wall) up to 8.8 m after the reference (Figure 3.3 and Figure 3.4);
2. Construction of a smoother transition - approach ramp - 5.8 m long with a 1/20 slope - beginning after 3 m from the reference (wall) and finishing at 5.2 m from the first deposit box (Figure 3.5 and Figure 3.6). The slope used is in agreement with similar studies on scour protections, *e.g.* De Vos *et al.* (2012) and De Schoesitter *et al.* (2014);
3. Waterproof isolation of the flume walls (near the wave paddle installation) and of the approach ramp from the reference (wall) until the end of the approach ramp (Figure 3.7);
4. Installation of a metallic plate, at the reference (wall) at 0.29 m from the floor, in order to separate the wave paddle (on the top) from the flow and currents passage (below the plate). The metallic plate is 3 m long by 1 m width with 4 mm thickness (Figure 3.8, Figure 3.9 and Figure 3.10);
5. Construction and assembly of two by-pass boxes (By-pass 1 - 0.28 m height, 1 m width and 1.25 m depth; By-pass 2 - 0.28 m height, 1 m width and 1 m depth). The boxes were placed beneath the metallic plate (Figure 3.11);
6. Construction and assembly of a protection gate, with 1 m height by 1 m width with 30 mm thickness, at the reference (wall). The gate is placed at a distance of 0.29 m from the floor at its location (Figure 3.16);

7. Installation of the wavemaker (including all its components) on the 3 m plate (Figure 3.20, Figure 3.21, Figure 3.22, Figure 3.23 and Figure 3.24). The paddle is designed to not be directly supported on the plate.

3.1.1. Adaptation Work Stages

In stage 1, the flume floor was broken at an extension of 11.06 m – 2.26 m behind the reference (wall) up to 8.8 m after the same reference - creating a 0.29 m floor gap at 5.2 m from the first sediment box – as shown in orange in Figure 3.3. With this work, the flume floor has been reduced and leveled at the extension aforementioned, thus allowing the construction and installation of the approach ramp and the metallic plate, respectively.

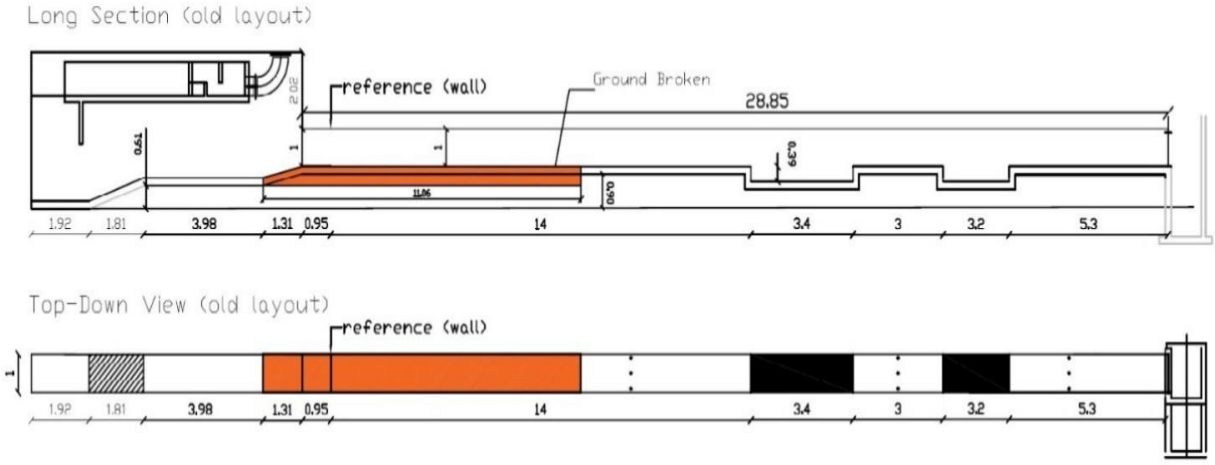

Figure 3.3 - Flume scheme layout for stage 1 (distances in meters).

Figure 3.4 - Stage 1: Breaking of 0.29 m of the ground thickness.

In stage 2, the approach ramp was built - from 3 m after the reference until 5.2 m before the first deposit box – with an extension of 5.8 m. The ramp was projected with a 1/20 slope (Figure 3.5), in order to overcome the gap between the two leveled floors and to avoid abrupt changes in the bathymetry, which

leads to changes in the wave's characteristics. The waves were also monitored at the monopile section, to ensure that the incident wave is the one considered in further analysis. The ramp has an initial sub-grade layer, of compact coarse material, and it is finished with a concrete layer (Figure 3.6). At the end of this stage, the walls on the zone of the ramp were slightly corrected and aligned since in certain areas they presented minor deformations.

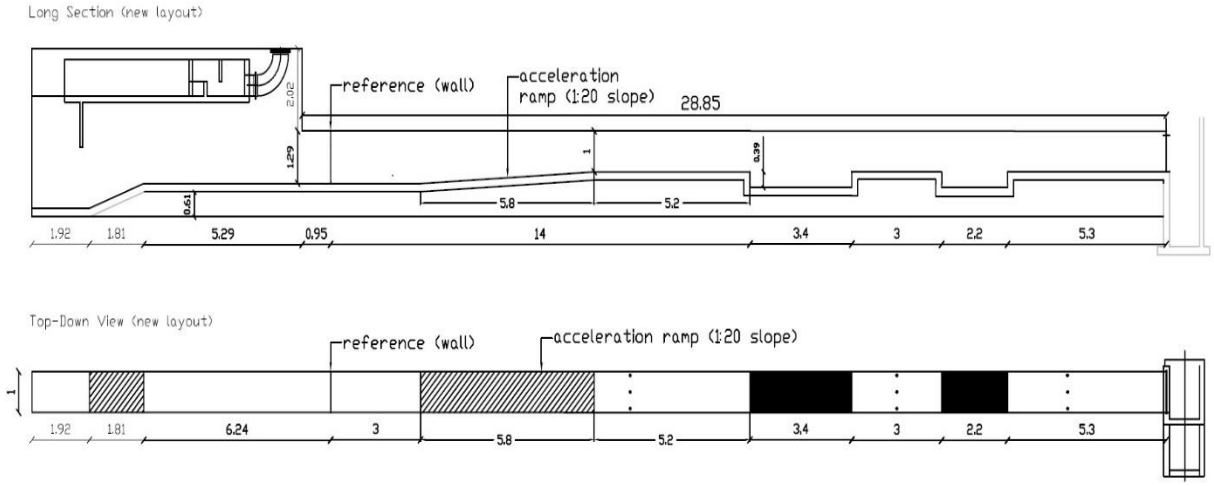

Figure 3.5 - Flume scheme layout at the end of stage 2 (distances in meters).

Figure 3.6 - Stage 2: Approach Ramp (5.8 m long with 1/20 slope).

In stage 3, the reconstructed flume section was isolated (Figure 3.7) in order to prevent leaks due to possible micro-cracks in the ground, or even in the walls.

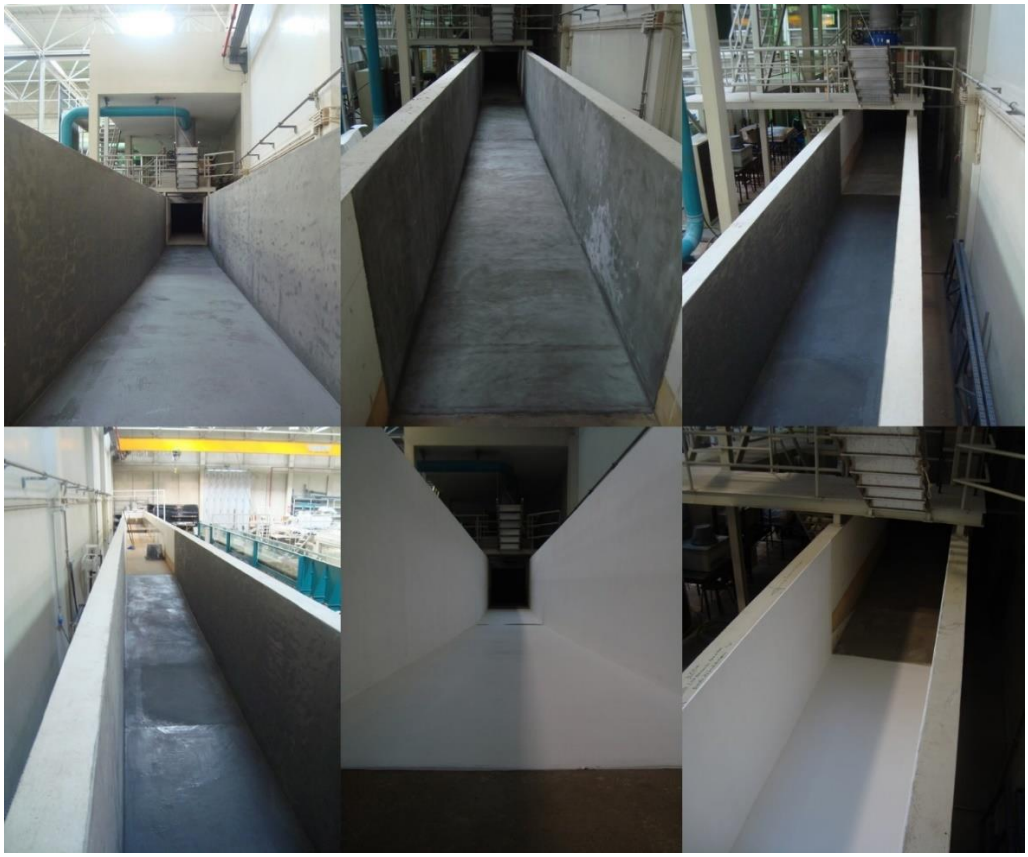

Figure 3.7 - Stage 3: Different phases of the walls and approach ramp waterproof isolation.

In stage 4, to protect and separate the wave paddle, and its electrical components, from the flow and currents, a set of 3 metallic plates – 1 m long, 1 m wide and 4 mm thick each - were connected to each other and placed from the reference (wall) forward. The distance from the plates to the ground is 0.29 m to accommodate two by-pass boxes (stage 5). The plates were attached to the flume walls using L-shaped stainless steel profiles, on each side.

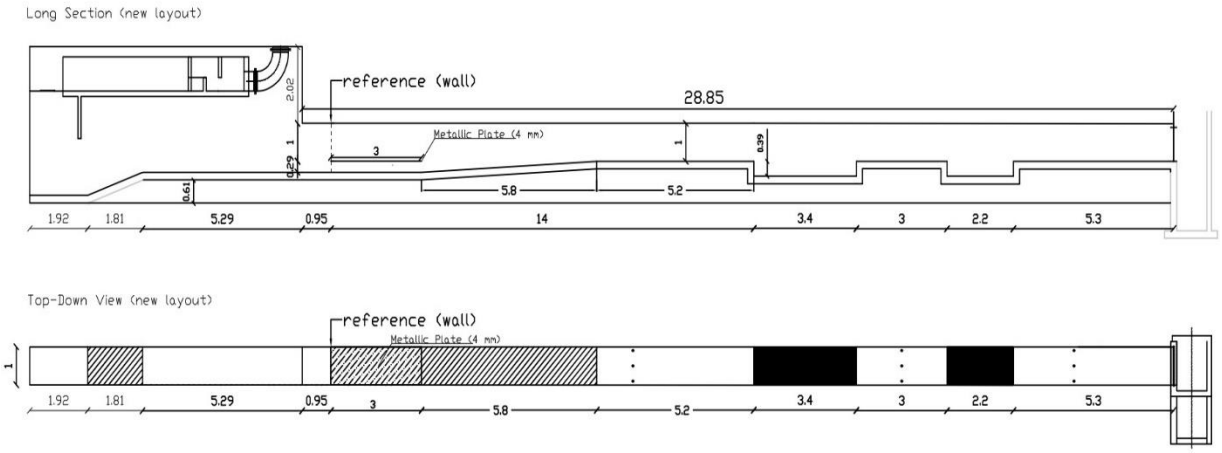

Figure 3.8 - Flume scheme layout at the end of stage 4 (distances in meters).

Figure 3.9 - Stage 4: Installation of the metallic plate.

Figure 3.10 – Flume reconstruction stage 4 conclusion.

In stage 5, the construction and assembly of two by-pass boxes were carried out. The by-passes were assembled with the objective of reducing turbulence, ensure a steady current at the monopile section and to serve as additional support to the metallic plate - preventing or reducing excessive vibrations.

Figure 3.11 shows the setup of the by-pass system. This system was made as a temporary solution to assess the conditions of the current, at an inlet section and the monopile section. In future research, depending on the flow measured conditions, a more definitive solution can be implemented.

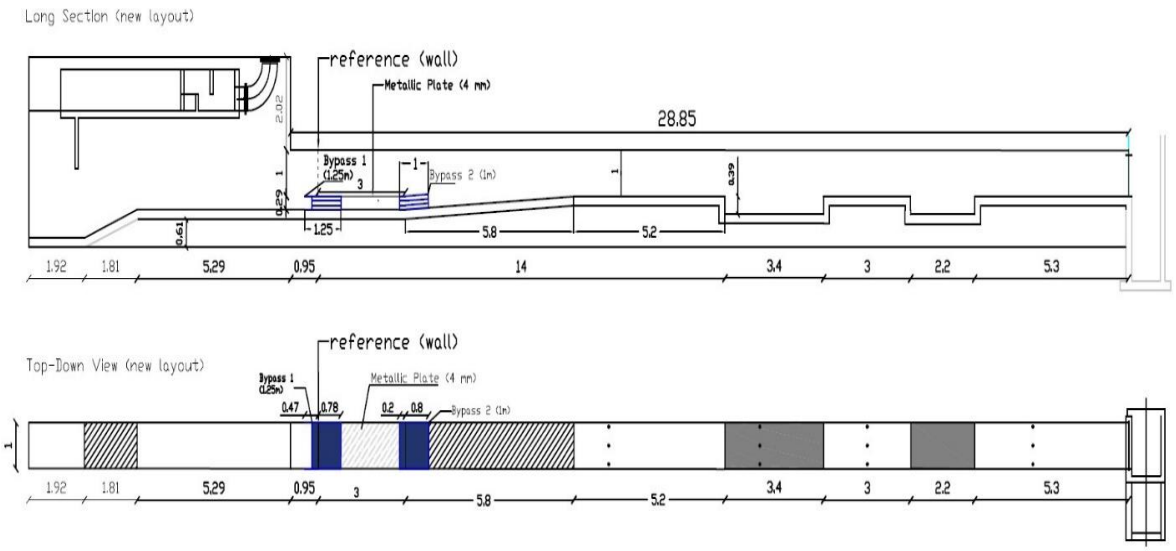

Figure 3.11 - Flume scheme layout at the end of stage 5 (distances in meters).

For each by-pass box, 33 PVC Metric Pressure PN6 pipes (Φ_{ext}=90 mm, e=1.5 mm, L=1 m) were used. In order to accommodate and strap the pipes to each other and over each other, 4 L-shaped galvanized steel (L60/40), for the edges, and 6 threaded stainless steel rods (Φ=5 mm, L=1 m), one for each row at the front and back of the box, were used. A plastic net – with a 5 mm×5 mm mesh – was placed at each face of the boxes. Figure 3.12, Figure 3.13 and Figure 3.14 provide the details of the by-pass setup.

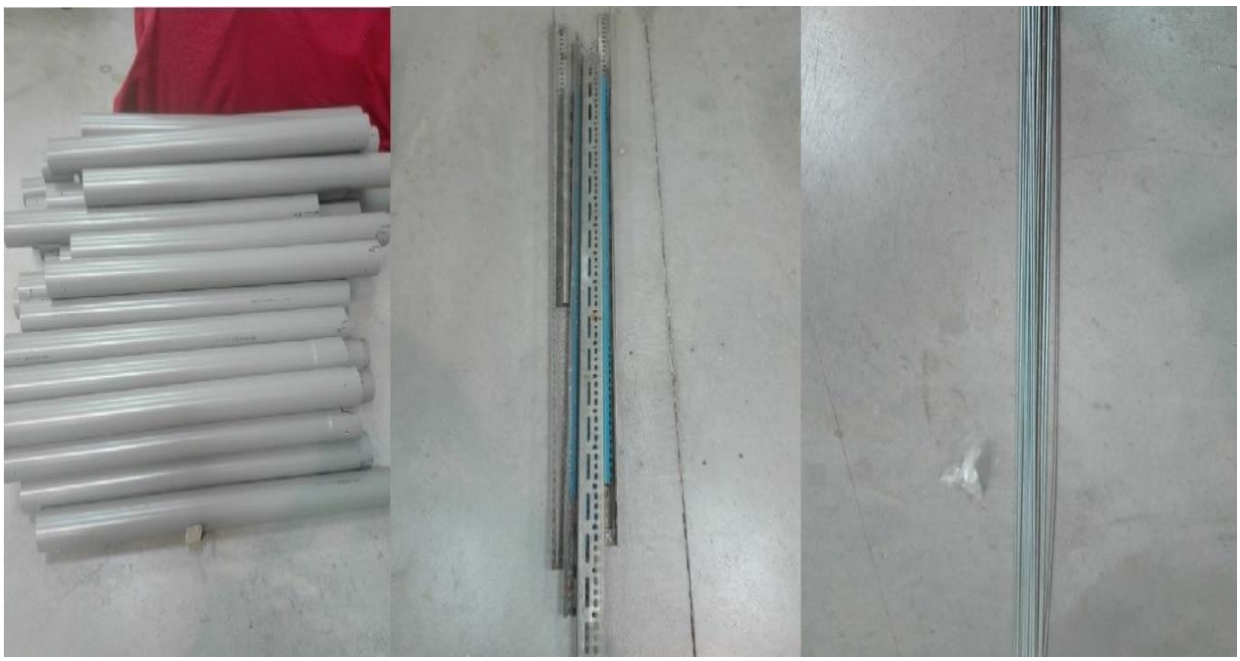

Figure 3.12 – By-pass boxes materials (PVC PN6 Φ=90 mm pipes; L60/40 galvanized steel profiles; Threaded Φ=5 mm stainless steel rods).

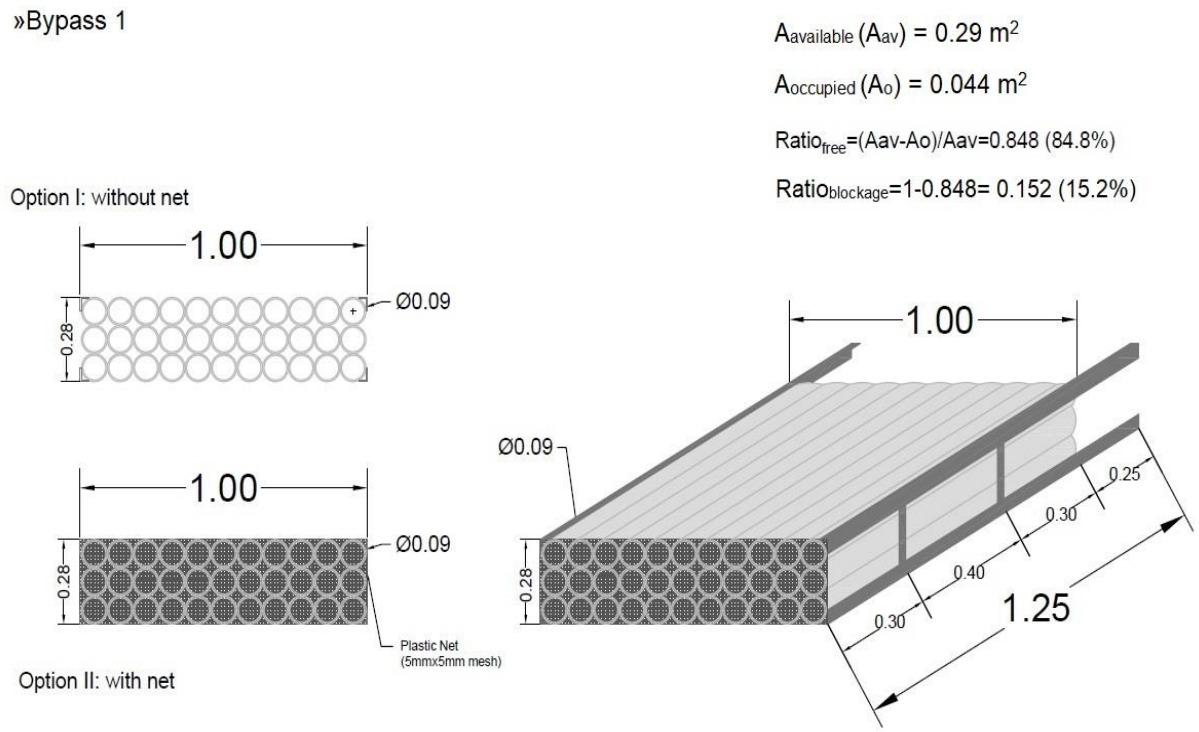

Figure 3.13 – By-pass 1 box (measurements in meters).

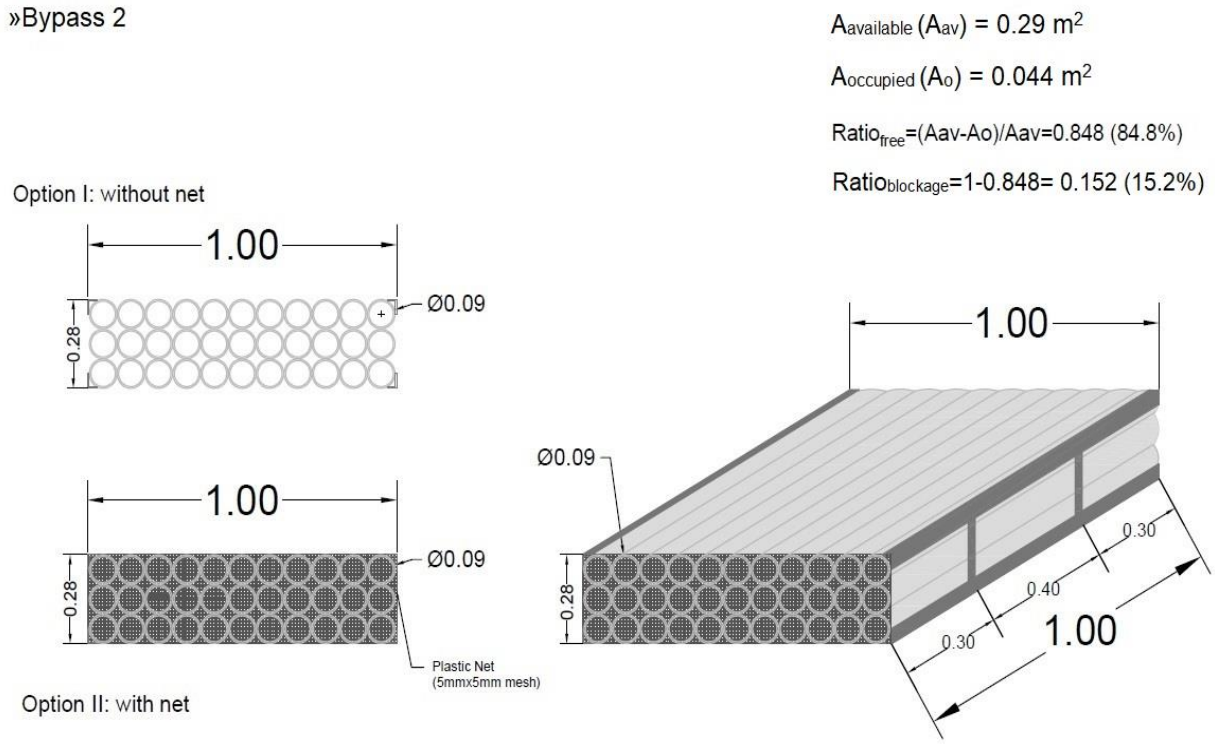

Figure 3.14 – By-pass 2 box (measurements in meters).

With the solution presented, the occupied area – without considering the residual influence of the net and of the threaded rods – is now of 0.044 m^2. The 0.29 m^2 of available area under the metallic plate, was reduced to 0.246 m^2 with the by-passes, representing a reduction of around 15% of the available area (Figure 3.13 and Figure 3.14).

The L-shaped profiles of the first box (by-pass 1), have a length of 1.25 m, opposite to 1 m in the second box (by-pass 2). The intention was to support the gate on that 0.25 m free span. In the end, those excesses of profiles were not necessary. Therefore, instead of cutting off the excess of profiles they were left out, since they allowed a better maneuver and placement of the box under the metallic plate.

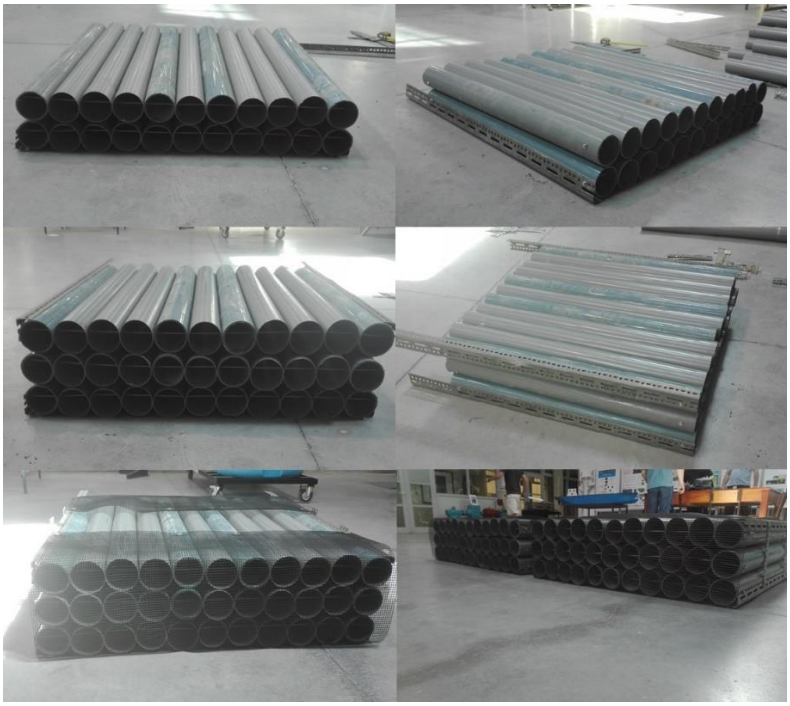

Figure 3.15 – Different assembly stages of the by-pass boxes.

In stage 6, for the back protection of the wave paddle – and its absorption beach - from the flow that arrives directly from the head reservoir a gate was assembled. The gate also allows the flow to be conducted to the by-pass system, under the metallic plate. In order to fit it in the flume, right above the metallic plate, at the reference (wall), the gate was designed with 1 m height and 1 m width and to facilitate its withdrawal whenever necessary, the gate was made of *Polymethyl methacrylate* (PMMA) – ρ=1190 kg/m^3 - instead of stainless steal - ρ=8000 kg/m^3. The gate was made with 30mm thickness. The Ultimate Limit State (ULS) of the gate was verified and it was concluded that the structure would withstand to the conditions - mainly hydrostatic thrust efforts - to which it would be subjected.

For the side supports of the gate, two square stainless steel tubes (40 mm×40 mm ASTM A-554) were adapted into two U-shaped profiles. For the bottom support, to ensure that the gate never gets in contact with the plate, since its weight could be detrimental, a *Styrene-butadiene* (SBR) rubber was adapted to the upper part of the metallic plate. Two holes were engraved in the rubber, in order to fit two stainless steel profiles fixed to the absorption beach support structure – as shown in Figure 3.17 – used as extra supports.

With this supporting system, the gate was ready to be put safely in place. However the gate placement was suspended until the absorption beach support structure was installed - part of the wavemaker assembly, described in section 3.2.

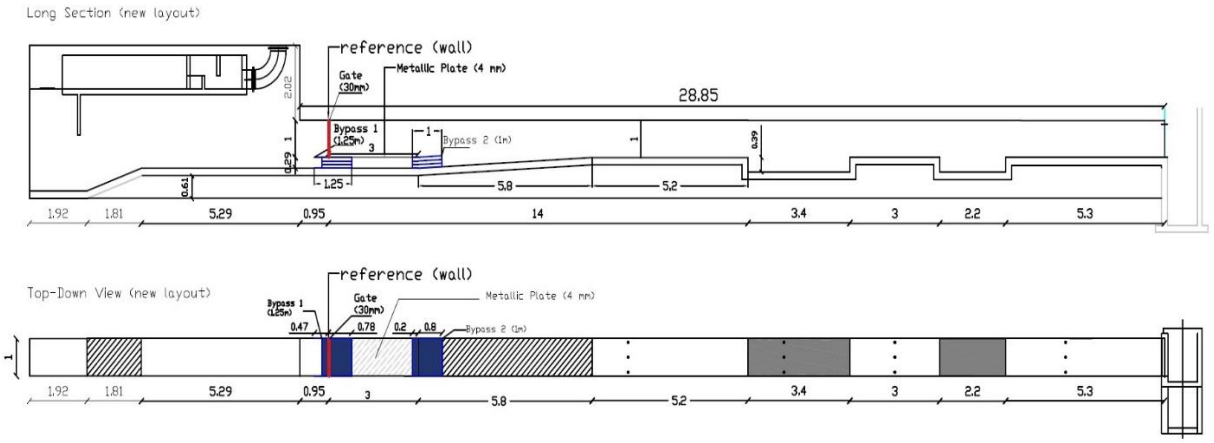

Figure 3.16 - Flume scheme layout at the end of stage 6 (distances in meters).

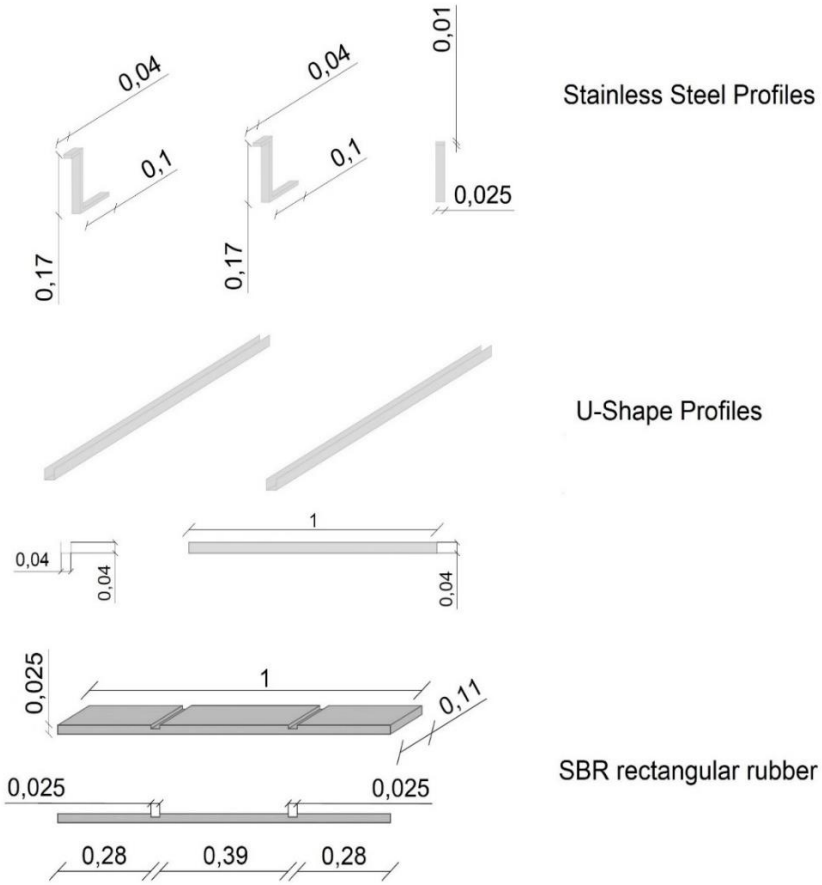

Figure 3.17 - Scheme of the materials used for the gate support (measurements in meters).

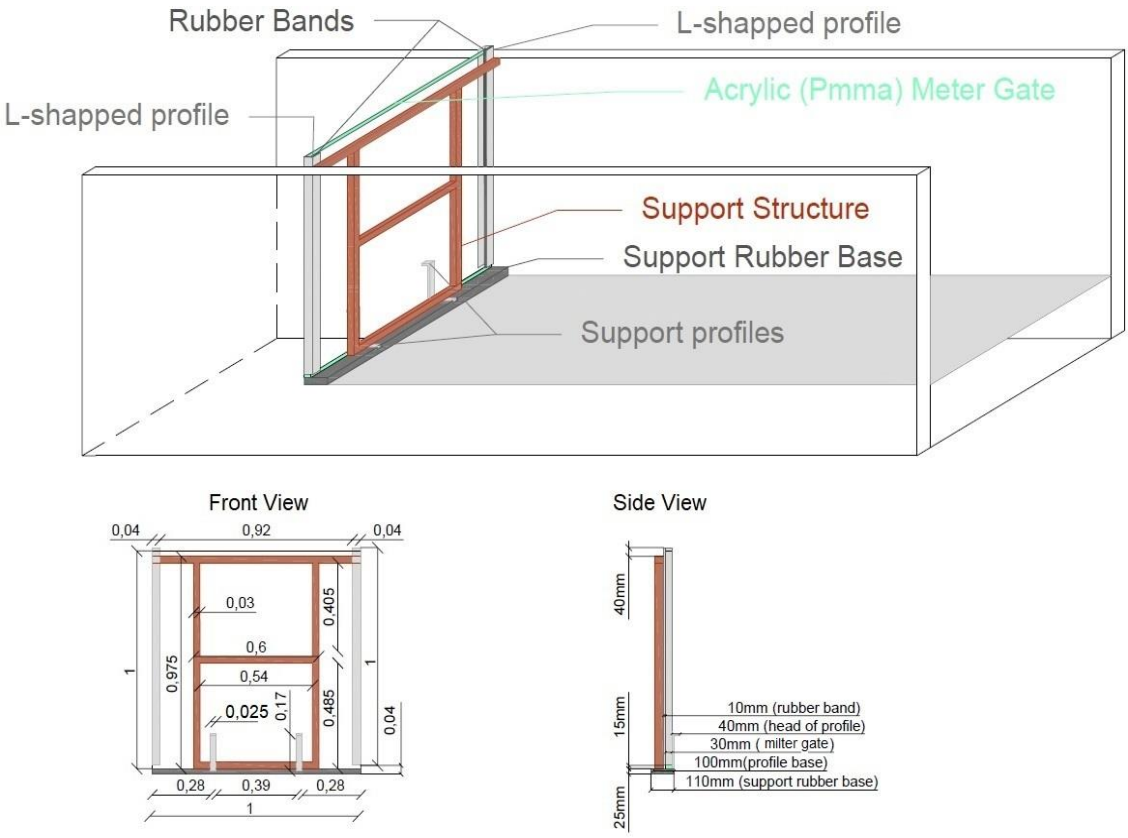

Figure 3.18 - Scheme of the Gate Disposition.

Figure 3.19 - Gate Pictures.

3.2. WAVEMAKER ASSEMBLY

After all the previous 6 stages, the adaptation works could be concluded with the installation of the wavemaker. The wavemaker was commissioned to *HR Wallingford (UK)*, taking into account the new flume layout – 1 m wide and 3 m free span of metallic plate available for the placement of the wavemaker components. The chosen equipment was a piston type flume wavemaker – that could also be described as a "wet back wave paddle" wavemaker – with only one axis. It has a single paddle that moves horizontally with 1 m width by 1 m height. The equipment allows the reproduction of solitary, regular

or irregular long-crested waves. The paddle can operate with 1 m of water depth, although, for safety reasons, the maximum water depth allowed in the flume should not be higher than 0.7 m. The wavemaker is equipped with an active absorption module of reflections, *Dynamic Wave Absorption System*, integrated into the paddle. This module aims to reduce reflected waves by the model, the flume walls or even by the downstream gate, propagating towards the wavemaker. This would lead to the re-reflection of the original wave by the wave paddle. This should be avoided since those re-reflections can overlap the generating waves, creating larger or smaller waves than the intended ones (Rosa-Santos, 2010). In the ultimate case, this could lead to the automatic activation of the safety trigger that shuts down the wave paddle as a safety measure.

The wavemaker has a computer with the wave generation software *HR Merlin*, necessary to control the wavemaker and simulate a wide range of sea states. The software allows the reproduction of irregular sea states from a wide variety of wave spectrums, including:

- Joint North Sea Wave Project (JONSWAP);
- Pierson-Moskowitz;
- International Towing Tank Congress (ITTC);
- Darbyshire Coastal;
- Darbyshire Ocean;
- Neumann;
- Top-Hat;
- Bretschneider.

In this case only the JONSWAP will be used, as it represents the typical sea-state at the North Sea.

Table 3.2 - Wavemaker main components.

Main Components		
Structural Components (Figure 3.21)	Beam covers; Main axis (beam + bearings); Front and Rear Beam support; 2 Flume Mounting Brackets; 4 Safety Covers;	Paddle and respective Wishbone Bracing; 2 Paddle Retainer Brackets; Foam Absorption Beach; Absorption Beach Support Structure and Retainer;
Electrical Components (Figure 3.22)	Electrical drive actuator (800 mm stroke); Low Inertia AC servo Motor; Motor Drive Control Panel (MDCP);	Light Beacon; Wave generating computer; Remote Paddle Safety Unit;
Wave Generation Software	*HR Merlin*	

According to the instruction manual, top/front view and cross-sections (Figure 3.20), some structural component and all the electrical components should be above the water level (even though all the structural components are made of stainless steel, except the foam absorption beach). The paddle is designed to be mounted under the electrical drive actuator that contains a beam between four bearings. The motor of low inertia (in order to achieve high-frequencies) on the top of the equipment, drives the beam horizontally, which in turn drives the paddle in the same direction. A light beacon composed of 4 different lights and a bell, in the top of the Motor Drive Control Panel (MDCP), gives information about the 6 possible wavemaker states. All electrical components are housed or connected to the MDCP. The absorption beach should be placed behind the paddle in order to prevent splashing and for wave dissipation at the back of the paddle. The remote paddle safety unit, composed by an emergency button, scheduled to be connected to the wave generating computer, allows to safely shut down the equipment in case of emergency.

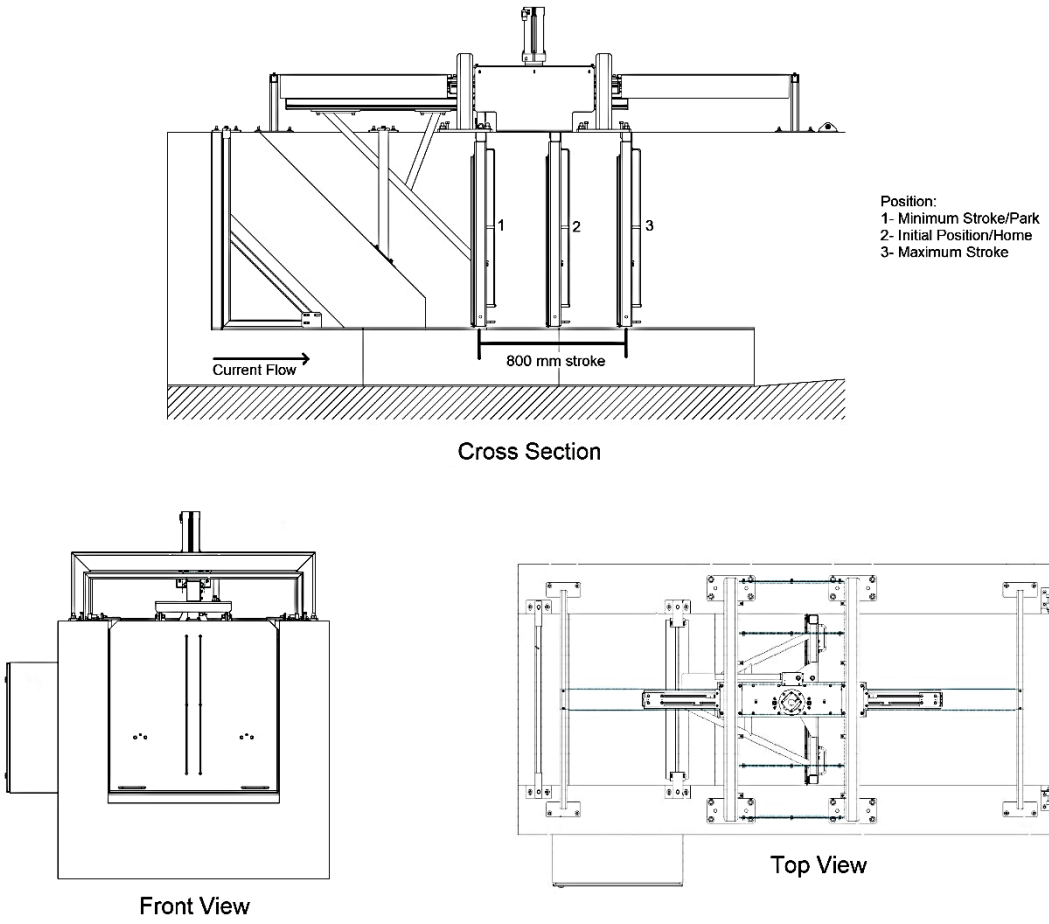

Figure 3.20 - Wavemaker Cross Section and Views.

Figure 3.21 – Wavemaker main structural elements.

Figure 3.22 – Wavemaker main electrical elements: (a) MDCP; b) Light Beacon; c) Wave generating computer and Remote Paddle Safety Unit; c) Low Inertia AC servo Motor.

For the installation of the equipment's structural elements, the top of the flume concrete walls had to be drilled and isolated with chemical anchors, in order to bolt the structural elements to it. The assembly and installation began with the "main support/component" – constituted by the main axis, the actuator, the flume mounting brackets, the safety covers and the motor. The next components were the front and rear beam support, its covers and the main axis, followed by the wishbone bracing and the paddle. The absorption beach and its support structure were the next components to be installed, allowing the gate to be put in place - closing the suspended stage 6. With the absorption beach in position, the beach retainer was fixed to the walls. In order to conclude the structural assembly, the paddle retainer brackets were bolted to the flume walls. These brackets allow to hinge and hold the paddle forward when is desired to retransform the flume into the "current only" mode.

Figure 3.23 - Pictures of the wavemaker assembly phases.

The next step was to install all the electrical components as close as possible to the wavemaker, but protected from the water contact. For that reason, the MDCP unit was placed outside the flume wall, while the wave generation computer and the remote paddle safety unit were placed on the balcony nearest to the flume, which is slightly above of the flume's top

As the flume is also used for fluvial experimental tests and research projects, one of the requirements was the ability of the wavemaker to be removable, by allowing the transformation of the infrastructure from a "wave and current" flume into a current flume, hence the inclusion of the paddle retainer brackets. For that reason, a disassembly plan was carried out. The plan has 7 steps that must be followed in order. The disassembly of the equipment does not corresponds directly to inverse path of the assembly stage aforementioned.

Figure 3.24 - Functional Wavemaker.

Table 3.3 - Disassembly Plan Steps.

Step 1	Removal of the rear beam cover
Step 2	Removal of the beach retainer
Step 3	Removal of the absorption beach
Step 4	Gate removal
Step 5	Removal of the beach support frame
Step 6	Removal of the wishbone bracing
Step 7	Hinge paddle forward and hold it to the paddle retainer brackets

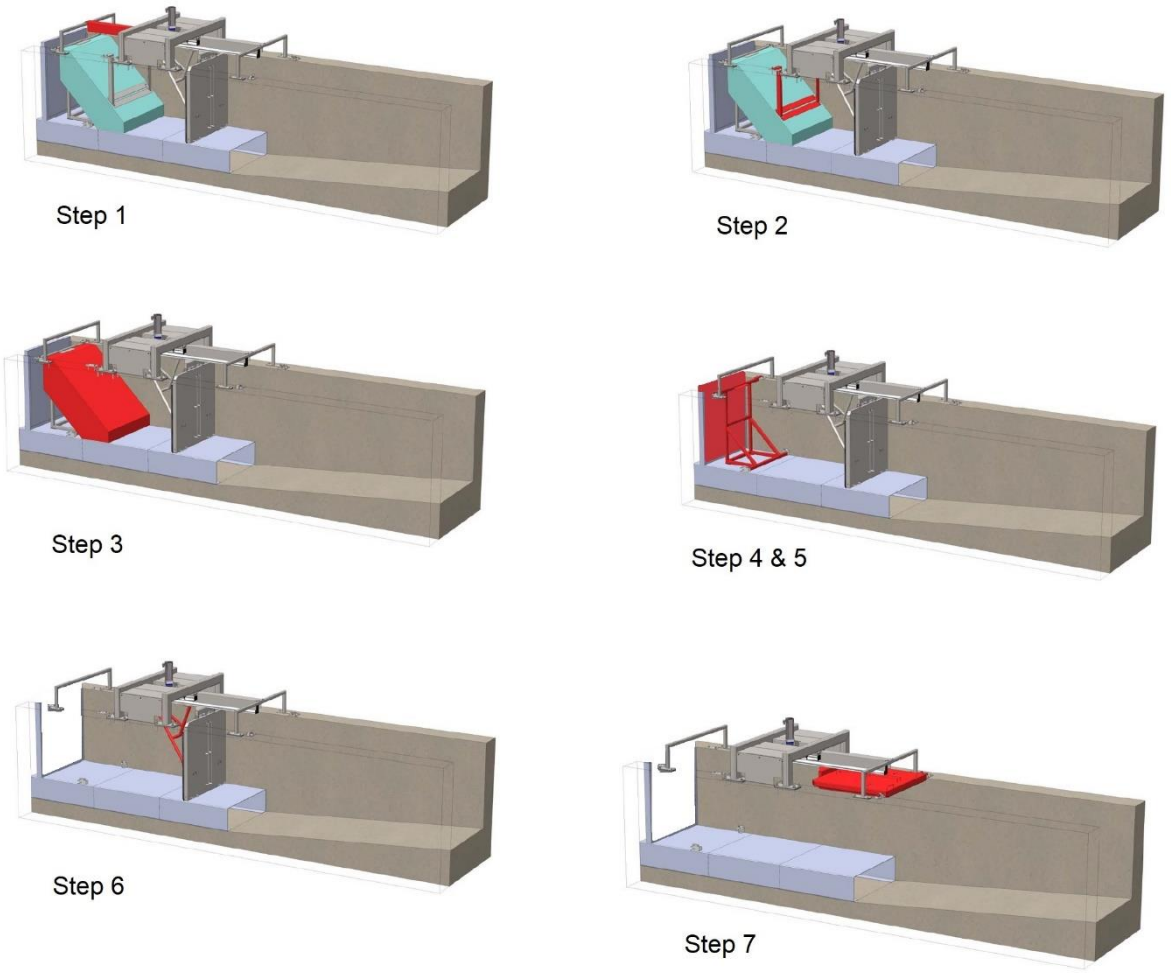

Figure 3.25 - Disassembly Plan Steps scheme.

After following these steps, both by-pass boxes and the metallic plates should be removed, in order to fulfill the transformation. However, if desired, the rest of the remaining structure can also be removed

by unscrewing the bolts from the wall to then, with the industrial crane, lift and place it in the desired place.

3.2.1. Data Acquisition System

The wave generating computer can also function as a sea state acquisition system if an acquisition board is connected to it, since the computer also possesses the data acquisition software *HR WaveData*.

However, the laboratory already has an individual sea state acquisition system (Figure 3.26), placed at the laboratory control room. It allows us to check if the wave generation software is producing the target waves (with the intended parameters). It also allows us to determine the water surface elevation at any given desired point of the flume.

In order to acquire information, it is necessary to connect hydrodynamic level probes (constituted by two steel conductor rods) to the acquisition system boards. The probes, due to the circulation of an electrical current between the two conductors - that leads to a potential difference measured in volts -, measure the free water surface level. In order to acquired valid results, and as accurate as possible, the probes must be calibrated every day and whenever the water level changes. For the entire duration of a test, the probes, placed in tripods, acquire a time series of voltages, which are subsequently converted into free water level surface records, allowing the determination of the sea state conditions at the probe locations, based on the calibration used for that same test. Then, using the Reflection Analysis tool of the data acquisition software, is possible to analyze if the test intended wave height was or not produced or achieved. In case the intended wave height is not reached, this software tool helps to determine the gain factor required to be introduced into the wave generation software, which will eventually lead to the intended wave height.

Figure 3.26 – Sea State Acquisition System.

3.3. BATHYMETRY ANALYSIS

In order to measure and describe the bathymetry of the bed profile and the monopile foundation, a close-range photogrammetry technique was used.

This technique is commonly used to study local scour around bridge pier foundations (Ramos *et al.*, 2016; Bento *et al.*, 2018). It enables the scanning and reconstruction of scour holes geometry, caused by the presence of an infrastructure - like a bridge pier, a monopile - in rivers or sea beds.

This technique requires a digital camera and a set of ground control points, to create 3D models. According to Ramos *et al.* (2016), the ground points consist in highlighted points in two sets of symmetric rulers – each one placed in opposite sides of the area of study – to create a spatial reference. For this dissertation, 4 rulers of 50 cm, two on each side of the flume, were used - one for the "positive" ground points and the other for the "negative" ground points. Each ruler was marked from the 0 cm to the 50 cm in 10 cm intervals generating 24 ground points, 6 points per ruler, but since 2 points on each side coincide as the "zero" mark, the total number of ground control points was 22.

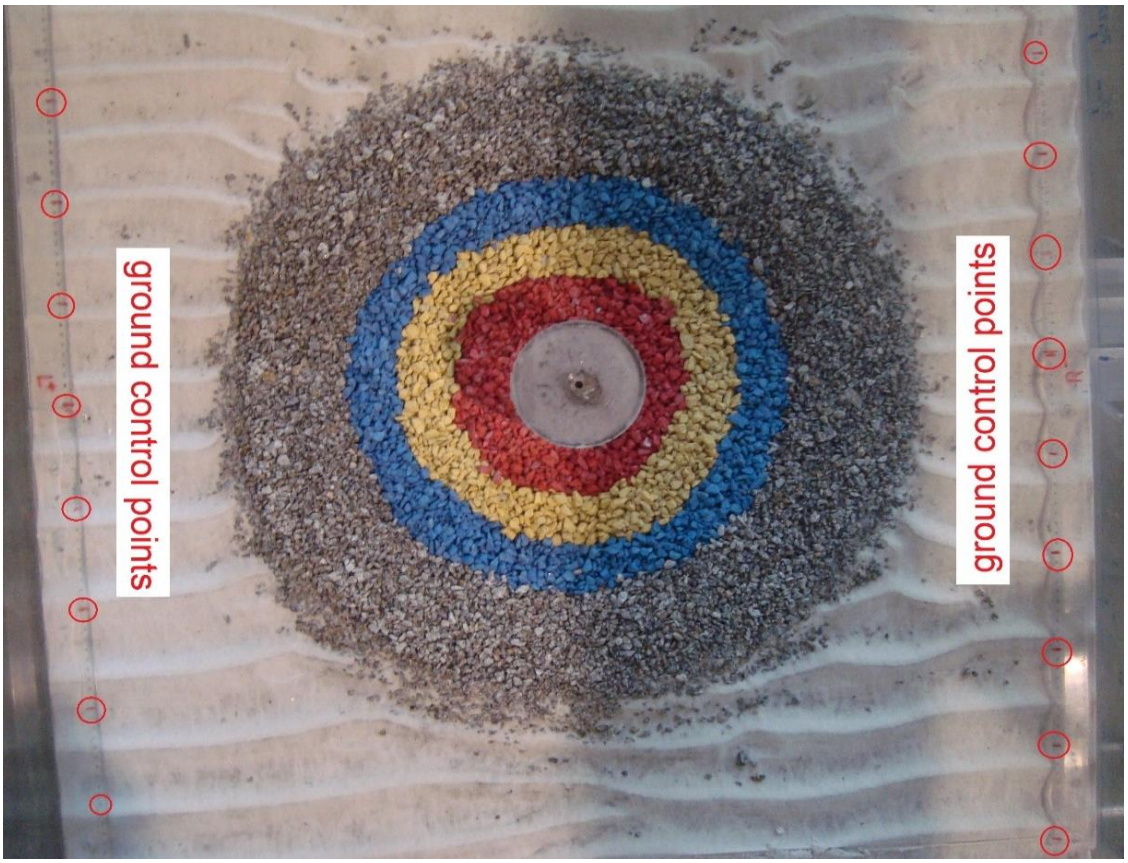

Figure 3.27 - Example of some ground points.

After each test, the camera needed to go through different sets of positions in different rows, allowing to photograph all the area of study. Agisoft (2018) suggests a 60% of side overlap, plus a 80% forward overlap between the coverage area of the camera in each position, in order to cover all the scour development. For that reason, it was important to define a certain number of rows, each one with a certain number of camera positions, in order to meet the overlap requirements. For this dissertation, 6

rows – with an increase spacing of 11.5, 12, 12, 12.5 and 13 cm between rows from downstream to upstream - and 16 camera positions per row – with 6 cm of spacing between positions - were used, resulting in 96 photos in the end of each test, surpassing the overlap recommended requirements. The camera was inserted in a structure sufficiently stable, allowing it to travel through the entire flume length, in order to cover the necessary rows. The structure also allowed the camera to move along the entire flume width, in order to cover all the camera positions. The rulers used for the ground control points were placed as leveled as possible, next to the flume walls, without interfering with the sediment bed forms.

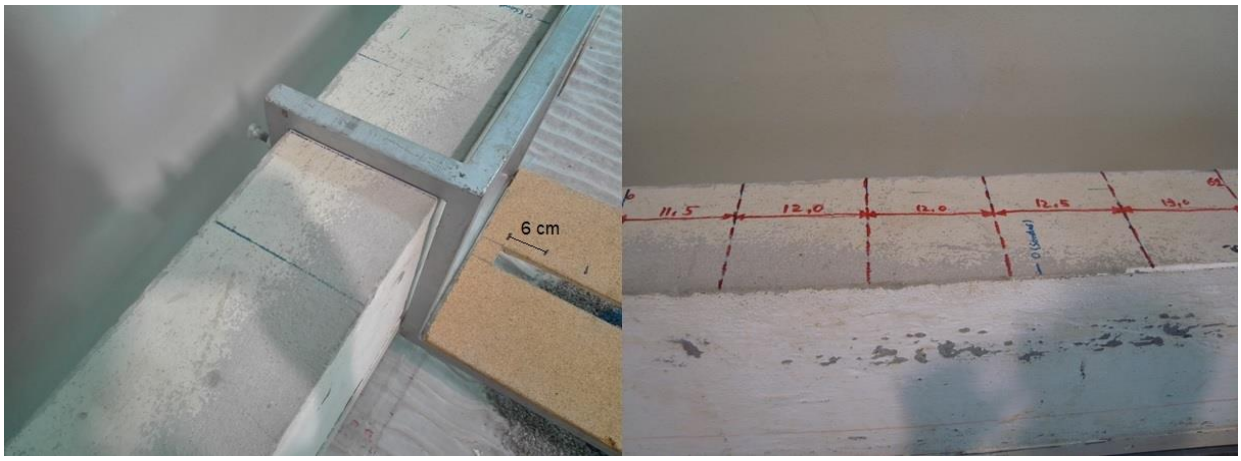

Figure 3.28 - Camera position spacing and row spacing.

Figure 3.29 - Camera support structure and photogrammetry layout.

Then, the photos are processed using the software *Agisoft PhotoScan Professional*, in order to obtain the digital terrain models (DTM). For the post-processing of the DTM's the *Paraview* software was used, resulting on the bed profiles and contours.

After each battery of tests, it is important to ensure that all the model surrounding area was as dry as possible before the photos were taken, since water and wet areas interfere with the precision of this technique.

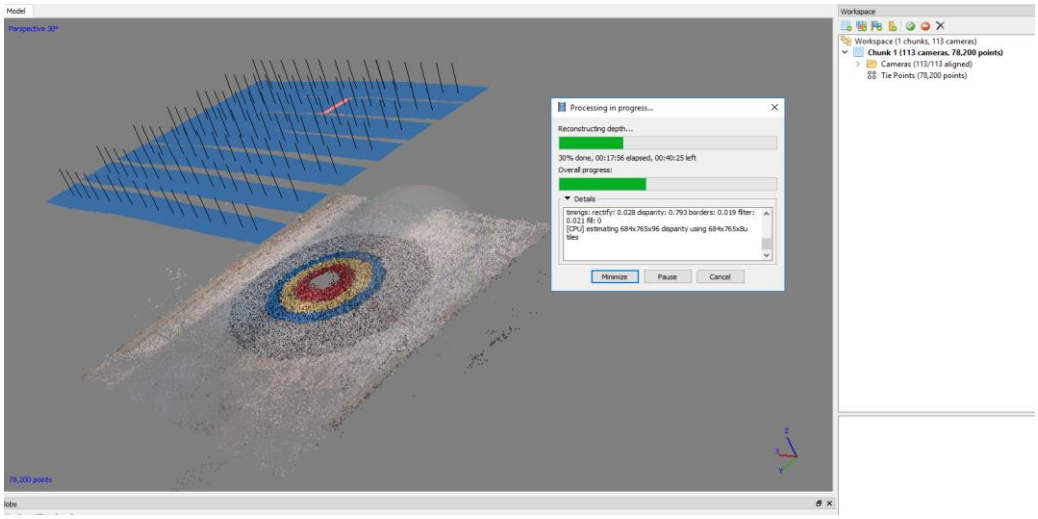

Figure 3.30 – *Agisoft PhotoScan Professional* software processing.

Although this method can be simply achieved with one digital camera, it can be quite time consuming due to the extent number of steps needed to follow, the amount of time needed to safely place the rulers - with the ground points - without damaging the model and the model bathymetry, the amount of time dispended to cover all the rows and all the camera positions, the amount of time required for the model surrounding area to dry and the difficulty to ensure, sometimes, the proper illumination conditions at the model location.

In order to photograph the area of study – structure, scour protection and surrounding area – it was used a *Sony Cybershot DSC-W120* digital camera with 7.2 megapixels, placed in a horizontal structure with a fixed height of 0.6 m to the sediment bed. The camera flash had to be turned off, since its brightness causes errors and noises on the software processing.

An important camera parameter for the photogrammetry is the ISO - assigned to correspond to the abbreviation of the organization that created the ISO scale (International Organization for Standardization). ISO is a measure of the sensitivity of the camera's sensor to light and for digital cameras can range from 50 to 204 800 (Nixon, 2019). The bigger the ISO value, the easier is to obtain pictures without blurring for low levels of light. Nevertheless, the picture will have a lower resolution. So big values of ISO are not advisable for this technique. For that reason, it was advised that, during the experimental works, the ISO values were maintained between 100 and 400.

3.4. Damage Monitoring Methodology in the Physical Model

In order to monitor the damage on the physical model, during the experimental phase, the visual damage assessment of the protection technique was used. This consists on the observation and interpretation of the scour protection's stones movement during and in the end of each test. De Vos (2008) reported that there is a clear relation between the visual damage and the damage number S_{3D}. In fact, as shown in Fazeres-Ferradosa (2018), that relation is not so clear since different values of the S_{3D} presented superimpositions in the transitions between the damage levels, *i.e.*, for the same value of S_{3D} two different visual damage levels can be attributed to the protection. The causes for possible disagreements between the S_{3D} and the visual damage levels are reviewed in Fazeres-Ferradosa *et al.* (2019).

As referred on section 2.4.3.2, the visual damage levels proposed by den Boon *et al.* (2004), and used in the OPTI-PILE project, have three categories: no movement, movement but not sufficient to cause failure and failure.

De Vos (2008) divided the second category into two different levels, resulting into a four level assessment of the damage (Figure 2.27 and Figure 3.31):

- Level 1: No movement;
- Level 2: Very limited movement;
- Level 3: Significant movement of stones, without failure;
- Level 4: Failure.

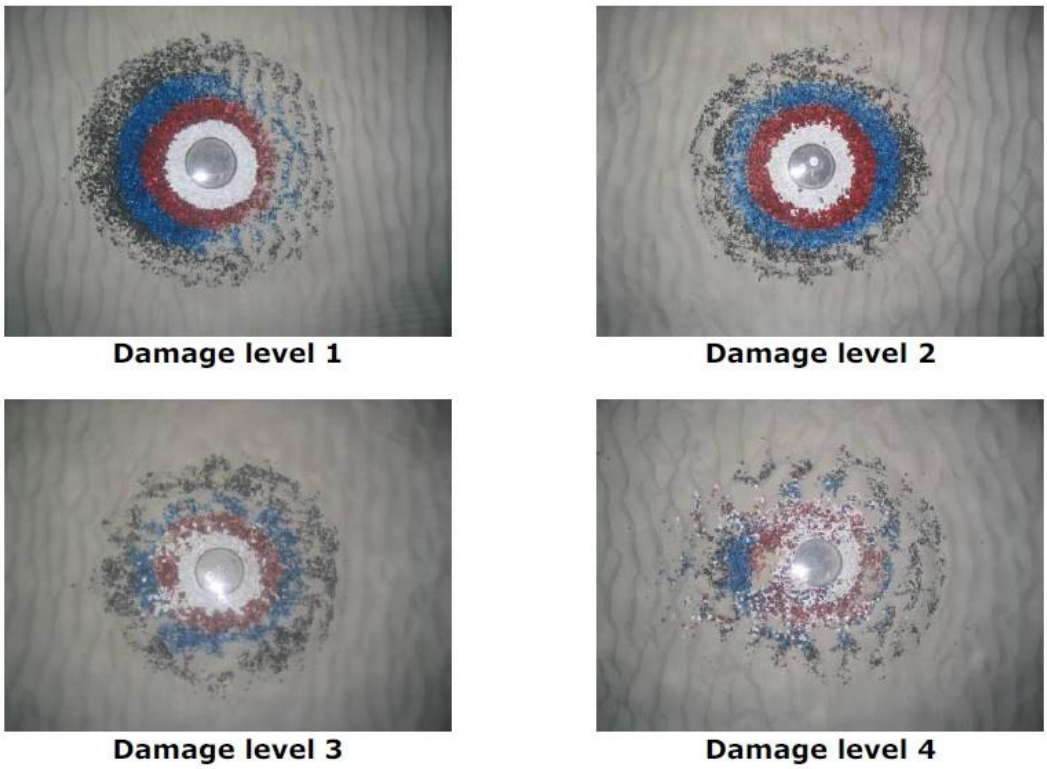

Figure 3.31 - Visual damage levels used by De Vos (De Vos, 2008).

This approach, although more detailed, was not followed. Instead, in continuous with the works of Fazeres-Ferradosa (2018), this dissertation used the damage levels proposed by den Boon *et al.* (2004) since most of the times the distinction between the damage level 2 and 3, at the laboratory, is hard to assess.

For the assessment of damage, in order to attach a damage level to each protection, observation of the model during and in the end of tests and the study of the photographic records taken in the end of each test were used.

3.5. PROTOTYPE AND EXPERIMENTAL MODEL CONDITIONS

As referred in section 2.7, physical modeling allows to understand the causes and effects of the conditions and phenomena that act on a prototype, through the study of its scaled model.

The experimental study of this dissertation was performed with loads, conditions and characteristics representative of the North Sea. This choice was made, since:

1. The North Sea region accounts for 70% of all wind offshore capacity in Europe (WindEurope, 2018);
2. The biggest European offshore industry stakeholders are from Northern or Central European countries such as Denmark, United Kingdom, Germany, Belgium or Netherlands (WindEurope, 2018);
3. One of the goals was to carry out tests with similar conditions to previous authors, in a sense of continuity with their works.

The experimental study was made for a single series of tests. The tests were carried out for an irregular sea state defined by a JONSWAP wave spectrum with a peak enhancement factor Υ=3.3 (typical of the North Sea).

The selected prototype conditions were defined for a monopile with a 5 m diameter (D_p=5 m):

Table 3.4 - Target prototype conditions.

Prototype	d (m)	H_s (m)	T_p (s)	U_c (m/s)	U_m (m/s)	D_p (m)
Conditions	18	6	14	0.5	1.29	5

The U_m value was calculated using the methodology developed by Wiberg *et al.* (2008). The input variables were the test series significant wave height, H_s, peak period, T_p, water depth, d, type of sea state and respective wave spectrum. The physical model was constructed according to a Froude similitude with a geometric scale of 1:50. The Froude similitude was chosen over the Reynolds similitude. Using Table 2.7 , it is possible to scale correctly the prototype conditions converting them for model values (preserving the Froude number both in the prototype and in the model).

The Reynolds number respecting the pile diameter, for the model target conditions, was calculated considering the U_m. The target $Re_p=1.79 \times 10^4$, according to the limit established by Frostick *et al.* (2011) and as referred in section 2.7.1, allows to surpass the fact that the Froude and Reynolds similitude cannot be preserved. However, it does not comply with other limits shown in section 2.7.1, that states, for waves-and-currents, that the vortex shedding can be disregarded for $Re_p>2 \times 10^5$. This problem was also reported in Fazeres-Ferradosa (2018) and may imply some scale effects that must be accepted to respect the Froude similitude. However, according to Sumer *et al.* (1992) those possible scale effects, due to inaccurate scaling of the Reynolds number, can be restrained for the range $10^3<Re<10^5$, in each the target Re_p fits in. Moreover, the target KC=3.564 - calculated using the model target U_m, T_p and D_p – is in conformity with the values obtained by other authors such Sumer *et al.* (1992), De Vos *et al.* (2012), Loosveldt *et al.* (2012), and De Schoesitter *et al.* (2014). Thus, according to Sumer *et al.* (1992), this KC value is consider small, therefore the influence of the Re_p on the vortex shedding is small. Since the KC number scales geometrically, since it depends on the U_m, T_p, and D_p, no scale effects are expected regarding this parameter, which is scaled correctly with the Froude similitude.

Table 3.5 - Target model conditions (Froude similitude - 1:50 geometric scale)

Model	d (m)	H_s (m)	T_p (s)	U_c (m/s)	U_m (m/s)	D_p (m)
Conditions	0.36	0.12	1.98	0.07	0.18	0.1

For a model peak period of T_p=1.98 s, 5000, 7000 or 9000 waves correspond, in prototype values, to storm durations of around 19h26min, 27h13min and 35h, respectively.

The tests on the flume are performed with fresh water (ρ_w=1000 kg/m^3), wheras the prototype, as an offshore structure, works under sea water (ρ_w=1025 kg/m^3). In order to maintain the ratio $\rho_{s/}\,\rho_w$ both in the prototype and in the model, it is necessary to apply a corrective factor χ to all the scale factors that depend on the water mass density, such as the scour protection material De Vos (2008).

$$\frac{\rho_{s,p}}{\rho_{w,p}} = \frac{\rho_{s,m}}{\rho_{w,m}}$$
$$\rho_{s,m} = \rho_{s,p}\frac{\rho_{w,m}}{\rho_{w,p}} = \rho_{s,p}\chi \tag{3.1}$$
$$\chi = \frac{1000\ kg/m^3}{1025\ kg/m^3} = 0.976$$

For the armour layer, previous authors (Table 2.5) have opted for a wide range of layer thicknesses: from $2D_{n50}$ to $8D_{n50}$. However, in this study, an armour layer thickness of $3D_{n50}$ was adopted. The damage number predicting equations, from De Vos (2008) - Eq. (2.68), Eq. (2.69), Eq. (2.70) and Eq. (2.71) –, were used to determine an indicative value of D_{n50} associated to a S_{3D}=1.0, based on the inputs of Table 3.6.

Table 3.6 - Algorithm input values (prototype)

Conditions	S_{3D}	d (m)	H_s (m)	Sea State	Uc (m/s)	T_p (s)	ρ_w (kg/m^3)	ρ_s (kg/m^3)	N	D_p (m)
	1.0	18	6	Irregular (Y=3.3)	0.5	14	1025	2650	3000	5

For these conditions, a $D_{n50,prototype}$ value of 0.262 m ($D_{50,prototype}$=0.312 m) was reached, as shown in Figure 3.32. Scaling these value, $D_{n50,model}$ =5.24 mm ($D_{50,model}$=6.24 mm). Since the density for the prototype armour material ($\rho_{s,prototype}$) is 2650 kg/m^3, by applying the corrective factor $\gamma = 0.976$, the selected material for the test should have a $\rho_{s,model}$=2586.4 kg/m^3. The tables used for these D_{n50} calculations are displayed in the Appendix A (Table A. 1 and Figure A.1), as also described in section 4.5.

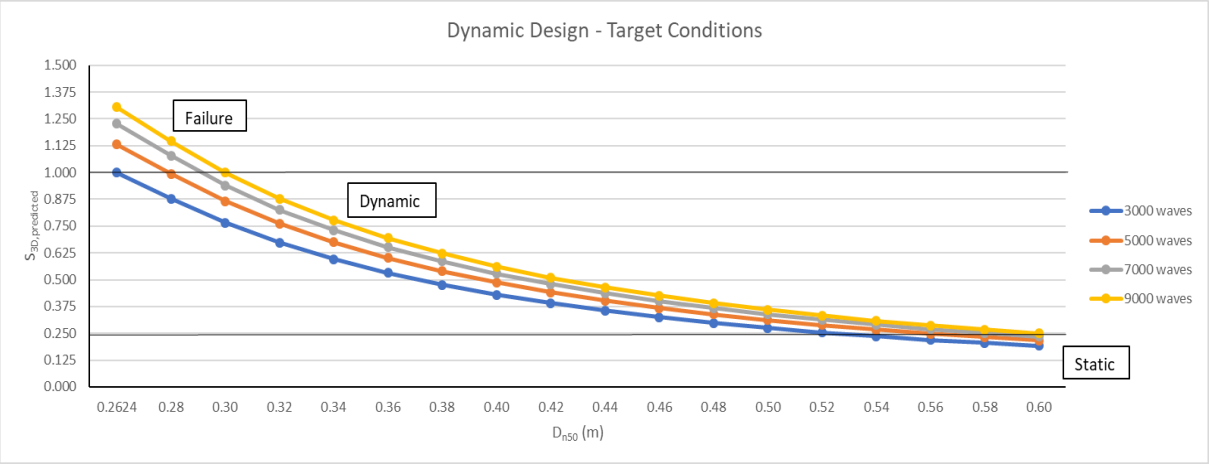

Figure 3.32 - Dynamic Design for Target Conditions.

Nevertheless, the available material was the gravel provided by the Construction Materials Testing Laboratory (LEMC) from FEUP. The 17 kg of provided gravel were sieved analyzed according to the norm NP-1379. The gravel had a mean diameter D_{50}=5.047 mm (D_{n50}=4.24 mm), a D_{15}=3.659 mm, a D_{85}=7.464 mm and a ρ_s=2630 kg/m^3. This leads to a ratio of $D85/D_{15}$=2.04, that according Table 2.2 is indicative of a wide grading material. Comparing the gravel mean diameter with the value reached in calculations (D_{n50}=5.24 mm), it is evident that the material is smaller than intended and, for the target conditions, will probably lead to the failure of the protection. Scaling the material to prototype values (Table 3.8), D_{n50}=0.21 m is less than the 0.2624 m intended on Figure 3.32. However, the value used for the experimental stage is within the values used in previous works by other authors (Table 2.5). The sediment analysis is provided by Table 3.7 and its grading curve by Figure 3.33.

Figure 3.33 - Armour Layer model material grading curve (adapted from the LEMC provided curve).

Table 3.7 – Armour Layer model material sediment analysis.

Sieve Opening (mm)	Mass Retained (g)	Retained (%)	Cumulative Retained (%)	Cumulative Passing (%)
63.0	0.0	0.0	0.0	100.0
45.0	0.0	0.0	0.0	100.0
31.25	0.0	0.0	0.0	100.0
22.4	0.0	0.0	0.0	100.0
16.0	0.0	0.0	0.0	100.0
11.2	0.0	0.0	0.0	100.0
8.0	77.8	9.89	9.89	90.11
5.6	180.0	22.87	32.76	67.24
4.0	392.0	49.87	82.63	17.37
2.0	107.8	13.70	96.33	3.67
1.0	14.2	1.80	98.13	1.87
0.500	5.0	0.64	98.77	1.23
0.250	2.8	0.36	99.12	0.88
0.125	1.9	0.24	99.36	0.64
0.063	1.7	0.22	99.58	0.42
<0.063	3.3	0.42	100.0	0.0

Table 3.8 - Test armour layer prototype and model values.

Armour layer	$D_{50,model}$ (mm)	$D_{n50,model}$ (mm)	$\rho_{s,model}$ (kg/m^3)	$D_{50,prototype}$ (m)	$D_{n50,prototype}$ (m)	$\rho_{s,prototype}$ (kg/m^3)
	5.047	4.239	2630	0.252	0.212	2694

For the conversion of the D_{50} values into D_{n50} values, Eq. (2.55) was used and for the ρ_s conversion, the corrective factor $\chi = 0.976$ was taken into account.

With a $D_{n50,model}$=4.239 mm, the $3D_{n50}$ armour layer corresponds to an approximate 63.6 cm armour layer - in prototype values.

As for the seabed sediment scaling, as explained in section 2.7, if they are scaled they will acquire cohesive properties, as the diameter decreases. Since in the prototype the seabed sediments have non-cohesive properties, by not scalling those sediments, in order to preserve those same non-cohesive properties, the study will incur in a scale effect. However, the option for non-cohesive sediments, although not scaled, is more representative of the real properties of the prototype seabed, than the option for a scaled model sediment with cohesive properties. For the model, the available material was a SP 55 silica sand, from *SIBELCO Portuguesa Lda*, with a mean diameter d_s=0.273 mm and sediment density ρ_s=2650 kg/m^3. According to Silva (2010), the sieving and the sediment analysis was performed according to the Portuguese norm NP EN 933-1. The sediment analysis is shown in Table 3.9 and the grading curve is shown in Figure 3.34.

Table 3.9 - SP55 silica sand sediment analysis (adapted from Silva (2010).

Sieve Opening (mm)	**Retained (%)**	**Cumulative Retained (%)**	**Cumulative Passing (%)**
1.0	0.0	0.0	100.0
0.710	0.0	0.0	100.0
0.500	0.0	0.0	100.0
0.355	4.67	4.67	95.33
0.250	58.20	62.87	37.13
0.180	29.66	92.53	7.47
0.125	7.12	99.65	0.35
0.090	0.34	99.99	0.01
0.063	0.01	100.0	0.0
<0.063	0.0	100.0	0.0

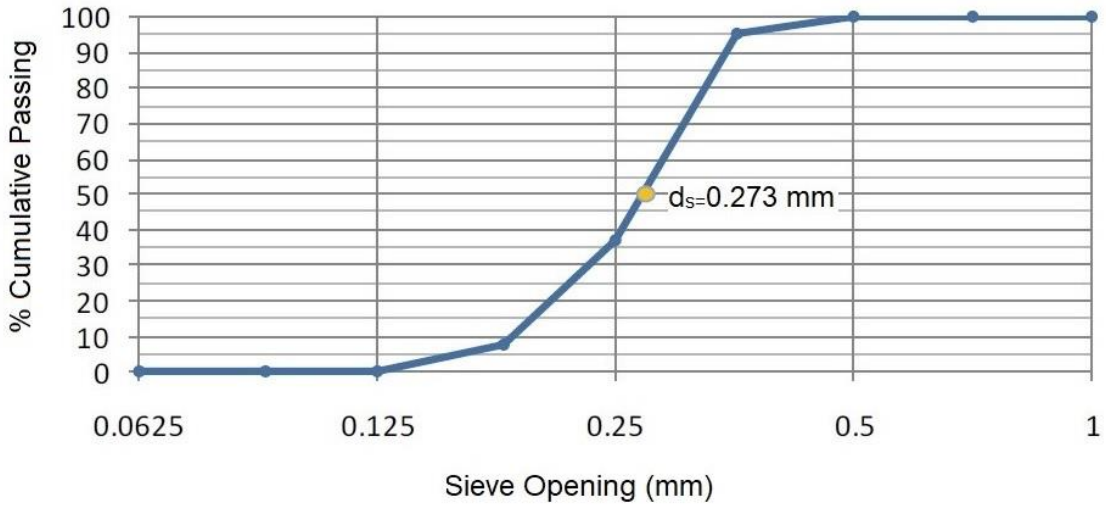

Figure 3.34 - SP55 grading curve (adapted from Silva (2010).

As for the filter layer, the proper choice should be to use coarse sand. Instead, the filter layer was built in geotextile as in (De Vos *et al.*, 2012). The geotextile thickness was approximately 1 cm, 0.5 m in prototype, with $5D_{p,model}$ diameter (50cm).The geotextile is made of *Polypropylene* (PP) with a surface density of 0.330 kg/m^2.

Most of the offshore wind turbines monopiles are made of steel (Ancona *et al.*, 2001; Zhang *et al.*, 2016). However, for the experimental study a circular monopile was used made of Pmma - the same material used for the milter gate described in section 3.1.1 - with a density of 1190 kg/m^3.

3.6. CALIBRATION OF THE EXPERIMENTAL CONDITIONS

In order to perform the experimental study of the model it was necessary to perform the calibration of the experimental conditions and of the measurement equipments used. For the experimental conditions, the calibration of the current velocities was made by creating, comparing and analyzing four velocity profiles - two for the target water depth (d=0.36 m) and two for a reference water level of 0.50 m. Then, a reflection analysis was performed in order to determine the reflection values after the wavemaker installation and guaranty that it would be under 15 to 10%, since reflection problems could lead to distortion and misrepresentations of the test conditions. Regarding the measurement equipments, the probes used during the reflection analysis and during the tests also needed to be calibrated before each test.

3.6.1. VELOCITY PROFILES

For the current flow calibration, velocity profiles were measured in different stages of this dissertation. The first stage of velocity measurements was made before the adaption works on the flume. The second stage was done right after these changes. The idea of these two measurements was to understand if and how much the changes made on the flume increased or decreased the flow conditions - and if the propose of the by-pass boxes was accomplished. Note that both measurement stages were done without the monopile model in place.

In order to measure the velocities an Acoustic Doppler Velocimetry (ADV) was used (Figure 3.35). It is an equipment that measures velocities (using the Doppler effect), distances and can also measure the water temperature. The equipment was a Nortek Vectrinoplus, with an accuracy of ±1 mm/s and with a max sampling rate of 200Hz.

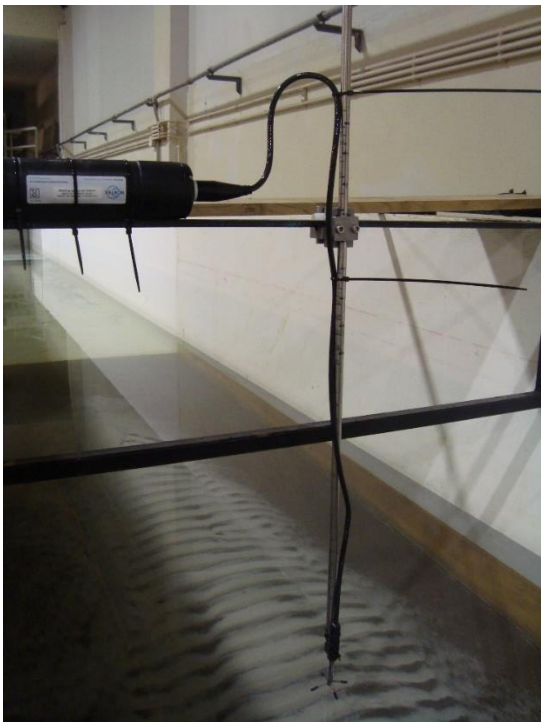

Figure 3.35 - SHRHA's ADV and its support structure.

For the two stages, the ADV was placed at 2.5 m before the first sediment box. In the first stage, three velocity profiles were taken: two for a water depth of 0.5 m – profile 1 (Figure 3.36) and 2 (Figure 3.37) - and another for the model target water depth 0.36 m – profile 3 (Figure 3.38). In the second stage, due to the lack of time, it was only possible to make another 0.36 m velocity profile (Figure 3.39). However, it is suggested that the 0.50 m profiles may be used for comparison reasons in future works. Also, the idea of the 0.50 m velocity profiles was to provide data for possible future adjustments that the flume may need. The velocity measurements were performed at consecutive 10% intervals of the total water depth, from the flume ground (d=0 m) until 90% of the water depth (d=0.45 m for the 0.50 m profiles and d=0.324 m for the 0.36 m profile). The last 10% of water depth are not possible to be measured, since the equipment only works when submerged and the probe that records the velocities has to be 5 cm above the desired measuring point. For each profile, the flume was filled with the target water depth. Then, after the water level and the currents stabilize, the measurements were made. The ADV was previously placed in a structure supported in the flume walls and attached to a circular ruler previously marked with all the measurement depths. Each measurement taken in both stages for each profile had a 30 s duration. For the 0.36 m, profiles only one valve was open, the one with the operational flowmeter, registering a 36.7 L/s flow. For the 0.50 m profiles, the second valve had to be opened, thus having been impossible to record the exact value of the flow. The results obtained are presented in Table 3.10:

Table 3.10 - Velocity measurements.

Measurement 1			Measurement 2		Measurement 3		Measurement 4	
d [m]:	0.5		d [m]:	0.5	d [m]:	0.36	d [m]:	0.36
Q [L/s]:	-		Q [L/s]:	-	Q [L/s]:	36.7	Q [L/s]:	36.7
Stage:	One						Stage:	Two
d	d_i [m]	U_{ci} [m/s]	d_i [m]	U_{ci} [m/s]	d_i [m]	U_{ci} [m/s]	d_i [m]	U_{ci} [m/s]
0d	0.00	0.001	0.00	0.000	0.000	0.001	0.000	0.001
0.1d	0.05	0.059	0.05	0.058	0.036	0.048	0.036	0.082
0.2d	0.10	0.066	0.10	0.064	0.072	0.054	0.072	0.090
0.3d	0.15	0.066	0.15	0.070	0.108	0.051	0.108	0.102
0.4d	0.20	0.083	0.20	0.063	0.144	0.058	0.144	0.097
0.5d	0.25	0.068	0.25	0.069	0.180	0.058	0.180	0.095
0.6d	0.30	0.069	0.30	0.070	0.216	0.061	0.216	0.097
0.7d	0.35	0.071	0.35	0.072	0.252	0.060	0.252	0.098
0.8d	0.40	0.071	0.40	0.071	0.288	0.059	0.288	0.098
0.9d	0.45	0.070	0.45	0.071	0.324	0.059	0.324	0.097

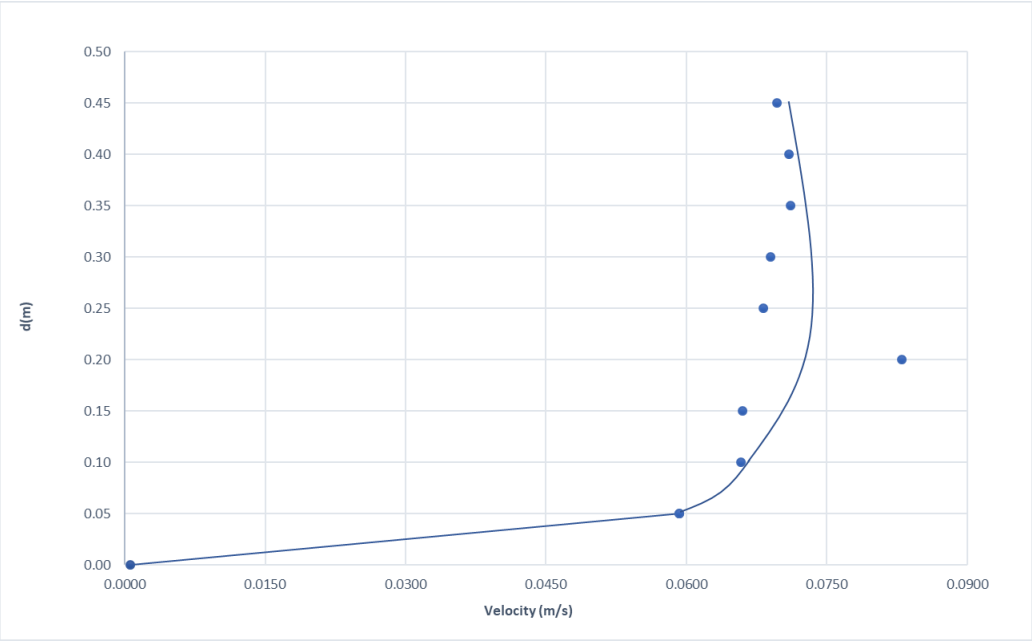

Figure 3.36 - Velocity profile 1 (d=0.5 m) - before flume changes.

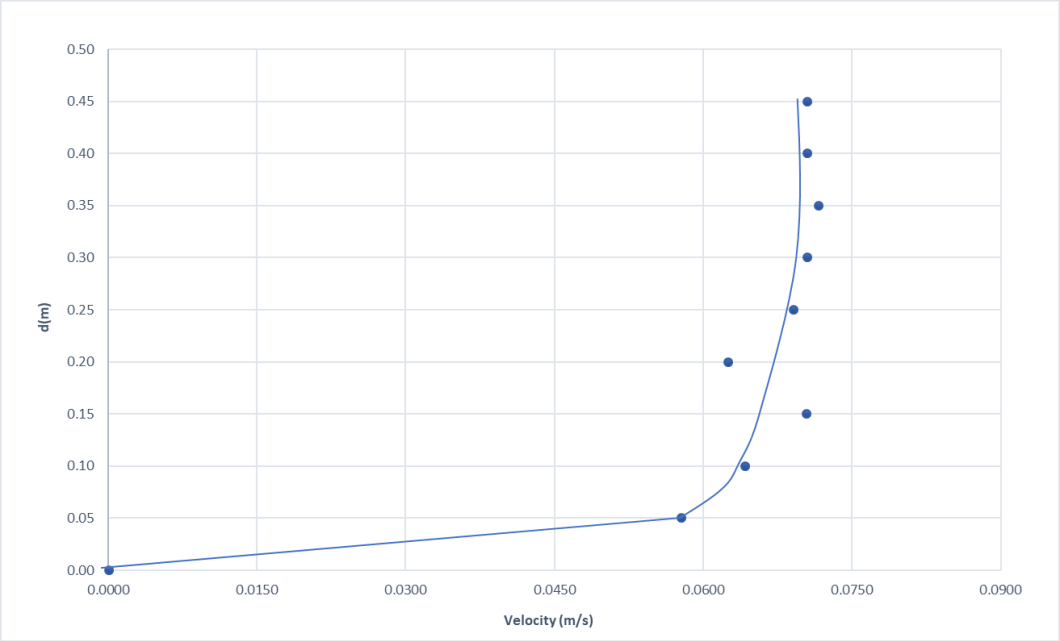

Figure 3.37 - Velocity profile 2 (d=0.5 m) - before flume changes.

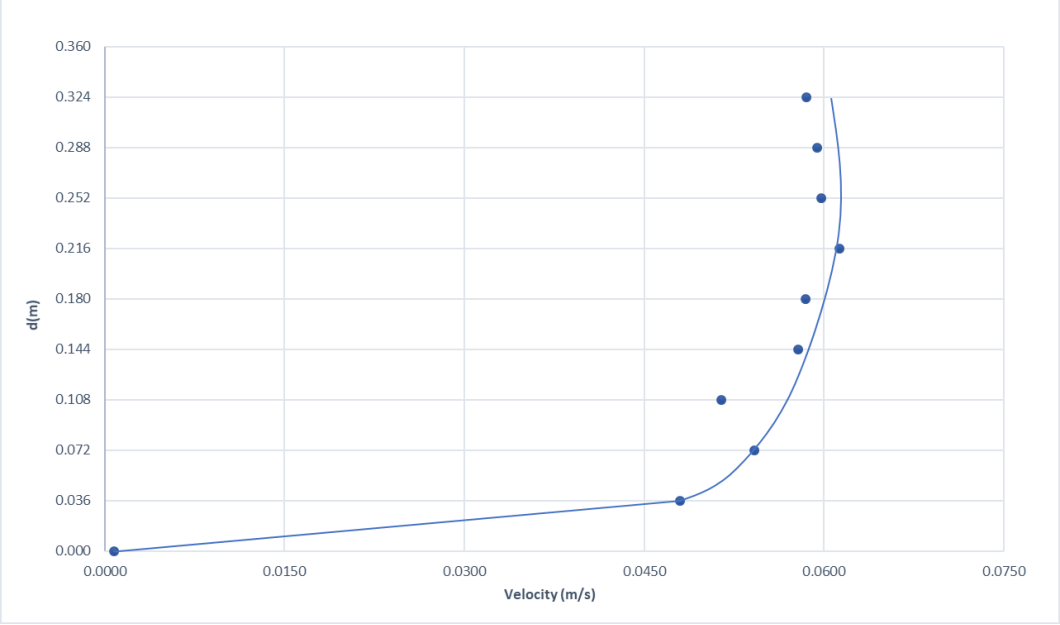

Figure 3.38 - Velocity profile 3 (d=0.36 m) - before flume changes.

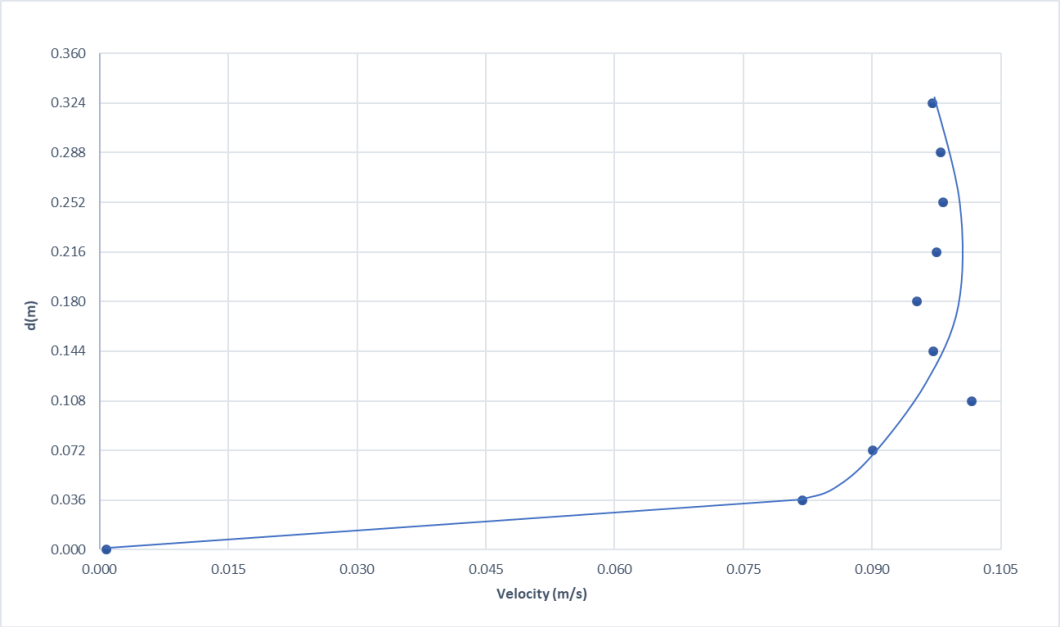

Figure 3.39 - Velocity profile 3 (d=0.36 m) - after flume changes.

After the analysis and comparison between graphics (Figure 3.38 andFigure 3.39), it was observed that in stage one the velocities for the velocity profile 3 were too low for the respective flow. Using the continuity equations, although being aware that it is not the best representative of the hydrodynamic situation in the flume, as an auxiliary check for the flow used in measurements 3 and 4, the velocities should be arround 0.102 m/s, far from the [0.05-0.06] m/s range registered in the profile 3. In the second stage, the velocities were higher, between the [0.09-0.1] m/s range. Since the flow and the water depth were preserved in the measurement 3 and 4, three situations could be possible:

- an ADV malfunction or outdated calibration;
- increase of the velocity and turbulence due to the adapations on the flume;
- wrong flow values provided by a malfunction on the only operational flowmeter.

In all measurements, were recorded some dificulties in the 0.3d and 0.4d range, with to much noise and high standard deviation amplitudes. This seems to appoint to the first problem, related to a possible malfunction or outdated calibration of the measuring equipment. Some seeding was added to the water, that allowed a slight improvement of the conditions. This was probably related to SNR (signal-to-noise ratio) problems of the equipment. The problem was hard to solve in all measurements - before and after the flume changes and even during the experimental tests - due to the extensive amount of seeding needed versus the amout of available seeding and due to the tight schedule for the measurements execution.

3.6.2. Wave Generation and Reflection Analysis

Since the wave paddle installed was new, a reflection analysis on the effect of the flume walls (to detect possible existence of cross-waves) and of the downstream gate in the wave generation had to be made. As explained in section 3.2, the wave reflections should be avoided or minimized since they could lead to distortion and misrepresentations of the test conditions and in ultimate case they can cause the abrupt

activation of the safety trigger of the wave paddle leading to the test's stoppage. This same analysis also made it possible to determine the gain factor that allows the wave generated by the wave paddle to reach the target wave height at the model.

3.6.2.1. Dissipation System

At the end of the installation of the wave paddle, short sample tests were made with random wave heights, periods and water depths. It was noticed that when the generated waves reached the downstream gate, they were heavily reflected in the direction of the paddle, activating in some cases the safety trigger. Moreover, when the active absorption was activated the paddle reached its maximum stroke in some cases, leading to the emergency shutdown of the equipment.

In order to solve this reflection problem, a solution was designed resulting into a dissipation system composed by two anti-"reflection boxes". These boxes were recreated based on the works of Fraga (2017). The two boxes had a structure 1.03 m long by 0.80 m width by 0.70 m height, made with 15 mm thick stainless steel. Inside the boxes, seven distended metal sheets were placed, three in the first box and four in the second box, with a decrease of the openings from upstream to downstream. Ideally, the sheets should have been placed with a decreasing spacing between each other. However, the structure already had some welded stainless steel fasteners. For time saving purposes, those same fasteners were re-used instead of welding new ones, as shown in Figure 3.40 and Figure 3.41.

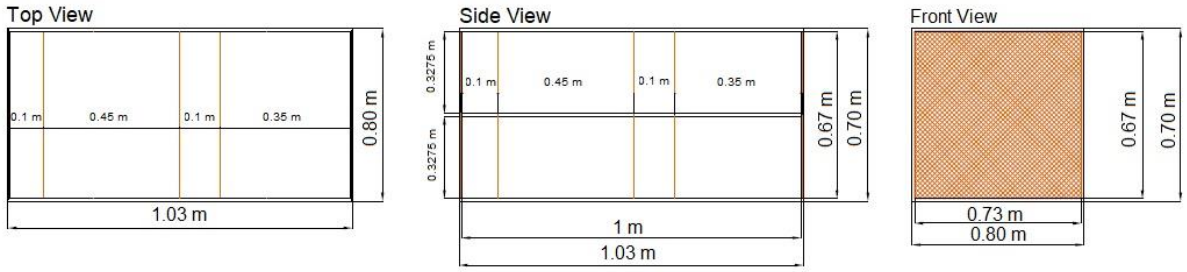

Figure 3.40 - First anti-reflection box layout.

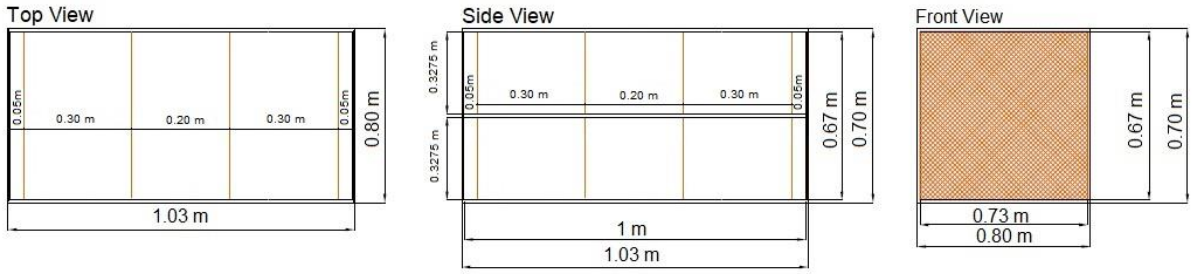

Figure 3.41 - Second anti-reflection box layout.

Figure 3.42 – Dissipation system.

Figure 3.43 – Dissipation system (front view).

After the assembly of the boxes, they were placed at the beginning of the free span between the second sediment box and the downstream gate and aligned at the center. Since the boxes had a 0.80 m width, there was a 10 cm gap on both sides between the walls and the structure. To prevent their possible displacement when the flume is being filled with water or during the tests, non-intrusive blocks of wood were placed between the walls and the boxes as shown in Figure 3.44.

Figure 3.44 – Boxes fixing to the flume walls.

In the next step, a profile of gravel inside the anti-reflection boxes was created. In Fraga (2017) corks were used instead of a gravel profile. In order to prevent the gravel from escaping through the available openings between the structure and the flume walls, a plastic net similar to those used in the by-pass boxes was placed on the downstream and upstream faces of the set of reflection boxes. The profile was divided into four sections: the first one almost flat with a 0.056 m height and the other three with a slope of 1:15, until the 0.156 m of height. The sections have a length of 0.50 m, making a total of 2 m. The gravel used has a particle median size between 11 and 20 mm.

Figure 3.45 - Plastic net at the downstream and upstream box faces.

Figure 3.46 - Gravel profile and anti-reflection box details.

Figure 3.47 - Gravel profile at the dissipation system.

3.6.2.2. Reflection Analysis

The reflection analysis is based on the measurement of the water surface elevation of 4 probes – all with a different relative spacing to the first probe. Using the tool *Reflection Analysis* of the software *HR DAQ*, by selecting the water depth of the model, it is possible to determine the most suitable probe spacing for the model conditions. By selecting a desirable spacing of the probes, the tool calculates a range of frequencies, a maximum and a minimum value, for the combination of the four probes. The most suitable spacing is obtained when the maximum and minimum frequencies calculated by the tool cover a range between $0.5f_p$ to $2f_p$ for the smoothest possible "Denominator" graphic. The f_p (peak frequency [s^{-1}]) and the frequency ranges were calculated using model values, as shown in Table 3.11.

Table 3.11 – Target frequency ranges (model values).

d (m)	$T_{p,model}$ (s)	f_p (s^{-1})	$0.5f_p$ (s^{-1})	$2f_p$ (s^{-1})
0.36	1.98	0.5051	0.2525	1.0101

The most suitable spacing as well as the maximum and minimum frequencies obtained are shown in Figure 3.48 and Figure 3.49.

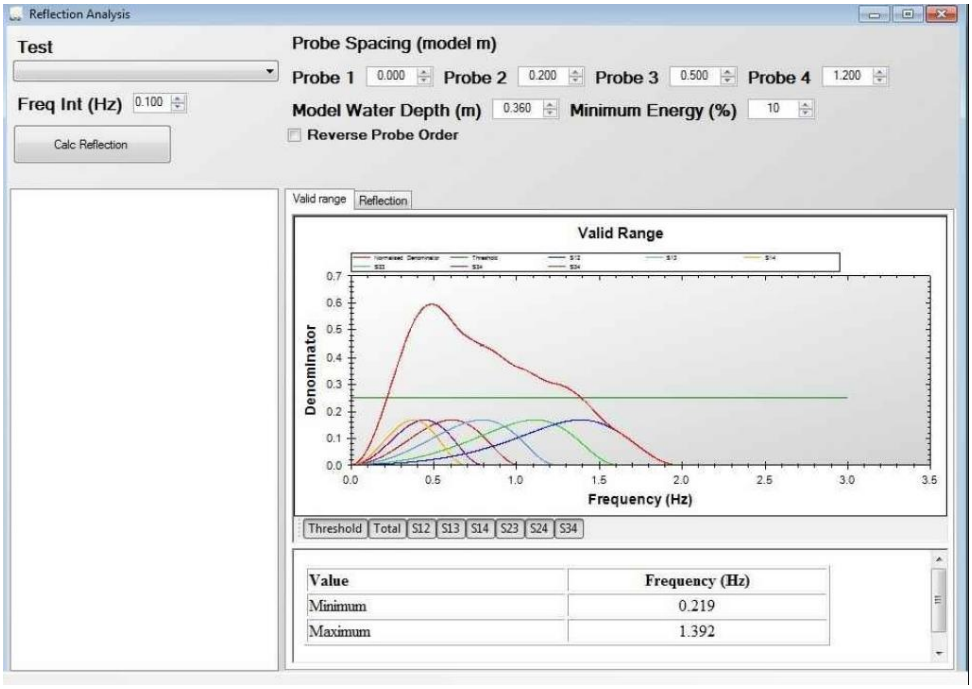

Figure 3.48 - *Reflection Analysis* tool.

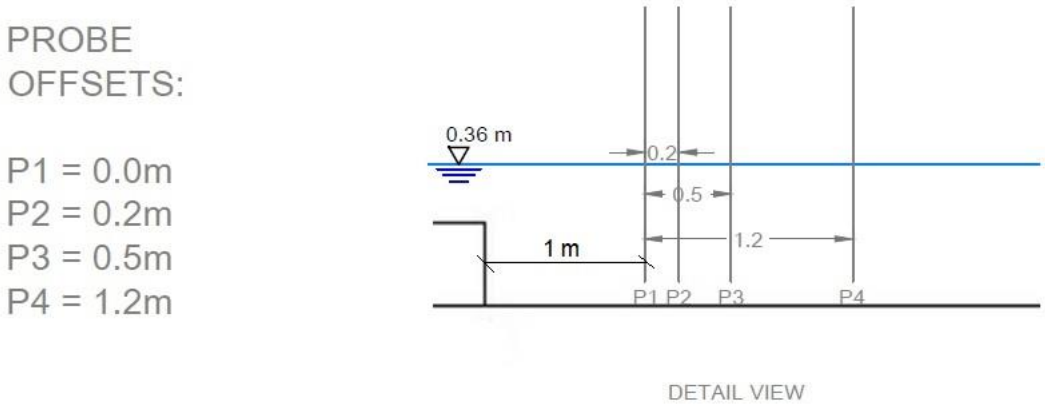

Figure 3.49 - Most suitable probe spacing (all measurements in meters).

The probes were then placed, supported in the flume walls, 1 m after the beginning of the first sediment box. The flume was filled and a series of tests were performed, after the probes were calibrated[2], analyzing the reflection value and the generated wave height. The reflection coefficient is recommended to be kept bellow 15%, if possible under 10% (Frostick *et al.*, 2011). This process was conducted until a reflection coefficient near the 15% benchmark was reached, for a duration correspondent to a wave number equal to 1000. In total, seven reflection tests and the respective analysis were performed, as shown in Table 3.12 and Table 3.13. This analysis was made using two frequency bands (Δf): $\Delta f_1 = f_p/15$ and $\Delta f_2 = f_p/20$.

Table 3.12 - Reflection Test Series.

Test	$H_{s,model}$ (m)	$T_{p,model}$ (s)	$f_{p,model}$ (s^{-1})	d (m)	Waves	Duration (s)	Gain Factor	Maximum Stroke/Failure	Active Abs.
1	0.12	1.98	0.505	0.36	Irreg.	1980	1.0	No	Off
2		1.98	0.505			633	2.0	Yes	
3		1.7	0.588			1700	1.5	No	
4		1.7	0.588			1700	1.5	No	
5		1.7	0.588			1700	1.5	No	
6		1.98	0.505			-	1.7	Yes	
7		1.56	0.641			1560	1.6	No	

Table 3.13 - *Reflection Analysis* tool results.

Test	Threshold (%)	Sampling Rate (s^{-1})	Reflection Coef. DAQ		HR DAQ[3]	
			Δf_1=0.03 Hz	Δf_2=0.002 Hz	$\overline{H}_{1/3}$ (m)	H_{max} (m)
1	1	100	20.9%	21.0%	[0.058-0.064]	[0.120-0.130]
2		40	19.6%	20.2%	[0.128-0.134]	[0.210-0.230]
3		40	18.2%	18.2%	[0.089-0.094]	[0.167-0.178]
4		100	15.7%	15.6%	[0.090-0.095]	[0.177-0.184]
5		100	15.7%	15.6%	[0.090-0.094]	[0.177-0.183]
6		-	-	-	-	-
7		100	15.2%	15.1%	[0.095-0.099]	[0.176-0.181]

[2] Process explained in section 3.6.3
[3] Highest and lowest wave height values registered by the four probes in the *Reflection Analysis*

The results were than re-checked with the help of a programmed Excel sheet, where the outputted results of the *Reflection Analysis* tool (Frequency, Incident Spectra, Reflected Spectra, Reflection Coefficient) were inputted in the Excel. The results are presented in Table 3.14.

Table 3.14 - Reflection Analysis results using Excel tool.

Test	Reflection Coef. Excel					
	Δf_1=0.03 Hz	H_{si} (m)	H_{ri} (m)	Δf_2=0.002 Hz	H_{si} (m)	H_{ri} (m)
1	20.9%	0.063	0.013	21.0%	0.063	0.013
2	19.7%	0.126	0.025	18.6%	0.125	0.025
3	18.2%	0.091	0.017	18.2%	0.090	0.017
4	15.8%	0.093	0.014	15.5%	0.093	0.014
5	15.8%	0.092	0.014	15.5%	0.092	0.014
6	-	-	-	-	-	-
7	15.3%	0.095	0.014	15.1%	0.095	0.014

In the test number 1, it was observed that the reflection was too high and that the significant wave height generated was too low. So, for the test number 2, an increase of the gain factor was carried out with the conscience that the reflection could increase. However, the wave maker safety trigger was activated during the test number 2 and the emergency button was pressed, stopping the test at the 633 s. Therefore, in the test number 3, the gain and the peak period were decreased. After the first three tests, it was concluded that the reflection was still very high.

In a second attempt to reduce reflection, it was created a rock mattress (Figure 3.51 and Figure 3.52) in the second sediment box. The box was filled with sand and a layer of gravel at the top, the same used inside the reflection boxes, extending the gravel profile of the reflection boxes and reducing the local water depth from 1.39 m to 1 m. The rock mattress has the same length of the second sediment box, 2.2 m. More distended metal sheets were also applied in the lower half of the boxes (Figure 3.50).

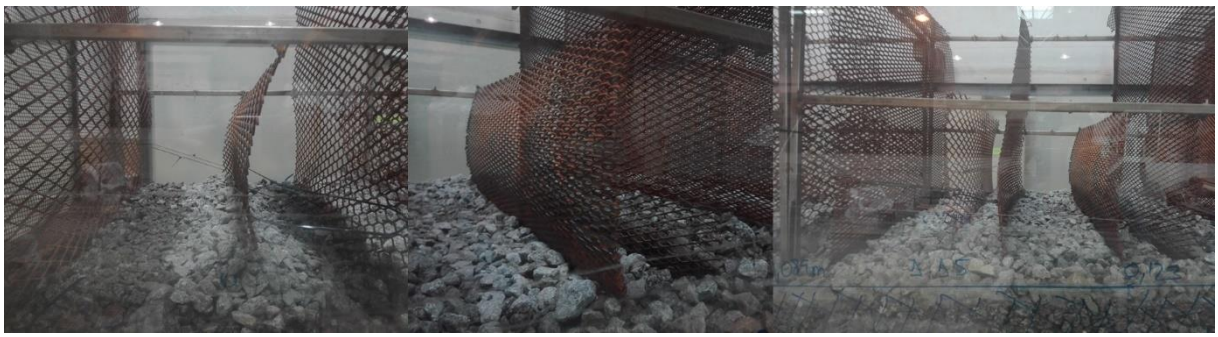

Figure 3.50 - Distended metal sheets (second reflection reducing attempt).

Figure 3.51 - Rock mattress details.

Figure 3.52 - Rock mattress (front and top view).

After the construction of the mattress, test number 4 was made as a repetition of test number 3 to access how much the changes implemented contributed to reflection decrease. In fact a reduction to 15% was obtained, so test number 5 was made as a validation of the previous test. Test number 6, it was made with a peak period similar to the first two tests but with an intermediate gain value. However, the random irregular wave sequence generated by the paddle reached the maximum stroke right in the first two

minutes and the test was considered invalid. In the last test an adjustment to the conditions of tests 3, 4 and 5 was made. The peak period was decreased and the gain was slightly increased and a reduction was obtained for the reflection coefficient almost equal to 15%. Due to the tight schedule for conducting the experimental component, it was then decided to advance to the next stage by adapting the target conditions to the ones used in the last reflection test. Note that before every change on the T_p value during the reflections tests, it was verified if the probe spacing in place still covered the changes on the frequency ranges. Fortunately, the offset of the wave probes covered all the changes on the frequency.

Since 15% of reflection coefficient is still close to the limits commonly considered for the reflection, further experimental results should be analysed with caution. However, these results are useful as a first set of scour tests than enable the proper adjustments to this new equipment, thus being important as a quick-off point for future research towards more accurate data. Nevertheless, the reduction of the reflection coefficient should be a priority in future setups.

The final conditions used for the physical model tests are presented in Table 3.15.

Table 3.15 - New target conditions.

Prototype	**d (m)**	**H_s (m)**	**T_p (s)**	**U_c (m/s)**	**U_m (m/s)**	**D_p (m)**	**Gain**
Conditions	18	6	11	0.5	1.14	5	1.6
Model	**d (m)**	**H_s (m)**	**T_p (s)**	**U_c (m/s)**	**U_m (m/s)**	**D_p (m)**	
Conditions	0.36	0.12	1.56	0.07	0.16	0.1	

3.6.3. WAVE PROBE CALIBRATION

As explained in section 3.2.1, the wave probes of the acquisition system are connected to 2 acquisitions boards. Those boards receive, convert and collect all the measurements sent by the probes. In order to obtain results as accurate as possible the wave probes are recommended to be calibrated at least once per day or whenever the water level changes. Although only one water level was used during all the duration of the experimental stage, the probes were calibrated every day, before each wave train, since at the end of each wave train the flume had to be emptied to capture the photos that are used for the photogrammetry technique and to access the visual damage of the protection.

The calibration of the wave probes starts with the creation of a calibration file, in the *HR WaveData*, where a calibration is defined and associated to each probe used. Then three different levels are defined in the probes, by varying the immersion depth of the probe in the water by raising or lowering the probe:

- Level 0
- Level +
- Level –

The “0” corresponds to the reference level and should be the first value to be calibrated. It corresponds to the mean water level registered by the probe. The potential difference of the probe, in the respective channel of the board, should be placed in the centre in order to cover the full voltage amplitude that the system can capture.

After the level 0 is calibrated, the “-“ value was defined. The probe rod was raised until the maximum. The offset between the “0” and the “-“ is registered in the calibration as a negative value, since it

corresponds to the minimum water depth capture by the probe. The fluctuations between the "0" and the "-" will be interpreted by the probe and acquisition system as wave troughs. Finally the "+" value was defined. The probe was lowered until its maximum (approximately one or two index fingers of distance between the flume floor and the probe). The offset between the "0" and the "+" is registered in the calibration as a positive value, since it corresponds to the maximum water depth captured by the probe. The fluctuations between the "0" and the "+" will be interpreted by the probe and acquisition system as wave crests. It is advisable that the two offsets between the "+"/"-" levels and the "0" are identical. In this dissertation the difference between levels was equal and with a value of 12 cm ("+"= 0.12 m; "0"= 0.00 m; "-"= -0,12 m).

By defining three points per probe, the final result of the calibration should be a linear regression for each one with the highest correlation coefficient R^2 as close as possible of 1.

For both phases of the experimental stage – reflection and model test – only the second board was used. For the reflection tests the probes 9 (channel 1, board 2), 11 (channel 3, board 2), 12 (channel 4, board 2) and probe 14 (channel 6, board 2) were used. For the model tests, only two probes were used: probe 12 (just before the first sediment box at 1.20 m of the monopile) and probe 14 (1.20 m downstream of the monopile location), as shown in Figure 3.54.

Figure 3.53 - Probe 12 and Probe 14.

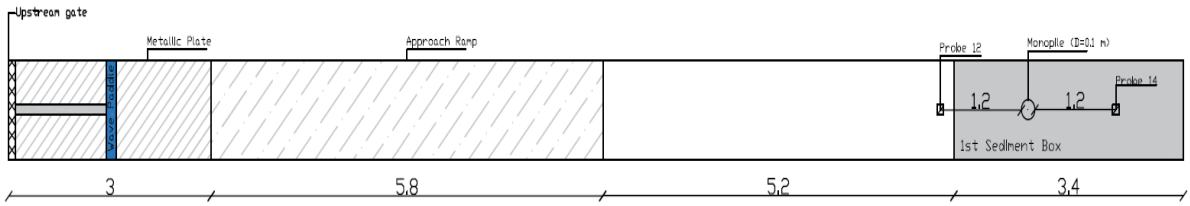

Figure 3.54 - Scheme of the setup used for the model tests (Test 1a, Test 1b, Test 2).

3.7. LABORATORY TESTS

The present study aims to provide a set of preliminary tests, and setup, focused on the analyses and assessment of long-term damage in scour protections.

In order to optimize the experimental component of this dissertation, as well as the results, a test plan was elaborated. The test plan was made taking into consideration representative long-term sea state characteristics from the North Sea (where most of the windfarms in Europe are located). As referred before, the characteristics considered were the:

- Significant wave height (H_s);
- Peak period (T_p);
- Number of waves (N);
- Depth-average current velocity (U_c);
- Orbital wave velocity (U_m).

Taking into consideration the new equipment installed and the uncertainties associated with the lack of knowledge and experience in its use, it was decided to set only one target value for each condition instead of a set of target values, except for the number of waves. For the significant wave height, 6 m was the value chosen for the tests. The peak period initially was set for 14 s and later one was adapted for the 11 s. The depth-average current was set to 0.5 m/s and the orbital velocity was initially calculated to 1.29 m/s. With the change of peak period, the U_m was also changed to 1.14 m/s. For the number of waves, since the main objective was to study long-term sea states, the target values range between 7000 and 9000 waves, in order to achieve valuable results that could lead to a comprehension of some of the gaps in literature regarding this type of conditions. During all the tests, a 1.6 gain factor was used.

Each test was performed by the following set of steps:

1. Correct positioning of the downstream gate for the intended water depth;
2. Slow filling of the flume, without destroying the model, by gradually opening the valve;
3. Calibration of the wave probes (as described in section 3.6.3) after steady-current stabilization;
4. Input the test data in *HR Merlin*;
5. Update zeros in the acquisition system;
6. Start data acquisition;
7. Start wave paddle;
8. Stop the wavemaker;
9. Complete the data acquisition and post-processing;
10. Slow emptying of the flume;
11. Wait until the location of the model was totally dried to take the photos to the photogrammetry;
12. Repetition of process from step 1 to 11 for each wave train of each test.

In order to facilitate the organization of all the files and data records, a designation was attributed to the calibration and test files, to the test records and finally to the post-processing files (Table 3.16).

During the tests slight modifications to the original test plan had to be made. As it can be perceived in Table 3.16, three groups of tests were performed - one for 5000 waves, one to 8000 waves and one to

9000 – instead of only using N values above 7000 waves. However, in chapter 4 the reason to this modification will be further explained.

Table 3.16 - Organization of the test files.

Calibration Designation (Files)	Wave Train Designation (Files)	Wave Train (data records)	Type of test	Post-Processing (Files)
O_00	O_00	O_00_02	Reflection	Irregular_012
O_01a	O_01a	O_01a_irreg	Reflection	Irregular_012_2
		O_01a_irreg2		Irregular_012_3
O_02	O_02	O_02_irreg1	Reflection	Irregular_012_4
		O_02_irreg1b		Irregular_012_4b
		O_02_irreg2		Irregular_012_5
		O_02_irreg3		Irregular_012_6
O_O3	O_O3a	O_03a_1000_1000	Model	1test_1000
O_04	O_04	O_04_2000_3000	Model	1test_3000
O_04II	O_04II	O_04II_2000_5000	Model	1test_5000
O_05	O_05	O_05_1000_1000	Model	2test_1000
O_05II	O_05II	O_05II_2000_3000	Model	2test_3000
O_05III	O_05III	O_05III_2000_5000	Model	2test_5000
O_05IV	O_05IV	O_05IV_3000_8000	Model	2test_8000
O_06	O_06	O_06_1000_1000	Model	3test_1000
O_06II	O_06II	O_06II_2000_3000	Model	3test_3000
O_06III	O_06III	O_06III_2000_5000	Model	3test_5000
O_06IV	O_06IV	O_06IV_2000_7000	Model	3test_7000
O_06V	O_06V	O_06V_2000_9000	Model	3test_9000

Due to schedule limitations, it was only possible to make three groups of tests. The ideal would be to perform three or four additional groups of tests in order to have a wider base of comparison between results. Nevertheless, these tests set a good starting point for future works.

3.8. MODEL CONSTRUCTION

For the model construction, the gravel was divided into four equal parts. Three of those were painted with different colours (yellow, red and blue), in order to obtained a distinction between four rings of

stones. This allows a more detailed and easier analysis of the protection behaviour, mainly through visual damage assessment.

Figure 3.55 - Painted stones.

Then the monopile model was placed in the first sediment box, 1.20 m after the beginning, and the sand bed was smoothed. Than, the geotextile filter layer was putted in place, four concentric rings were marked in the geotextile with a distance from the center of $2D_p$, $3D_p$, $4D_p$ and $5D_p$. Since the protection thickness was set to the $3D_{n50}$, the armour layer was constructed with an auxiliary ring with around 13 mm height - with the diameters of the four concentric rings. The ring was only placed as guide. The stones were not compressed to each other in order to fit perfectly inside the ring. After all the four rings were filled, the protection was finished with a 1:3 slope and the upper part of the monopile was fixed to the base. The assembly sequence can be seen in Figure 3.56.

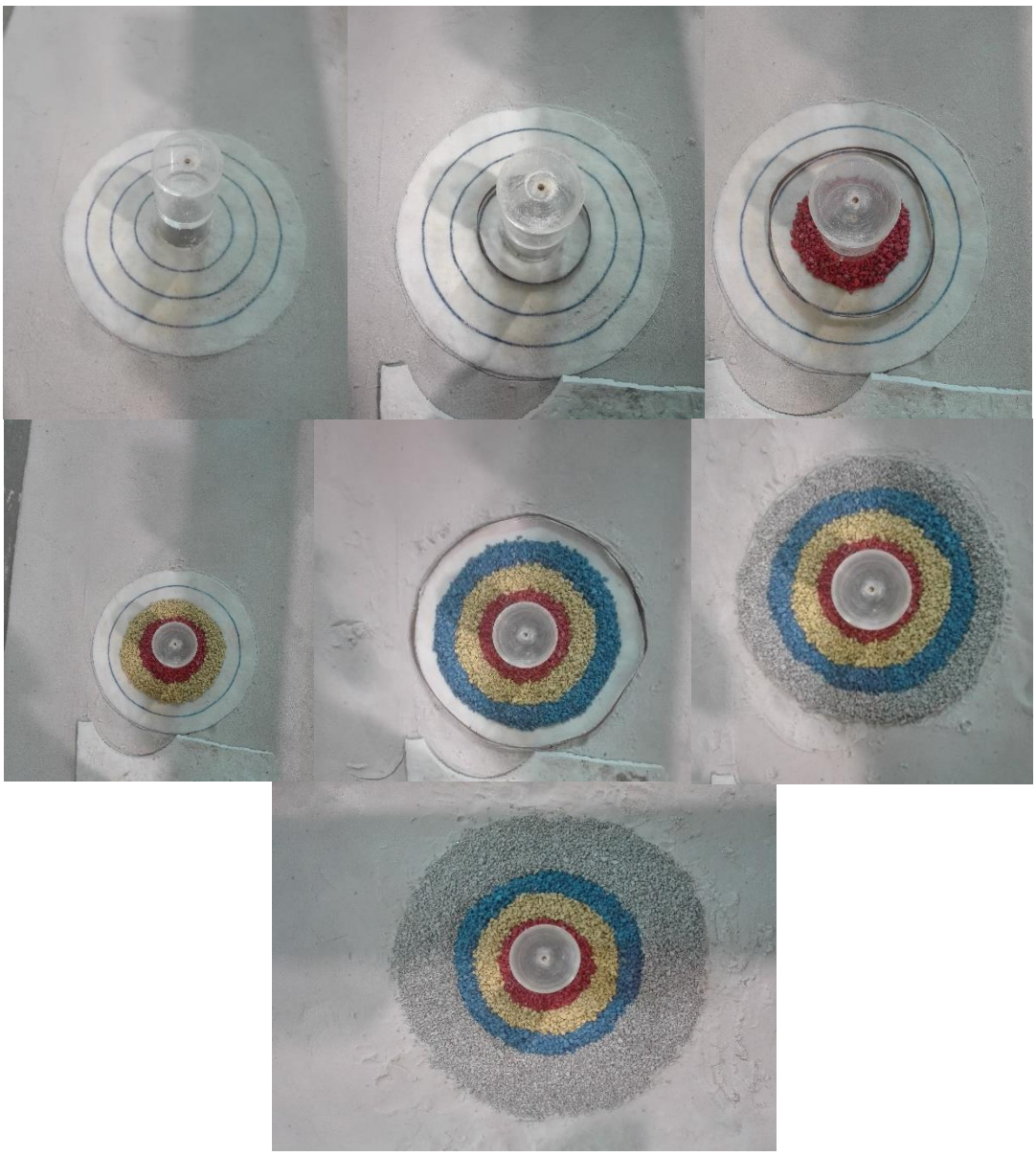

Figure 3.56 - Monopile foundation model assembly.

Figure 3.57 - Top View of the monopile model.

Figure 3.58 - Final layout of the flume with the model ready to test.

4
RESULTS, ANALYSIS AND DISCUSSION

4.1. SCOUR PROTECTION TESTS

The scour protection tests were performed in one series of three groups of tests in a total of 12 wave trains. Due to the large amount of time required to perform each test (as described in section 3.7), the experimental work was subdivided in those three scour tests. Nevertheless, these tests open the way to further research on the present topic of long-term damage in protections. Moreover, due to the new wave generator, these tests become useful for a proper calibration and understanding of the new setup and equipment. The information acquired can then be used for new testing series on this topic at the same facilities. Initially the idea was to perform two tests of 9000 waves and one of 7000 waves. However, as describe next, the tests consisted in:

- Test 1a: 5000 waves (1 wave train of 1000 waves and 2 wave trains of 2000 waves);
- Test 1b: 8000 waves (1 wave train of 1000 waves, 2 wave trains of 2000 waves and 1 wave train of 3000 waves);
- Test 2: 9000 waves (1 wave train of 1000 waves and 4 wave trains of 2000 waves).

Regarding the hydrodynamic conditions, the first test was performed taking into consideration the target conditions of the Table 3.15. However, after 5000 waves no significant changes and movements were registered in the model, with the exception of two or three movements of smaller stones (considered not significant). The model did not have the expected behaviour at the end of a such significant number of waves. Therefore it was decided to classify the protection, at the end of 5000 waves, as static and increase the hydrodynamic conditions (Table 4.1). Since the conditions were changed, the test designation had to be changed – from Test 1a to Test 1b. The reasonable option would be to remove and remake the model. However, since the model seemed static until that stage, and in order to have time to perform a third test, it was decided to perform the second test with the model of the first test – with the conscience that a cumulative wave and current induced shear stress effect of 5000 waves was already present on the model – reason to nominate the second test of 1b . Therefore, at the end of the Test 1b the model was in fact subjected to 13000 waves, instead of the 8000 waves performed during the test. After the Test 1b, significant movements were registered– that ultimately led to the protection's failure. Therefore, the third test planned was initiated with the same target hydrodynamic conditions. Before the Test 2, the model was removed and rebuilt and the sand bed was restored and profiled again. The third test was finally performed for the target number of waves, 9000 waves, without the failure of the

protection. Therefore, the goal of achieving an evident dynamic behaviour of the model, for the experimental stage of this dissertation, was not reached. In the future, a detailed revision of the calculations and of the hydrodynamic conditions, the use of a different nominal diameter used in the model, a reduction of the reflection and a new and more extensive test plan (including the repetition of the tests performed in this dissertation in order to validate the results) should be made.

Table 4.1 - Target Conditions for all the tests.

Target Conditions					
Test	H_s (m)	T_p (s)	U_c (m/s)	U_m (m/s)	U_{cw} (m/s)
Test 1a	0.12	1.56	0.07	0.16	0.304
Test 1b	0.12	1.56	0.14	0.16	0.467
Test 2	0.12	1.56	0.14	0.16	0.467

As recommended by Whitehouse (1998) the values of U_c, during tests, were measured for a 0.4d depth. Therefore at d=0.36 m, the ADV was placed at 0.144 m from the bottom of the flume and the values were registered after the water depth and currents were stabilized.

The tests were performed with a duration of 1560 s for the 1000 wave trains and 3200 s for the 2000 wave trains for a H_s=0.12 m and a T_p=1.56 s.

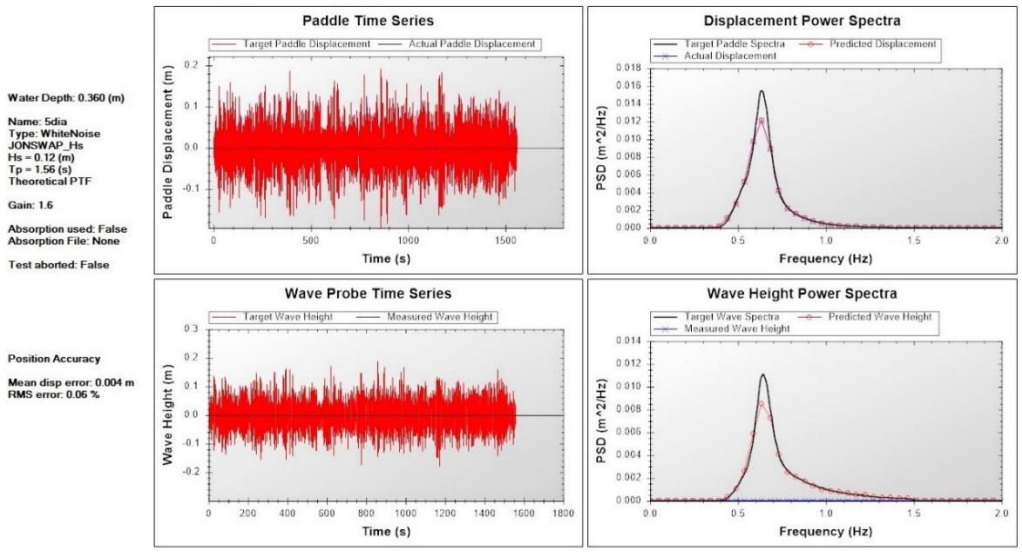

Figure 4.1 - *HR Merlin* (Example for the 1000 wave train).

The results registered by the two wave probes (Figure 3.54) for the three tests are presented in Table 4.2 and Table 4.3:

Table 4.2 – Test 1a and Test 1b Results.

Test 1a				
1000 waves		O_03a_1000		
Channel:	H_{max} (m)	H_{m0} (m)	$H_{1/3}$ (m)	T_p (s)
Probe12	0.190	0.108	0.102	1.540
Probe14	0.171	0.104	0.098	1.628
3000 waves		O_04_2000_3000		
Channel:	H_{max} (m)	H_{m0} (m)	$H_{1/3}$ (m)	T_p (s)
Probe12	0.180	0.095	0.092	1.547
Probe14	0.170	0.090	0.089	1.547
5000 waves		O_04II_2000_5000		
Channel:	H_{max} (m)	H_{m0} (m)	$H_{1/3}$ (m)	T_p (s)
Probe12	0.196	0.111	0.108	1.497
Probe14	0.174	0.106	0.103	1.497
Test 1b				
1000 waves		O_05_1000_1000		
Channel:	H_{max} (m)	H_{m0} (m)	$H_{1/3}$ (m)	T_p (s)
Probe12	0.178	0.106	0.102	1.608
Probe14	0.183	0.101	0.990	1.608
3000 waves		O_05II_2000_3000		
Channel:	H_{max} (m)	H_{m0} (m)	$H_{1/3}$ (m)	T_p (s)
Probe12	0.187	0.108	0.104	1.543
Probe14	0.196	0.101	0.099	1.543
5000 waves		O_05III_2000_5000		
Channel:	H_{max} (m)	H_{m0} (m)	$H_{1/3}$ (m)	T_p (s)
Probe12	0.176	0.107	0.102	1.614
Probe14	0.177	0.104	0.100	1.614
8000 waves		O_05IV_3000_8000		
Channel:	H_{max} (m)	H_{m0} (m)	$H_{1/3}$ (m)	T_p (s)
Probe12	0.190	0.105	0.102	1.623
Probe14	0.180	0.101	0.099	1.623

Table 4.3 - Test 2 Results.

Test 2				
1000 waves		O_06_1000_1000		
Channel:	H_{max} (m)	H_{m0} (m)	$H_{1/3}$ (m)	T_p (s)
Probe12	0.188	0.109	0.104	1.622
Probe14	0.201	0.105	0.101	1.622
3000 waves		O_06II_2000_3000		
Channel:	H_{max} (m)	H_{m0} (m)	$H_{1/3}$ (m)	T_p (s)
Probe12	0.177	0.105	0.103	1.569
Probe14	0.213	0.100	0.098	1.477
5000 waves		O_06III_2000_5000		
Channel:	H_{max} (m)	H_{m0} (m)	$H_{1/3}$ (m)	T_p (s)
Probe12	0.178	0.105	0.103	1.569
Probe14	0.200	0.100	0.098	1.477
7000 waves		O_06IV_2000_7000		
Channel:	H_{max} (m)	H_{m0} (m)	$H_{1/3}$ (m)	T_p (s)
Probe12	0.190	0.107	0.105	1.569
Probe14	0.234	0.102	0.101	1.477
9000 waves		O_06V_2000_9000		
Channel:	H_{max} (m)	H_{m0} (m)	$H_{1/3}$ (m)	T_p (s)
Probe12	0.181	0.105	0.103	1.623
Probe14	0.203	0.101	0.099	1.623

Figure 4.2, Figure 4.3 and Figure 4.4 also provide a summary of the information regarding the hydrodynamic measured conditions.

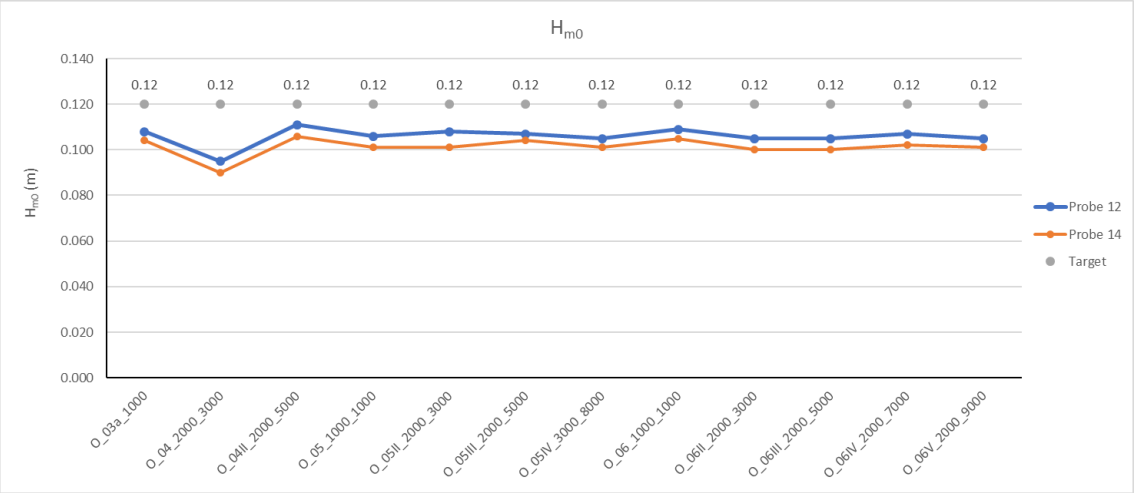

Figure 4.2 - H_{m0} measured values.

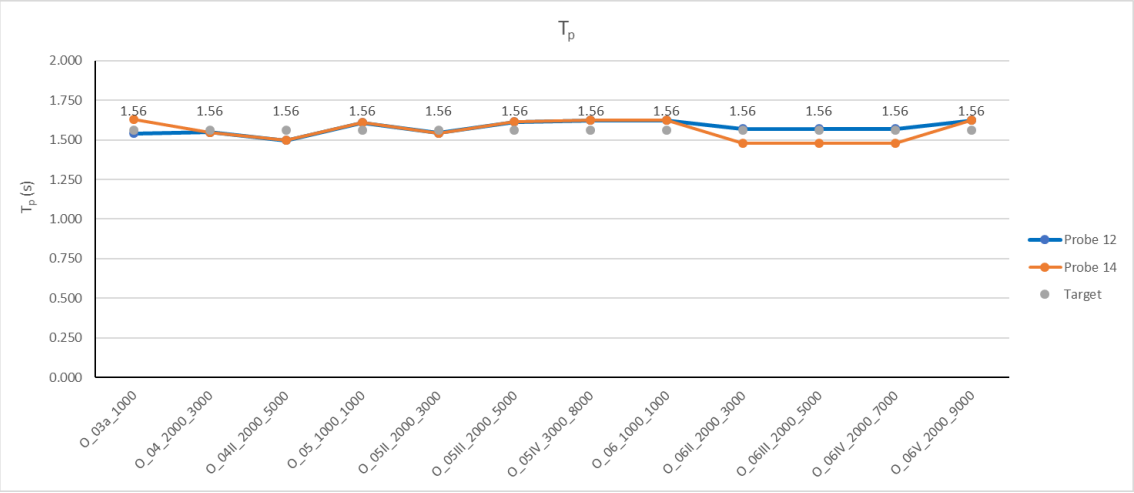

Figure 4.3 - T_p measured values.

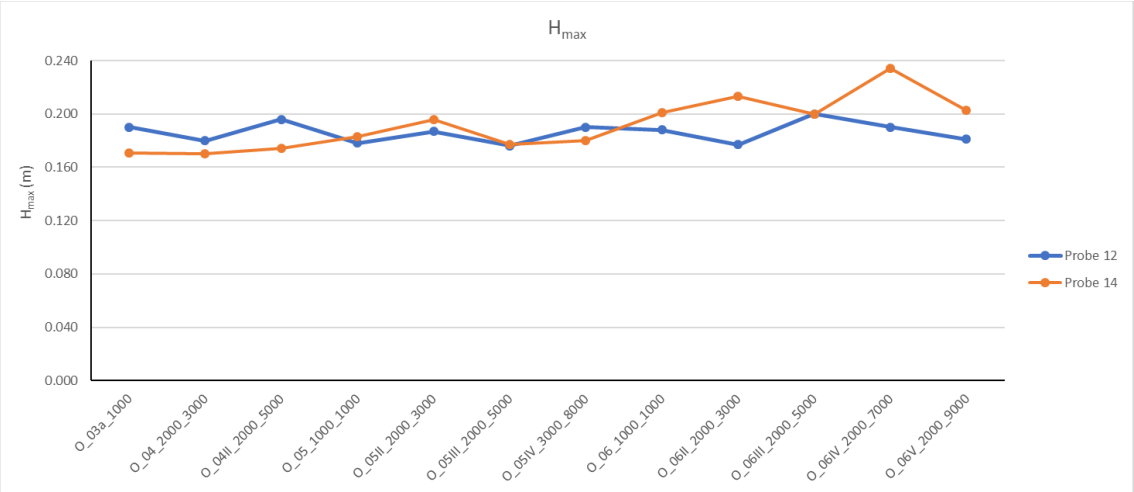

Figure 4.4 - H_{max} measured values.

In Figure 4.2, it is observed that the values of the H_{m0} registered in the downstream probe (probe 14), are lower that the values registered on the upstream probe (probe 12). This difference was expected, since the monopile creates an obstacle to the wave movement, causing the wave to lose energy and thus the wave height decrease. It is also visible that both wave probes registered a similar behaviour of the H_{m0} evolution during the tests. Compared to the target conditions, all the values of $H_{m0,measured}$ failed to reach the target value of 0.12 m.

Regarding the Figure 4.3 and Figure 4.4, both wave probes seem to have similar and consistent values between each other for the first and second tests. However, in the Test 2 some differences appeared, with the rear end (downstream) wave probe presenting lower values, for the peak period, and higher values, for the maximum wave height, than the upstream probe. While in the peak period, the differences can be noticed but could be considered residual, in the maximum wave height, in the wave trains O_06II_2000_3000 and O_06_IV_2000_7000, they seem a little bit more evident. Since both wave probes were placed at more than 10 times their own diameter, as recommended by Whitehouse (1998), no major influence is expected from the probes presence. However, these influences can always be present and hard to quantify. Further research should be carried to address this aspect, preferably with the future test repetition. Nevertheless, it is also important to note that the calibration of the downstream wave probe presented slightly worse R^2 values. Thus in the present and remaining analysis, the upstream probe with the incident wave height was considered as the reference probe for further analysis of the $S_{D,predicted}$ and of the shear stresses. With that in mind, a summary table was made for each test. Each table contains the target values for the test, the measured values of each test wave train and the average results of the test. For the average results, the $H_{m0,Nfinal}$ of each test was calculated using Eq. (2.65). For the $T_{p,Nfinal}$ the same equation was used but for T_p values. For the U_c, U_m and U_{cw} the average value is the test mean value of those parameters. For the U_{cw} calculation was used Eq. (2.64). Finally, for the KC and $Re_{,p}$ average number, they were calculated using the average values of U_m and T_p, for the KC number, and the U_c average value for the pile Reynolds number.

Table 4.4 - Target vs Measured conditions (Test 1a)

Test 1a		Target Conditions						
		H_s (m)	T_p (s)	U_c (m/s)	U_m (m/s)	U_{cw} (m/s)	KC	$Re_{,p}$
		0.12	1.56	0.07	0.16	0.304	2.50	6972
		Measured Conditions						
N	ΣN	H_{m0} (m)	T_p (s)	U_c (m/s)	U_m (m/s)	U_{cw} (m/s)	KC	$Re_{,p}$
1000	1000	0.108	1.540	0.104	0.144	0.419	2.22	10359
2000	3000	0.095	1.547	0.099	0.127	0.438	1.96	9861
2000	5000	0.111	1.497	0.103	0.146	0.414	2.19	10259
Average		0.104	1.526	0.102	0.139	0.424	2.12	10159

Table 4.5 - Target vs Measured conditions (Test 1b)

Test 1b		Target Conditions						
		H_s (m)	T_p (s)	U_c (m/s)	U_m (m/s)	U_{cw} (m/s)	KC	$Re_{,p}$
		0.12	1.56	0.14	0.16	0.467	2.50	13944
		Measured Conditions						
N	ΣN	H_{m0} (m)	T_p (s)	U_c (m/s)	U_m (m/s)	U_{cw} (m/s)	KC	$Re_{,p}$
1000	1000	0.106	1.608	0.143	0.146	0.495	2.35	14263
2000	3000	0.108	1.543	0.158	0.145	0.522	2.24	15777
2000	5000	0.107	1.614	0.158	0.147	0.517	2.37	15687
3000	8000	0.105	1.623	0.144	0.145	0.498	2.35	14313
Average		0.106	1.599	0.151	0.146	0.508	2.33	15010

Table 4.6 - Target vs Measured conditions (Test 2)

Test 2		Target Conditions						
		H_s (m)	T_p (s)	U_c (m/s)	U_m (m/s)	U_{cw} (m/s)	KC	$Re_{,p}$
		0.12	1.56	0.14	0.16	0.467	2.50	13944
		Measured Conditions						
N	ΣN	H_{m0} (m)	T_p (s)	U_c (m/s)	U_m (m/s)	U_{cw} (m/s)	KC	$Re_{,p}$
1000	1000	0.109	1.622	0.150	0.150	0.500	2.43	14930
2000	3000	0.105	1.569	0.150	0.142	0.514	2.23	14930
2000	5000	0.105	1.569	0.150	0.142	0.514	2.23	14950
2000	7000	0.107	1.569	0.152	0.145	0.512	2.28	15159
2000	9000	0.105	1.623	0.150	0.145	0.509	2.35	14980
Average		0.106	1.587	0.151	0.145	0.510	2.30	14990

As we seen through Table 4.4, Table 4.5 and Table 4.6 in all the tests performed, the target significant wave height was not reached, being the difference a little above 10%. In the first test the values registered suffered a little more fluctuation than in the others tests. The fact that the H_{m0} values have not reached the target values could be possibly explained by the fact that the measured wave height, by the probes, is the result of the difference between the incident wave, H_{si}, and the reflected wave, H_{sr}.

The fact that the measured wave height failed to achieve the target conditions could be one of the reasons for lack of damage. However, by just observing the values on the Figure 4.5 and the previously mentioned tables, since the H_{m0} overall values in each test are almost equivalent, no conclusions can be taken regarding the small amount of damage and stone movement in the protection on all three group of tests.

Figure 4.5 - Registered H_{m0} values by the upstream wave probe.

Regarding the peak period, in the first test, the values were slightly under the target values but in the second and third test, most of the values for the peak period were reached, and sometimes exceed. A possible reason could be the fact that the wave generation software (*HR Merlin*) generates random irregular sea states for every test. So, for example, the 2000 wave train generated to reach the 3000 waves in a test does not have the same sequence of waves and all the exact wave heights of the 2000 wave train generated to reach the 5000 waves. The other reason could be related with the increase of the U_c value, between tests, once the increase of the currents velocity leads to the wave stretching, increasing their wave length and period, while reducing their height.

The influence of the peak periods on scour and on the damage number was studied by De Vos (2008) and De Vos *et al.* (2012), which concluded that the S_{3D} increases for the increase of the T_p.

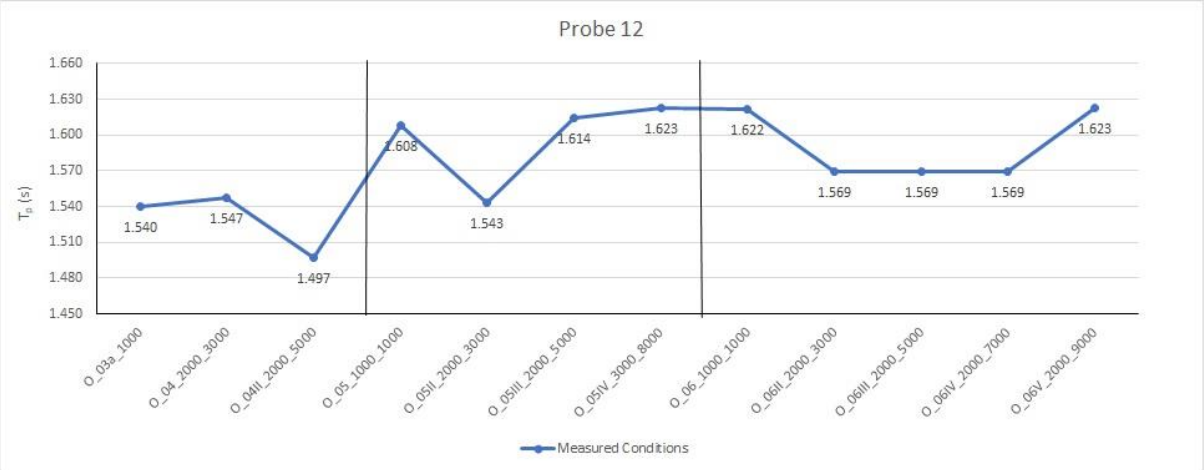

Figure 4.6 – Registered T_p values by upstream probe.

Regarding U_c, the values in Test 1a surpassed the target values. However, as stated before, those values were not enough to cause damage and movement of stones in the protection (reason for the increase of

the hydrodynamic conditions in the Test 1b and Test 2). Nevertheless, the influence of the increase of the U_c value, on the stones movement was visually noticed when the test was performed with higher values of current velocities were the ones with higher stone movements. This is in agreement with the main findings reported in De Vos *et al.* (2012) and Fazeres-Ferradosa (2018).

For the U_m values, since the wave height did not reach the target values it was expected that the orbital bottom target velocity was not reached also, since this parameter depends, in addition to other parameters, on the wave height. Also, like the wave height, no conclusions can be taken in this dissertation regarding its influence, since there is almost no significant difference in between tests, regarding this parameter. However, some tests in Fazeres-Ferradosa (2018) shown increases on the damage number with the increase of the U_m, also reported in Whitehouse *et al.* (2014) and De Vos *et al.* (2012). This effect is expected since the increase in U_m leads to an increase in the wave-induced bed shear stress.

As for the U_{cw}, this parameter is a good indicator of the dominance of waves and currents in the tests performed. For values of 0, the flow regime corresponds to waves only, whereas for values of 1, the flow is matching a current only situation. For values of U_{cw}=0.5, the regime is equally dominated by waves and currents. In the first test, if target conditions were applied the regime would be dominated by waves. However, looking for the measured values the regime was still dominated slightly by waves but not in the same proportion as the target conditions. With the increase of the hydrodynamic conditions, values around 0.5 were reached and the regime was equally dominated by waves and currents in both Test 1b and Test 2. As reported in Sumer *et al.* (2001), scour depths tend to increase for increasing values of U_{cw}. This was slightly observed when performing this analysis. In the Test 1a, the test with the lowest value of U_{cw}, damage and significant scour was not observed. In the second test, even with the reservation that the model had cumulative effects, the U_{cw} was higher and so the observed scour effects. Even in the Test 2, the stone movement was higher, although not so significant as initially foreseen.

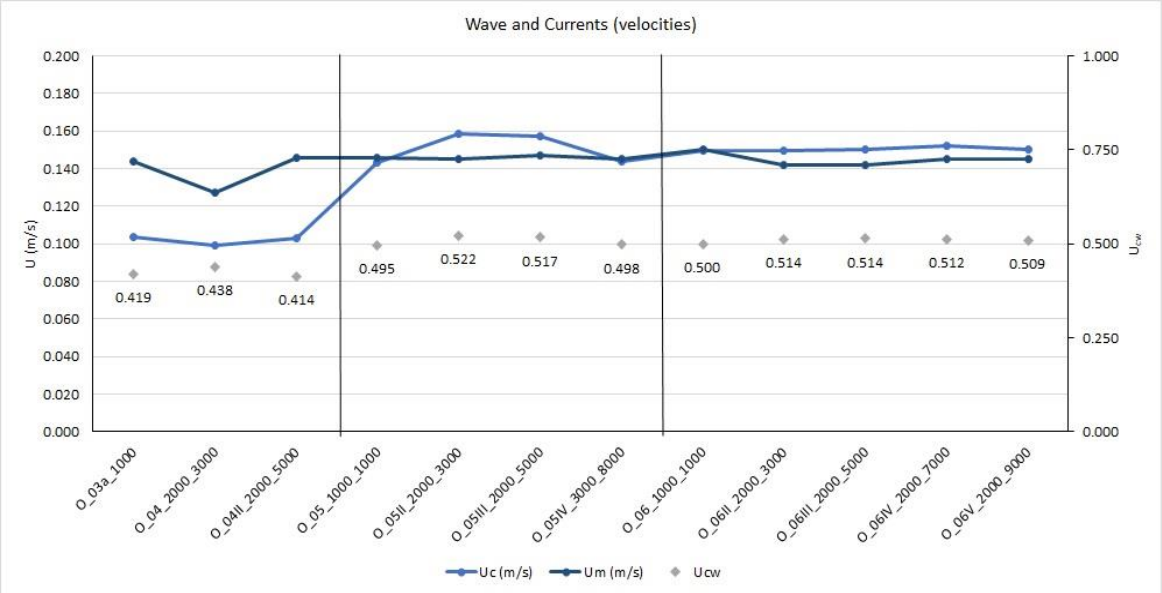

Figure 4.7 - Wave and currents interaction (U_{cw} values).

The KC target value was not reached in every wave train. This was also expected since it is dependent of the U_m value ($KC=U_mT/D_p$). So, since U_m failed to reach the target conditions, the KC also failed to reach the target conditions. As for the Re_p, in all wave trains, the calculated values, with the measured conditions, exceeded the target condition value. As shown in Eq. (2.15) the Re depends on the value of the flow velocity, therefore the fact that the U_c values in all tests exceeded the target values represents the main reason for the values obtained. Note, that the test with the least values of KC and mainly of Re_p, was the test with least damage development (as shown next). However, the sample of tests and the range of conditions was to small to verify this influence. In order to prove this assessment, more tests with wider range of conditions and/or with different pile diameters needed to be performed.

4.2. DAMAGE NUMBER ANALYSIS

For the damage number analysis, due to time constraints, the calculation of the S_{3D} based on the bathymetry was possible only for the 9000 wave train of the Test 2. However, with the D_{n50} available, a calculation of the $S_{3D,predicted}$ was made for every measured condition in all three tests, for the average conditions and for all the adjustments on the target conditions (after the reflection analysis and after the increase of the hydrodynamic conditions). The calculation of these parameters is important in a perspective of continuity of the present research. These values might then be compared with future S_{3D} calculations obtained from the bathymetry profiles. The extended calculation of the parameters used in the Eq. (2.68) and the S_{3D} value – for the $D_{n50,model}$ and $D_{n50,prototype}$, but also for a wide range of other D_{n50} values - are available in the Appendix A. A comparison of the predicted values obtained for the experimental stage conditions is presented in this section.

After the calculation, a comparison between the predicted S_{3D} was made, with respect to the number of waves. Figure 4.8 provides the calculations made for the $S_{3D,predicted}$ for every test condition, i.e the figure shows the value of the predicted damage number from 1000 waves to 9000 waves, even if the test had been planed for 5000 waves. For example, if the same conditions of the O_04_2000_3000 wave train, representative of N=3000 waves, were used for a N=1000 waves, the $S_{3D,predicted}$ should be lower than 0.25 (illustrative of a static configuration). However, for N=3000 waves, its conditions are expected to generate damaged representative of a S_{3D} value that indicates a dynamic configuration. Figure 4.9, shows the same process but for the average conditions of each test.

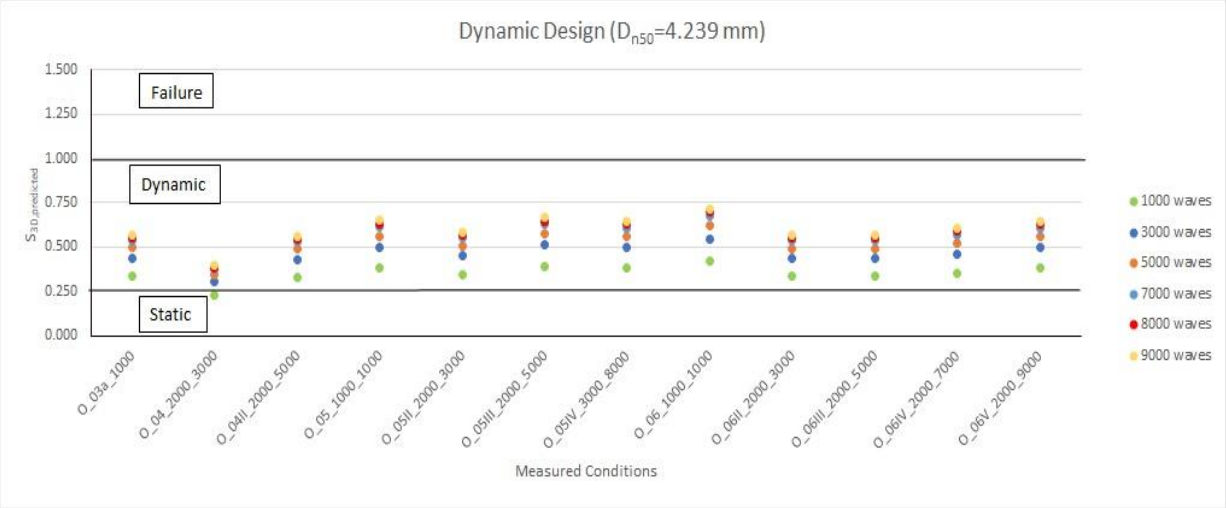

Figure 4.8 - $S_{3D,predicted}$ evolution for all measured conditions.

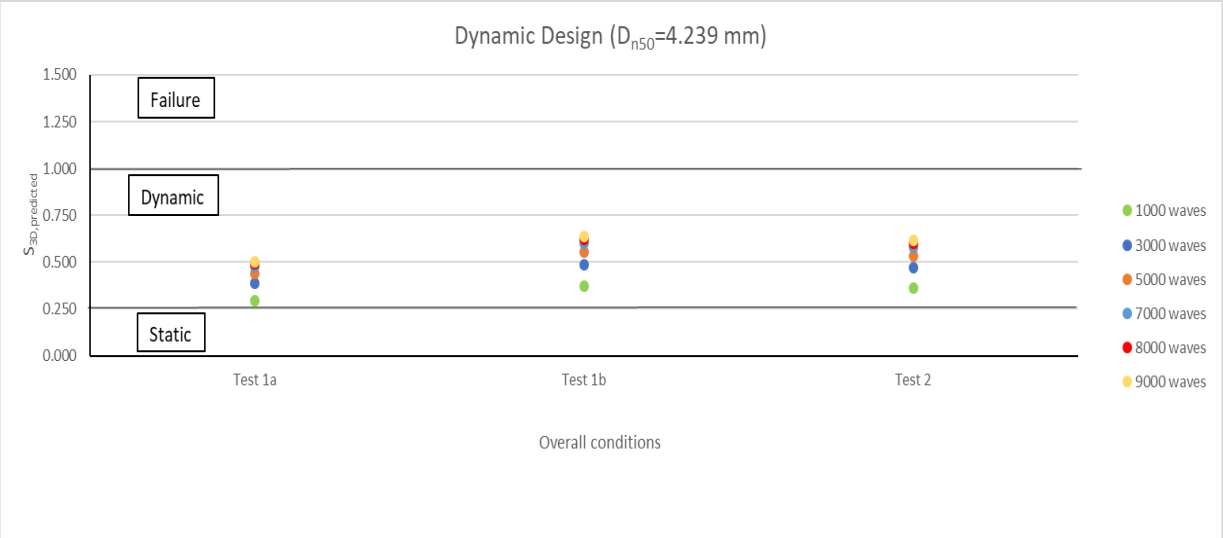

Figure 4.9 - $S_{3D,predicted}$ evolution for average test conditions.

Analysing Figure 4.8 and Figure 4.9, the value of the $S_{3D,predicted}$ increases with the increase of the N value, as expected and as pointed out by De Vos *et al.* (2012). It is also evident that for the exact same set of conditions, the relative increment on the $S_{3D,predicted}$ value tends to decrease as the N value increases. That difference is more evident for N>7000 waves. As explained before, by only analysing the H_{m0} values and the visual damage after every wave train, no correlation was possible to make between the damage and the wave height. However, in both Figure 4.8 and Figure 4.9 it was visible that most $S_{3D,predicted}$ values seem to follow the same evolution of the line in the H_{m0} graphic (Figure 4.5). Nevertheless, due to the small sample of tests, that assessment can not be generalised and further research is required to address this topic.

It was also compared, for each wave train of each test, the $S_{3D,predicted}$ for the measured conditions, the test target conditions and the average test conditions.

Table 4.7 - $S_{3D,predicted}$ comparison for the Test 1a.

N	Test 1a (Average)	Test 1a	Target Cond. II
	$S_{3D,predicted}$	$S_{3D,predicted}$	$S_{3D,predicted}$
1000 waves	0.296	0.335	0.480
3000 waves	0.386	0.303	0.627
5000 waves	0.437	0.488	0.710

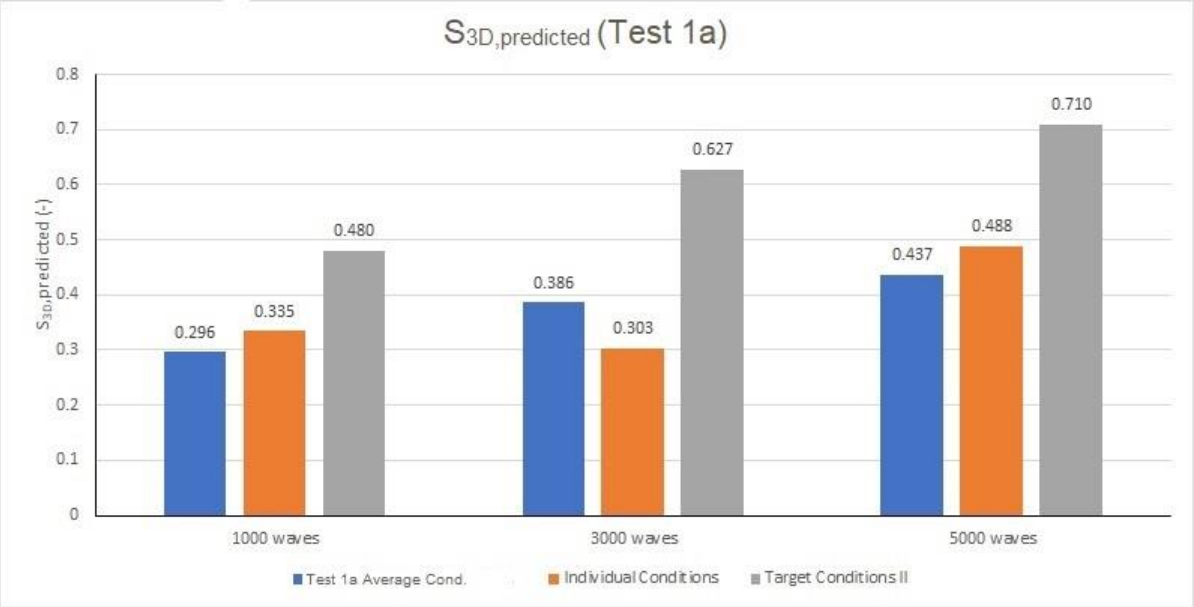

Figure 4.10 - Comparison of the $S_{3D,predicted}$ for the Test 1a.

Analyzing the Table 4.7 and Figure 4.10 it is possible to conclude that the conditions imposed on the model failed to meet the target conditions. In a similar manner, it is expected that the future damage calculations based on the bathymetry are also smaller than the predicted damage for the target conditions. In fact, that situation was observed in the Test 1a since the model did not suffer any significant visual damage. Since the values of $S_{3D,predicted}$ are higher than 0.25, the protections should correspond had a dynamic behaviour. However, the model seemed to be static. Note, that for 3000 waves the $S_{3D,predicted}$ value decreases from the 1000 waves value. This is only possible in calculations, since the damage parameter for each wave train was calculated with the respective measured conditions and with the respective number of waves, thus not taking into account the accumulated damaged from the previous wave train. Note, that the $S_{3D,predicted}$ for the measured conditions is higher than the one obtained for the average conditions in the two wave trains with higher value of H_{m0}, while the $S_{3D,predicted}$ for the measured conditions failed to reach the average value for the lowest value of the H_{m0} (Figure 4.10).

Table 4.8 - $S_{3D,predicted}$ comparison for the Test 1b.

N	Test 1b (Average)	Test 1b	Target Cond. III
	$S_{3D,predicted}$	$S_{3D,predicted}$	$S_{3D,predicted}$
1000 waves	0.374	0.381	0.480
3000 waves	0.489	0.488	0.627
5000 waves	0.553	0.579	0.710
8000 waves	0.620	0.629	0.796

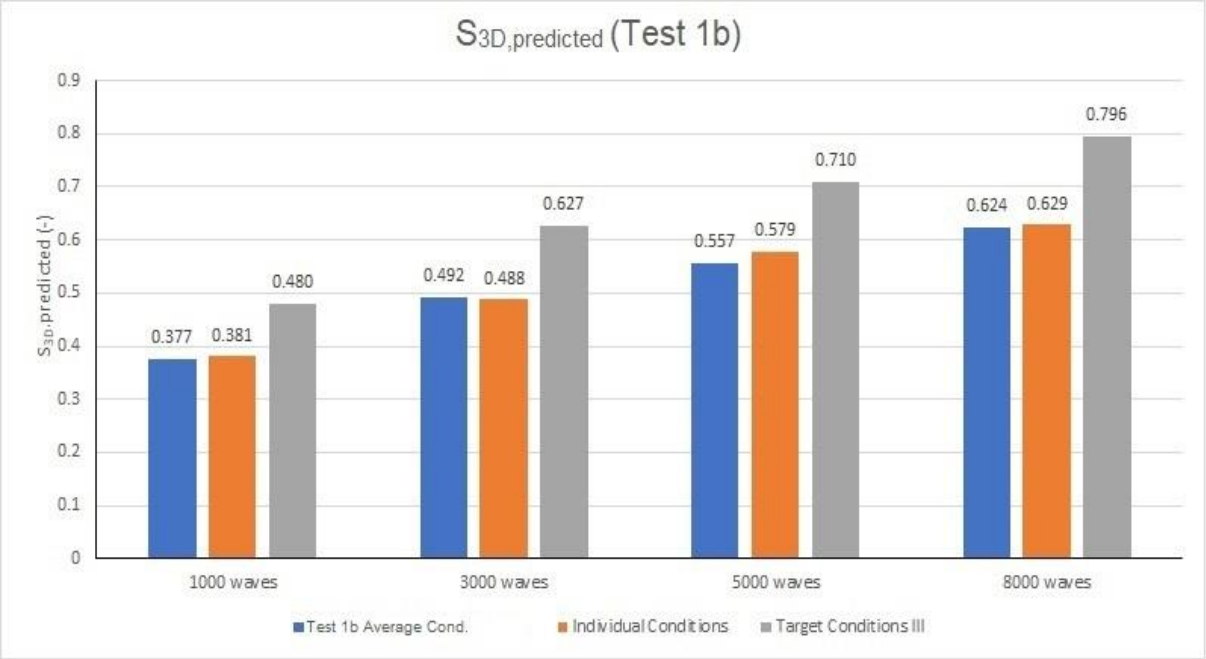

Figure 4.11 - Comparison of the $S_{3D,predicted}$ for the Test 1b.

For the Test 1b, analysing the Table 4.8 and Figure 4.11 it is also visible that the conditions imposed on the model failed to achieve the target conditions. By comparing Figure 4.10 and Figure 4.11, it is visible that the difference between the $S_{3D,predicted,}$ calculated using the measured conditions and using the target conditions, between the Test 1a and 1b, is significantly lower in the second test as shown by the gap between the orange and grey bars. The increased proximity between the measured values and the target values of the $S_{3D,predicted}$ on the second test could be explained with the increase of the hydrodynamic conditions and with the lower fluctuation on the H_{m0} values. The values of the $S_{3d,predicted}$ are also higher than in the previous test, since the hydrodynamic conditions were aggravated. In fact, more stone movement and damage was observed in Test 1b. Also, in this test the protection failed. Since the values of the damage numbers were lower than 1.0, the failure of the protection should not have been reached. However, this observations, plus the increase of stone movement compared to the first test, could be explained with the aforementioned fact that between the first and second test the model was not removed and rebuild. Therefore, the model at the end of the Test 1b, was in fact subjected to 13000 waves instead of only 8000 waves, as analysed, due to the cumulative effects of the previous test, leading to the enhancement of stone movements and ultimately to the failure of the structure, with the filter layer being exposed. Consequently, a new analyse to the second test should be performed in the future, calculating the values of the $S_{3D,predicted}$ as in Figure 4.11 and Table 4.8, but for the cumulative wave values of 6000, 8000, 10000 and 13000 waves. Due to the reduce number of tests and in order to validate these results, and to verify the influence of cumulative effects on the protection failure, when a change in the hydrodynamic conditions is made, a larger sample of tests should be done in the future. Note, that the $S_{3D,predicted}$ for the measured conditions is almost equal to the average conditions $S_{3D,predicted}$. This could be explained with the fact that the H_{m0} and U_c measured conditions did not had significant fluctuations during the tests, thus making the measured conditions matching the average conditions for both parameters (that are directly related in the S_{3D} calculation).

Table 4.9 - $S_{3D,predicted}$ comparison for the Test 2.

N	Test 2 (Average)	Test 2	Target Cond. III
	$S_{3D,predicted}$	$S_{3D,predicted}$	$S_{3D,predicted}$
1000 waves	0.362	0.420	0.480
3000 waves	0.472	0.435	0.627
5000 waves	0.535	0.493	0.710
7000 waves	0.580	0.569	0.770
9000 waves	0.617	0.648	0.819

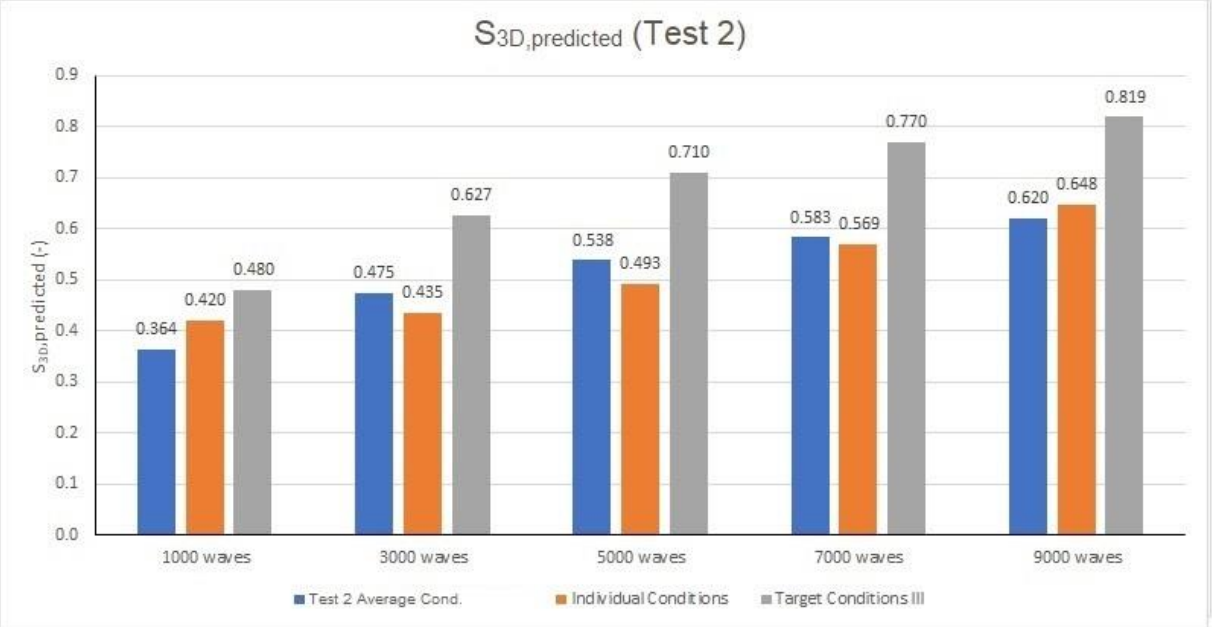

Figure 4.12 - Comparison of the $S_{3D,predicted}$ for the Test 2.

Regarding the last tests, the Table 4.9 and Figure 4.12 show the same tendency of the previous ones. However, since the Test 1b and the Test 2 were performed with almost similar overall conditions, comparing the Figure 4.11 and Figure 4.12 its visible that the difference between the grey and the orange bars are higher in the Figure 4.12 than in the Figure 4.11. Also, the value of the $S_{3D,predicted}$ is generally higher in the second test than in the third. This could be explained by the fact that the T_p and U_c values on the second test are higher than in third, as the H_{m0} value is almost similar between tests. As explained next, in section 4.3, the stone movement in the third test and its visual damage is smaller than in the second test. Although the cumulative effect that the protection on the second test was submitted to might have played an important role in that difference, the calculation of the $S_{3D,predicted}$ does not take into account that effect. So, by analysing just the $S_{3D,predicted}$ with the measured conditions in both tests, a lower damage rate would be expected for the third test, as it turned out.

Comparing the calculation with the average effects and the measured effects, the values of the $S_{3d,predicted}$ for 3000, 5000, 7000 waves for the measured values are lower than the average values, somehow coincident with the lower values registered for the H_{m0} and the T_p registered for that test.

These comparisons and analysis of the $S_{3D,predicted}$ are only useful in the idea of understanding what the behaviour to expect from the model before each wave train. They could also be used for a first read and comprehension of possible outliers in the results obtained. However, they could not be used to accurately determine and classify the behaviour of the model. Those assessments could only be done with the calculation of the real value of the $S_{3D,measuresed}$, which derived from the DTM's . This analysis of the $S_{3D,predicted}$ is somehow, the preparation of future works that could be done with the results obtained with this dissertation. Moreover, it is important to note the methodology presented by De Vos *et al.* (2012) was developed for tests performed with a maximum range of 3000 to 5000 waves. Since the inherent formula was developed through regression the accuracy of these calculations will enable future conclusions on the accuracy of the methodology for tests with long duration, *e.g.* tests with 7000, 9000 waves or even more.

In addition, these tests and predicted values can also be compared with different approaches to the calculation and method of analysis of the $S_{3D,measured}$ as the one recently discussed in Fazeres-Ferradosa *et al.* (2019). In this sense, the predicted damage presented and the tests performed allow for two key contributions. Firstly, they represent a first set of long-duration tests which contribute to perform and increase the data base in future research on this topic. Long-duration tests of scour protection performance remain as an important knowledge gap to be addressed. Secondly, these tests and the predicted damage for target and measured conditions enable a better perception of the future hydrodynamic conditions and model setup that should be implemented for create a proper benchmark data set on dynamic scour protections under the long effect of waves and current combined.

4.3. LONG-TERM DAMAGE EVOLUTION

As referred in the section 3.4, the monitorization and analysis of damage on the physical model will be performed using the visual damage assessment technique. After every test and after the photogrammetry pictures were taken, pictures were taken to the overall protection. Some closer pictures were also taken to the most meaningful stone movements or even failures of the respective test. Than, a comparison was made to the initial protection and between the following protections subjected to the tests. After comparing and analyzing every picture taken for every wave train on every test, a table for every test (Table 4.10, Table 4.11 and Table 4.12) was built with a visual damage classification for every test. That visual damage classification was also compared with the $S_{3D,predicted}$ of every test resulting in Figure 4.38.

4.3.1. 1ST TEST: TEST 1A

This test was the one classified as static at the end of 5000 waves. Observing the Figure 4.16, no difference seems to be noticeable between the initial profile and the 1000 waves profile. Using a closer picture of the 1000 wave profile - Figure 4.13 - two stone movements were detected (one of the red ring and the other from the blue ring). However, they were not consider significant since the remain of the structure seemed motionless.

Figure 4.13 - 1000 waves (Test 1a).

Between the 1000 waves and the 3000 waves profile some differences are detected mainly on the bottom and left edges of the protection. The edge seems to have lost its perfect circular shape, due to some stone movement, but some accretion of sand over the protection was noticed also. It is important to note that the edge scour of the protection can be attributed to the influence of abrupt changes of the bed roughness in the bed boundary layer (Petersen *et al.*, 2015; Fazeres-Ferradosa, 2018). In addition, Figure 4.14 shows some differences also occurred in the red circle. The previous blue stone came back to the blue ring, as the red stone remained in the same place. This could be an indicator of dynamic behaviour, but just one stone movement in the overall size of the protection was not considered to be significant since, according the S_{3D} classification, a very reduced movement of stones could also be representative of a static protection since until a S_{3D}=0.25 the protection is static. Note, that in the top right corner one red stone appears to have moved. However, that stone was not consider for the remaining analysis since it moved when the flume was being filled. This situation often occurs as reported in De Vos *et al.* (2012) and Fazeres-Ferradosa (2018) and emphasizes the need for a careful observation of the model while the current is being stabilised.

Figure 4.14 - 3000 waves (Test 1a).

After the 5000 waves, at first sight, the edges appeared to be more damaged. However, watching the blue squares in Figure 4.15 it is possible to observe some sand accumulation at the edges. This sand gathering made it difficult to understand if there was damage beneath, *i.e.* at the armour layer. As for the previous locals where some movement of stones occurred, no changes happened comparing to the 3000 waves, although one stone movement, again from the blue ring, was detected as shown after the pile. Since that small movement was not considered significant the three wave trains performed during this test were all classified with a visual damage of 1 (Table 4.10) and the protection was classified as static, even though the $S_{3D,predicted}$ for this foundation was indicative of a dynamic protection.

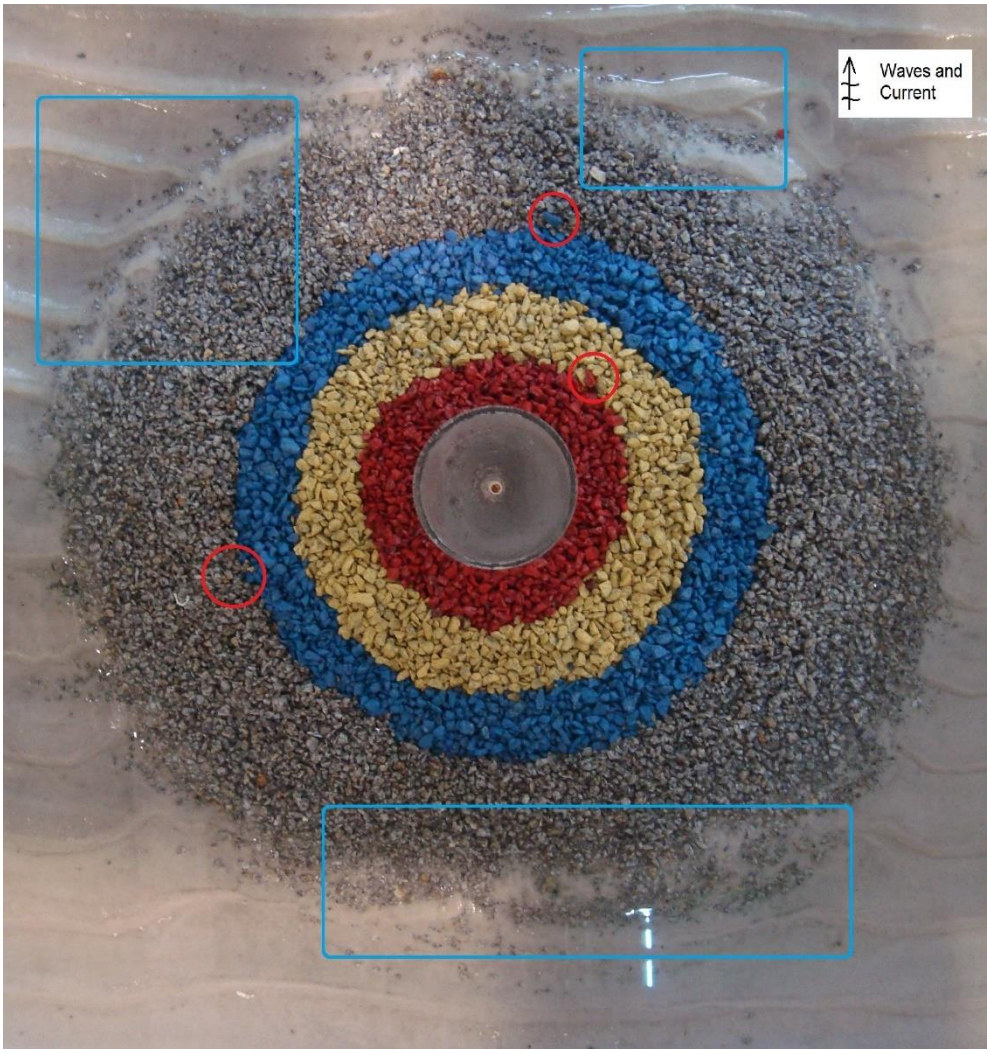

Figure 4.15 - 5000 waves (Test 1a).

Table 4.10 – Test 1a Visual Damage Classification.

Test Reference:		Test 1a	
Wave Train Ref.:	N	$S_{3D,predicted}$	Visual Damage
O_03a_1000	1000	0.335	1
O_04_2000_3000	3000	0.303	1
O_04II_2000_5000	5000	0.488	1

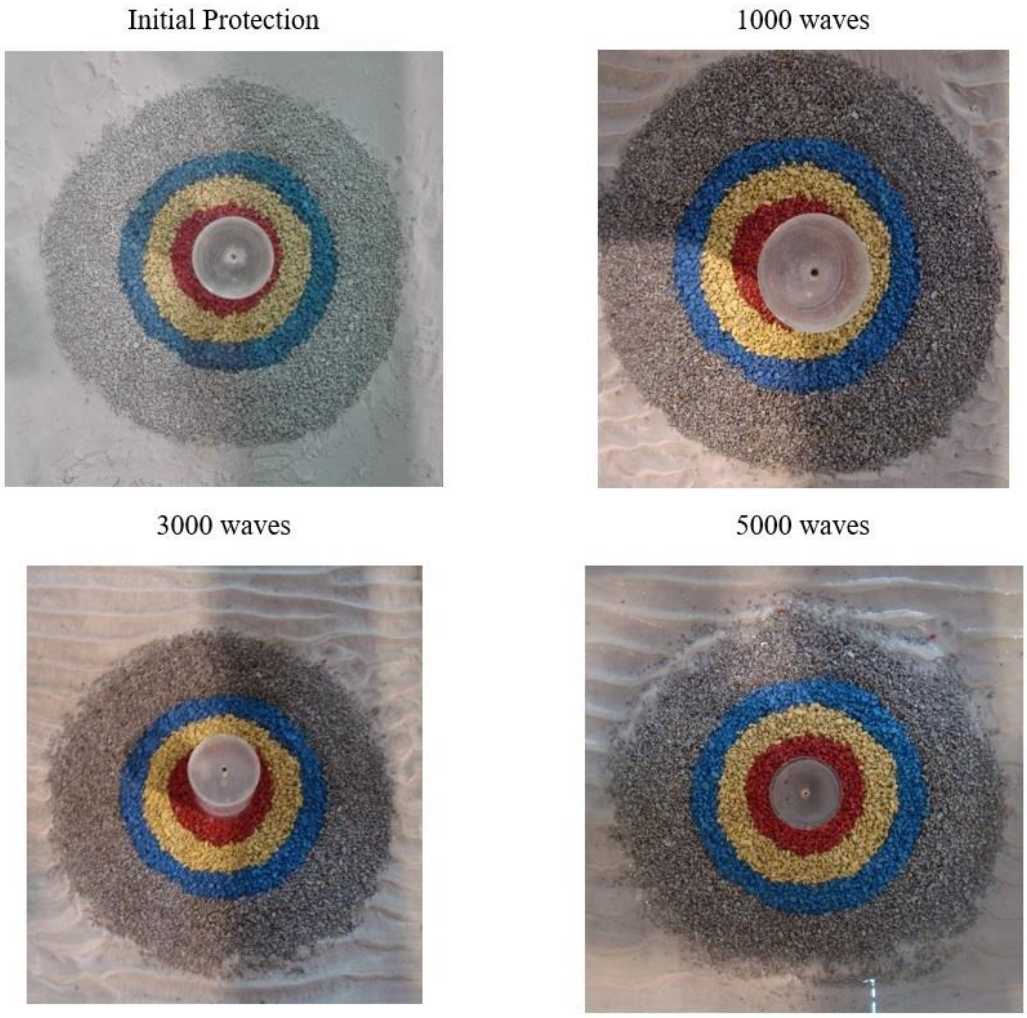

Figure 4.16 - Scour protection evolution for the Test 1a (Waves and current direction from the bottom to the top of the pictures).

4.3.2. 2ND TEST: TEST 1B

This test was performed with the model of the first test after 5000 waves, as aforementioned. So for comparison reasons, the initial profile of this test was the last profile from the previous test. It is important to remember that this option was only taken since after a significant number of waves the previous protection did not show signs of significant damage at all. However, there is also the awareness that accumulated effects on the protection stones were already present at the beginning of this new test. In this test, the U_c value was increased from around 0.1 m/s to approximately 0.15 m/s.

After the first wave train with the new hydrodynamic conditions it was visible that an increase of the stone movement and damage occurred comparing to the previous test. On the right side of the Figure 4.17 the two red circles are the same as in Figure 4.15, so no movement occurred there. However a new red circle on the left side of the Figure 4.17 shows a stone movement. The damage is clearly visible on the edges of the protection, mainly on the top, left and bottom edge. The damage in the bottom edge is consistent with the general scour pattern defined by Sousa (2013). However, the bottom and top edge also present some accretion of sediments - higher on the top edge as also described by Sousa (2013) -

that could be confused as damage. The accretion of sand on top of the armour layer is an important aspect that difficults the accuracy of the visual analysis, This emphasizes the importance of using methods with better resolution. Until this wave train, no significant movement was detected in the coloured rings of the protection.

Figure 4.17 - 1000 waves (Test 1b).

With some damage already visible on the edges, obtained with the new hydrodynamic conditions, the expectation was that the stone displacement would increase. After the 3000 waves, the results obtained are illustrated in Figure 4.18. In Figure 4.18, it is visible that an increased amount of stones moved from their previous locations. The red circles represent the most significant stone movements and their associated numbers (1 through 4) were subject of greater attention. In this test, it was also detected an opening on the protection that exposed the filter - orange G1 circle (Figure 4.20). However, as described in section 2.4.3.2, failure is reached for an exposure of the filter equivalent to $4D_{n50}^2$. Without the possibility to determine the exact exposed area in this test, and although it seems in the Figure 4.20 exposure was reached, further analysis is required. Visually in the model the exposure seemed slightly smaller, this aspect is to be confirmed in future analysis. The next test was performed to observe the evolution of the filter exposure. Note, that at the bottom edge, part of the sand accretion was reduced, in comparison with the previous test, and the stones appear to have spread.

Figure 4.18 - 3000 waves (Test 1b).

Figure 4.19 - Stone movement (A - zone 4; B - zone 3).

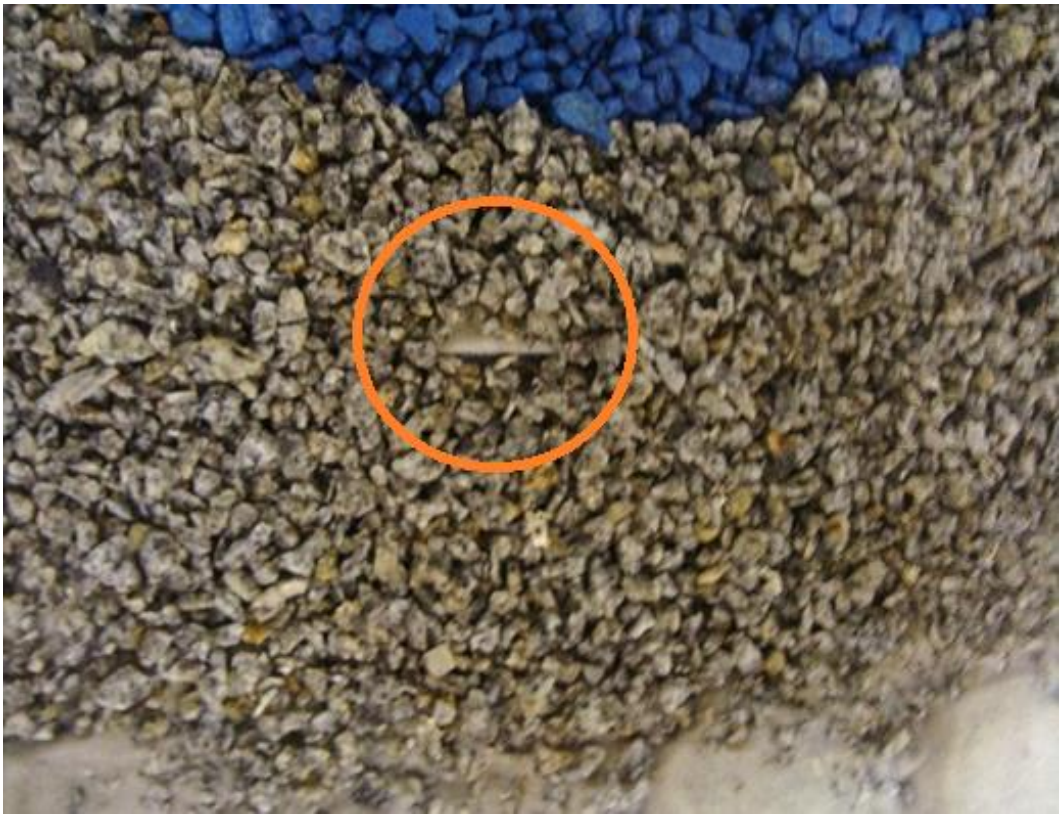

Figure 4.20 - Filter exposure (G1) for 3000 waves in the Test 1b.

After the 5000 wave train, the scour on the edges continued to increase (Figure 4.21). On the top edge, it is visible some stone movement but also an increase in the sand accretion. However the bottom edges seemed to suffer more stone displacements than in the top edge, as reported by Sousa (2013). Other displacement or sand accretions are highlighted in blue circles. Regarding the red circles, only the zone 1 circle (Figure 4.23) showed changes compared with the previous test. But the most important situation reported in this test is the fact that the G1 filter size exposure increased and two other filter exposures appeared (G2 and G3). These three exposures (Figure 4.22) were sufficient to visually classify this protection as failed after 5000 waves. In a certain way, this second test opened some new possibilities and questions regarding future researches. With this wave train (5000 waves representing a cumulative effect of 10000 waves), for considerable number of wave with increased hydrodynamic conditions, failure appears to occur even when the protection previously seemed static. Another interesting fact is that, in literature, there are no records of tests with variable conditions in terms of consecutive storms, being this set of consecutive tests (Test 1a an 1b) a good starting point.

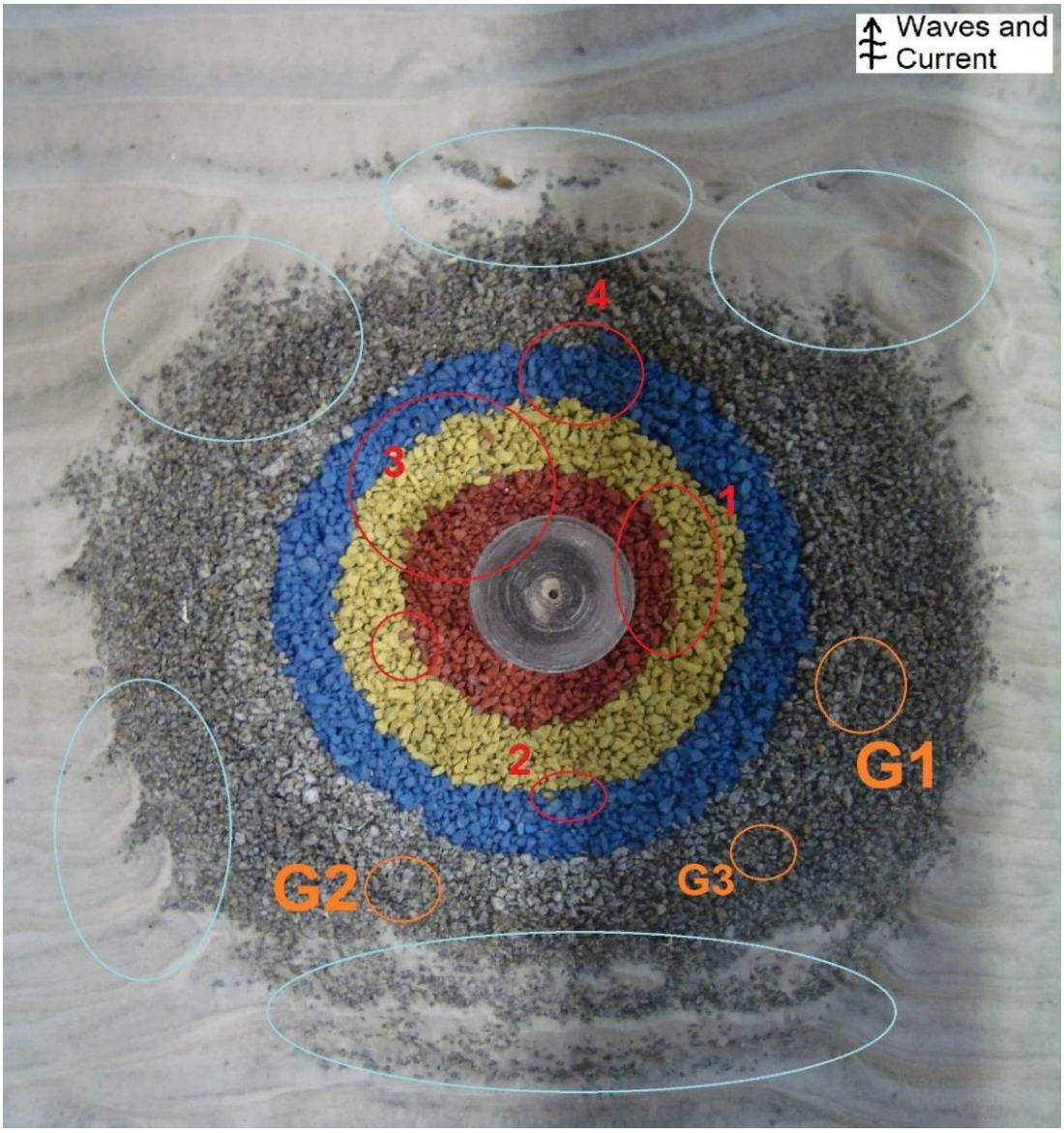

Figure 4.21 - 5000 waves (Test 1b).

Figure 4.22 - Filter exposures for 5000 waves (A - G1; B - G2; C - G3).

Figure 4.23 - Stone movement for 5000 waves (zone 1).

Regardless of the protection's failure, a final wave train was performed in order to understand if those failures would lead to an increase of the scour rates in the armour layer, since this was clearly an example of edge scour. This dissertation was focused on the study of top layer erosions and despite an increase on the stone movement on the top layer compared to the previous test, the scour rate still was not the expected. However, the results were practically the same, regarding top layer movements. The only significant differences were detected in the blue stone of zone 4 - that returned to its ring - and some yellow and blue stones meshed between each others in the zone 2. Other blue stones moved away from their ring (highlighted with red circles in the left and right side of the Figure 4.24). On the edges small movements occurred as some sand accretions. The evolution registered for the filter exposures were noticeable (Figure 4.25). The areas increased and a new filter exposure (G4) occurred.

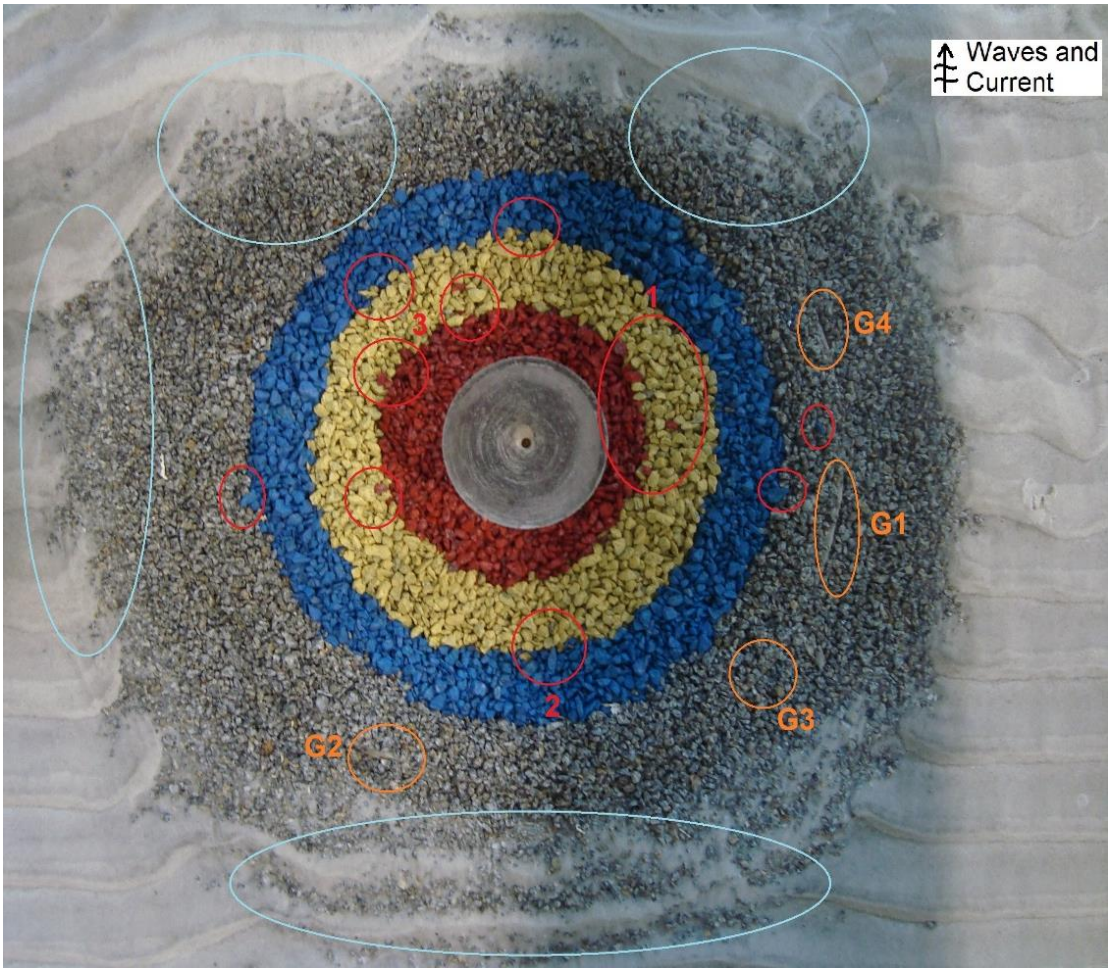

Figure 4.24 - 8000 waves (Test 1b).

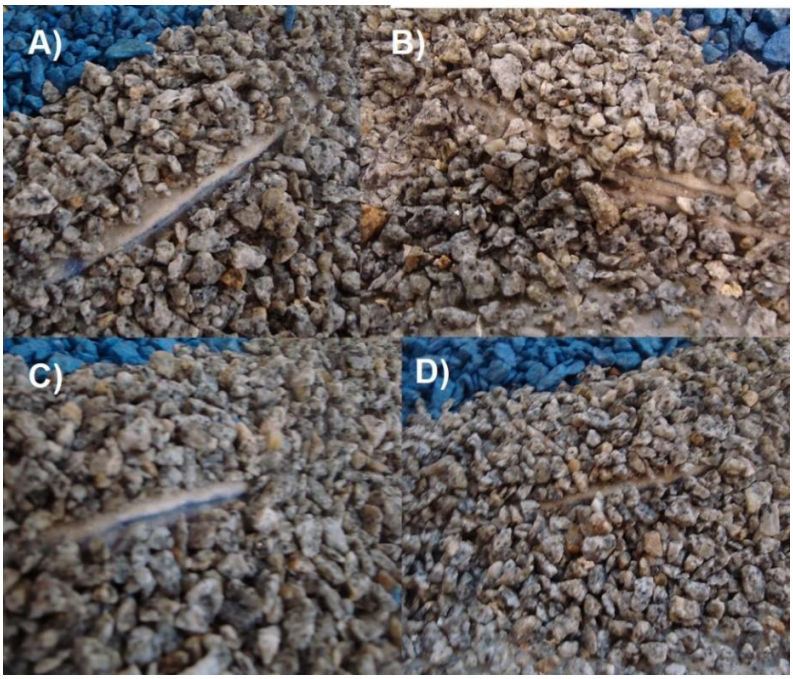

Figure 4.25 - Filter exposures for 8000 waves (A - G1; B - G2; C - G3; D - G4).

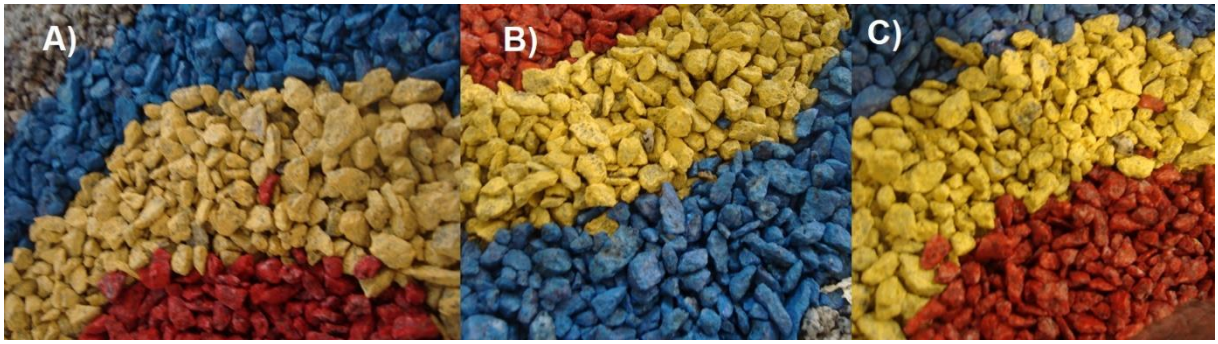

Figure 4.26 - Monitorization of stone movements for 8000 waves (A - zone 1; B - zone 2; C - zone 3).

As conclusion, from the 1000 waves forward some stones were displaced during the tests. In De Vos *et al.* (2012) a typical damage profile was described for scour protection with waves flowing currents, were most of the damage rate occurs between 0 and 1000 waves. This was not the case in these two tests. For this kind of conditions, most of damage occurs immediately behind the pile over a distance of $1.35D_p$ and the eroded area is wider than the pile. In fact, although without the expected scour rate, most of the detected movements occur behind the pile. Also the general scour pattern defined by Sousa (2013), appointed the ring closest to the pile (mainly behind the pile) and upstream half edge as the locations where scour effects are typically higher. In this model most of the displaced stones came from the red ring (ring closest to the pile) and from the edges of the protection, in some aspects similar to the reported by Sousa (2013).

As for the motives of the failure, clearly this was a case of edge scour. One reason that could explained this type of scour could be the difference between the bed roughness and the roughness of the protection. Typically, this type of failure lead to the progress of damage from the outer to the inner rings (as verified by the Figure 4.23 and the Figure 4.26 but without much significance in this case).

Overall, the visual damage assessment of the Test 1b is summarized in Table 4.11, where for the first two wave trains the protection seemed to have a very small dynamic behaviour but that quickly turned into a failed structure both for 5000 and 8000 waves (corresponding to a cumulative number of waves of 10000 and 13000 waves, respectively). For future works, the analysis of the bathymetric profiles could by important in order to clarify and support these visual observations and consequent assessments.

Table 4.11 – Test 1b Visual Damage Classification.

Test Reference:	Test 1b		
Wave Train Ref.:	N	$S_{3D,predicted}$	Visual Damage
O_05_1000_1000	1000	0.381	2
O_05II_2000_3000	3000	0.448	2
O_05III_2000_5000	5000	0.579	3
O_05IV_3000_8000	8000	0.629	3

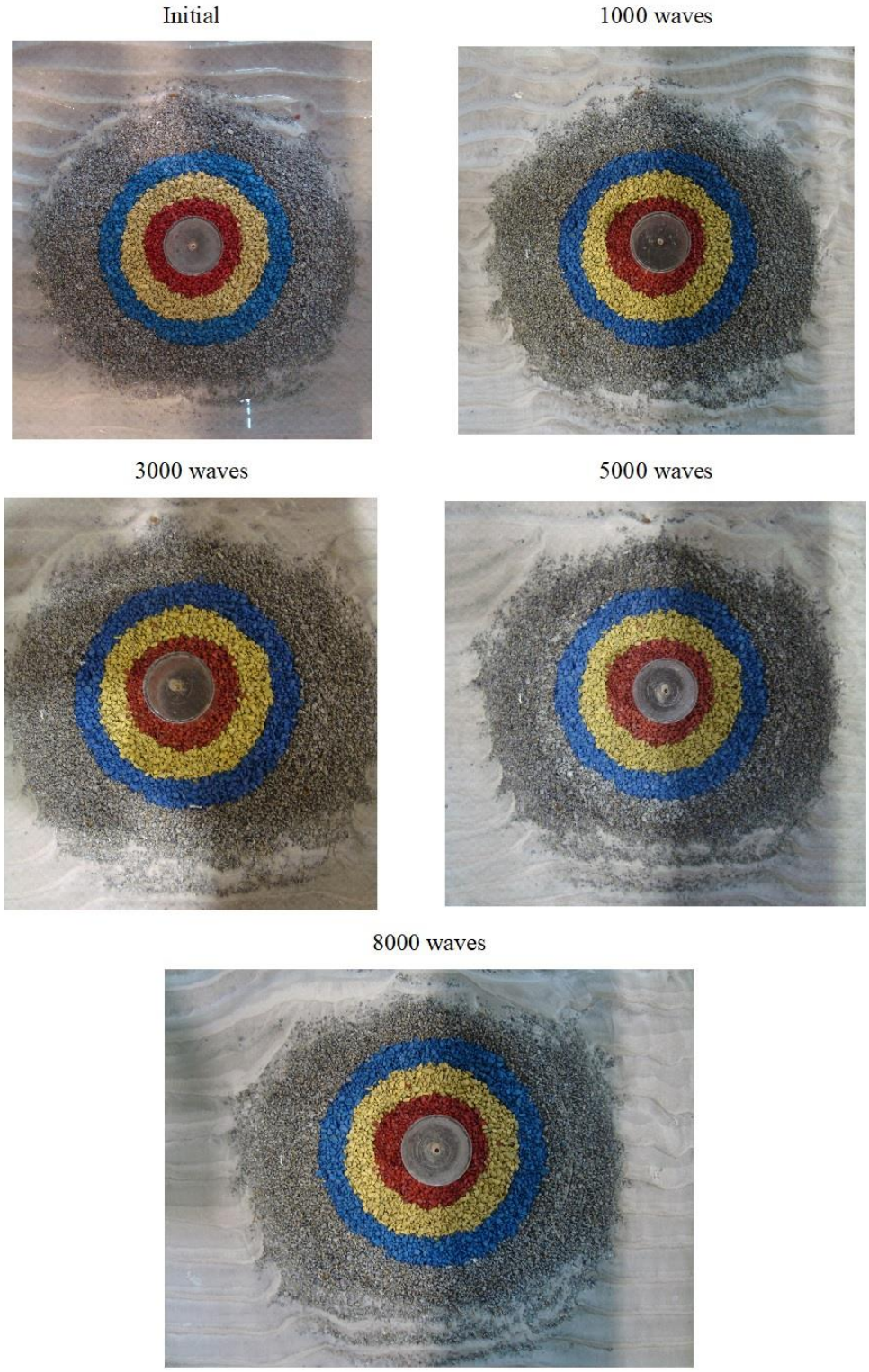

Figure 4.27 - Scour protection evolution for the Test 1b (Waves and current direction from the bottom to the top of the pictures).

4.3.3. 3RD TEST: TEST 2

After the second test and after reaching failure, a new model was build for the final test. The expectation was trying to reach a model where the dynamic stability was more evident since both previous scour protections failed in the attempt to reach the objective of this dissertation – a dynamic configuration with significant movement of the armour layer.

For the first wave train – 1000 waves – no considerable movements and scour were obtained. The only movement worth notice was the displacement of two red stones highlighted by zone 1 (Figure 4.29).

Figure 4.28 - 1000 waves (Test 2).

Figure 4.29 - Stone movement (zone 1).

For the 3000 wave train the situation almost remained the same. The only difference detected (Figure 4.30) was the accretion of sand plus movement of the stones on the bottom edge of the protection.

Figure 4.30 - 3000 waves (Test 2).

The results until this stage were quite different from the ones obtained in the second test if taken into account that this test was also tested for the same target hydrodynamic conditions. One reason, possibly the main reason, could be the fact that the second test was performed with a model that already had cumulative effect of the previous 5000 waves and currents. Another potential reason, is the fact that the third test had lower U_c and U_m values (Figure 4.7). However the difference of those values between tests does not seem to be large enough for such disparity in results.

Therefore, a new wave train was performed and again, a slight movement and accretion on the bottom edge of the protection was visualized.

Figure 4.31 - 5000 waves (Test 2).

Without a considerable movement registered for two consecutive 2000 wave trains the protection seemed static despite small movements observed on the bottom edge of the protection (as some very small displacements of the top of the protection as described for the 3000 wave profile). So a decision was made regarding the tests. Instead of increasing the hydrodynamic conditions again, as previously, the decision was to perform a last wave train of 2000 waves just to re-check if no significant movements occurred for the third straight time. For the "final" wave train, corresponding to a total of 7000 waves, small movements were detected in the inner rings (red highlights zones from 1 through 5) and more

considerable stone displacements were observed on the top edge of the protection (blue rectangles). Since the measured hydrodynamic values for the 7000 wave train were not significantly higher in comparison to the previous wave trains, one of the reasons found for this amount of movements, compared with the previous wave trains, could be the accumulated effects over 7000 waves. Despite an obvious difference between this and the previous wave train of this tests, it is not correct so say that these movements were significant compared to data sets analysed by other authors, *e.g* De Vos *et al.* (2012) or Fazeres-Ferradosa (2018).

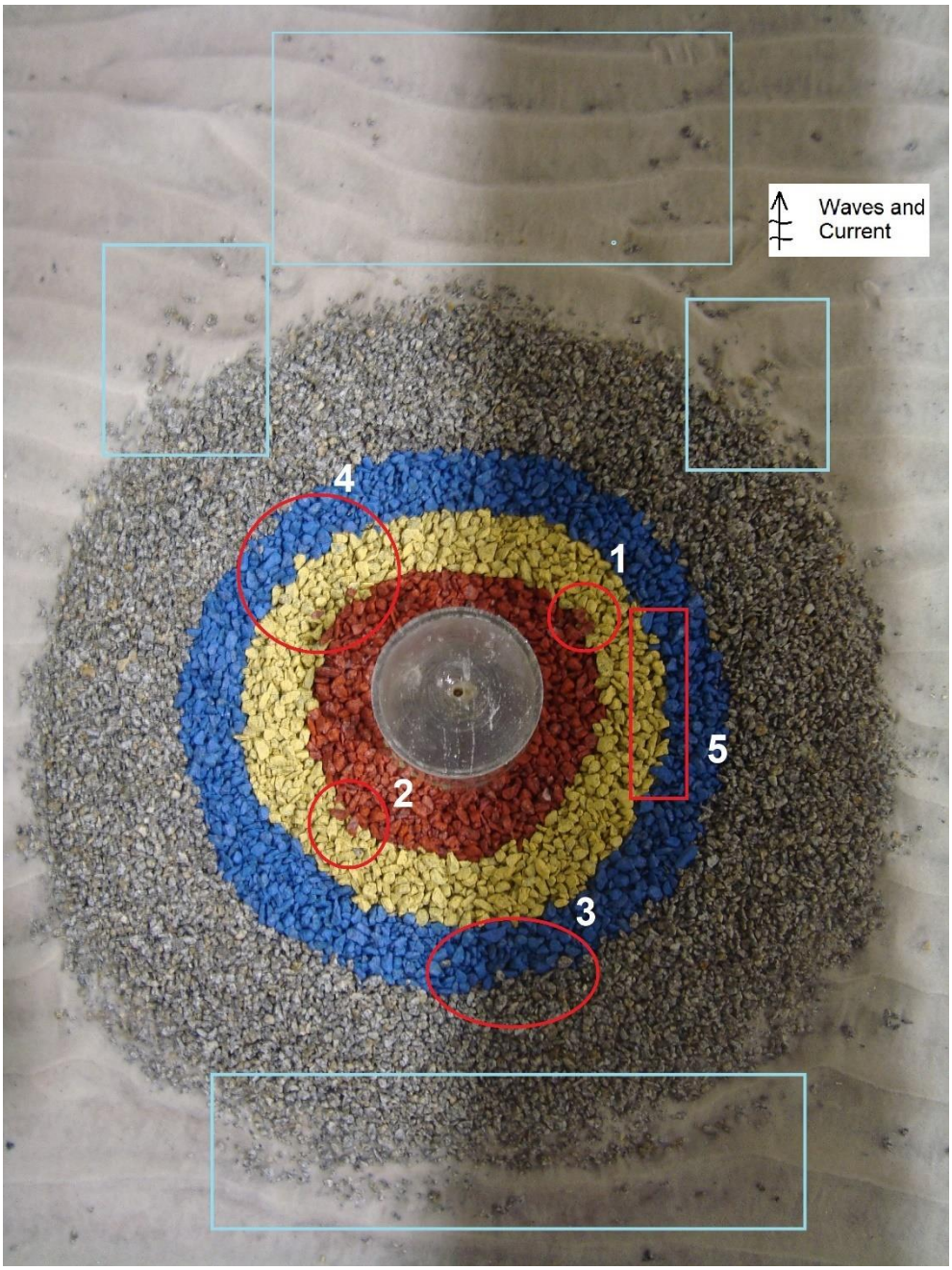

Figure 4.32 - 7000 waves (Test 2).

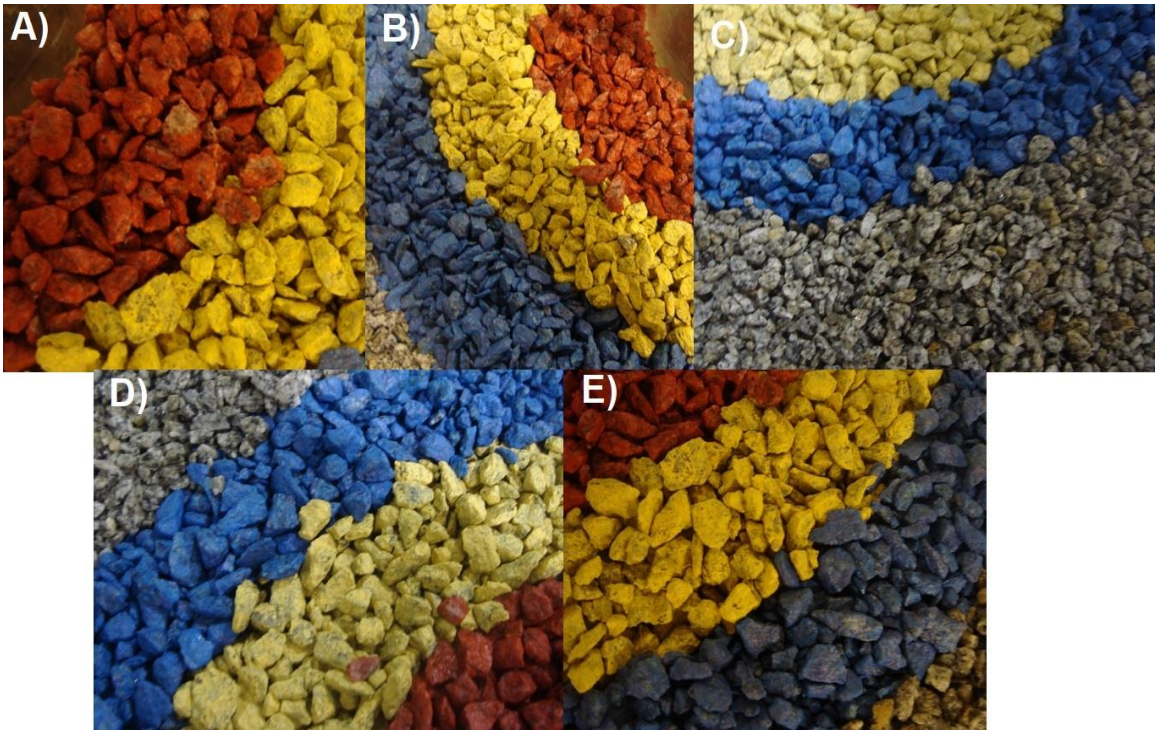

Figure 4.33 - Stone movement for 7000 waves (A: zone 1; B: zone 2; C: zone 3; D: zone 4; E: zone 5).

It is also important to note, unlike the second test, the stone displacement in the inner rings did not follow the general pattern stated by De Vos *et al.* (2012) and Sousa (2013).

A final wave train was performed, reaching the 9000 waves, that was one of the main objectives of this dissertation. Comparing the 7000 wave train with the 9000 wave train no visible differences seemed to happen, unless on the edges of the protection. However, two curious movements were detected. The zone 1, detected by the movement of two stones in the 1000 wave train, was re-filled with other red stone, and near that place another red stone was detected that was not there on the previous four wave trains. Although the movements registered seem to be practically insignificant, the re-fill is indeed a quality that is required for dynamic stability.

Figure 4.34 - Comparison between zones for the 1000 wave and the 9000 wave train.

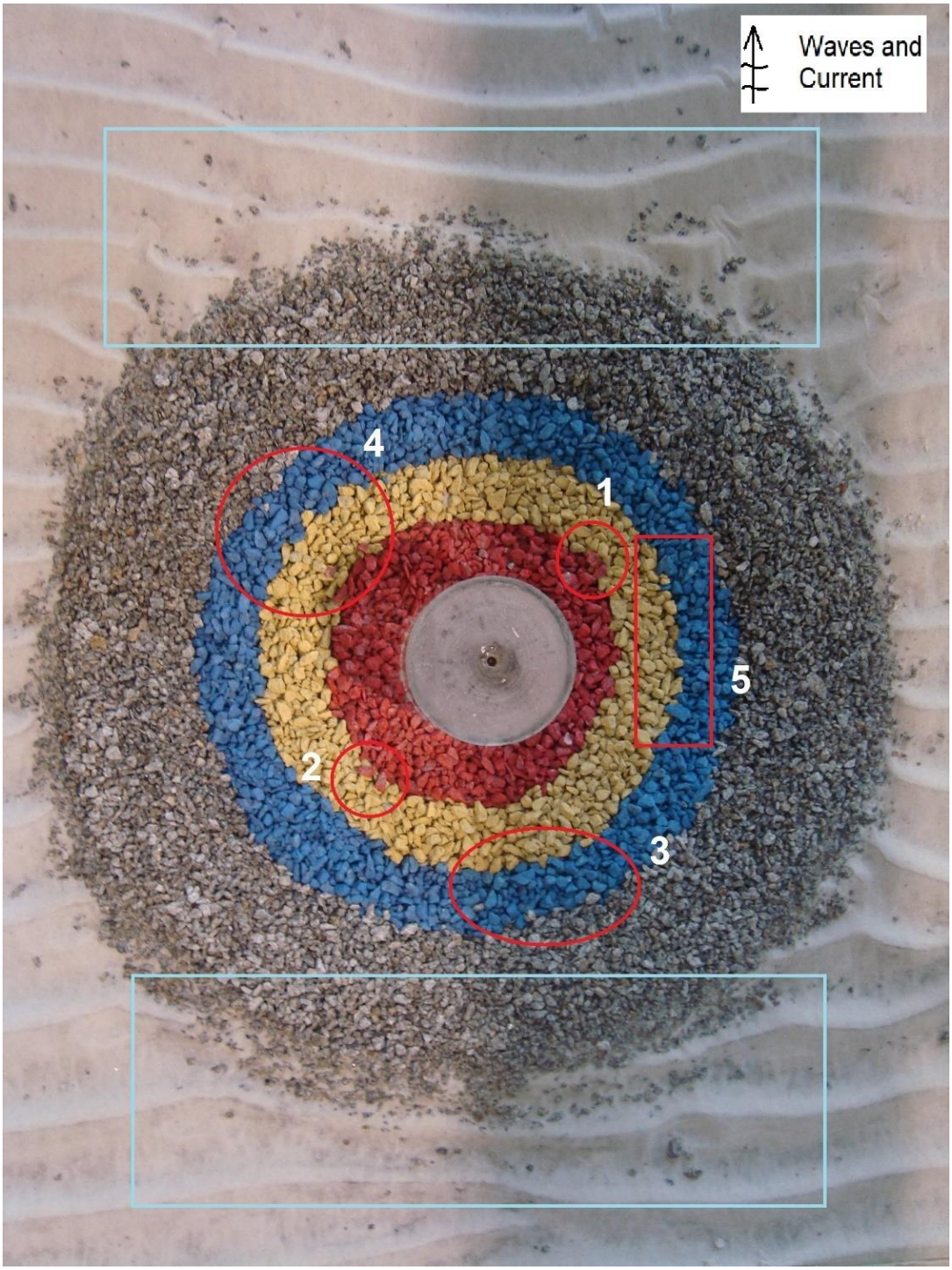

Figure 4.35 - 9000 waves (Test 2).

Figure 4.36 - Bottom edge after 9000 waves.

In this wave train, the protection had minor indications of dynamic stability. However, the scour was not the expected at the armour layer. Plus, the results registered in the second test were not the same results achieved on this test (even for similar hydrodynamic conditions). With the exception of some scour on the bottom edge, the remaining areas of the protection of this final test did not present the scour patterns identified in the second test and also described by De Vos *et al.* (2012) and Sousa (2013). For that reason, this third test should be repeated for further confirmation of the results. It would also be recommended the extension of the present data set for a proper discussion of some of the outlined findings in this dissertation. In the end, this Test 2 was classified as dynamic and the visual damage assessment of each test of this test is presented in Table 4.12.

Table 4.12 – Test 2 Visual Damage Classification.

Test Reference:	Test 2		
Wave Train Ref.:	N	$S_{3D,predicted}$	Visual Damage
O_06_1000_1000	1000	0.420	1
O_06II_2000_3000	3000	0.435	1
O_06III_2000_5000	5000	0.493	2
O_06IV_2000_7000	7000	0.569	2
O_06V_2000_9000	9000	0.648	2

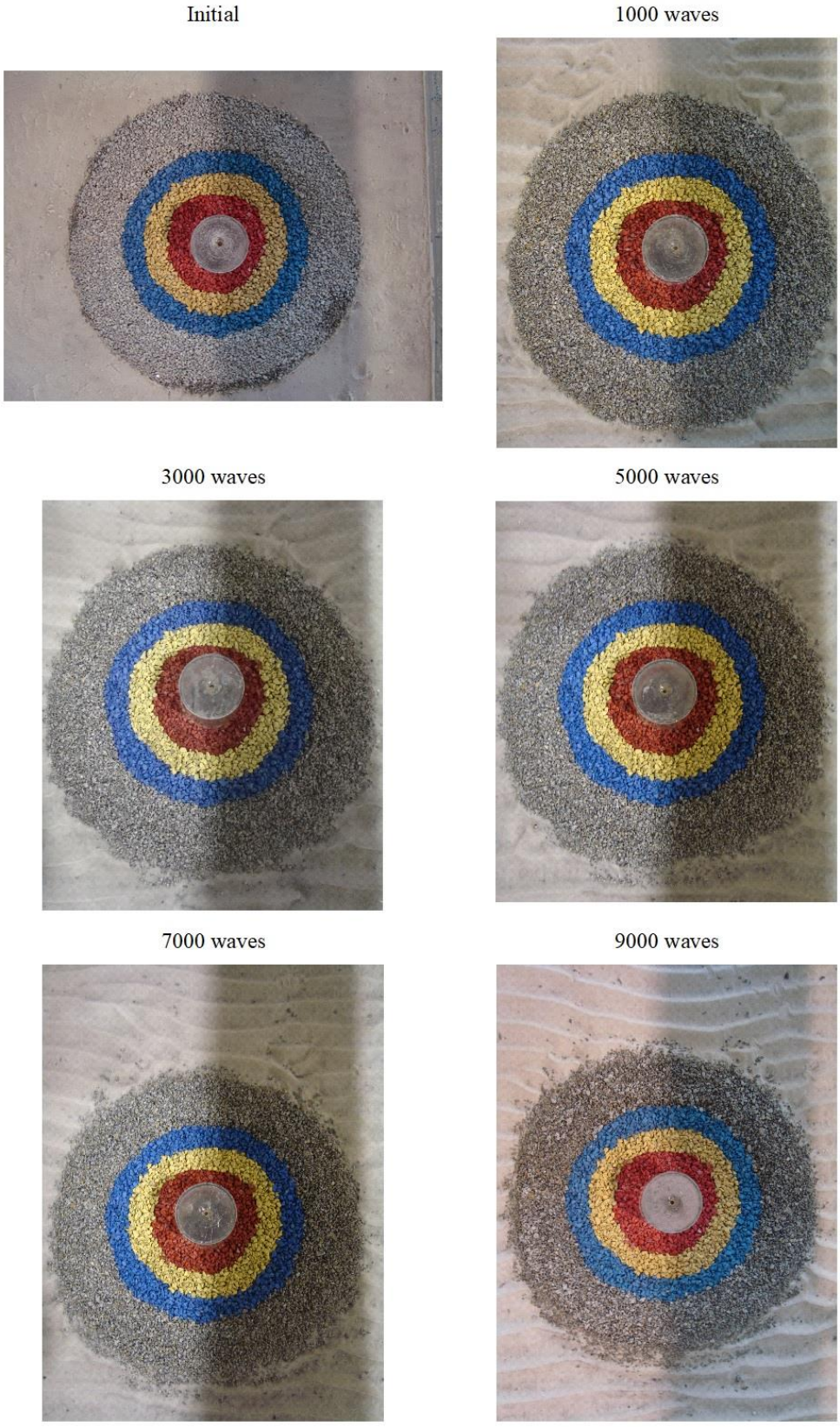

Figure 4.37 - Scour protection evolution for the Test 2 (Waves and current direction from the bottom to the top of the pictures).

Finally a comparison was made between the visual damage detected on every test and the $S_{3D,predicted}$ calculated previously. Regarding the Test 1a (classified as static) we can observed that the first two values of the predicted damage number seems to be, relatively close to 0.25. In Table 4.10, the values of the first two wave trains of that test are 0.335 and 0.303. Different authors such De Vos *et al.* (2012) and Fazeres-Ferradosa (2018), also obtained static protections for damage numbers above 0.25. These limits are further discussed in Fazeres-Ferradosa *et al.* (2018) and alternative ways to quantify the S_{3D}, by means of the DTM's, is discussed in Fazeres-Ferradosa *et al.* (2019).

The same occurs for failure, as occurred in Test 1b, when the protection failed when the $S_{3D,predicted}$ pointed out for a dynamic behaviour. Using the S_{3D} as a criteria to define the failure of a protection, protections should fail for values of $S_{3D}>1$ (see Fazeres-Ferradosa (2018) for a discussion of this topic). Other authors also registered failure in protections for S_{3D} values lower than 1. However, is recognizable that those cases did not presented such lower levels of S_{3D} - in their case $S_{3D,measured}$, in case of this dissertation $S_{3D,predicted}$. Another aspect that this dissertation differs from other authors, was the fact that their protections failed due to the erosion on the top layer. In these three tests performed, no significant erosion on the top layer was significant. Instead, the protection on the second test failed due to edge scour.

As for the Test 2, the protection was classified as dynamic, as shown by the values of the predicted damage number for that test. Despite that, the amount of non-significant damage on the armour layer, due to the small movement of stones detected, probably will not be enough for $S_{3D,measured}$ to be close to the $S_{3D,predicted}$. However, that statement can only be proved by the effective calculation of the damage parameter. It is believed that the work and measures of this dissertation compose a base for future works and researches, namely for future calculations of damage for tests made in the same facilities. Moreover, despite the limited conclusions that can be derived from the present tests, this experiments were important to calibrate the setup and testing conditions for the upcoming research, namely the ORACLE project already being developed (see Fazeres-Ferradosa *et al.* (2019)).

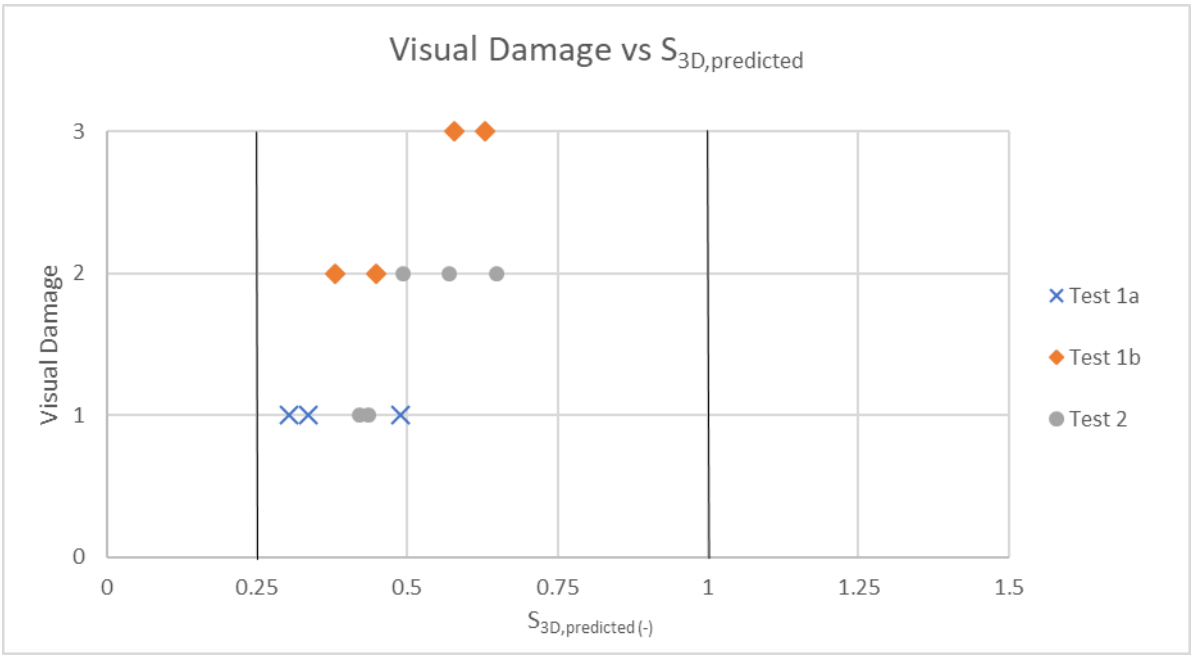

Figure 4.38 - $S_{3D,predicted}$ vs Visual Damage

4.4. LONG-TERM SCOUR PROTECTION DESIGN BASED ON THE S_{3D} PARAMETER

The design of dynamic scour protections using the limits of an acceptable damage number as design criteria led to an optimization of the mean stone diameter compared to the design using the *stab* parameter or even a better optimization if we consider the static design approach. This optimization occurred since the $S_{3D,predicted}$ formula directly relates the damage number with the D_{n50}, thus being suitable to obtain the minimum stone for a dynamic behaviour of the protection (Fazeres-Ferradosa, 2018). In order to obtain a dynamic protection De Vos *et al.* (2012) suggests an acceptable damage number of S_{3D}=1.0. Despite that, De Vos *et al.* (2012) also obtained dynamic profiles for values of S_{3D}=1.25. Also in Fazeres-Ferradosa (2018) (with protections designed based on the S_{3D}), failed protections were obtained for damage numbers lower than 1 and static protections were obtained for damage numbers higher than 0.25. These data demonstrate that the proposed equation may still have some gaps, namely in considering all the variables that may influence the behaviour of the protection, such the amplification factor.

Taking these notes into consideration, during this dissertation different designs were made, which were divided in 5 major groups:

- first set of target conditions (Target Conditions I);
- second set of target conditions: adjusted target conditions after reflections analysis (Target Conditions II);
- third set of target conditions: increase of the hydrodynamic conditions relatively to the Target Conditions II - $U_{c,prototype}$ from 0.5 to 1 m/s (Target Conditions III);
- for the average conditions of each test;
- for the specific conditions of each wave train of all tests;

For the first four points, the design was made using prototype values and, not only for the selected stone diameter studied, but also for a wide range of diameters. The results of calculations for the first point determined the $D_{n50,prototype}$ value mentioned on section 3.5, as the protection diameter value for the initial target conditions. For the last point, the design was made using the model values obtained in each specific test. Note, that the values of the $S_{3D,predicted}$ used on Table 4.7, Table 4.8, Table 4.9, Table 4.10, Table 4.11 and Table 4.12 were the resulted of this extensive calculation. In this section, a graphic comparison between the dynamic design approach and the static design approach will be done for the Test 1a average conditions. For the remaining points and conditions, all the graphics and all the tables created and used for the design calculation will be available on the Appendix A.

4.4.1. DYNAMIC DESIGN DISCUSSION: TEST 1A.

For this test and its average conditions, presented on the Table 4.4, using the Eq. (2.68) to achieve a dynamic configuration (S_{3D}=1.0) for 3000 waves, same number of waves used by Fazeres-Ferradosa (2018), the diameter achieved was aproximatelly D_{n50}=0.132 m, that corresponds to a D_{50}=0.157 m. Observing Figure 4.39 and comparing that value with the D_{n50} used in the protection, 0.21 m, it was expected that the protection also had a dynamic behaviour, although being more conservative than the necessary. It is important to remind, that the values are in prototype values. Analysing Figure 4.39, it would be expected that the model would have a dynamic behaviour early on the beginning of test (1000 waves). However, at the end of 5000 waves and with absence of visual scour damage the protection was consider static. Despite not being a considerable sample, since for validation proposes the repetition of the test would be advisable, this could be another indicative that the equation sometimes fails to predict

the exact behaviour of a protection. If we take into account the 0.25 deviation observed by De Vos *et al.* (2012) for the limit boundary between dynamic and failed protections and apply that deviation for this case - and for the limit between static and dynamic protections - all three wave trains performed in this test would be under the 0.25 limit for static protections (just as observed after 5000 waves in the model).

Another aspect visible in the Figure 4.39, and also in all the dynamic design graphics in the Appendix A (Figure A.2, Figure A.7, Figure A.12, Figure A.17, Figure A.22, Figure A.27), is the fact that for Eq. (2.68), as the D_{n50} increases, the number of waves used in the equation tends to lose influence and the curves tend for the same value of damage number (never reaching a S_{3D}=0).

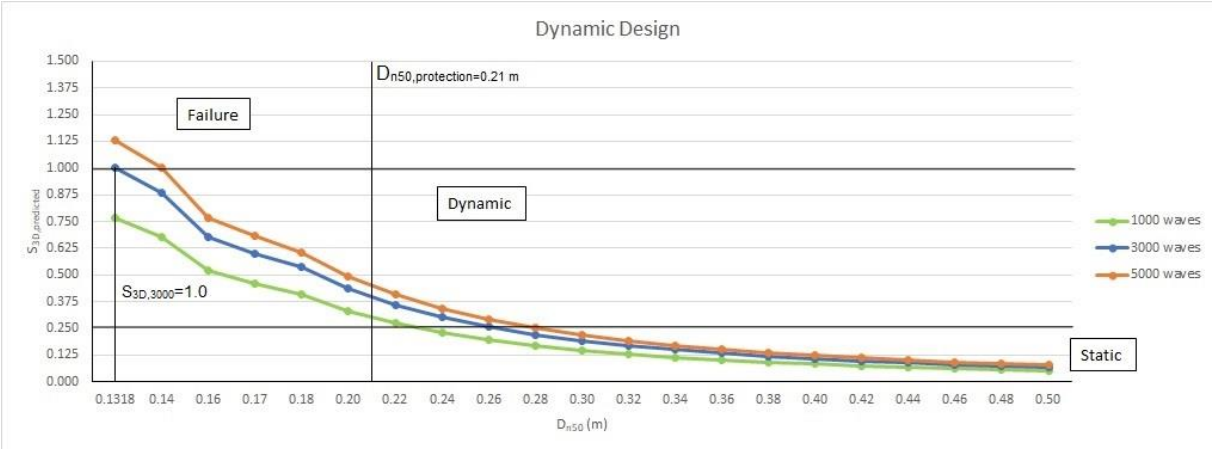

Figure 4.39 - Dynamic Design for the Test 1a.

Now comparing the dynamic design with the static design. The dynamic design was introduced as an optimization in the design of protections, since static design tends to oversize the value of the mean diameter of the protection stones. In order to confirm this, static calculations were also performed for different values of $D_{n50,prototype}$ and for the prototype conditions, using the three most common amplification factors used in the literature as shown in Table 2.1 (instead of 2.2 to 2.5 it was used 2, for the sake of simplicity). As expected most of the calculations showed that the first diameter to fulfil the static design criteria used by Soulsby (1997) - $\tau_{crit}>\alpha\tau_{cw}$ – were higher for an α=4 (Figure 4.42) and higher for α=3 (Figure 4.41), than the D_{n50} determined for a S_{3D}=1.0 using Eq. (2.68). It can be seen that the S_{3D}=1 for 3000 waves leads to larger values of D_{n50} than the static design for an amplification factor of 2 (Figure 4.40). As mentioned in Fazeres-Ferradosa (2018), normally the amplification factor used is α=4. But the author also mentioned, and as observed in Eq. (2.68), that the static approach proposed by De Vos (2008) does not take into account the amplification factor. Therefore a direct relation between the static approach and the amplification factor should be carefully interpreted. However, De Vos *et al.* (2012) reported that, for waves and currents, the combined alpha should be at least 3 or 4 - while for waves only might vary from 2.2 to 2.5 (De Vos *et al.*, 2011). Thus, the aforementioned comparison is directly valid. Therefore, is important to discuss and perform a deeper research about this aspect in order to understand which of the two situations is the most accurate designing dynamic protections. Other aspects that could be addressed are: which one fails to predict a dynamic behaviour more often; if the equation proposed by De Vos (2008) should be adapted in order to consider the amplification factor; if an new equation should be developed in order to understand and optimize even more the determination of a mean stone diameter capable of display a more effective dynamic behaviour.

Note that in Figure 4.41, the prototype value of the D_{n50} used in the model is slightly higher than the D_{n50} calculated using the static design. According to this design with an α=3, the protection tested should behave as a static protection. In fact after 5000 waves, the protection was considered static. So this could be another indicator of some gaps that the Eq. (2.68) maybe fails to cover.

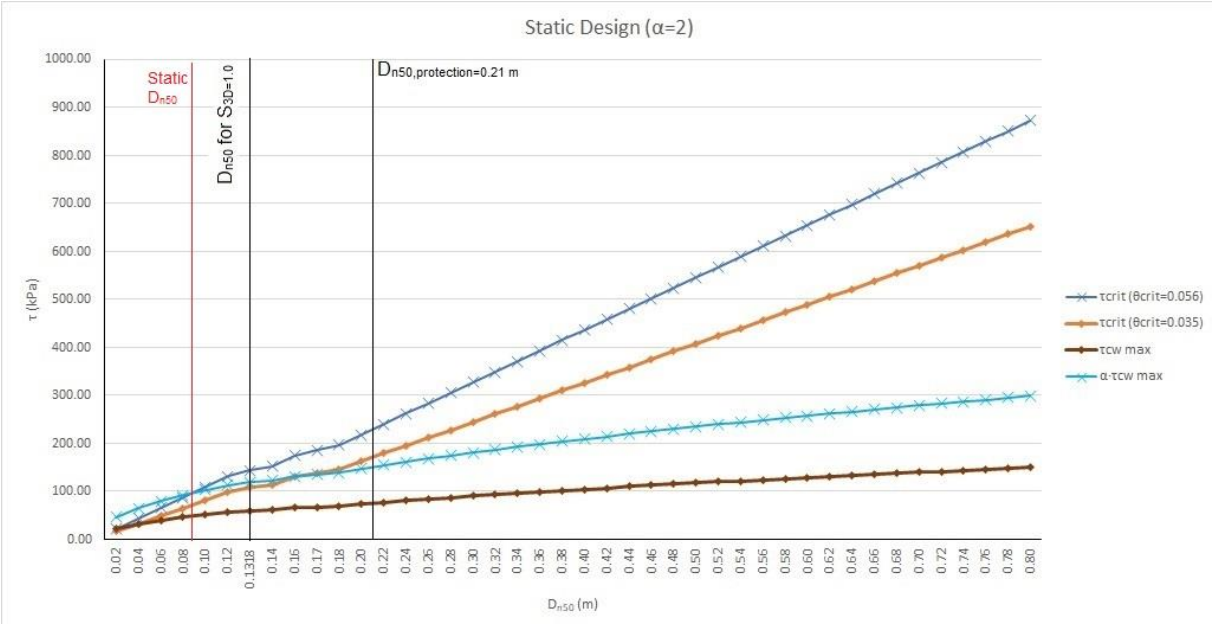

Figure 4.40 - Static Design for an amplification factor (α) equals to 2 (Test 1a – prototype values).

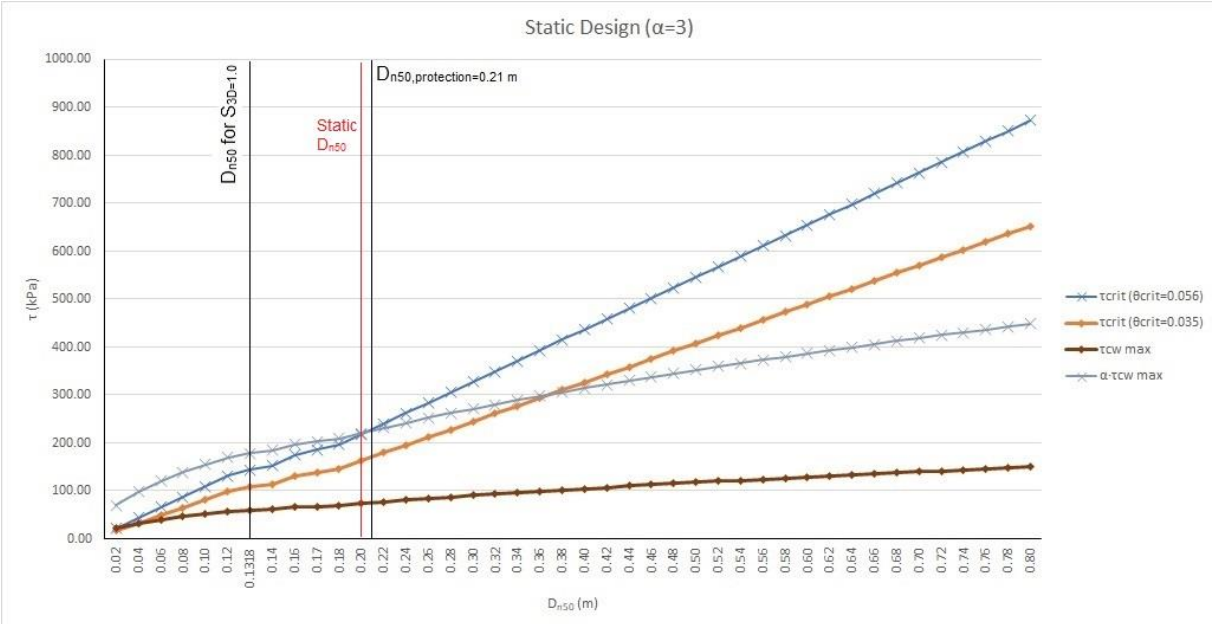

Figure 4.41 - Static Design for an amplification factor (α) equals to 3 (Test 1a – prototype values).

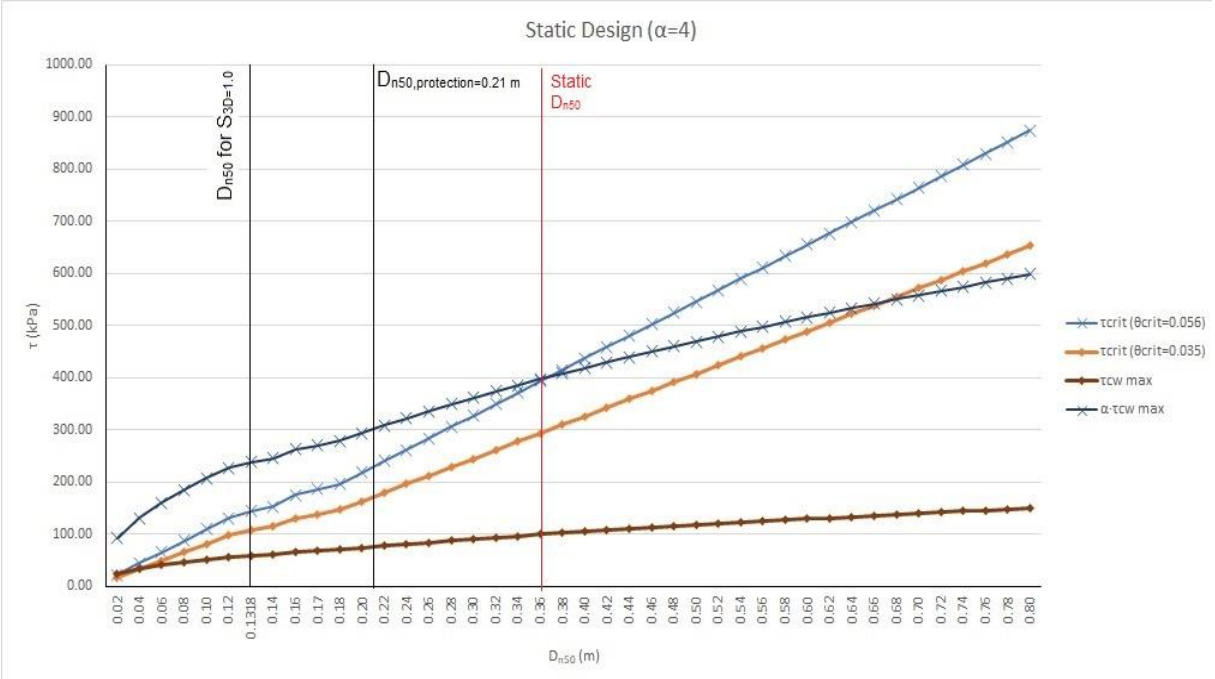

Figure 4.42 - Static Design for an amplification factor (α) equals to 4 (Test 1a – prototype values).

4.5. DAMAGE NUMBER DISCUSSION BASED ON BATHYMETRY MEASUREMENTS

Although the visual analysis of damage and the comparison with predicted measurements of damage is an important aspect that enables a better perception of the protection's behaviour, it is crucial to have an actual damage number derived from the bathymetric measurements, since that is the most accurate assessment of the erosion occurring on the armour layer. Throughout the present work, it was not possible to address this aspect with the desired detail. However, as an example, a simple and summarized approach was performed to one of the tests in order to provide a small prospective for the research that follows the present work.

The damage number obtained from the bathymetry of the physical model was calculated according to the overlapping circles as suggested in Fazeres-Ferradosa *et al.* (2019) (see section 2.4.3.2.). The methodology is not hereby described in detail, since it is still an ongoing research work of the NEMAR research group and presently under review. Due to time constraints, the calculation of the S_{3D} was only possible for the 9000 wave train of the Test 2.

The mesh used for the S_{3D} analysis had a grid resolution of 3 mm and was analyzed with an arrangement of overlapping circles, where the overlapping area of each circle is 50%. Covering the total area of the protection, the mesh was composed of 4170 circles, each one with an area of 8.98×10^{-5} m^2 (Figure 4.43). The grid ratio, *i.e.* the ratio between an equivalent square shaped stone nominal area and the sub-area was 0.2, which exceeds the range of De Vos *et al.* (2012) and Fazeres-Ferradosa (2018). The effect of the grid ratio was not analyzed under the present work. However, it is important to note that this has an effect on the calculation of the damage number. Nevertheless, the proper value of the grid ratio is a topic that requires further research. Here the sub-area is slightly higher than the reference value of $4D_{n50}^2$, formerly used to define the visual failure. Nevertheless, the grid ratio used already enables a good perception on the damage magnitude occurring in the protection.

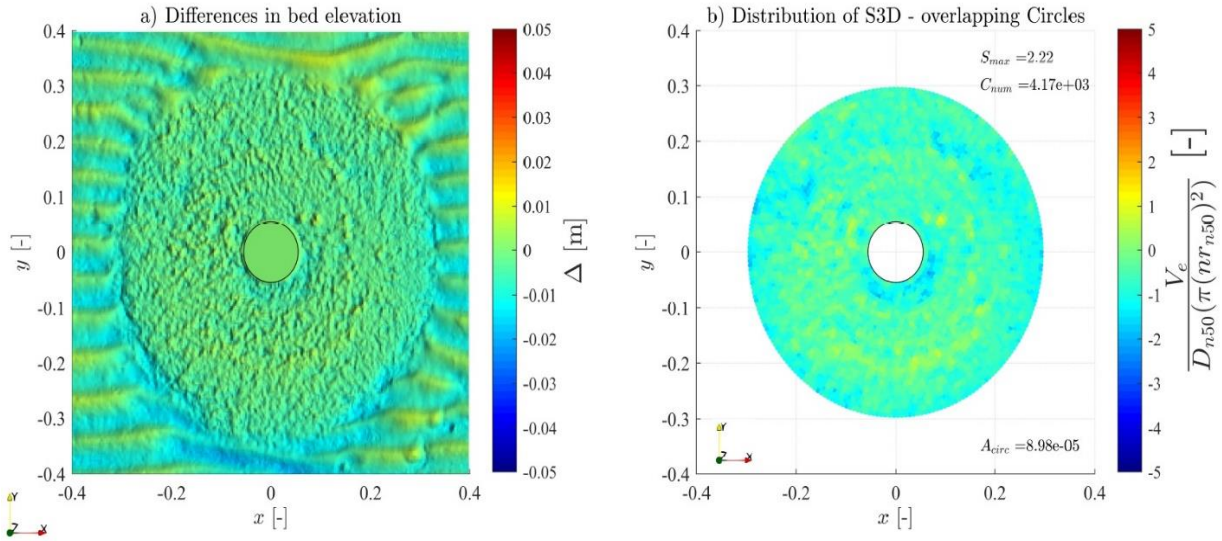

Figure 4.43 - DTM and S_{3D} analysis of the scour protection for the 9000 wave train (Test 2).

With this method, the maximum S_{3D} in the protection was of 2.2. As the small areas at dark blue, surrounding the upstream side of the pile and at some zones on the downstream side of the protection, were the zones with higher values of S_{3D}. Note that negative values on the S_{3D} scale (Figure 4.43) correspond to eroded areas, as for positive values correspond to areas with accretion. Considering the stone movements occurred in the protection, as shown in Figure 4.35, only the identified red circle 4 seems to be in correspondence with the scour pattern on Figure 4.43. However, the stone movement observed in that area did not seem as severe as Figure 4.43 shows. The other zones identified in red circles, in Figure 4.35, are in places were the protection seems to have both minor erosion and accretion. This is in agreement with the visual damage observation made of the protection, since no major stone movements were detected.

The other eroded zones identified in Figure 4.43, were completely impossible to observe at naked eye in the visual damage assessment of the protection. This is an indication that this method allows a detailed observation and analysis of the scour patterns in the protection, even when the armour layer seems to have non-significant damage. It is important to note that for this particular case, although being evident that there are movements at the protection, these movements seem to be within the transition between static and dynamic stability. Somehow in the potential transition zone described by Fazeres-Ferradosa *et al.* (2018). This indicates that in future scour tests seeking for more dynamic configurations, with the same setup, a reduction in the D_{50} could be considered. Comparing now the S_{3D} with the calculated $S_{3D,predicted}$ for this wave train (Table 4.13), it is obvious that the difference between numbers is significative. However, it is evident that such comparison may not be entirely valid, mainly because the sub-areas arrangement is completely different. The method used here tends to capture much larger damage numbers than the one presented by De Vos (2008), which averages the eroded volumes over much larger areas. Moreover the predicting equation was not developed for the overlapping sub-areas. Therefore, a new discussion on alternative predicting equations should be the focus of further research. Regarding this aspect, it is also not clear that the maximum S_{3D} is the most adequate value to be analysed. In fact the new method also enables the statistical analysis of a larger sample of $S_{3D,sub}$ values, thus allowing for other failure definitions.

Table 4.13 - Damage number comparison.

9000 waves (Test 2)	
$S_{3D,measured}$	$S_{3D,predicted}$
2.200	0.648

More significative is the fact that, as stated in section 4.3.3, the amount of non-significant damage in the armour layer, indicated that the S_{3D} would be smaller than the $S_{3D,measured}$, as opposed to the verified. This leads to the idea that this method is in fact way too detailed, allowing us to determine and predict possible zones of failure that otherwise were undetectable or underestimated.

Regarding the classification of the protection, taking into account the S_{3D} herein calculated, since this protection has an $S_{3D}>1$. The protection should be considered as failed, even without showing a significant dynamic behaviour. As mentioned in Fazeres-Ferradosa *et al.* (2019), the S_{3D} gives us an indication of the height decrease on the scour protection over a distance equal to $D_{n50.}$ So, the S_{3D} =2.2 represents the decrease of around two stones in the armour layer sub-area. According to den Boon *et al.* (2004), failure is reached when the area of exposed filter exceeds $4D_{n50}^2$. By De Schoesitter *et al.* (2014), failure depends on the armour layer thickness. So the limit of failure $S_{3D}=1$ proposed by De Vos *et al.* (2012), applied to protections with different values of the armour layer thickness (represented in D_{n50}), could be misrepresentative and questionable. Again, considering the S_{3D} =2.2, and its meaning, in the entire protection the filter has not been exposed – as confirmed visually. So, the question that needs to be asked is: "Should not the S_{3D} failure limit depend on the protection specifications, mainly on the armour layer thickness?" The analysis of this particular wave train, considering the results based on the concept described by Fazeres-Ferradosa *et al.* (2019), indicate that further discussion and review should be done, regarding the specific limits and criteria of failure based on the damage number of the protection, particularly when the sub-areas arrangement changes. Although not analyzing all tests, the present section also provides a small insight on the research presently being conducted towards new methodologies for damage assessment.

5
CONCLUSIONS AND FUTURE WORKS

The present work aimed at the analysis of long-term damage of Offshore Wind Turbine foundations. An adaption to the SHRHA's flume, in order to install a new wave paddle, and a laboratorial work regarding dynamic scour protections for long-term sea states was also performed. A small set of scour tests was presented based on the new setup. This set contributed for further research on scour and scour protections under waves and current combined.

The works and adaptations made in order to install the new wave paddle were successfully accomplished, enabling the upgrade of the flume conditions. As a result a new installation was obtained, which places the Hydraulics Laboratory in the small set of facilities that a allow for a proper simulation of scour phenomena in offshore maritime conditions. In addition the present setup also enables the testing of other maritime and hydraulic structures, typically subjected to the aforementioned hydraulic conditions. The present case study enabled a maximum geometric scale, with Froude similitude, of 1:50. However, other scales can be used, particularly when scour phenomena is being addressed without protections, as the blockage and wall effects tend to be slightly smaller.

With minor adjustments the experimental setup can still be improvement. At the current stage, and as described extensively in Chapter 3 , the preliminary tests and the reflection analysis enabled to conclude that the following aspects should be the aim of further improvement:

- Dissipation beach – new configurations should be tested to ensure that the reflection of 15% is reduced. Although 15% may be already an acceptable limit, it is highly recommended that this value is reduced (see Frostick *et al.* (2011));
- Extreme range of sea-states – throughout the preliminary testing it was noted that the wave paddle had a tendency to reach its rail limit, for large periods and wave heights. Further testing is required for a proper comparison between the equipment's theoretical limit and its practical limit within this particular flume.
- By-pass system – testing alternative by-pass solutions, eventually with a more definitive configuration and more endurable material is also advisable for a long-term lifecycle of the installation.

Other fundamental aspects should also be addressed in order to improve the testing conditions. The repair of the one of the flowmeters in the supply system, to enable an accurate measurement of the inlet flow. Correction of the flume's leaks in the glass-windows zone and at the bottom of the sediment box is also important to ensure the still-water-level that is essential for an accurate use of the active-absorption system. Additionally, an acquisition of additional wave probes and an alternative to the ADV

system can be considered as next steps to develop the quality of the studies performed in this installation, both for offshore wind foundations and other maritime and coastal structures.

The work performed in Chapter 4 was not enough to obtain the intended dynamic configurations. Although, scour protections with minor movements were obtained, there was not the same scour rate as presented in other studies, *e.g.* De Vos *et al.* (2012), Whitehouse *et al.* (2014), Fazeres-Ferradosa *et al.* (2018). The main reason for this was the median stone size used at the protection, which due to the available material was already very large for the hydrodynamic conditions tested. It was concluded that following research should be focused on new tests with smaller stone sizes.

In one test, the protection seemed to be static, in the second test the protection failed and in the last attempt a dynamic profile was achieved for 9000 waves but with less movement than expected. These results should be carefully analysed, since further confirmation of this is required, namely through the method presented in section 4.5. An interesting aspect of the results, was the fact that the first scour protection seemed to be static but the long-duration (up to 9000 waves) actually produced damage. This provides an indication that long-term evolution of damage should, indeed, be studied with more detail, as no conclusions could yet be drawn on the potential failure caused by very large wave series, even when the scour protection is apparently static. Also, the second test performed for 8000 waves with an increment of hydrodynamic conditions, in a protection already submitted to 5000 waves with lower hydrodynamic conditions (first test), opened a possible research or debate regarding a gap in literature, where no records of tests with variable conditions, in terms of consecutive storms, seems exist. Chapter 4 also showed that the major scour did not occur for the first 1000 waves, which is not in agreement with the results and the discussion presented in De Schoesitter *et al.* (2014). More tests are required to address this aspect. It was also concluded that the overlapping sub-areas provides insight to damage occurrence even when damage is not detected visually. Moreover, it was concluded that this method provides damage numbers, which are not directly comparable to the former methodologies, *i.e.* De Vos *et al.* (2012). It was concluded that further discussion of the S_{3D} limits is required in addition to the work presented by Fazeres-Ferradosa *et al.* (2018) and Fazeres-Ferradosa *et al.* (2019), this discussion an the new methodology applied in section 4.5 opens the way for alternative predicting equations for damage.

Another positive aspect, was the fact that regarding the design of dynamic protection some limitations in the design formulas were also noticed as previously referred by other authors. In fact, some good ideas were left in this dissertation, namely an argument for a possible discussion, or a more extensive research, about the fact that the amplification factor present on literature (α=2), commonly used only for waves and for static designs proposes, provides lower values of the protection stone dimension than the one provided by the dynamic design using an S_{3D}=1 for currents and waves. This could lead to a discussion regarding a possible used of the the amplification factor (α=2) also for current and waves, creating a new possible dynamic design method. Chapter 4 also allowed to perceive that the overlapping sub-areas arrangement could be used with photogrammetric data. Note that former studies were performed with laser profiles.

Future works should primarily focus on improving the setup conditions, as pointed before. Then, it is recommended that a more extensive set of tests is addressed, namely with smaller median stone sizes, in order to achieve “more dynamic configurations”. These tests, should be start by a reproduction of the data set presented in De Vos (2008). The application of the methodology presented in section 4.5 to the remaining tests should be carried and compared with former assessment methodologies. Finally, the study of other aspects such as the filter influence (sand or geotextile), the influence of the armour layer thickness, or the study of the protection behaviour when subjected to a more realistic representation of a storm, with sequential variations of the wave height and of the hydrodynamic conditions, remain as interesting and crucial topics for a more detailed knowledge on dynamic scour protections.

REFERENCES

Agisoft, L. L. C. (2018). "Agisoft PhotoScan User Manual: Professional Edition (Version 1.4)."

Airy, G. B. (1841). "Tides and Waves." Encyclopaedia Metropolitana.

Ancona, D. and J. McVeigh (2001). "Wind turbine-materials and manufacturing fact sheet." Princeton Energy Resources, LLC **19**.

Baker, C. J. (1979). "The laminar horseshoe vortex." Journal of fluid mechanics **95**(2): 347-367.

Bento, A. M., L. Couto, J. P. Pêgo and T. Viseu (2018). "Advanced characterization techniques of the scour hole around a bridge pier model." E3S Web of Conferences, EDP Science **40**.

Bhattacharya, S. (2014). "Challenges in Design of Foundations for Offshore Wind Turbines." Engineering & Technology Reference.

Branch, P. S. S. W. M. (2000). Riprap Design and Construction Guide, BC Ministry of Environment, Lands and Parks.

Breusers, H. N. C. and A. J. Raudkivi (1991). Scouring: Hydraulic structure design manual series - IAHR Design Manual. Rotterdam, Balkema, A.

Brkić, D. and P. Praks (2018). "Unified friction formulation from laminar to fully rough turbulent flow." Applied Sciences **8**(11): 2036.

Bruserud, K. and S. Haver (2019). "Waves and associated currents–experiences from 5 years metocean measurements in the northern North Sea." Marine Structures **63**: 429-443.

Bruserud, K., S. Haver and D. Myrhaug (2018). "Joint description of waves and currents applied in a simplified load case." Marine Structures **58**: 416-433.

Buffington, J. M. and D. R. Montgomery (1997). "A systematic analysis of eight decades of incipient motion studies, with special reference to gravel-bedded rivers." Water Resources Research **33**(8): 1993-2029.

Chopra, A. K. (2017). Dynamics of structures: theory and applications to earthquake engineering, Pearson Prentice Hall.

CIRIA, CUR and CETMEF (2007). The Rock Manual: The use of rock in hydraulic engineering. London, CIRIA.

Collins, C. (2017). Development and application of a computational model for scour around offshore wind turbine foundations PhD thesis, University of Hull.

De Schoesitter, P., S. Audenaert, L. Baelus, A. Bolle, A. Brown, L. das Neves, T. Fazeres-Ferradosa, P. Haerens, F. Taveira-Pinto and P. Troch (2014). "Feasibility of a dynamically stable rock armour layer scour protection for offshore wind farms." ASME 2014 33rd International Conference on Ocean, Offshore and Artic Engineering, American Society of Mechanical Engineers: V003T010A026-V003T010A026.

De Vos, L. (2008). Optimisation of Scour Protection Design for Monopiles and Quantification of Waver Run-Up PhD thesis, Ghent University.

De Vos, L., J. De Rouck, P. Troch and P. Frigaard (2011). "Empirical design of scour protections around monopile foundations: Part 1: Static approach." Coastal Engineering **58**(6): 540-553.

De Vos, L., J. De Rouck, P. Troch and P. Frigaard (2012). "Empirical design of scour protections around monopile foundations. Part 2: Dynamic approach." Coastal Engineering **60**: 286-298.

den Boon, J. H., J. Sutherland, R. J. S. Whitehouse, R. L. Soulsby, C. J. M. Stam, K. Verhoeven, M. Høgedal and T. Hald (2004). "Scour behaviour and scour protection for monopile foundations of offshore wind turbines." Proceedings of the European Wind Energy Conference & Exhibition **14**.

Dixen, M., F. Hatipoglu, B. M. Sumer and J. Fredsøe (2008). "Wave boundary layer over a stone-covered bed." Coastal Engineering **55**(1): 1-20.

E-Connection, V. W. S. D.K. and G. L. W. D. (2002-2004). OPTI-PILE, Fifth Research and Technological Development Framework Programme.

Fazeres-Ferradosa, T. (2018). Reliability analysis applied to the optimization of dynamic scour protections for offshore windfarm foundations PhD Thesis, University of Porto.

Fazeres-Ferradosa, T., F. Taveira-Pinto, M. T. Reis and L. das Neves (2018). "Physical modelling of dynamic scour protections: analysis of the damage number." Proceedings of the Institution of Civil Engineers - Maritime Engineering **171**(1): 11-24.

Fazeres-Ferradosa, T., F. Taveira-Pinto, P. Rosa-Santos and J. Chambel (2019). "Reliability Analysis of Offshore Scour Protections – Review of scientific and technical challenges." Proceedings of the Institution of Civil Engineers - Maritime Engineering: 1-49.

Fenton, J. D. (1988). "The numerical solution of steady water wave problems." Computers & Geosciences **14**(3): 357-368.

Fenton, J. D. (1999). Numerical methods for nonlinear waves. Advances in coastal and ocean engineering, World Scientific**:** 241-324.

Fernandes, M. M. (2006). Mecânica dos solos: conceitos e princípios fundamentais, FEUP edições.

Fraga, T. (2017). Estudo de Metodologias para Controlo das Reflexões em Laboratório.

Fredsøe, J. and R. Deigaard (1992). "Mechanics of coastal sediment transport, Adv. Ser." Ocean Engineering **3**: 369.

Frostick, L. E., S. J. McLelland and T. G. Mercer (2011). Users guide to physical modelling and experimentation: Experience of the HYDRALAB network, CRC Press.

Gee, G. W. and D. Or (2002). "2.4 Particle-size analysis." Methods of soil analysis **Part 4**(598): 255-293.

Harris, J. M., R. J. S. Whitehouse and T. Benson (2010). "The time evolution of scour around offshore structures." Proceedings of the Institution of Civil Engineers: Maritime Engineering **163**(1): 3-17.

Holthuijsen, L. H. (2010). Waves in oceanic and coastal waters, Cambridge university press.

Kamphuis, J. W. (1975). "Friction factor under oscillatory waves." Journal of the Waterways, Harbors and Coastal Engineering Division **101**(2): 135-144.

LeBlond, P. H., S. M. Calisal and M. Isaacson (1982). Wave spectra in Canadian waters. Marine Environmental Data Services Branch - Department of Fisheries and Oceans, Citeseer.

Liu, Z. (1998). Sediment transport (1 ed.), Aalborg Universitetsforlag.

Loosveldt, N. and K. Vannieuwenhuyse (2012). Experimental validation of empirical design of a scour protection around monopiles under combined wave and current loading PhD thesis & MSc thesis, Ghent University.

Malarkey, J. and A. G. Davies (2012). "A simple procedure for calculating the mean and maximum bed stress under wave and current conditions for rough turbulent flow based on method." Computers & geosciences **43**: 101-107.

Matutano, C. (2013). Caracterización de los sistemas de protección basados en materiales naturales destinados al control de la socavación en obras marítimas presentes en instalaciones eólicas marinas PhD Thesis, Universidad Politécnica de Madrid

Matutano, C., V. Negro, J. S. Lopez-Gutierrez and M. D. Esteban (2013). "Scour prediction and scour protections in offshore wind farms." Renewable Energy **57**: 358-365.

Melville, B. W. and Y. Chiew (1999). "Time scale for local scour at bridge piers." Journal of Hydraulic Engineering **125**(1): 59-65.

Michell, J. H. (1893). "XLIV. The highest waves in water." The London, Edinburgh, and Dublin Philosophical Magazine and Journal of Science **36**(222): 430-437.

Miller, M. C., I. N. McCave and P. D. Komar (1977). "Threshold of sediment motion under unidirectional currents." Sedimentology **24**(4): 507-527.

Negro, V., J. S. Lopez-Gutierrez, M. D. Esteban and C. Matutano (2014). "Uncertainties in the design of support structures and foundations for offshore wind turbines." Renewable Energy **63**: 125-132.

Nielsen, A. W., X. Liu, B. M. Sumer and J. Fredsøe (2013). "Flow and bed shear stresses in scour protections around a pile in a current." Coastal Engineering **72**: 20-38.

Nielsen, P. (1992). Coastal bottom boundary layers and sediment transport, World scientific.

Nixon. (2019). "Understanding ISO Sensitivity." 2019, from https://www.nikonusa.com/en/learn-and-explore/a/tips-and-techniques/understanding-iso-sensitivity.html.

Novais-Barbosa, J. (1985). Mecânica dos fluidos e Hidráulica Geral, Porto Editora.

ODOT (2014). Hydraulics Design Manual. O. D. o. T. H. Division. Oregon**:** 90.

Petersen, T. U., B. M. Sumer, J. Fredsøe, T. C. Raaijmakers and J. Schouten (2015). "Edge scour at scour protections around piles in the marine environment — Laboratory and field investigation." Coastal Engineering **106**: 42-72.

Quintela, A. C. (2005). Hidráulica. 9ª edição, Fundação Calouste Gulbenkian.

Raaijmakers, T. C., M. C. van Oeveren, D. Rudolph, V. Leenders and W. C. P. Sinjou (2010). Field Performance of Scour Protection Around Offshore Monopiles. Scour and Erosion - Proceedings of the Fifth International Conference on Scour and Erosion (ICSE-5). San Francisco, California, American Society of Civil Engineers (ASCE).

Ramos, P. X., A. M. Bento, R. Maia and J. P. Pêgo (2016). "Characterization of the scour cavity evolution around a complex bridge pier." Journal of Applied Water Engineering and Research **4**(2): 128-137.

Rosa-Santos, P. (2010). Análise da Interação de Navios com Dispositivos de Acostagem e Amarração. Estudo em Modelo Físico do Posto "A" do Terminal de Petroleiros do Porto de Leixões. PhD Thesis, University of Porto.

Saruwatari, A., Y. Yoneko and Y. Tajima (2014). "Effects of wave, tidal current and ocean current coexistence on the wave and current predictions in the tsugaru strait." Coastal Engineering Proceedings **1**(34): 42.

Schendel, A., N. Goseberg and T. Schlurmann (2014). "Experimental study on the performance of coarse grain materials as scour protection." Coastal Engineering Proceedings **1**(34): 58.

Schlichting, H. and E. A. Truckenbrodt (2013). Aerodynamik des Flugzeuges: Erster Band: Grundlagen aus der Strömungstechnik Aerodynamik des Tragflügels, Springer-Verlag.

Shields, A. (1936). Anwendung der Aehnlichkeitsmechanik und der Turbulenzforschung auf die Geschiebebewegung PhD Thesis, Technical University of Berlin.

Silva, R. C. A. F. (2010). Avaliação experimental e numérica de parâmetros associados a modelos de evolução da linha de costa PhD thesis, University of Porto.

Sørensen, S. P. H. and L. B. Ibsen (2013). "Assessment of foundation design for offshore monopiles unprotected against scour." Ocean Engineering **63**: 17-25.

Soulsby, R. L. (1997). Dynamics of marine sands, a manual for practical applications, Thomas Telford Publications.

Soulsby, R. L. and S. Clarke (2005). "Bed shear-stress under combined waves and currents on smooth and rough beds (TR 137)." HR Wallingford.

Sousa, T. D. S. (2013). Avaliação e Verificação dos Niveis de Segurança da Protecção de Fundações de Estruturas Offshore do tipo Monopilar MSc Thesis, University of Porto.

Sumer, B. M. (2002). The Mechanics of Scour in the Marine Environment, World Scientific.

Sumer, B. M., N. Christiansen and J. Fredsøe (1992). Time scale of scour around a vertical pile. The Second International Offshore and Polar Engineering Conference, International Society of Offshore and Polar Engineers.

Sumer, B. M., N. Christiansen and J. Fredsøe (1997). "The horseshoe vortex and vortex shedding around a vertical wall-mounted cylinder exposed to waves." Journal of Fluid Mechanics **332**: 41-70.

Sumer, B. M. and J. Fredsøe (2001). "Scour around Pile in Combined Waves and Current." Journal of Hydraulic Engineering **127**(5): 403-411.

Sumer, B. M., J. Fredsøe and N. Christiansen (1992). "Scour Around Vertical Pile in Waves." Journal of Waterway, Port, Coastal, and Ocean Engineering **118**(1): 15-31.

Sumer, B. M., R. J. S. Whitehouse and A. Tørum (2001). "Scour around coastal structures: A summary of recent research." Coastal Engineering **44**(2): 153-190.

Sumer, M. B. and J. Fredsøe (1997). Hydrodynamics around cylindrical structures, World Scientific.

Sutherland, J. and R. J. S. Whitehouse (1998). "Scale effects in the physical modelling of seabed scour." HR Wallingford.

Taveira-Pinto, F. (2011). Modelação Física (Trabalhos Marítimos 2). FEUP, Faculdade de Engenharia da Universidade do Porto.

Teixeira, L., P. Rosa-Santos, F. Taveira-Pinto and J. P. Ribeiro (2011). Estudo Experimental de um Novo Dispositivo de Aproveitamento da Energia das Ondas (Experimental Study of a New Wave Energy Converter). 7as Jornadas de Hidráulica, Recursos Hídricos e Ambiente FEUP, University of Porto.

Tran, T. T. and D. H. Kim (2015). "The platform pitching motion of floating offshore wind turbine: A preliminary unsteady aerodynamic analysis." Journal of Wind Engineering and Industrial Aerodynamics **142**: 65-81.

Tulsi, K. R. (2016). Three dimensional method for monitoring damage to dolos breakwaters PhD thesis, Stellenbosch University.

US Army Corps of Engineers (2012). Coastal Engineering Manual. USA, USACE - Army Publications.

Van Der Meer, J. W. (1990). Rock slopes and gravel beaches under wave attack PhD Thesis, TU Delft.

van der Temple, J. (2006). Design of support structures for offshore wind turbines PhD Thesis, TU Delft.

Vogel, F., S. Holm and O. Lingjærde (2001). Spectral Moments and Time Domain Representation of Photoacoustic Signals used for Detection of Crude Oil in Produced Water. Norway, Proc. Nordic Symp. on Physical Acoustics.

Webber, N. B. (1971). Fluid Mechanics for Civil Engineers. London, England, Chaspman and Hall.

Whitehouse, R. J. S. (1998). Scour at marine structures : a manual for practical applications. London, Thomas Telford.

Whitehouse, R. J. S., A. Brown, S. Audenaert, A. Bolle, P. de Schoesitter, P. Haerens, L. Baelus, P. Troch, L. Das Neves and T. Fazeres-Ferradosa (2014). Optimising scour protection stability at offshore foundations. Proceeding of 7th International Conference on Scour and Erosion, Perth.

Whitehouse, R. J. S., J. M. Harris, J. Sutherland and J. Rees (2011). "The nature of scour development and scour protection at offshore windfarm foundations." Marine Pollution Bulletin **62**(1): 73-88.

Whitehouse, R. J. S., J. Sutherland and J. M. Harris (2011). "Evaluating scour at marine gravity foundations." Proceedings of the Institution of Civil Engineers: Maritime Engineering **164**(4): 143-157.

Wiberg, P. L. and C. R. Sherwood (2008). "Calculating wave-generated bottom orbital velocities from surface-wave parameters." Computers & Geoscience **34**(10): 1243-1262.

WindEurope (2017). Wind Energy in Europe: Scenarios for 2030. Belgium, WindEurope**:** 32.

WindEurope (2018). Offshore Wind in Europe: Key trends and statistics 2018. Belgium, WindEurope**:** 40.

Zaaijer, M. B. (2002). "Tripod support structure-pre-design and natural frequency assessment for the 6 MW DOWEC." TU Delft, DOWEC **63**.

Zanke, U. C. E., T. W. Hsu, A. Roland, O. Link and R. Diab (2011). "Equilibrium scour depths around piles in noncohesive sediments under currents and waves." Coastal Engineering **58**(10): 986-991.

Zhang, J., I. Fowai and K. Sun (2016). "A glance at offshore wind turbine foundation structures." Brodogradnja: Teorija i praksa brodogradnje i pomorske tehnike **67**: 101-113.

Zhu, Q., B. C. van Prooijen, Z. B. Wang, Y. X. Ma and S. L. Yang (2016). "Bed shear stress estimation on an open intertidal flat using in situ measurements." Estuarine, Coastal and Shelf Science **182**: 190-201.

APPENDIX

APPENDIX: DESIGN TABLES

A.1: TARGET CONDITIONS I

Table A. 1 - Prototype and model inputs (Target Conditions I).

Prototype Target Conditions			
H_s (m)	T_p (s)	d (m)	U_c (m/s)
6	14	18	0.5
MATLAB:	U_m (m/s)	1.29	

Model Target Conditions			
H_s (m)	T_p (s)	d (m)	U_c (m/s)
0.12	1.98	0.36	0.071
MATLAB:	U_m (m/s)	0.182	

Scale (Froude)	
Scale λ_L:	0.020
Scale λ_T:	0.141
Scaçe λ_V:	0.141

Prototype (Other Parameters)				
ρ_w (kg/m^3):	1025	s	delta	g
ρ_s (kg/m^3):	2650	2.585	1.585	9.81
A (m):	2.874			

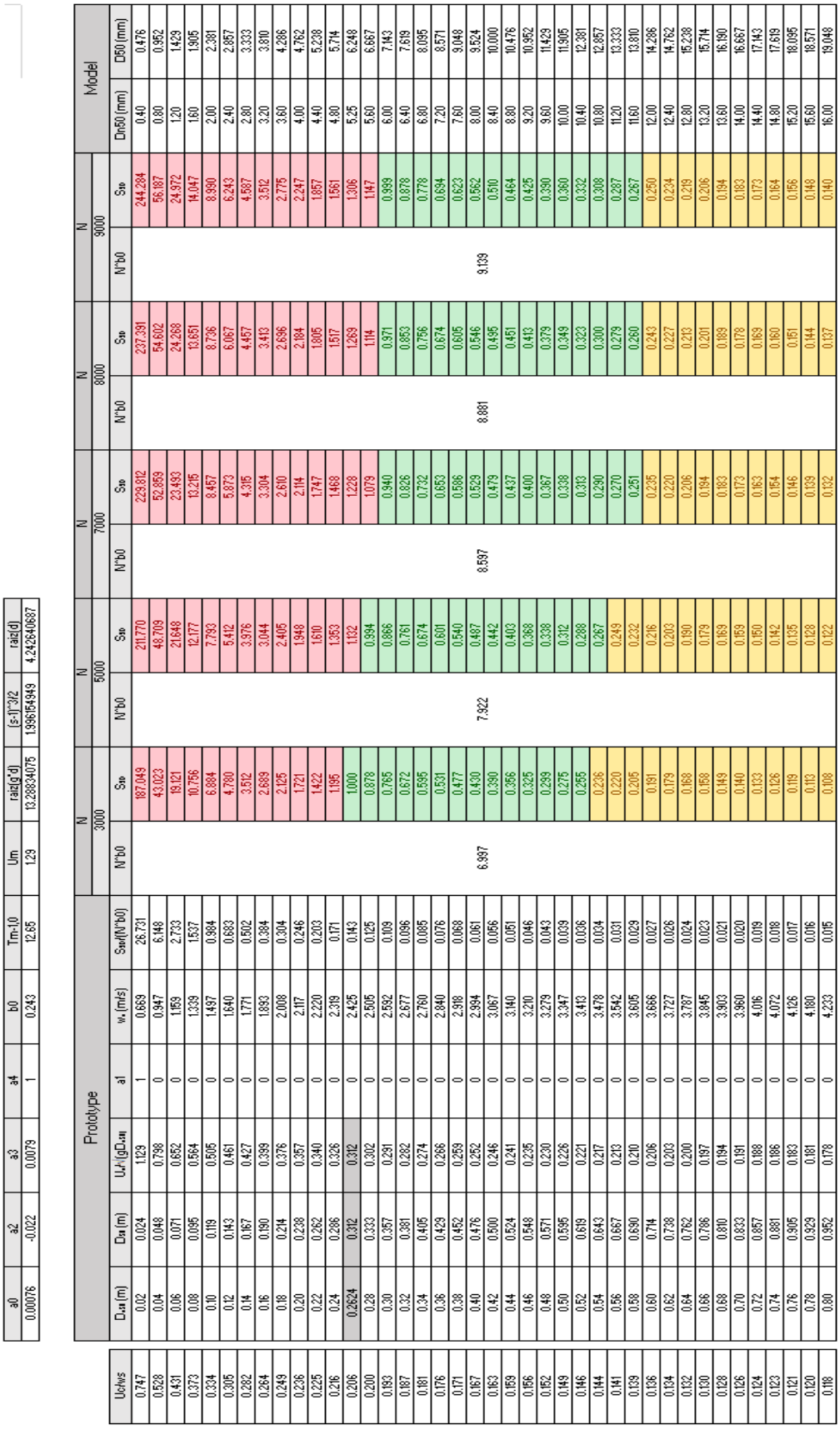

a0	a2	a3	a4	b0	Tm-1,0	Um	raiz(g*d)	(s-1)^3/2	raiz(d)
0,00076	-0,022	0,0079	1	0,243	12,65	1,29	13,28834075	1,996154943	4,242640687

Ucr/ws	Prototype						N		N		N		N		Model	
							3000		5000		7000		8000		9000	
	Dcat (m)	Dai (m)	Ui,rif/(gDcat)	ai	wt (m/s)	Sw0/(N^b0)	N^b0	Sw0	N^b0	Sw0	N^b0	Sw0	N^b0	Sw0	Dn50 (mm)	D50 (mm)
0,747	0,02	0,024	1,129	1	0,669	26,731		187,049		211,770		229,812		237,391	244,284	0,40	0,476
0,528	0,04	0,048	0,798	0	0,947	6,148		43,023		48,709		52,859		54,602	56,187	0,80	0,952
0,431	0,06	0,071	0,652	0	1,159	2,733		19,121		21,648		23,493		24,268	24,972	1,20	1,429
0,373	0,08	0,095	0,564	0	1,339	1,537		10,756		12,177		13,215		13,651	14,047	1,60	1,905
0,334	0,10	0,119	0,505	0	1,497	0,984		6,884		7,793		8,457		8,736	8,990	2,00	2,381
0,305	0,12	0,143	0,461	0	1,640	0,683		4,780		5,412		5,873		6,067	6,243	2,40	2,857
0,282	0,14	0,167	0,427	0	1,771	0,502		3,512		3,976		4,315		4,457	4,587	2,80	3,333
0,264	0,16	0,190	0,399	0	1,893	0,384		2,689		3,044		3,304		3,413	3,512	3,20	3,810
0,249	0,18	0,214	0,376	0	2,008	0,304		2,125		2,405		2,610		2,696	2,775	3,60	4,286
0,236	0,20	0,238	0,357	0	2,117	0,246		1,721		1,948		2,114		2,184	2,247	4,00	4,762
0,225	0,22	0,262	0,340	0	2,220	0,203		1,422		1,610		1,747		1,805	1,857	4,40	5,238
0,216	0,24	0,286	0,326	0	2,319	0,171		1,195		1,353		1,468		1,517	1,561	4,80	5,714
0,206	0,2624	0,312	0,312	0	2,425	0,143		1,000		1,132		1,228		1,269	1,306	5,25	6,248
0,200	0,28	0,333	0,302	0	2,505	0,125		0,878		0,994		1,079		1,114	1,147	5,60	6,667
0,193	0,30	0,357	0,291	0	2,592	0,109		0,765		0,866		0,940		0,971	0,999	6,00	7,143
0,187	0,32	0,381	0,282	0	2,677	0,096		0,672		0,761		0,826		0,853	0,878	6,40	7,619
0,181	0,34	0,405	0,274	0	2,760	0,085		0,595		0,674		0,732		0,756	0,778	6,80	8,095
0,176	0,36	0,429	0,266	0	2,840	0,076		0,531		0,601		0,653		0,674	0,694	7,20	8,571
0,171	0,38	0,452	0,259	0	2,918	0,068		0,477		0,540		0,586		0,605	0,623	7,60	9,048
0,167	0,40	0,476	0,252	0	2,994	0,061	6,997	0,430	7,322	0,487	8,597	0,529	8,881	0,546	0,562	8,00	9,524
0,163	0,42	0,500	0,246	0	3,067	0,056		0,390		0,442		0,479		0,495	0,510	8,40	10,000
0,159	0,44	0,524	0,241	0	3,140	0,051		0,356		0,403		0,437		0,451	0,464	8,80	10,476
0,156	0,46	0,548	0,235	0	3,210	0,046		0,325		0,368		0,400		0,413	0,425	9,20	10,952
0,152	0,48	0,571	0,230	0	3,279	0,043		0,299		0,338		0,367		0,379	0,390	9,60	11,429
0,149	0,50	0,595	0,226	0	3,347	0,039		0,275		0,312		0,338		0,349	0,360	10,00	11,905
0,146	0,52	0,619	0,221	0	3,413	0,036		0,255		0,288		0,313		0,323	0,332	10,40	12,381
0,144	0,54	0,643	0,217	0	3,478	0,034		0,236		0,267		0,290		0,300	0,308	10,80	12,857
0,141	0,56	0,667	0,213	0	3,542	0,031		0,220		0,249		0,270		0,279	0,287	11,20	13,333
0,139	0,58	0,690	0,210	0	3,605	0,029		0,205		0,232		0,251		0,260	0,267	11,60	13,810
0,136	0,60	0,714	0,206	0	3,666	0,027		0,191		0,216		0,235		0,243	0,250	12,00	14,286
0,134	0,62	0,738	0,203	0	3,727	0,026		0,179		0,203		0,220		0,227	0,234	12,40	14,762
0,132	0,64	0,762	0,200	0	3,787	0,024		0,168		0,190		0,206		0,213	0,219	12,80	15,238
0,130	0,66	0,786	0,197	0	3,845	0,023		0,158		0,179		0,194		0,201	0,206	13,20	15,714
0,128	0,68	0,810	0,194	0	3,903	0,021		0,149		0,169		0,183		0,189	0,194	13,60	16,190
0,126	0,70	0,833	0,191	0	3,960	0,020		0,140		0,159		0,173		0,178	0,183	14,00	16,667
0,124	0,72	0,857	0,188	0	4,016	0,019		0,133		0,150		0,163		0,169	0,173	14,40	17,143
0,123	0,74	0,881	0,186	0	4,072	0,018		0,126		0,142		0,154		0,160	0,164	14,80	17,619
0,121	0,76	0,905	0,183	0	4,126	0,017		0,119		0,135		0,146		0,151	0,156	15,20	18,095
0,120	0,78	0,929	0,181	0	4,180	0,016		0,113		0,128		0,139		0,144	0,148	15,60	18,571
0,118	0,80	0,952	0,178	0	4,233	0,015		0,108		0,122		0,132		0,137	0,140	16,00	19,048

Figure A.1 – Dynamic design calculation (Target Conditions I).

Table A.2 - Static design calculation (Target Conditions I - 1 of 3).

Prototype							
D_{n50} (m)	D50 (m)	τcrit (θcrit=0.056) (kPa)	τcrit (θcrit=0.035) (kPa)	τ_c (kPa)	f_c	ks (m)	$z0_c$
0.02	0.024	21.255	13.284	4.15	4.86E-03	0.060	1.98E-03
0.04	0.048	42.510	26.569	4.96	5.81E-03	0.119	3.97E-03
0.06	0.071	63.765	39.853	5.55	6.50E-03	0.179	5.95E-03
0.08	0.095	85.020	53.138	6.03	7.07E-03	0.238	7.94E-03
0.10	0.119	106.275	66.422	6.45	7.57E-03	0.298	9.92E-03
0.12	0.143	127.530	79.706	6.83	8.01E-03	0.357	1.19E-02
0.14	0.167	148.785	92.991	7.18	8.41E-03	0.417	1.39E-02
0.16	0.190	170.040	106.275	7.50	8.79E-03	0.476	1.59E-02
0.18	0.214	191.295	119.559	7.80	9.14E-03	0.536	1.79E-02
0.20	0.238	212.550	132.844	8.08	9.48E-03	0.595	1.98E-02
0.22	0.262	233.805	146.128	8.36	9.80E-03	0.655	2.18E-02
0.24	0.286	255.060	159.413	8.62	1.01E-02	0.714	2.38E-02
0.26	0.310	276.315	172.697	8.87	1.04E-02	0.774	2.58E-02
0.28	0.333	297.570	185.981	9.11	1.07E-02	0.833	2.78E-02
0.30	0.357	318.825	199.266	9.34	1.10E-02	0.893	2.98E-02
0.32	0.381	340.080	212.550	9.57	1.12E-02	0.952	3.17E-02
0.34	0.405	361.335	225.834	9.79	1.15E-02	1.012	3.37E-02
0.36	0.429	382.590	239.119	10.01	1.17E-02	1.071	3.57E-02
0.38	0.452	403.845	252.403	10.22	1.20E-02	1.131	3.77E-02
0.40	0.476	425.100	265.688	10.42	1.22E-02	1.190	3.97E-02
0.42	0.500	446.355	278.972	10.62	1.25E-02	1.250	4.17E-02
0.44	0.524	467.610	292.256	10.82	1.27E-02	1.310	4.37E-02
0.46	0.548	488.865	305.541	11.02	1.29E-02	1.369	4.56E-02
0.48	0.571	510.120	318.825	11.21	1.31E-02	1.429	4.76E-02
0.50	0.595	531.375	332.109	11.39	1.34E-02	1.488	4.96E-02
0.52	0.619	552.630	345.394	11.58	1.36E-02	1.548	5.16E-02
0.54	0.643	573.885	358.678	11.76	1.38E-02	1.607	5.36E-02
0.56	0.667	595.140	371.963	11.94	1.40E-02	1.667	5.56E-02
0.58	0.690	616.395	385.247	12.12	1.42E-02	1.726	5.75E-02
0.60	0.714	637.650	398.531	12.29	1.44E-02	1.786	5.95E-02
0.62	0.738	658.905	411.816	12.47	1.46E-02	1.845	6.15E-02
0.64	0.762	680.160	425.100	12.64	1.48E-02	1.905	6.35E-02
0.66	0.786	701.415	438.384	12.81	1.50E-02	1.964	6.55E-02
0.68	0.810	722.670	451.669	12.97	1.52E-02	2.024	6.75E-02
0.70	0.833	743.925	464.953	13.14	1.54E-02	2.083	6.94E-02
0.72	0.857	765.180	478.238	13.30	1.56E-02	2.143	7.14E-02
0.74	0.881	786.435	491.522	13.46	1.58E-02	2.202	7.34E-02
0.76	0.905	807.690	504.806	13.63	1.60E-02	2.262	7.54E-02
0.78	0.929	828.945	518.091	13.78	1.62E-02	2.321	7.74E-02
0.80	0.952	850.200	531.375	13.94	1.63E-02	2.381	7.94E-02

Table A.3 - Static design calculation (Target Conditions I - 2 of 3).

Prototype							
τ_w (kPa)	f_w	$z0_w$	τ_{cw_m} (kPa)	τ_{cw_max} (kPa)	α4	α2	α3
26.93	3.16E-02	1.98E-03	7.29	34.22			
38.61	4.53E-02	3.97E-03	9.00	47.61			
47.67	5.59E-02	5.95E-03	10.23	57.90			
55.37	6.49E-02	7.94E-03	11.23	66.60			
62.18	7.29E-02	9.92E-03	12.10	74.28			
68.36	8.02E-02	1.19E-02	12.87	81.24			
74.07	8.68E-02	1.39E-02	13.58	87.65			
79.39	9.31E-02	1.59E-02	14.24	93.63			
84.41	9.90E-02	1.79E-02	14.85	99.26			
89.16	1.05E-01	1.98E-02	15.43	104.59			
93.69	1.10E-01	2.18E-02	15.98	109.68			
98.03	1.15E-01	2.38E-02	16.51	114.54			
102.20	1.20E-01	2.58E-02	17.02	119.21			
106.21	1.25E-01	2.78E-02	17.51	123.72			
110.09	1.29E-01	2.98E-02	17.98	128.07			
113.85	1.33E-01	3.17E-02	18.44	132.29			
117.49	1.38E-01	3.37E-02	18.88	136.38			
121.04	1.42E-01	3.57E-02	19.32	140.36			
124.49	1.46E-01	3.77E-02	19.74	144.23			
127.86	1.50E-01	3.97E-02	20.15	148.01			
131.14	1.54E-01	4.17E-02	20.56	151.70	4.00	3.00	2.00
134.35	1.58E-01	4.37E-02	20.96	155.31			
137.49	1.61E-01	4.56E-02	21.34	158.84			
140.57	1.65E-01	4.76E-02	21.73	162.30			
143.59	1.68E-01	4.96E-02	22.10	165.69			
146.54	1.72E-01	5.16E-02	22.47	169.02			
149.45	1.75E-01	5.36E-02	22.84	172.28			
152.30	1.79E-01	5.56E-02	23.19	175.50			
155.11	1.82E-01	5.75E-02	23.55	178.65			
157.87	1.85E-01	5.95E-02	23.90	181.76			
160.58	1.88E-01	6.15E-02	24.24	184.82			
163.25	1.91E-01	6.35E-02	24.58	187.83			
165.89	1.95E-01	6.55E-02	24.92	190.80			
168.48	1.98E-01	6.75E-02	25.25	193.73			
171.04	2.01E-01	6.94E-02	25.58	196.62			
173.56	2.04E-01	7.14E-02	25.90	199.47			
176.06	2.06E-01	7.34E-02	26.23	202.28			
178.51	2.09E-01	7.54E-02	26.55	205.06			
180.94	2.12E-01	7.74E-02	26.86	207.80			
183.34	2.15E-01	7.94E-02	27.18	210.52			

Table A.4 - Static design calculation (Target Conditions I - 3 of 3).

Prototype							Model	
$\alpha 4 \cdot \tau_{cw\_max}$ (kPa)	$\alpha 3 \cdot \tau_{cw\_max}$ (kPa)	$\alpha 2 \cdot \tau_{cw\_max}$ (kPa)	Φ (◦)	θ_{max}	θ_{crit} (Shields)	θ_{crit} (De Vos)	Dn50 (mm)	D50 (mm)
136.88	102.66	68.44		0.090			0.40	0.476
190.44	142.83	95.22		0.063			0.80	0.952
231.61	173.70	115.80		0.051			1.20	1.429
266.39	199.79	133.20		0.044			1.60	1.905
297.11	222.83	148.55		0.039			2.00	2.381
324.94	243.71	162.47		0.036			2.40	2.857
350.60	262.95	175.30		0.033			2.80	3.333
374.53	280.89	187.26		0.031			3.20	3.810
397.04	297.78	198.52		0.029			3.60	4.286
418.38	313.78	209.19		0.028			4.00	4.762
438.71	329.03	219.35		0.026			4.40	5.238
458.17	343.62	229.08		0.025			4.80	5.714
476.86	357.64	238.43		0.024			5.20	6.190
494.88	371.16	247.44		0.023			5.60	6.667
512.28	384.21	256.14		0.022			6.00	7.143
529.15	396.86	264.57		0.022			6.40	7.619
545.51	409.13	272.76		0.021			6.80	8.095
561.43	421.07	280.71		0.021			7.20	8.571
576.92	432.69	288.46		0.020			7.60	9.048
592.04	444.03	296.02	0	0.019	0.056	0.035	8.00	9.524
606.80	455.10	303.40		0.019			8.40	10.000
621.23	465.92	310.61		0.019			8.80	10.476
635.35	476.51	317.68		0.018			9.20	10.952
649.19	486.89	324.59		0.018			9.60	11.429
662.75	497.07	331.38		0.017			10.00	11.905
676.07	507.05	338.03		0.017			10.40	12.381
689.14	516.85	344.57		0.017			10.80	12.857
701.99	526.49	350.99		0.017			11.20	13.333
714.62	535.96	357.31		0.016			11.60	13.810
727.05	545.29	363.52		0.016			12.00	14.286
739.29	554.46	369.64		0.016			12.40	14.762
751.34	563.50	375.67		0.015			12.80	15.238
763.22	572.41	381.61		0.015			13.20	15.714
774.93	581.20	387.46		0.015			13.60	16.190
786.48	589.86	393.24		0.015			14.00	16.667
797.88	598.41	398.94		0.015			14.40	17.143
809.13	606.85	404.57		0.014			14.80	17.619
820.24	615.18	410.12		0.014			15.20	18.095
831.22	623.41	415.61		0.014			15.60	18.571
842.06	631.55	421.03		0.014			16.00	19.048

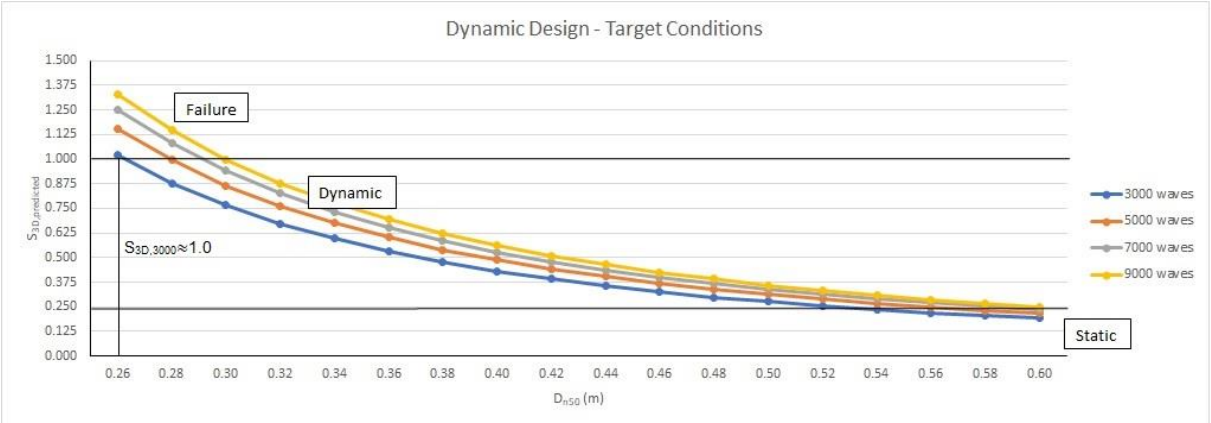

Figure A.2 - D_{n50} for S_{3D}=1.0 (Target Conditions I).

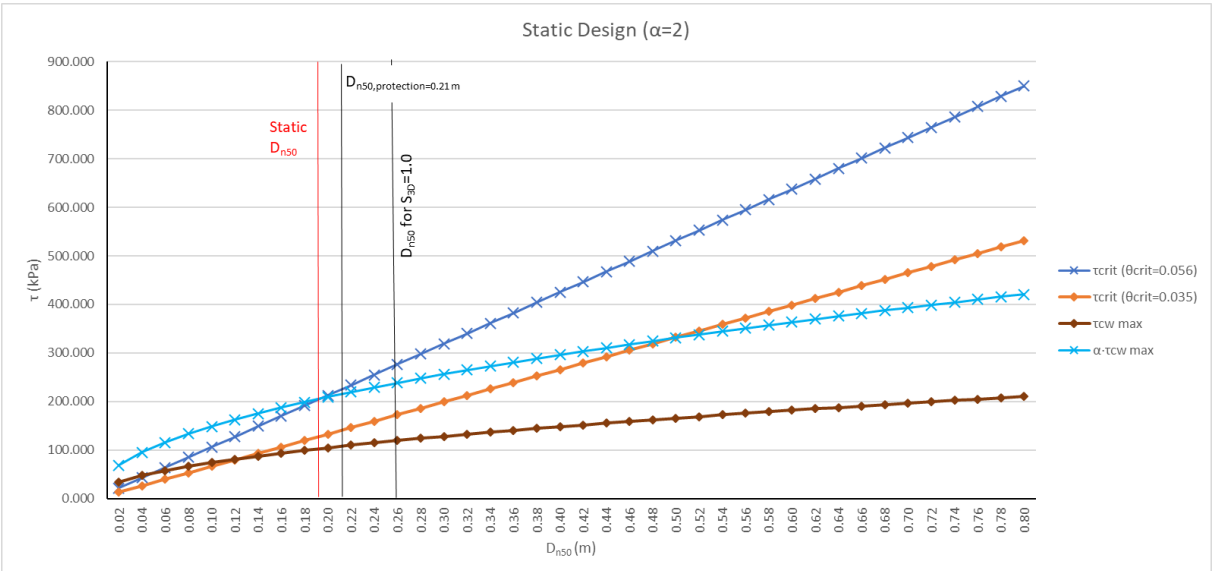

Figure A.3 - Static design α=2 (Target Conditions I).

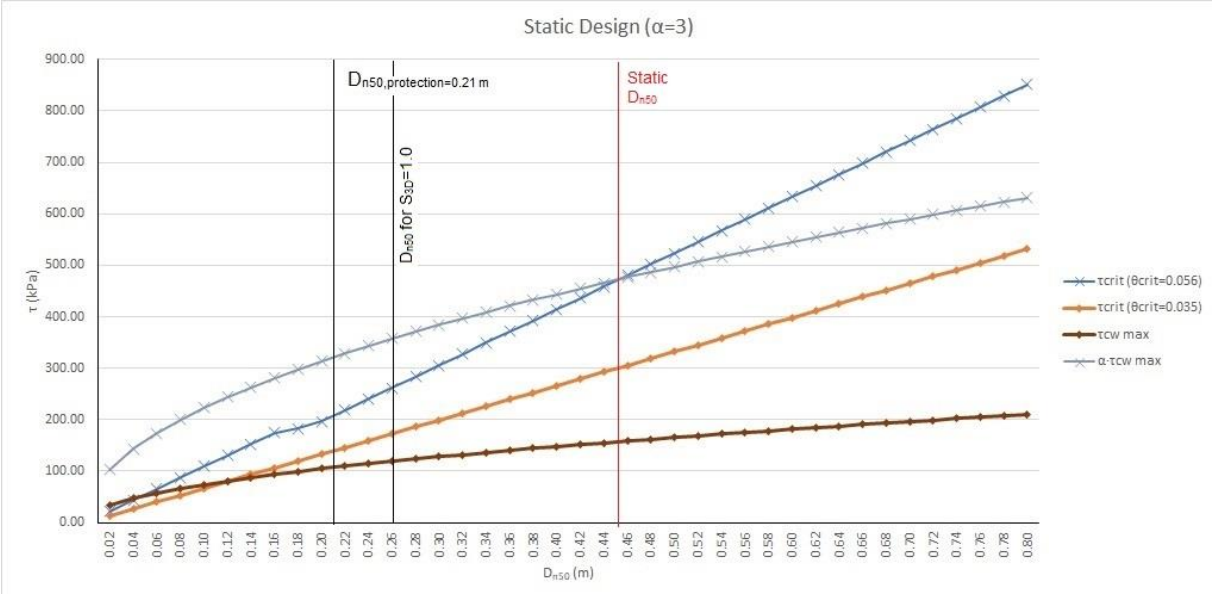

Figure A.4 - Static design α=3 (Target Conditions I).

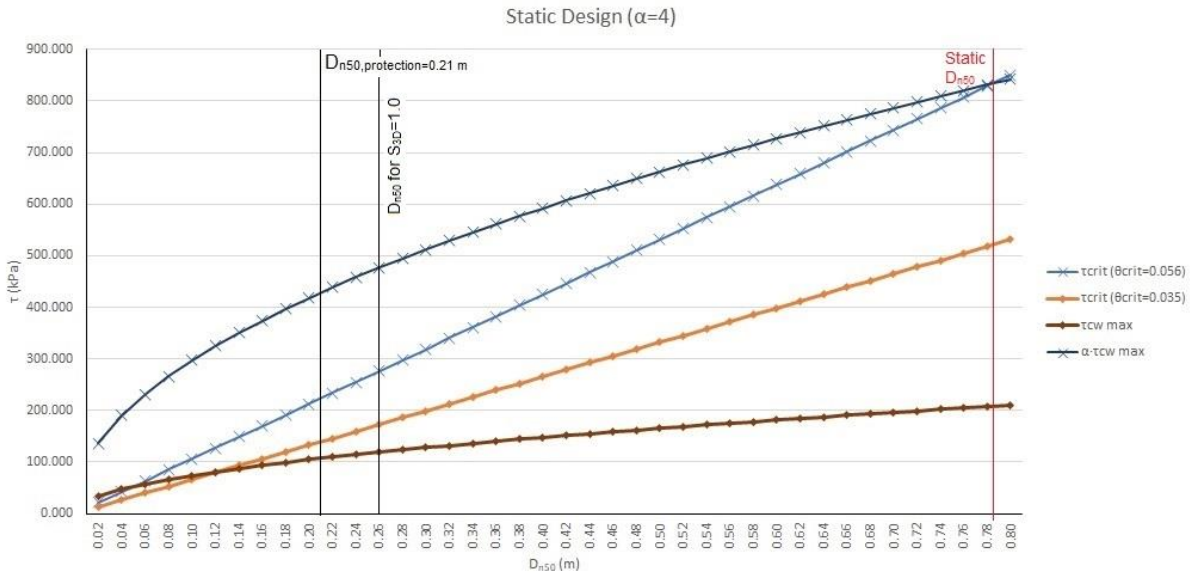

Figure A.5 - Static design α=4 (Target Conditions I).

A.2: TARGET CONDITIONS II

Table A.5 - Prototype and model inputs (Target Conditions II).

Prototype Target Conditions			
H_s (m)	T_p (s)	d (m)	U_c (m/s)
6	11	18	0.5
MATLAB:	U_m (m/s)	1.14	

Model Target Conditions			
H_s (m)	T_p (s)	d (m)	U_c (m/s)
0.12	1.56	0.36	0.07
MATLAB:	U_m (m/s)	0.16	

Escalas (Froude)	
Escala λ_L:	0.020
Escala λ_T:	0.141
Escala λ_V:	0.141

Prototype (Other Parameters)					
ρ_w (kg/m^3):	1025	s	delta	g	σ_U
ρ_s (kg/m^3):	2694	2.628	1.628	9.81	2.04
A (m):	1.996				

a0	a2	a3	a4	b0	Tm-10	Um	raio(g*d)	(s-1)^3/2	raio(d)
0.000076	-0.022	0.0079	1	0.243	9.94	1.14	13.28834075	2.077775911	4.242640687

Ucr/w	Prototype					N 3000		N 5000		N 7000		N 8000		N 9000		Model	
	Dca (m)	Dss (m)	Ucr/(gD.ca	a1	w. (m/s)	Sa∞/(N^b0)	N^b0	Sa∞	N^b0	Sa∞	N^b0	Sa∞	N^b0	Sa∞	N^b0	Sa∞	Dn50 (mm)	D50 (mm)
0.737	0.02	0.024	1.129	1	0.678	11.810		82.638		93.560		101.531		104.879		107.925	0.40	0.476
0.521	0.04	0.048	0.798	0	0.959	2.517		17.610		19.938		21.637		22.359		22.999	0.80	0.952
0.426	0.06	0.071	0.652	0	1.175	1.119		7.827		8.861		9.616		9.933		10.222	1.20	1.429
0.369	0.08	0.095	0.564	0	1.357	0.629		4.403		4.984		5.409		5.588		5.750	1.60	1.905
0.330	0.10	0.119	0.505	0	1.517	0.403		2.818		3.190		3.462		3.576		3.680	2.00	2.381
0.301	0.12	0.143	0.461	0	1.662	0.280		1.957		2.215		2.404		2.483		2.555	2.40	2.857
0.279	0.14	0.167	0.427	0	1.795	0.205		1.438		1.628		1.766		1.824		1.877	2.80	3.333
0.261	0.16	0.190	0.399	0	1.919	0.157		1.101		1.246		1.352		1.397		1.437	3.20	3.810
0.254	0.1679	0.200	0.390	0	1.966	0.143		1.000		1.132		1.228		1.269		1.305	3.36	3.998
0.246	0.18	0.214	0.376	0	2.035	0.124		0.870		0.985		1.068		1.104		1.136	3.60	4.286
0.233	0.20	0.238	0.357	0	2.145	0.101		0.704		0.798		0.865		0.894		0.920	4.00	4.762
0.222	0.22	0.262	0.340	0	2.250	0.083		0.582		0.659		0.715		0.739		0.760	4.40	5.238
0.213	0.24	0.286	0.326	0	2.350	0.070		0.489		0.554		0.601		0.621		0.639	4.80	5.714
0.204	0.26	0.310	0.313	0	2.446	0.060		0.417		0.472		0.512		0.529		0.544	5.20	6.190
0.197	0.28	0.333	0.302	0	2.538	0.051		0.359		0.407		0.442		0.456		0.469	5.60	6.667
0.190	0.30	0.357	0.291	0	2.627	0.045		0.313		0.354		0.385		0.397		0.409	6.00	7.143
0.184	0.32	0.381	0.282	0	2.713	0.039		0.275		0.312		0.338		0.349		0.359	6.40	7.619
0.179	0.34	0.405	0.274	0	2.797	0.035		0.244		0.276		0.299		0.309		0.318	6.80	8.095
0.174	0.36	0.429	0.266	0	2.878	0.031		0.217		0.246		0.267		0.276		0.284	7.20	8.571
0.169	0.38	0.452	0.259	0	2.957	0.028		0.195		0.221		0.240		0.248		0.255	7.60	9.048
0.165	0.40	0.476	0.252	0	3.034	0.025	6.997	0.176	7.922	0.199	8.597	0.216	8.881	0.224	9.139	0.230	8.00	9.524
0.161	0.42	0.500	0.246	0	3.109	0.023		0.160		0.181		0.196		0.203		0.209	8.40	10.000
0.157	0.44	0.524	0.241	0	3.182	0.021		0.146		0.165		0.179		0.185		0.190	8.80	10.476
0.154	0.46	0.548	0.235	0	3.253	0.019		0.133		0.151		0.164		0.169		0.174	9.20	10.952
0.150	0.48	0.571	0.230	0	3.323	0.017		0.122		0.138		0.150		0.155		0.160	9.60	11.429
0.147	0.50	0.595	0.226	0	3.392	0.016		0.113		0.128		0.138		0.143		0.147	10.00	11.905
0.145	0.52	0.619	0.221	0	3.459	0.015		0.104		0.118		0.128		0.132		0.136	10.40	12.381
0.142	0.54	0.643	0.217	0	3.525	0.014		0.097		0.109		0.119		0.123		0.126	10.80	12.857
0.139	0.56	0.667	0.213	0	3.590	0.013		0.090		0.102		0.110		0.114		0.117	11.20	13.333
0.137	0.58	0.690	0.210	0	3.653	0.012		0.084		0.095		0.103		0.106		0.109	11.60	13.810
0.135	0.6	0.714	0.206	0	3.716	0.011		0.078		0.089		0.096		0.099		0.102	12.00	14.286
0.132	0.62	0.738	0.203	0	3.777	0.010		0.073		0.083		0.090		0.093		0.096	12.40	14.762
0.130	0.64	0.762	0.200	0	3.837	0.010		0.069		0.078		0.085		0.087		0.090	12.80	15.238
0.128	0.66	0.786	0.197	0	3.897	0.009		0.065		0.073		0.079		0.082		0.084	13.20	15.714
0.126	0.68	0.810	0.194	0	3.956	0.009		0.061		0.069		0.075		0.077		0.080	13.60	16.190
0.125	0.70	0.833	0.191	0	4.013	0.008		0.058		0.065		0.071		0.073		0.075	14.00	16.667
0.123	0.72	0.857	0.188	0	4.070	0.008		0.054		0.062		0.067		0.069		0.071	14.40	17.143
0.121	0.74	0.881	0.186	0	4.126	0.007		0.051		0.058		0.063		0.065		0.067	14.80	17.619
0.120	0.76	0.905	0.183	0	4.182	0.007		0.049		0.055		0.060		0.062		0.064	15.20	18.095
0.118	0.78	0.929	0.181	0	4.236	0.007		0.046		0.052		0.057		0.059		0.060	15.60	18.571
0.117	0.8	0.952	0.178	0	4.290	0.006		0.044		0.050		0.054		0.056		0.057	16.00	19.048
										Model Armour Layer Sa∞ calculation/verification:								
0.226	0.21	0.252	0.347	0	2.208	0.090	6.997	0.627	7.922	0.710	8.597	0.770	8.881	0.796	9.139	0.819	4.24	5.047

Figure A.6 - Dynamic design calculation (Target Conditions II).

Table A.6 - Static design calculation (Target Conditions II - 1 of 3).

Prototype							
D67.5 (m)	Dn50 (m)	D50 (m)	τcrit (θcrit=0.056) (kPa)	τcrit (θcrit=0.035) (kPa)	τc (kPa)	fc	ks (m)
0.028	0.02	0.024	21.83	16.31	0.62	4.86E-03	0.060
0.057	0.04	0.048	43.66	32.61	0.74	5.81E-03	0.119
0.085	0.06	0.071	65.49	48.92	0.83	6.50E-03	0.179
0.114	0.08	0.095	87.32	65.22	0.91	7.07E-03	0.238
0.142	0.10	0.119	109.15	81.53	0.97	7.57E-03	0.298
0.171	0.12	0.143	130.98	97.84	1.03	8.01E-03	0.357
0.199	0.14	0.167	152.81	114.14	1.08	8.41E-03	0.417
0.228	0.16	0.190	174.64	130.45	1.13	8.79E-03	0.476
0.239	0.1679	0.200	183.27	136.89	1.14	8.93E-03	0.500
0.256	0.18	0.214	196.47	146.76	1.17	9.14E-03	0.536
0.285	0.20	0.238	218.31	163.06	1.21	9.48E-03	0.595
0.313	0.22	0.262	240.14	179.37	1.26	9.80E-03	0.655
0.341	0.24	0.286	261.97	195.67	1.29	1.01E-02	0.714
0.370	0.26	0.310	283.80	211.98	1.33	1.04E-02	0.774
0.398	0.28	0.333	305.63	228.29	1.37	1.07E-02	0.833
0.427	0.30	0.357	327.46	244.59	1.40	1.10E-02	0.893
0.455	0.32	0.381	349.29	260.90	1.44	1.12E-02	0.952
0.484	0.34	0.405	371.12	277.20	1.47	1.15E-02	1.012
0.512	0.36	0.429	392.95	293.51	1.50	1.17E-02	1.071
0.541	0.38	0.452	414.78	309.82	1.53	1.20E-02	1.131
0.569	0.40	0.476	436.61	326.12	1.57	1.22E-02	1.190
0.598	0.42	0.500	458.44	342.43	1.60	1.25E-02	1.250
0.626	0.44	0.524	480.27	358.74	1.63	1.27E-02	1.310
0.654	0.46	0.548	502.10	375.04	1.65	1.29E-02	1.369
0.683	0.48	0.571	523.93	391.35	1.68	1.31E-02	1.429
0.711	0.50	0.595	545.76	407.65	1.71	1.34E-02	1.488
0.740	0.52	0.619	567.59	423.96	1.74	1.36E-02	1.548
0.768	0.54	0.643	589.42	440.27	1.77	1.38E-02	1.607
0.797	0.56	0.667	611.25	456.57	1.79	1.40E-02	1.667
0.825	0.58	0.690	633.09	472.88	1.82	1.42E-02	1.726
0.854	0.60	0.714	654.92	489.18	1.85	1.44E-02	1.786
0.882	0.62	0.738	676.75	505.49	1.87	1.46E-02	1.845
0.911	0.64	0.762	698.58	521.80	1.90	1.48E-02	1.905
0.939	0.66	0.786	720.41	538.10	1.92	1.50E-02	1.964
0.967	0.68	0.810	742.24	554.41	1.95	1.52E-02	2.024
0.996	0.70	0.833	764.07	570.72	1.97	1.54E-02	2.083
1.024	0.72	0.857	785.90	587.02	2.00	1.56E-02	2.143
1.053	0.74	0.881	807.73	603.33	2.02	1.58E-02	2.202
1.081	0.76	0.905	829.56	619.63	2.05	1.60E-02	2.262
1.110	0.78	0.929	851.39	635.94	2.07	1.62E-02	2.321
1.138	0.80	0.952	873.22	652.25	2.09	1.63E-02	2.381

Table A.7 - Static design calculation (Target conditions - 2 of 3).

Prototype							
z0_c	τw (kPa)	fw	z0_w	τcw_m (kPa)	τcw_max (kPa)	α4	α3
1.98E-03	25.42	3.82E-02	1.98E-03	1.31	26.74		
3.97E-03	36.45	5.47E-02	3.97E-03	1.58	38.03		
5.95E-03	45.01	6.76E-02	5.95E-03	1.78	46.78		
7.94E-03	52.27	7.85E-02	7.94E-03	1.94	54.21		
9.92E-03	58.70	8.81E-02	9.92E-03	2.07	60.78		
1.19E-02	64.54	9.69E-02	1.19E-02	2.20	66.74		
1.39E-02	69.93	1.05E-01	1.39E-02	2.31	72.24		
1.59E-02	74.95	1.13E-01	1.59E-02	2.41	77.37		
1.67E-02	76.86	1.15E-01	1.67E-02	2.45	79.31		
1.79E-02	79.69	1.20E-01	1.79E-02	2.51	82.20		
1.98E-02	84.18	1.26E-01	1.98E-02	2.61	86.78		
2.18E-02	88.45	1.33E-01	2.18E-02	2.70	91.15		
2.38E-02	92.55	1.39E-01	2.38E-02	2.78	95.33		
2.58E-02	96.48	1.45E-01	2.58E-02	2.86	99.34		
2.78E-02	100.27	1.51E-01	2.78E-02	2.94	103.21		
2.98E-02	103.93	1.56E-01	2.98E-02	3.02	106.95		
3.17E-02	107.48	1.61E-01	3.17E-02	3.09	110.57		
3.37E-02	110.92	1.67E-01	3.37E-02	3.16	114.09		
3.57E-02	114.27	1.72E-01	3.57E-02	3.23	117.50		
3.77E-02	117.53	1.76E-01	3.77E-02	3.30	120.83		
3.97E-02	120.71	1.81E-01	3.97E-02	3.37	124.07	4.00	3.00
4.17E-02	123.81	1.86E-01	4.17E-02	3.43	127.24		
4.37E-02	126.84	1.90E-01	4.37E-02	3.50	130.34		
4.56E-02	129.81	1.95E-01	4.56E-02	3.56	133.37		
4.76E-02	132.71	1.99E-01	4.76E-02	3.62	136.33		
4.96E-02	135.56	2.04E-01	4.96E-02	3.68	139.24		
5.16E-02	138.35	2.08E-01	5.16E-02	3.74	142.10		
5.36E-02	141.09	2.12E-01	5.36E-02	3.80	144.90		
5.56E-02	143.79	2.16E-01	5.56E-02	3.86	147.65		
5.75E-02	146.43	2.20E-01	5.75E-02	3.92	150.35		
5.95E-02	149.04	2.24E-01	5.95E-02	3.98	153.01		
6.15E-02	151.60	2.28E-01	6.15E-02	4.03	155.63		
6.35E-02	154.12	2.31E-01	6.35E-02	4.09	158.21		
6.55E-02	156.61	2.35E-01	6.55E-02	4.14	160.75		
6.75E-02	159.06	2.39E-01	6.75E-02	4.20	163.26		
6.94E-02	161.48	2.42E-01	6.94E-02	4.25	165.73		
7.14E-02	163.86	2.46E-01	7.14E-02	4.31	168.16		
7.34E-02	166.21	2.50E-01	7.34E-02	4.36	170.57		
7.54E-02	168.53	2.53E-01	7.54E-02	4.41	172.94		
7.74E-02	170.82	2.56E-01	7.74E-02	4.46	175.29		
7.94E-02	173.09	2.60E-01	7.94E-02	4.51	177.60		

Table A.8 - Static design calculation (Target Conditions II - 3 of 3).

Prototype							
$\alpha 2$	$\alpha 4 \cdot \tau_{cw\_max}$ (kPa)	$\alpha 3 \cdot \tau_{cw\_max}$ (kPa)	$\alpha 2 \cdot \tau_{cw\_max}$ (kPa)	Φ (◦)	θ_{max}	$\theta_{crit\ (Shields)}$	θ_{crit} (De Vos)
	106.94	80.21	53.47		0.069		
	152.14	114.10	76.07		0.049		
	187.14	140.35	93.57		0.040		
	216.83	162.62	108.41		0.035		
	243.10	182.33	121.55		0.031		
	266.95	200.21	133.47		0.029		
	288.95	216.71	144.47		0.026		
	309.48	232.11	154.74		0.025		
	317.25	237.93	158.62		0.024		
	328.81	246.61	164.40		0.023		
	347.13	260.35	173.57		0.022		
	364.60	273.45	182.30		0.021		
	381.31	285.98	190.66		0.020		
	397.37	298.03	198.69		0.020		
	412.85	309.64	206.43		0.019		
	427.81	320.85	213.90		0.018		
	442.29	331.72	221.15		0.018		
	456.35	342.26	228.17		0.017		
	470.01	352.51	235.01		0.017		
	483.32	362.49	241.66		0.016		
2.00	496.30	372.22	248.15	0	0.016	0.056	0.035
	508.97	381.73	254.48		0.016		
	521.35	391.01	260.68		0.015		
	533.47	400.10	266.73		0.015		
	545.33	409.00	272.67		0.015		
	556.97	417.73	278.48		0.014		
	568.38	426.29	284.19		0.014		
	579.59	434.69	289.79		0.014		
	590.59	442.94	295.30		0.014		
	601.41	451.06	300.71		0.013		
	612.06	459.04	306.03		0.013		
	622.54	466.90	311.27		0.013		
	632.85	474.64	316.43		0.013		
	643.02	482.26	321.51		0.012		
	653.03	489.78	326.52		0.012		
	662.91	497.18	331.46		0.012		
	672.66	504.49	336.33		0.012		
	682.27	511.71	341.14		0.012		
	691.77	518.82	345.88		0.012		
	701.14	525.86	350.57		0.012		
	710.40	532.80	355.20		0.011		

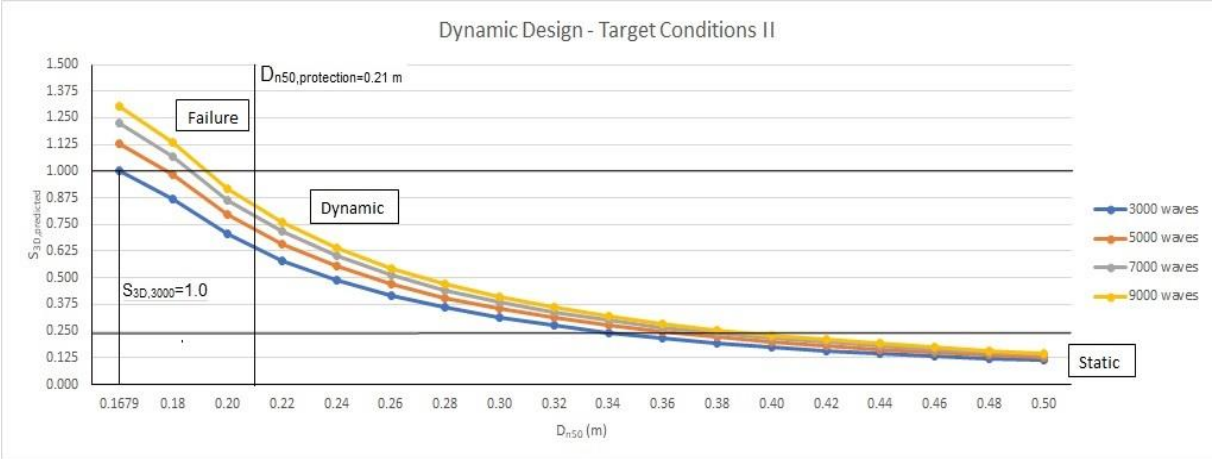

Figure A.7 - D_{n50} for S_{3D}=1.0 (Target Conditions II).

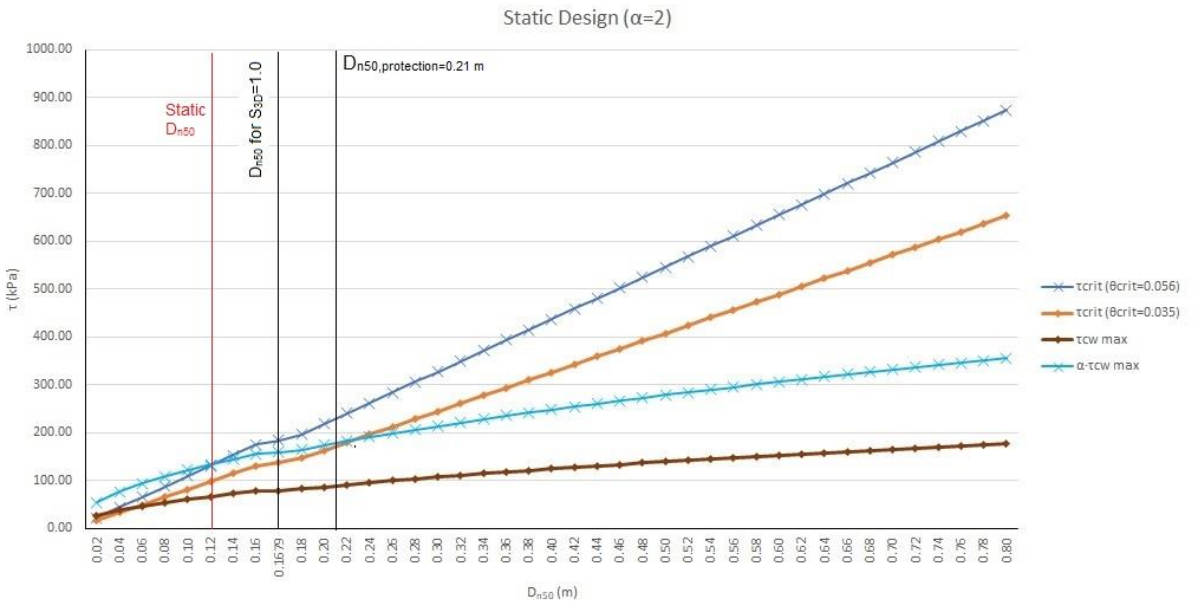

Figure A.8 - Static design α=2 (Target Conditions II).

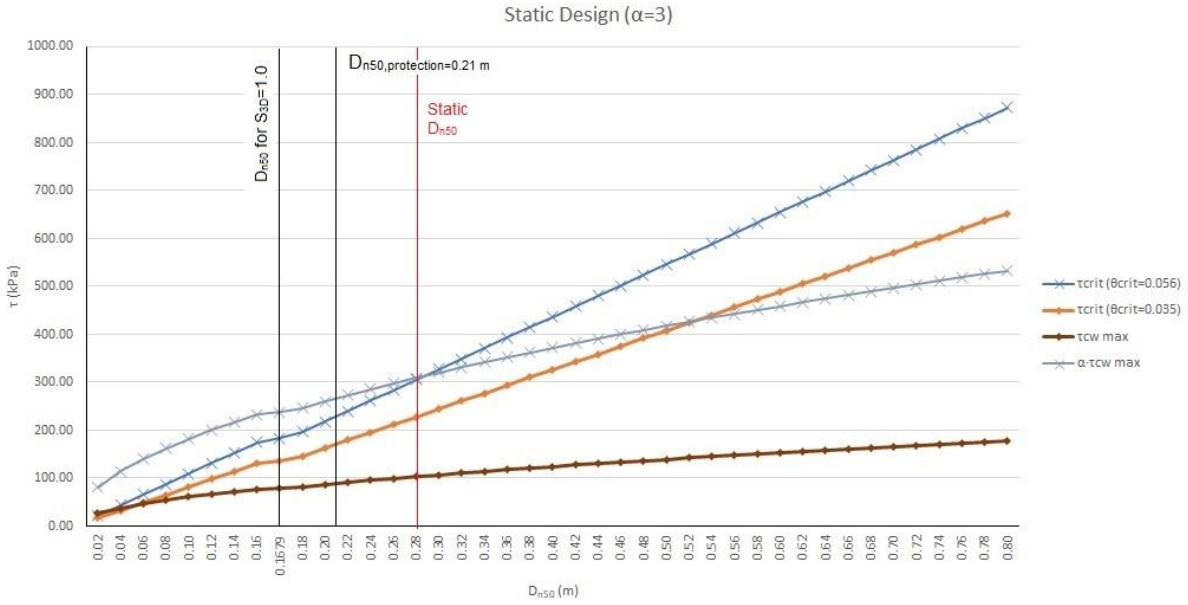

Figure A.9 - Static design α=3 (Target Conditions II).

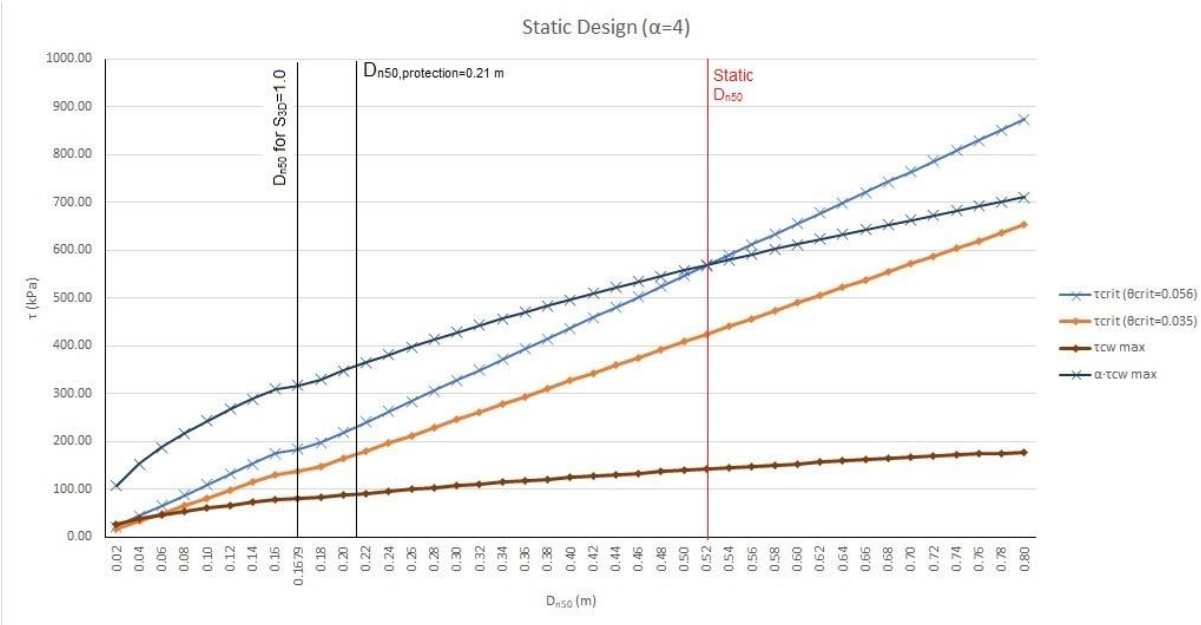

Figure A.10 - Static design α=4 (Target Conditions II).

A.3: TARGET CONDITIONS III

Table A.9 - Prototype and model inputs (Target Conditions III).

Prototype Target Conditions			
H_s (m)	T_p (s)	d (m)	U_c (m/s)
6	11	18	1
MATLAB:	U_m (m/s)	1.14	

Model Target Conditions			
H_s (m)	T_p (s)	d (m)	U_c (m/s)
0.12	1.56	0.36	0.14
MATLAB:	U_m (m/s)	0.16	

Scale (Froude)	
Scale λ_L:	0.020
Scale λ_T:	0.141
Scale λ_V:	0.141

Prototype (Other Parameters)					
ρ_w (kg/m^3):	1025	s	delta	g	σ_U
ρ_s (kg/m^3):	2694				
A (m):	1.996	2.628	1.628	9.81	2.04

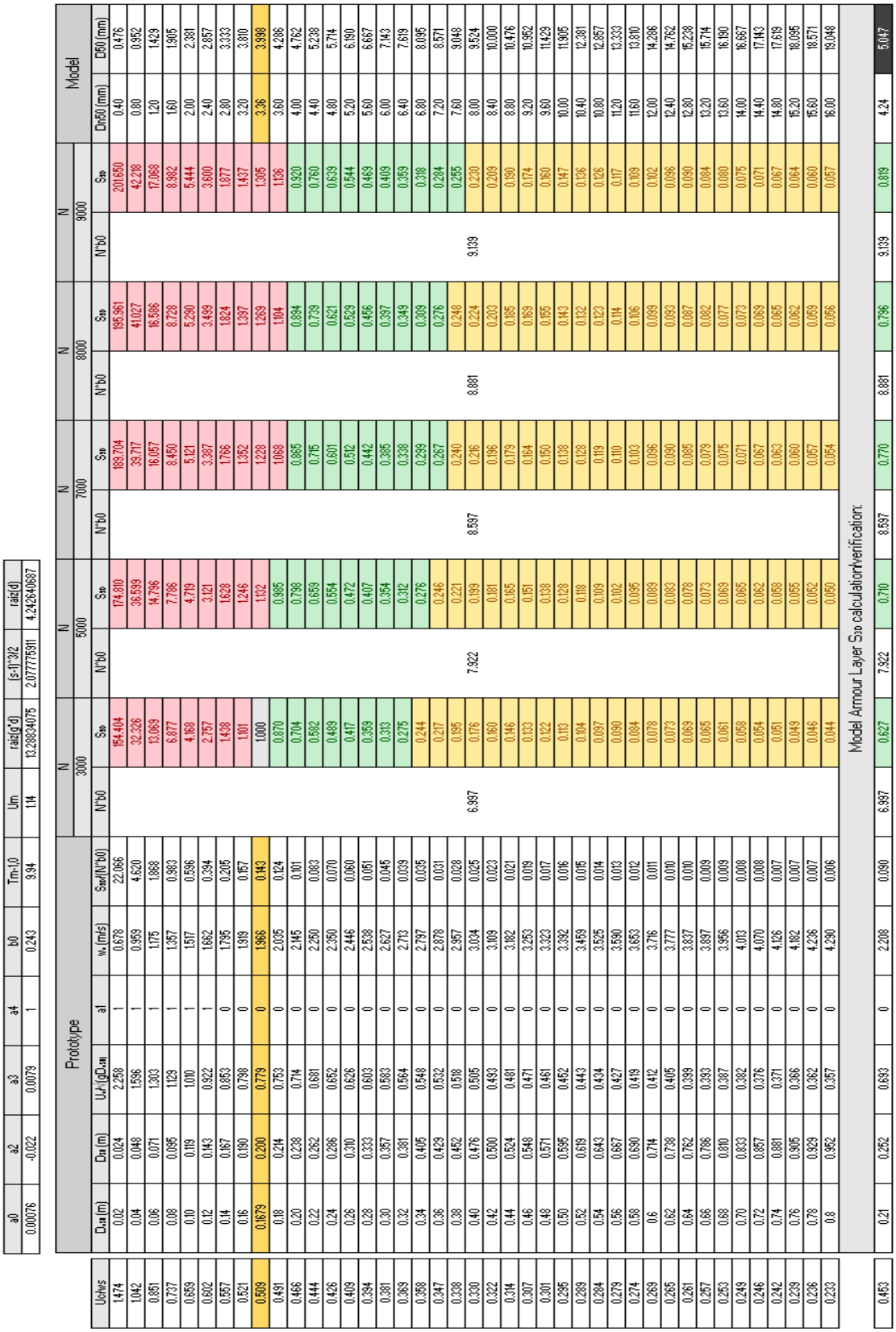

a0	a2	a3	a4	b0	Tm-10	Um	raiz(g*d)	(s-1)^2/2	raiz(d)
0,000076	-0,022	0,0079	1	0,243	9,94	1,14	13,28834075	2,077775391	4,242640687

Uc/ws	Prototype							N 3000		N 5000		N 7000		N 8000		N 9000		Model	
	Dcat (m)	Dss (m)	UA²/(gDcat)	a1	wc (m/s)	Sss/(N°b0)		N°b0	Sss	N°b0	Sss	N°b0	Sss	N°b0	Sss	N°b0	Sss	Dn50 (mm)	D50 (mm)
1,474	0,02	0,024	2,258	1	0,678	22,066			154,404		174,810		189,704		195,961		201,650	0,40	0,476
1,042	0,04	0,048	1,596	1	0,959	4,620			32,326		36,599		39,717		41,027		42,238	0,80	0,952
0,851	0,06	0,071	1,303	1	1,175	1,868			13,069		14,796		16,057		16,586		17,068	1,20	1,429
0,737	0,08	0,095	1,129	1	1,357	0,953			6,877		7,788		8,450		8,728		8,982	1,60	1,905
0,659	0,10	0,119	1,010	1	1,517	0,596			4,168		4,719		5,121		5,290		5,444	2,00	2,381
0,602	0,12	0,143	0,922	1	1,662	0,394			2,767		3,121		3,387		3,499		3,600	2,40	2,857
0,557	0,14	0,167	0,853	0	1,795	0,205			1,438		1,628		1,766		1,824		1,877	2,80	3,333
0,521	0,16	0,190	0,798	0	1,919	0,157			1,101		1,246		1,352		1,397		1,437	3,20	3,810
0,503	0,1679	0,200	0,779	0	1,966	0,143		1,000		1,102		1,228		1,269		1,305		3,36	3,998
0,491	0,18	0,214	0,753	0	2,035	0,124		0,870		0,985		1,068		1,104		1,136		3,60	4,286
0,466	0,20	0,238	0,714	0	2,145	0,101		0,704		0,798		0,865		0,894		0,920		4,00	4,762
0,444	0,22	0,262	0,681	0	2,250	0,083		0,582		0,659		0,715		0,739		0,760		4,40	5,238
0,426	0,24	0,286	0,652	0	2,350	0,070		0,489		0,554		0,601		0,621		0,639		4,80	5,714
0,409	0,26	0,310	0,626	0	2,446	0,060		0,417		0,472		0,512		0,529		0,544		5,20	6,190
0,394	0,28	0,333	0,603	0	2,538	0,051		0,359		0,407		0,442		0,456		0,469		5,60	6,667
0,381	0,30	0,357	0,583	0	2,627	0,045		0,313		0,354		0,385		0,397		0,409		6,00	7,143
0,369	0,32	0,381	0,564	0	2,713	0,039		0,275		0,312		0,338		0,349		0,359		6,40	7,619
0,358	0,34	0,405	0,548	0	2,797	0,035		0,244		0,276		0,299		0,309		0,318		6,80	8,095
0,347	0,36	0,429	0,532	0	2,878	0,031		0,217		0,246		0,267		0,276		0,284		7,20	8,571
0,338	0,38	0,452	0,518	0	2,957	0,028		0,195		0,221		0,240		0,248		0,255		7,60	9,048
0,330	0,40	0,476	0,505	0	3,034	0,025	6,997	0,176	7,922	0,199	8,597	0,216	8,881	0,224	9,139	0,230		8,00	9,524
0,322	0,42	0,500	0,493	0	3,109	0,023		0,160		0,181		0,196		0,203		0,209		8,40	10,000
0,314	0,44	0,524	0,481	0	3,182	0,021		0,146		0,165		0,179		0,185		0,190		8,80	10,476
0,307	0,46	0,548	0,471	0	3,253	0,019		0,133		0,151		0,164		0,169		0,174		9,20	10,952
0,301	0,48	0,571	0,461	0	3,323	0,017		0,122		0,138		0,150		0,155		0,160		9,60	11,429
0,295	0,50	0,595	0,452	0	3,392	0,016		0,113		0,128		0,138		0,143		0,147		10,00	11,905
0,289	0,52	0,619	0,443	0	3,459	0,015		0,104		0,118		0,128		0,132		0,136		10,40	12,381
0,284	0,54	0,643	0,434	0	3,525	0,014		0,097		0,109		0,119		0,123		0,126		10,80	12,857
0,279	0,56	0,667	0,427	0	3,590	0,013		0,090		0,102		0,110		0,114		0,117		11,20	13,333
0,274	0,58	0,690	0,419	0	3,653	0,012		0,084		0,095		0,103		0,106		0,109		11,60	13,810
0,269	0,6	0,714	0,412	0	3,716	0,011		0,078		0,089		0,096		0,099		0,102		12,00	14,286
0,265	0,62	0,738	0,405	0	3,777	0,010		0,073		0,083		0,090		0,093		0,096		12,40	14,762
0,261	0,64	0,762	0,399	0	3,837	0,010		0,069		0,078		0,085		0,087		0,090		12,80	15,238
0,257	0,66	0,786	0,393	0	3,897	0,009		0,065		0,073		0,079		0,082		0,084		13,20	15,714
0,253	0,68	0,810	0,387	0	3,956	0,009		0,061		0,069		0,075		0,077		0,080		13,60	16,190
0,249	0,70	0,833	0,382	0	4,013	0,008		0,058		0,065		0,071		0,073		0,075		14,00	16,667
0,246	0,72	0,857	0,376	0	4,070	0,008		0,054		0,062		0,067		0,069		0,071		14,40	17,143
0,242	0,74	0,881	0,371	0	4,126	0,007		0,051		0,058		0,063		0,065		0,067		14,80	17,619
0,239	0,76	0,905	0,366	0	4,182	0,007		0,049		0,055		0,060		0,062		0,064		15,20	18,095
0,236	0,78	0,929	0,362	0	4,236	0,007		0,046		0,052		0,057		0,059		0,060		15,60	18,571
0,233	0,8	0,952	0,357	0	4,290	0,006		0,044		0,050		0,054		0,056		0,057		16,00	19,048
													Model Armour Layer Sss calculation/verification:						
0,453	0,21	0,252	0,633	0	2,208	0,090	6,997	0,627	7,922	0,710	8,597	0,770	8,881	0,796	9,139	0,819		4,24	5,047

Figure A.11 - Dynamic Design calculation (Target Conditions III).

Table A.10 - Static design calculation (Target Conditions III - 1 of 4).

Prototype					
D67.5 (m)	D_{n50} (m)	D50 (m)	τcrit (θcrit=0.056) (kPa)	τcrit (θcrit=0.035) (kPa)	τ_c (kPa)
0.028	0.02	0.024	21.83	16.31	2.49
0.057	0.04	0.048	43.66	32.61	2.98
0.085	0.06	0.071	65.49	48.92	3.33
0.114	0.08	0.095	87.32	65.22	3.62
0.142	0.10	0.119	109.15	81.53	3.88
0.171	0.12	0.143	130.98	97.84	4.10
0.199	0.14	0.167	152.81	114.14	4.31
0.228	0.16	0.190	174.64	130.45	4.50
0.239	0.1679	0.200	183.27	136.89	4.58
0.256	0.18	0.214	196.47	146.76	4.69
0.285	0.20	0.238	218.31	163.06	4.86
0.313	0.22	0.262	240.14	179.37	5.02
0.341	0.24	0.286	261.97	195.67	5.18
0.370	0.26	0.310	283.80	211.98	5.33
0.398	0.28	0.333	305.63	228.29	5.47
0.427	0.30	0.357	327.46	244.59	5.61
0.455	0.32	0.381	349.29	260.90	5.75
0.484	0.34	0.405	371.12	277.20	5.88
0.512	0.36	0.429	392.95	293.51	6.01
0.541	0.38	0.452	414.78	309.82	6.14
0.569	0.40	0.476	436.61	326.12	6.26
0.598	0.42	0.500	458.44	342.43	6.38
0.626	0.44	0.524	480.27	358.74	6.50
0.654	0.46	0.548	502.10	375.04	6.62
0.683	0.48	0.571	523.93	391.35	6.73
0.711	0.50	0.595	545.76	407.65	6.85
0.740	0.52	0.619	567.59	423.96	6.96
0.768	0.54	0.643	589.42	440.27	7.07
0.797	0.56	0.667	611.25	456.57	7.18
0.825	0.58	0.690	633.09	472.88	7.28
0.854	0.60	0.714	654.92	489.18	7.39
0.882	0.62	0.738	676.75	505.49	7.49
0.911	0.64	0.762	698.58	521.80	7.59
0.939	0.66	0.786	720.41	538.10	7.70
0.967	0.68	0.810	742.24	554.41	7.80
0.996	0.70	0.833	764.07	570.72	7.89
1.024	0.72	0.857	785.90	587.02	7.99
1.053	0.74	0.881	807.73	603.33	8.09
1.081	0.76	0.905	829.56	619.63	8.19
1.110	0.78	0.929	851.39	635.94	8.28
1.138	0.80	0.952	873.22	652.25	8.38

Table A.11 - Static design calculation (Target Conditions III - 2 of 4).

Prototype				
f_c	ks (m)	$z0_c$	τ_w (kPa)	f_w
4.86E-03	0.060	1.98E-03	25.42	3.82E-02
5.81E-03	0.119	3.97E-03	36.45	5.47E-02
6.50E-03	0.179	5.95E-03	45.01	6.76E-02
7.07E-03	0.238	7.94E-03	52.27	7.85E-02
7.57E-03	0.298	9.92E-03	58.70	8.81E-02
8.01E-03	0.357	1.19E-02	64.54	9.69E-02
8.41E-03	0.417	1.39E-02	69.93	1.05E-01
8.79E-03	0.476	1.59E-02	74.95	1.13E-01
8.93E-03	0.500	1.67E-02	76.86	1.15E-01
9.14E-03	0.536	1.79E-02	79.69	1.20E-01
9.48E-03	0.595	1.98E-02	84.18	1.26E-01
9.80E-03	0.655	2.18E-02	88.45	1.33E-01
1.01E-02	0.714	2.38E-02	92.55	1.39E-01
1.04E-02	0.774	2.58E-02	96.48	1.45E-01
1.07E-02	0.833	2.78E-02	100.27	1.51E-01
1.10E-02	0.893	2.98E-02	103.93	1.56E-01
1.12E-02	0.952	3.17E-02	107.48	1.61E-01
1.15E-02	1.012	3.37E-02	110.92	1.67E-01
1.17E-02	1.071	3.57E-02	114.27	1.72E-01
1.20E-02	1.131	3.77E-02	117.53	1.76E-01
1.22E-02	1.190	3.97E-02	120.71	1.81E-01
1.25E-02	1.250	4.17E-02	123.81	1.86E-01
1.27E-02	1.310	4.37E-02	126.84	1.90E-01
1.29E-02	1.369	4.56E-02	129.81	1.95E-01
1.31E-02	1.429	4.76E-02	132.71	1.99E-01
1.34E-02	1.488	4.96E-02	135.56	2.04E-01
1.36E-02	1.548	5.16E-02	138.35	2.08E-01
1.38E-02	1.607	5.36E-02	141.09	2.12E-01
1.40E-02	1.667	5.56E-02	143.79	2.16E-01
1.42E-02	1.726	5.75E-02	146.43	2.20E-01
1.44E-02	1.786	5.95E-02	149.04	2.24E-01
1.46E-02	1.845	6.15E-02	151.60	2.28E-01
1.48E-02	1.905	6.35E-02	154.12	2.31E-01
1.50E-02	1.964	6.55E-02	156.61	2.35E-01
1.52E-02	2.024	6.75E-02	159.06	2.39E-01
1.54E-02	2.083	6.94E-02	161.48	2.42E-01
1.56E-02	2.143	7.14E-02	163.86	2.46E-01
1.58E-02	2.202	7.34E-02	166.21	2.50E-01
1.60E-02	2.262	7.54E-02	168.53	2.53E-01
1.62E-02	2.321	7.74E-02	170.82	2.56E-01
1.63E-02	2.381	7.94E-02	173.09	2.60E-01

Table A. 12 - Static design calculation (Target Conditions III - 3 of 4).

Prototype					
z0_w	τcw_m (kPa)	τcw_max (kPa)	α4	α3	α2
1.98E-03	4.71	30.13			
3.97E-03	5.76	42.21			
5.95E-03	6.52	51.52			
7.94E-03	7.13	59.41			
9.92E-03	7.67	66.37			
1.19E-02	8.15	72.69			
1.39E-02	8.58	78.51			
1.59E-02	8.99	83.94			
1.67E-02	9.14	86.00			
1.79E-02	9.37	89.06			
1.98E-02	9.73	93.91			
2.18E-02	10.07	98.52			
2.38E-02	10.40	102.95			
2.58E-02	10.71	107.19			
2.78E-02	11.01	111.29			
2.98E-02	11.31	115.24			
3.17E-02	11.59	119.07			
3.37E-02	11.87	122.79			
3.57E-02	12.14	126.41			
3.77E-02	12.40	129.93			
3.97E-02	12.65	133.36	4.00	3.00	2.00
4.17E-02	12.91	136.71			
4.37E-02	13.15	139.99			
4.56E-02	13.39	143.20			
4.76E-02	13.63	146.34			
4.96E-02	13.86	149.42			
5.16E-02	14.09	152.44			
5.36E-02	14.32	155.41			
5.56E-02	14.54	158.33			
5.75E-02	14.76	161.20			
5.95E-02	14.98	164.02			
6.15E-02	15.19	166.79			
6.35E-02	15.41	169.53			
6.55E-02	15.62	172.23			
6.75E-02	15.82	174.88			
6.94E-02	16.03	177.50			
7.14E-02	16.23	180.09			
7.34E-02	16.43	182.64			
7.54E-02	16.63	185.16			
7.74E-02	16.83	187.65			
7.94E-02	17.02	190.11			

Table A. 13 - Static design calculation (Target Conditions III - 4 of 4).

Prototype						
$\alpha 4 \cdot \tau_{cw\_max}$ (kPa)	$\alpha 3 \cdot \tau_{cw\_max}$ (kPa)	$\alpha 2 \cdot \tau_{cw\_max}$ (kPa)	Φ (◦)	θ_{max}	θ_{crit} (Shields)	θ_{crit} (De Vos)
120.52	90.39	60.26		0.077		
168.85	126.63	84.42		0.054		
206.10	154.57	103.05		0.044		
237.62	178.22	118.81		0.038		
265.49	199.11	132.74		0.034		
290.75	218.06	145.38		0.031		
314.05	235.53	157.02		0.029		
335.78	251.83	167.89		0.027		
344.00	258.00	172.00		0.026		
356.24	267.18	178.12		0.025		
375.62	281.72	187.81		0.024		
394.10	295.57	197.05		0.023		
411.78	308.84	205.89		0.022		
428.77	321.58	214.38		0.021		
445.14	333.86	222.57		0.020		
460.97	345.72	230.48		0.020		
476.29	357.22	238.15		0.019		
491.16	368.37	245.58		0.019		
505.63	379.22	252.81		0.018		
519.71	389.78	259.85		0.018		
533.44	400.08	266.72	0	0.017	0.056	0.035
546.85	410.14	273.43		0.017		
559.96	419.97	279.98		0.016		
572.80	429.60	286.40		0.016		
585.36	439.02	292.68		0.016		
597.69	448.26	298.84		0.015		
609.78	457.33	304.89		0.015		
621.65	466.24	310.82		0.015		
633.31	474.99	316.66		0.015		
644.79	483.59	322.39		0.014		
656.07	492.05	328.04		0.014		
667.18	500.38	333.59		0.014		
678.12	508.59	339.06		0.014		
688.90	516.68	344.45		0.013		
699.53	524.65	349.77		0.013		
710.01	532.51	355.01		0.013		
720.36	540.27	360.18		0.013		
730.56	547.92	365.28		0.013		
740.64	555.48	370.32		0.012		
750.60	562.95	375.30		0.012		
760.44	570.33	380.22		0.012		

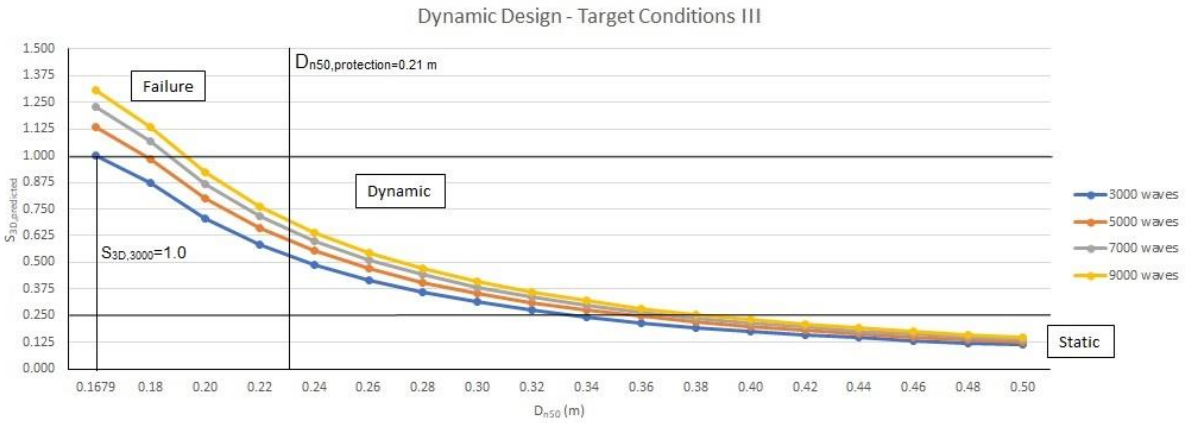

Figure A.12 - D_{n50} for S_{3D}=1.0 (Target Conditions III).

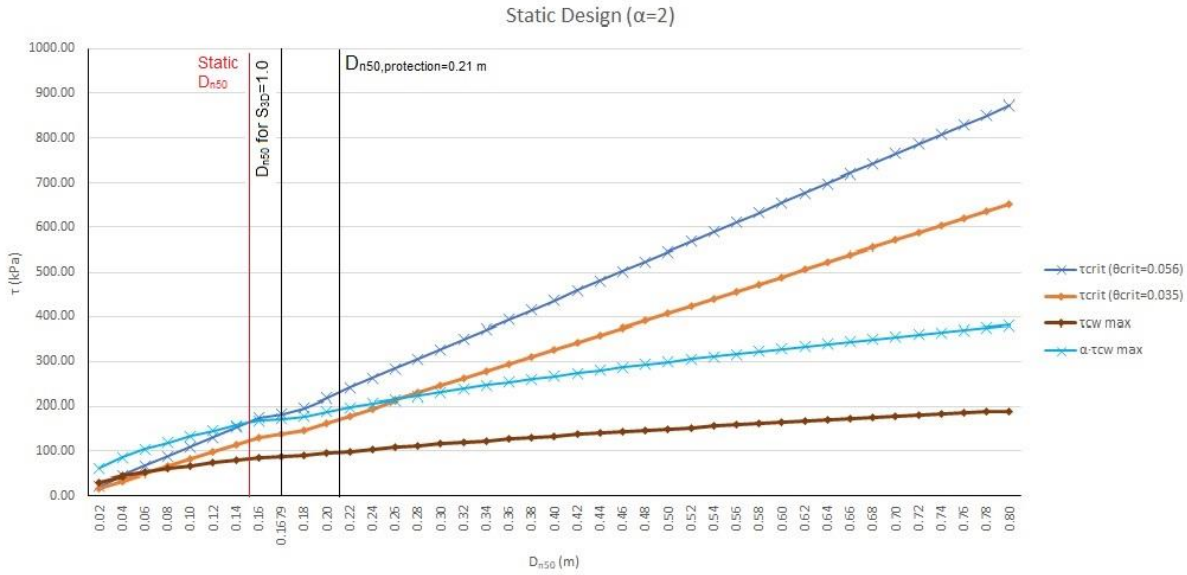

Figure A.13 - Static design α=2 (Target Conditions III).

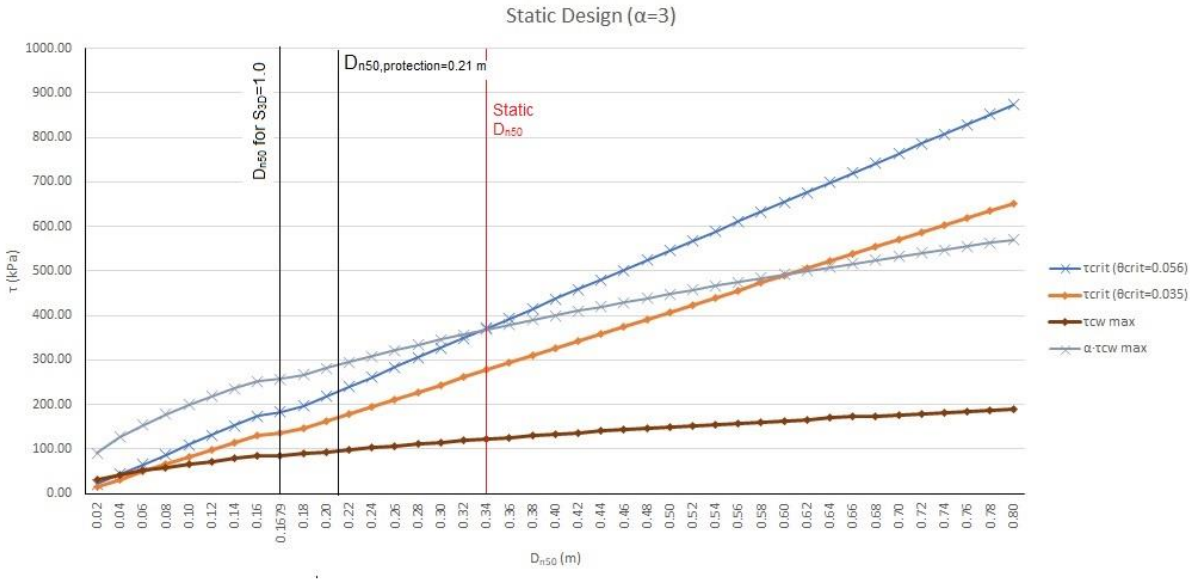

Figure A.14 - Static design α=3 (Target Conditions III).

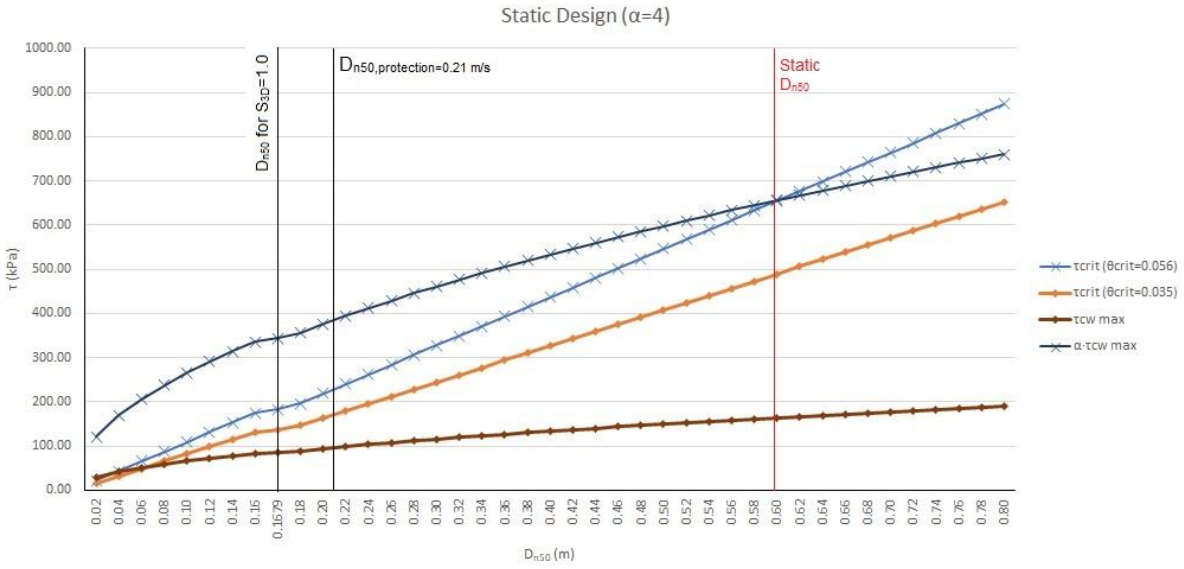

Figure A.15 - Static design α=4 (Target Conditions III).

A.4: TEST 1A

Table A.14 - Prototype and model inputs (Test 1a).

Prototype Target Conditions			
H_{m0} (m)	T_p (s)	d (m)	U_c (m/s)
5.2	10.79	18.00	0.721
MATLAB:	U_m (m/s)	0.983	

Model Target Conditions			
H_{m0} (m)	T_p (s)	d (m)	U_c (m/s)
0.104	1.53	0.36	0.102
MATLAB:	U_m (m/s)	0.139	

Scale (Froude)	
Scale λ_L:	0.020
Scale λ_T:	0.141
Scale λ_V:	0.141

Prototype (Other Parameters)					
ρ_w (kg/m^3):	1025	s	delta	g	σ_U
ρ_s (kg/m^3):	2694				
A (m):	1.688	2.628	1.628	9.81	2.04

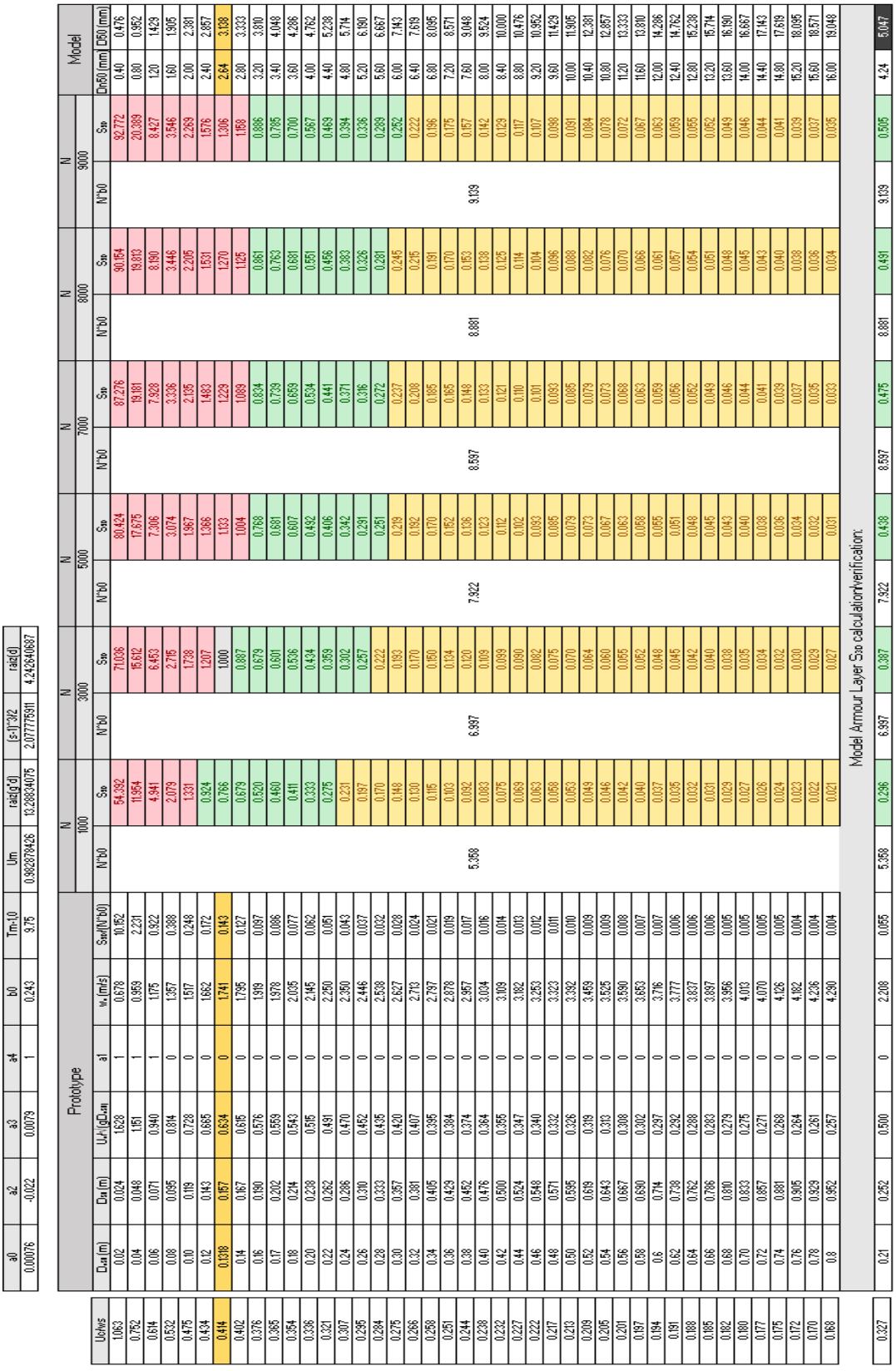

a0	a2	a3	a4	b0	Tm-10	Um	rair(g*d)	(s-r)^2/2	rair(d)
0.000076	-0.022	0.0079	1	0.243	9.75	0.982878426	12.28834075	2.077775911	4.242649687

Prototype							N 1000		N 3000		N 5000		N 7000		N 8000		N 9000		Model	
Dn,st (m)	Dm (m)	Un*(gDn,st)	a1	vw (m/s)	Sae/(N*b0)	N*b0	Sa0	N*b0	Sa0	N*b0	Sa0	N*b0	Sa0	N*b0	Sa0	N*b0	Sa0	Dn50 (mm)	D50 (mm)
0.02	0.024	1.628	1	0.678	10.162		54.392		71.036		80.424		87.276		90.154		92.772	0.40	0.476
0.04	0.048	1.151	1	0.959	2.231		11.954		15.612		17.675		19.181		19.813		20.389	0.80	0.952
0.06	0.071	0.940	1	1.175	0.922		4.941		6.453		7.306		7.926		8.190		8.427	1.20	1.429
0.08	0.095	0.814	0	1.357	0.388		2.079		2.715		3.074		3.336		3.446		3.546	1.60	1.905
0.10	0.119	0.728	0	1.517	0.248		1.331		1.738		1.967		2.135		2.205		2.269	2.00	2.381
0.12	0.143	0.665	0	1.662	0.172		0.924		1.207		1.366		1.483		1.531		1.576	2.40	2.857
0.1398	0.167	0.614	0	1.741	0.143		0.766		1.000		1.133		1.229		1.270		1.306	2.64	3.138
0.14	0.167	0.615	0	1.795	0.127		0.679		0.887		1.004		1.089		1.125		1.158	2.80	3.333
0.16	0.190	0.576	0	1.919	0.097		0.520		0.679		0.768		0.834		0.861		0.886	3.20	3.810
0.17	0.202	0.559	0	1.978	0.086		0.460		0.601		0.681		0.739		0.763		0.785	3.40	4.048
0.18	0.214	0.543	0	2.035	0.077		0.411		0.536		0.607		0.659		0.681		0.700	3.60	4.286
0.20	0.238	0.515	0	2.145	0.062		0.333		0.434		0.492		0.534		0.551		0.567	4.00	4.762
0.22	0.262	0.491	0	2.250	0.051		0.275		0.359		0.406		0.441		0.456		0.469	4.40	5.238
0.24	0.286	0.470	0	2.350	0.043		0.231		0.302		0.342		0.371		0.383		0.394	4.80	5.714
0.26	0.310	0.452	0	2.446	0.037		0.197		0.257		0.291		0.316		0.326		0.336	5.20	6.190
0.28	0.333	0.435	0	2.538	0.032		0.170		0.222		0.251		0.272		0.281		0.289	5.60	6.667
0.30	0.357	0.420	0	2.627	0.028		0.148		0.193		0.219		0.237		0.245		0.252	6.00	7.143
0.32	0.381	0.407	0	2.713	0.024		0.130		0.170		0.192		0.208		0.215		0.222	6.40	7.619
0.34	0.405	0.395	0	2.797	0.021		0.115		0.150		0.170		0.185		0.191		0.196	6.80	8.095
0.36	0.429	0.384	0	2.878	0.019		0.103		0.134		0.152		0.165		0.170		0.175	7.20	8.571
0.38	0.452	0.374	0	2.957	0.017	5.358	0.092	6.997	0.120	7.322	0.136	8.597	0.148	8.881	0.153	9.139	0.157	7.60	9.048
0.40	0.476	0.364	0	3.034	0.016		0.083		0.109		0.123		0.133		0.138		0.142	8.00	9.524
0.42	0.500	0.355	0	3.109	0.014		0.075		0.099		0.112		0.121		0.125		0.129	8.40	10.000
0.44	0.524	0.347	0	3.182	0.013		0.069		0.090		0.102		0.110		0.114		0.117	8.80	10.476
0.46	0.548	0.340	0	3.253	0.012		0.063		0.082		0.093		0.101		0.104		0.107	9.20	10.952
0.48	0.571	0.332	0	3.323	0.011		0.058		0.075		0.085		0.093		0.096		0.098	9.60	11.429
0.50	0.595	0.326	0	3.392	0.010		0.053		0.070		0.079		0.085		0.088		0.091	10.00	11.905
0.52	0.619	0.319	0	3.459	0.009		0.049		0.064		0.073		0.079		0.082		0.084	10.40	12.381
0.54	0.643	0.313	0	3.525	0.009		0.046		0.060		0.067		0.073		0.076		0.078	10.80	12.857
0.56	0.667	0.308	0	3.590	0.008		0.042		0.055		0.063		0.068		0.070		0.072	11.20	13.333
0.58	0.690	0.302	0	3.653	0.007		0.040		0.052		0.058		0.063		0.066		0.067	11.60	13.810
0.6	0.714	0.297	0	3.716	0.007		0.037		0.048		0.055		0.059		0.061		0.063	12.00	14.286
0.62	0.738	0.292	0	3.777	0.006		0.035		0.045		0.051		0.056		0.057		0.059	12.40	14.762
0.64	0.762	0.288	0	3.837	0.006		0.032		0.042		0.048		0.052		0.054		0.055	12.80	15.238
0.66	0.786	0.283	0	3.897	0.006		0.031		0.040		0.045		0.049		0.051		0.052	13.20	15.714
0.68	0.810	0.279	0	3.956	0.005		0.029		0.038		0.043		0.046		0.048		0.049	13.60	16.190
0.70	0.833	0.275	0	4.013	0.005		0.027		0.035		0.040		0.044		0.045		0.046	14.00	16.667
0.72	0.857	0.271	0	4.070	0.005		0.026		0.034		0.038		0.041		0.043		0.044	14.40	17.143
0.74	0.881	0.268	0	4.126	0.005		0.024		0.032		0.036		0.039		0.040		0.041	14.80	17.619
0.76	0.905	0.264	0	4.182	0.004		0.023		0.030		0.034		0.037		0.038		0.039	15.20	18.095
0.78	0.929	0.261	0	4.236	0.004		0.022		0.029		0.032		0.035		0.036		0.037	15.60	18.571
0.8	0.952	0.257	0	4.290	0.004		0.021		0.027		0.031		0.033		0.034		0.035	16.00	19.048
0.21	0.252	0.500	0	2.208	0.055	5.358	0.296	6.997	0.387	7.322	0.438	8.597	0.475	8.881	0.491	9.139	0.505	4.24	5.047

Model Armour Layer Sa0 calculation/verification:

Ustws
1.063
0.752
0.614
0.532
0.475
0.434
0.414
0.402
0.376
0.365
0.354
0.336
0.321
0.307
0.295
0.284
0.275
0.266
0.258
0.251
0.244
0.238
0.232
0.227
0.222
0.217
0.213
0.209
0.205
0.201
0.197
0.194
0.191
0.188
0.185
0.182
0.180
0.177
0.175
0.172
0.170
0.168
0.327

Figure A.16 - Dynamic design calculation (Test 1a).

Table A.15 - Static design calculation (Test 1a - 1 of 4).

Prototype					
D67.5 (m)	D_{n50} (m)	D50 (m)	τcrit (θcrit=0.056) (kPa)	τcrit (θcrit=0.035) (kPa)	τ_c (kPa)
0.028	0.02	0.024	21.83	16.31	1.30
0.057	0.04	0.048	43.66	32.61	1.55
0.085	0.06	0.071	65.49	48.92	1.73
0.114	0.08	0.095	87.32	65.22	1.89
0.142	0.10	0.119	109.15	81.53	2.02
0.171	0.12	0.143	130.98	97.84	2.14
0.188	0.1318	0.157	143.86	107.46	2.20
0.199	0.14	0.167	152.81	114.14	2.24
0.228	0.16	0.190	174.64	130.45	2.34
0.242	0.17	0.202	185.56	138.60	2.39
0.256	0.18	0.214	196.47	146.76	2.44
0.285	0.20	0.238	218.31	163.06	2.53
0.313	0.22	0.262	240.14	179.37	2.61
0.341	0.24	0.286	261.97	195.67	2.69
0.370	0.26	0.310	283.80	211.98	2.77
0.398	0.28	0.333	305.63	228.29	2.85
0.427	0.30	0.357	327.46	244.59	2.92
0.455	0.32	0.381	349.29	260.90	2.99
0.484	0.34	0.405	371.12	277.20	3.06
0.512	0.36	0.429	392.95	293.51	3.13
0.541	0.38	0.452	414.78	309.82	3.19
0.569	0.40	0.476	436.61	326.12	3.26
0.598	0.42	0.500	458.44	342.43	3.32
0.626	0.44	0.524	480.27	358.74	3.38
0.654	0.46	0.548	502.10	375.04	3.44
0.683	0.48	0.571	523.93	391.35	3.50
0.711	0.50	0.595	545.76	407.65	3.56
0.740	0.52	0.619	567.59	423.96	3.62
0.768	0.54	0.643	589.42	440.27	3.68
0.797	0.56	0.667	611.25	456.57	3.73
0.825	0.58	0.690	633.09	472.88	3.79
0.854	0.60	0.714	654.92	489.18	3.84
0.882	0.62	0.738	676.75	505.49	3.90
0.911	0.64	0.762	698.58	521.80	3.95
0.939	0.66	0.786	720.41	538.10	4.00
0.967	0.68	0.810	742.24	554.41	4.06
0.996	0.70	0.833	764.07	570.72	4.11
1.024	0.72	0.857	785.90	587.02	4.16
1.053	0.74	0.881	807.73	603.33	4.21
1.081	0.76	0.905	829.56	619.63	4.26
1.110	0.78	0.929	851.39	635.94	4.31
1.138	0.80	0.952	873.22	652.25	4.36

Table A.16 - Static design calculation (Test 1a - 2 of 4).

Prototype					
fc	ks (m)	z0_c	τw (kPa)	fw	z0_w
4.86E-03	0.060	1.98E-03	20.62	4.16E-02	1.98E-03
5.81E-03	0.119	3.97E-03	29.56	5.97E-02	3.97E-03
6.50E-03	0.179	5.95E-03	36.50	7.37E-02	5.95E-03
7.07E-03	0.238	7.94E-03	42.39	8.56E-02	7.94E-03
7.57E-03	0.298	9.92E-03	47.61	9.62E-02	9.92E-03
8.01E-03	0.357	1.19E-02	52.34	1.06E-01	1.19E-02
8.25E-03	0.392	1.31E-02	54.96	1.11E-01	1.31E-02
8.41E-03	0.417	1.39E-02	56.71	1.15E-01	1.39E-02
8.79E-03	0.476	1.59E-02	60.79	1.23E-01	1.59E-02
8.97E-03	0.506	1.69E-02	62.74	1.27E-01	1.69E-02
9.14E-03	0.536	1.79E-02	64.63	1.31E-01	1.79E-02
9.48E-03	0.595	1.98E-02	68.27	1.38E-01	1.98E-02
9.80E-03	0.655	2.18E-02	71.74	1.45E-01	2.18E-02
1.01E-02	0.714	2.38E-02	75.06	1.52E-01	2.38E-02
1.04E-02	0.774	2.58E-02	78.25	1.58E-01	2.58E-02
1.07E-02	0.833	2.78E-02	81.32	1.64E-01	2.78E-02
1.10E-02	0.893	2.98E-02	84.29	1.70E-01	2.98E-02
1.12E-02	0.952	3.17E-02	87.17	1.76E-01	3.17E-02
1.15E-02	1.012	3.37E-02	89.96	1.82E-01	3.37E-02
1.17E-02	1.071	3.57E-02	92.67	1.87E-01	3.57E-02
1.20E-02	1.131	3.77E-02	95.32	1.93E-01	3.77E-02
1.22E-02	1.190	3.97E-02	97.89	1.98E-01	3.97E-02
1.25E-02	1.250	4.17E-02	100.41	2.03E-01	4.17E-02
1.27E-02	1.310	4.37E-02	102.87	2.08E-01	4.37E-02
1.29E-02	1.369	4.56E-02	105.27	2.13E-01	4.56E-02
1.31E-02	1.429	4.76E-02	107.63	2.17E-01	4.76E-02
1.34E-02	1.488	4.96E-02	109.94	2.22E-01	4.96E-02
1.36E-02	1.548	5.16E-02	112.20	2.27E-01	5.16E-02
1.38E-02	1.607	5.36E-02	114.43	2.31E-01	5.36E-02
1.40E-02	1.667	5.56E-02	116.61	2.36E-01	5.56E-02
1.42E-02	1.726	5.75E-02	118.76	2.40E-01	5.75E-02
1.44E-02	1.786	5.95E-02	120.87	2.44E-01	5.95E-02
1.46E-02	1.845	6.15E-02	122.95	2.48E-01	6.15E-02
1.48E-02	1.905	6.35E-02	125.00	2.52E-01	6.35E-02
1.50E-02	1.964	6.55E-02	127.01	2.57E-01	6.55E-02
1.52E-02	2.024	6.75E-02	129.00	2.61E-01	6.75E-02
1.54E-02	2.083	6.94E-02	130.96	2.65E-01	6.94E-02
1.56E-02	2.143	7.14E-02	132.89	2.68E-01	7.14E-02
1.58E-02	2.202	7.34E-02	134.80	2.72E-01	7.34E-02
1.60E-02	2.262	7.54E-02	136.68	2.76E-01	7.54E-02
1.62E-02	2.321	7.74E-02	138.54	2.80E-01	7.74E-02
1.63E-02	2.381	7.94E-02	140.37	2.84E-01	7.94E-02

Table A.17 - Static design calculation (Test 1a - 3 of 4).

Prototype					
τ_{cw_m} (kPa)	τ_{cw_max} (kPa)	α4	α3	α2	$\alpha4 \cdot \tau_{cw\_max}$ (kPa)
2.58	23.19				92.77
3.13	32.69				130.77
3.53	40.03				160.12
3.85	46.25				184.98
4.14	51.74				206.98
4.39	56.73				226.93
4.53	59.49				237.95
4.62	61.33				245.33
4.84	65.62				262.50
4.94	67.67				270.69
5.04	69.66				278.66
5.23	73.49				293.98
5.41	77.14				308.58
5.58	80.64				322.55
5.75	83.99				335.98
5.91	87.23				348.91
6.06	90.35				361.42
6.21	93.38				373.53
6.36	96.32				385.28
6.50	99.18				396.71
6.64	101.96	4.00	3.00	2.00	407.84
6.78	104.67				418.69
6.91	107.32				429.28
7.04	109.91				439.64
7.17	112.44				449.77
7.30	114.93				459.70
7.42	117.36				469.43
7.54	119.75				478.98
7.66	122.09				488.36
7.78	124.39				497.57
7.90	126.66				506.63
8.01	128.88				515.54
8.13	131.08				524.31
8.24	133.24				532.95
8.35	135.36				541.46
8.46	137.46				549.85
8.57	139.53				558.12
8.68	141.57				566.28
8.79	143.58				574.34
8.89	145.57				582.29
9.00	147.54				590.14
9.10	149.48				597.90

Table A.18 - Static design calculation (Test 1a - 4 of 4).

Prototype					
α3·τcw_max (kPa)	α2·τcw_max (kPa)	Φ (◦)	θmax	θcrit (Shields)	θcrit (De Vos)
69.58	46.38		0.059		
98.08	65.38		0.042		
120.09	80.06		0.034		
138.74	92.49		0.030		
155.23	103.49		0.027		
170.20	113.46		0.024		
178.46	118.97		0.023		
184.00	122.66		0.022		
196.87	131.25		0.021		
203.02	135.35		0.020		
208.99	139.33		0.020		
220.48	146.99		0.019		
231.43	154.29		0.018		
241.91	161.28		0.017		
251.98	167.99		0.017		
261.69	174.46		0.016		
271.06	180.71		0.015		
280.15	186.76		0.015		
288.96	192.64		0.015		
297.53	198.35		0.014		
305.88	203.92		0.014		
314.02	209.34	0	0.013	0.056	0.035
321.96	214.64		0.013		
329.73	219.82		0.013		
337.33	224.89		0.013		
344.78	229.85		0.012		
352.08	234.72		0.012		
359.24	239.49		0.012		
366.27	244.18		0.012		
373.18	248.79		0.011		
379.97	253.31		0.011		
386.65	257.77		0.011		
393.23	262.16		0.011		
399.71	266.47		0.011		
406.09	270.73		0.011		
412.38	274.92		0.010		
418.59	279.06		0.010		
424.71	283.14		0.010		
430.75	287.17		0.010		
436.72	291.14		0.010		
442.61	295.07		0.010		
448.43	298.95		0.010		

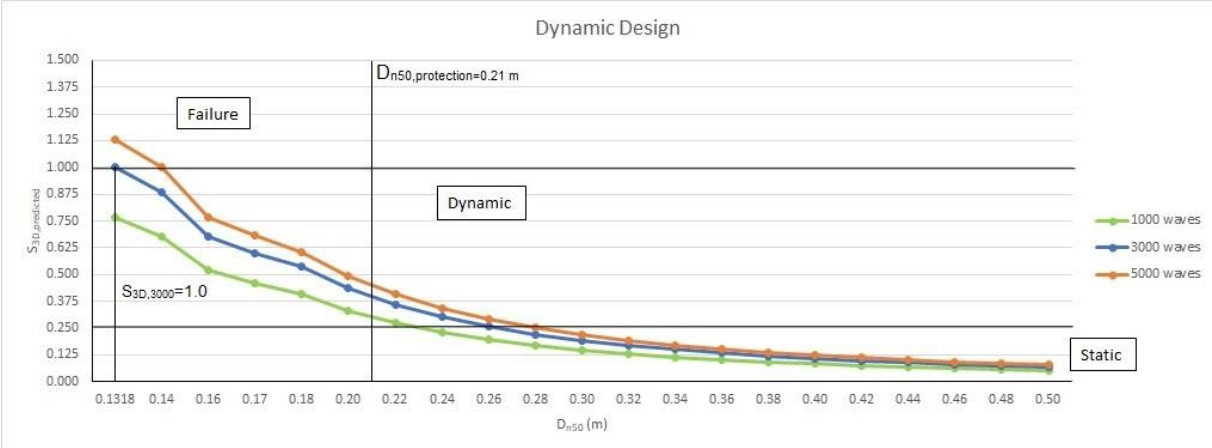

Figure A.17 - D_{n50} for S_{3D}=1.0 (Test 1a).

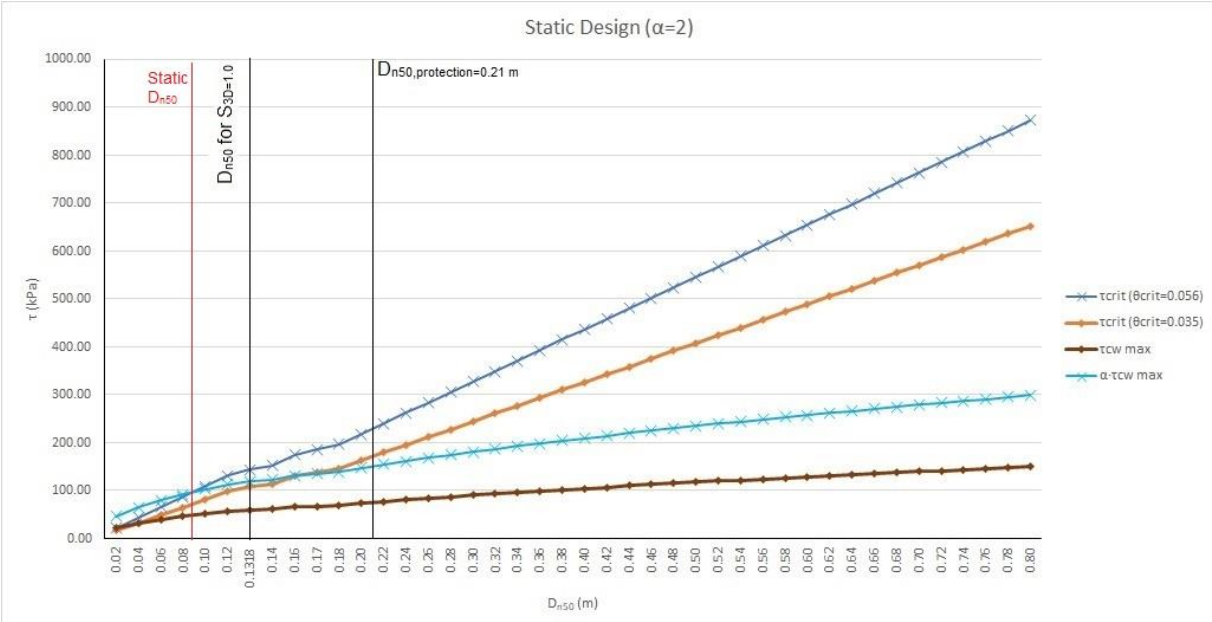

Figure A.18 - Static design α=2 (Test 1a).

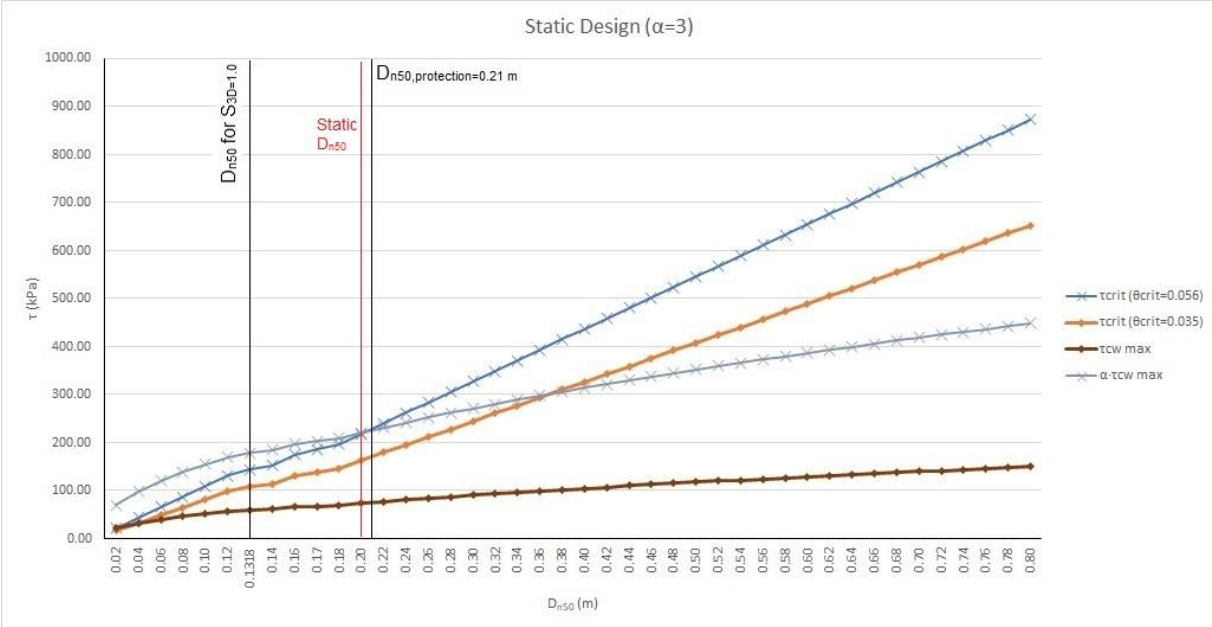

Figure A.19 - Static design α=3 (Test 1a).

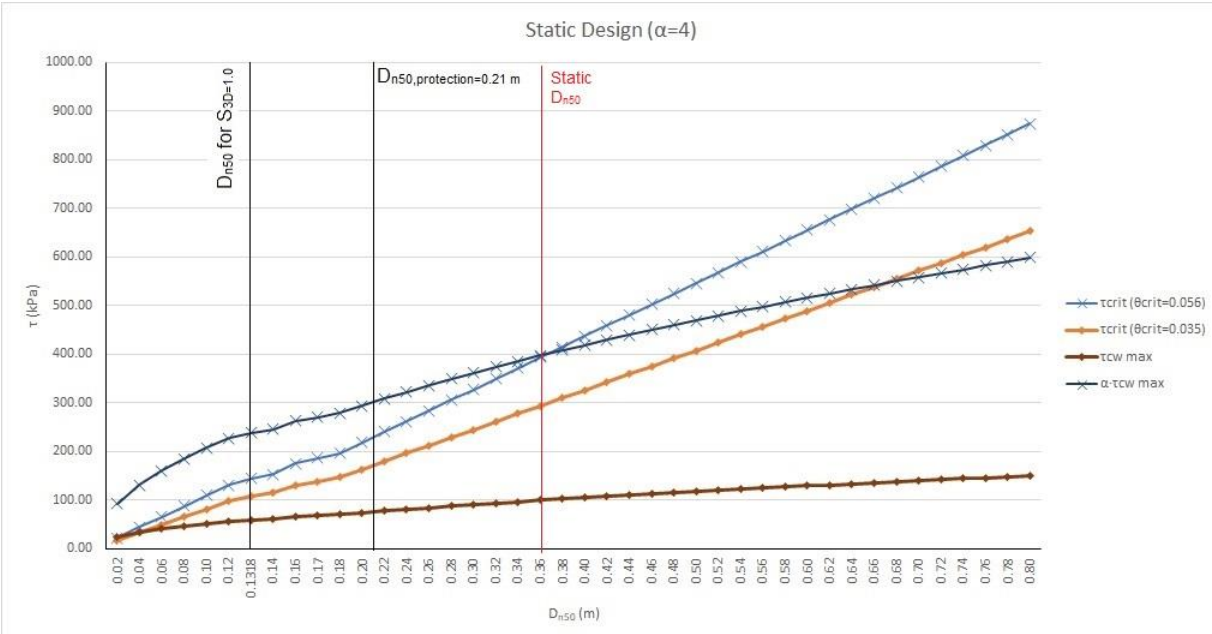

Figure A. 20 - Static design α=4 (Test 1a).

A.5: TEST 1B

Table A.19 - Prototype and model inputs (Test 1b).

Prototype Target Conditions			
H_{m0} (m)	T_p (s)	d (m)	U_c (m/s)
5.3	11.31	18.00	1.068
MATLAB:	U_m (m/s)	1.032	

Model Target Conditions			
H_{m0} (m)	T_p (s)	d (m)	U_c (m/s)
0.106	1.60	0.36	0.151
MATLAB:	U_m (m/s)	0.146	

Scale (Froude)	
Scale λ_L:	0.020
Scale λ_T:	0.141
Scale λ_V:	0.141

Prototype (Other Parameters)					
ρ_w (kg/m^3):	1025	s	delta	g	σ_U
ρ_s (kg/m^3):	2694	2.628	1.628	9.81	2.04
A (m):	1.858				

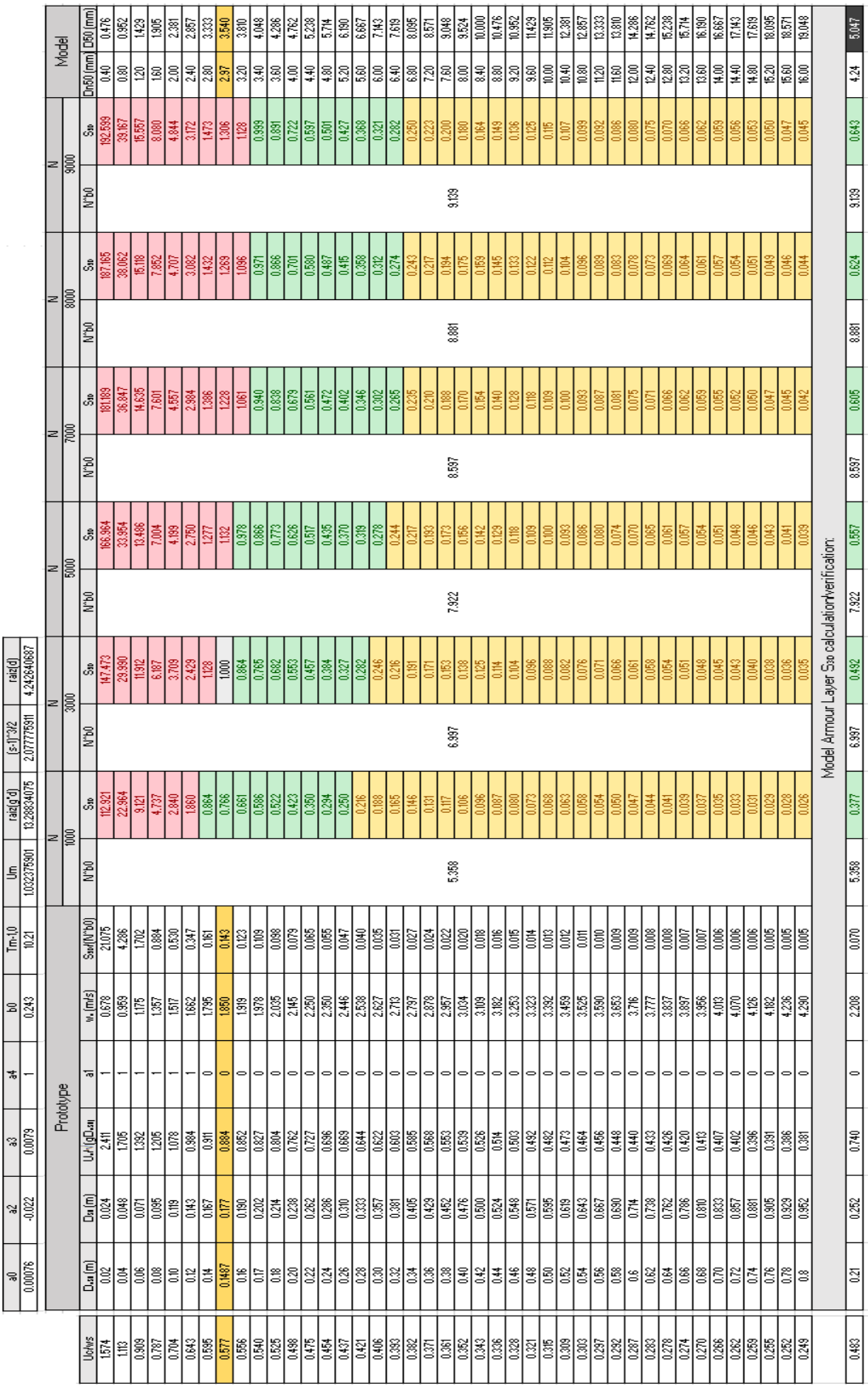

a0	a2	a3	a4	b0	Tm-10	Um	raiz(g*d)	(s-1)^3/2	raiz(d)
0,00076	-0,022	0,0079	1	0,243	10,21	1,032276901	13,28834075	2,077775911	4,242640687

Ucrivs	Prototype							N 1000		N 3000		N 5000		N 7000		N 8000		N 9000		Model	
	Dₙ₅₀ (m)	Dₙ₅₀ (m)	Ur-r/gDₙ₅₀	a1	wₛ (m/s)	Sw#(N^b0)	N^b0	Sw	N^b0	Sw	N^b0	Sw	N^b0	Sw	N^b0	Sw	N^b0	Sw	Dn50 (mm)	D50 (mm)
1,574	0,02	0,024	2,411	1	0,678	21,075		112,921		147,473		166,964		181,189		187,165		192,599	0,40	0,476
1,113	0,04	0,048	1,705	1	0,959	4,286		22,964		29,990		33,954		36,847		38,062		39,167	0,80	0,952
0,909	0,06	0,071	1,392	1	1,175	1,702		9,121		11,912		13,486		14,635		15,118		15,557	1,20	1,429
0,787	0,08	0,095	1,205	1	1,357	0,884		4,737		6,187		7,004		7,601		7,852		8,080	1,60	1,905
0,704	0,10	0,119	1,078	1	1,517	0,530		2,840		3,709		4,199		4,557		4,707		4,844	2,00	2,381
0,643	0,12	0,143	0,984	1	1,662	0,347		1,860		2,429		2,750		2,984		3,082		3,172	2,40	2,857
0,595	0,14	0,167	0,911	0	1,795	0,161		0,864		1,128		1,277		1,386		1,432		1,473	2,80	3,333
0,577	0,1487	0,177	0,884	0	1,850	0,143		0,766		1,000		1,132		1,228		1,269		1,306	2,97	3,540
0,566	0,16	0,190	0,862	0	1,919	0,123		0,681		0,884		0,978		1,061		1,096		1,128	3,20	3,810
0,540	0,17	0,202	0,827	0	1,978	0,109		0,586		0,765		0,866		0,940		0,971		0,999	3,40	4,048
0,525	0,18	0,214	0,804	0	2,035	0,098		0,522		0,682		0,773		0,838		0,866		0,891	3,60	4,286
0,498	0,20	0,238	0,762	0	2,145	0,079		0,423		0,553		0,626		0,679		0,701		0,722	4,00	4,762
0,475	0,22	0,262	0,727	0	2,250	0,065		0,350		0,457		0,517		0,561		0,580		0,597	4,40	5,238
0,454	0,24	0,286	0,696	0	2,350	0,055		0,294		0,384		0,435		0,472		0,487		0,501	4,80	5,714
0,437	0,26	0,310	0,669	0	2,446	0,047		0,250		0,327		0,370		0,402		0,415		0,427	5,20	6,190
0,421	0,28	0,333	0,644	0	2,538	0,040		0,216		0,282		0,319		0,346		0,358		0,368	5,60	6,667
0,406	0,30	0,357	0,622	0	2,627	0,035		0,188		0,246		0,278		0,302		0,312		0,321	6,00	7,143
0,393	0,32	0,381	0,603	0	2,713	0,031		0,165		0,216		0,244		0,265		0,274		0,282	6,40	7,619
0,382	0,34	0,405	0,585	0	2,797	0,027		0,146		0,191		0,217		0,235		0,243		0,250	6,80	8,095
0,371	0,36	0,429	0,568	0	2,878	0,024		0,131		0,171		0,193		0,210		0,217		0,223	7,20	8,571
0,361	0,38	0,452	0,553	0	2,957	0,022	5,358	0,117	6,997	0,153	7,922	0,173	8,597	0,188	8,881	0,194	9,109	0,200	7,60	9,048
0,352	0,40	0,476	0,539	0	3,034	0,020		0,106		0,138		0,156		0,170		0,175		0,180	8,00	9,524
0,343	0,42	0,500	0,526	0	3,109	0,018		0,096		0,125		0,142		0,154		0,159		0,164	8,40	10,000
0,336	0,44	0,524	0,514	0	3,182	0,016		0,087		0,114		0,129		0,140		0,145		0,149	8,80	10,476
0,328	0,46	0,548	0,503	0	3,253	0,015		0,080		0,104		0,118		0,128		0,133		0,136	9,20	10,952
0,321	0,48	0,571	0,492	0	3,323	0,014		0,073		0,096		0,109		0,118		0,122		0,125	9,60	11,429
0,315	0,50	0,595	0,482	0	3,392	0,013		0,068		0,088		0,100		0,109		0,112		0,115	10,00	11,905
0,309	0,52	0,619	0,473	0	3,459	0,012		0,063		0,082		0,093		0,100		0,104		0,107	10,40	12,381
0,303	0,54	0,643	0,464	0	3,525	0,011		0,058		0,076		0,086		0,093		0,096		0,099	10,80	12,857
0,297	0,56	0,667	0,456	0	3,590	0,010		0,054		0,071		0,080		0,087		0,089		0,092	11,20	13,333
0,292	0,58	0,690	0,448	0	3,653	0,009		0,050		0,066		0,074		0,081		0,083		0,086	11,60	13,810
0,287	0,6	0,714	0,440	0	3,716	0,009		0,047		0,061		0,070		0,075		0,078		0,080	12,00	14,286
0,283	0,62	0,738	0,433	0	3,777	0,008		0,044		0,058		0,065		0,071		0,073		0,075	12,40	14,762
0,278	0,64	0,762	0,426	0	3,837	0,008		0,041		0,054		0,061		0,066		0,069		0,070	12,80	15,238
0,274	0,66	0,786	0,420	0	3,897	0,007		0,039		0,051		0,057		0,062		0,064		0,066	13,20	15,714
0,270	0,68	0,810	0,413	0	3,956	0,007		0,037		0,048		0,054		0,059		0,061		0,062	13,60	16,190
0,266	0,70	0,833	0,407	0	4,013	0,006		0,035		0,045		0,051		0,055		0,057		0,059	14,00	16,667
0,262	0,72	0,857	0,402	0	4,070	0,006		0,033		0,043		0,048		0,052		0,054		0,056	14,40	17,143
0,259	0,74	0,881	0,396	0	4,126	0,006		0,031		0,040		0,046		0,050		0,051		0,053	14,80	17,619
0,255	0,76	0,905	0,391	0	4,182	0,005		0,029		0,038		0,043		0,047		0,049		0,050	15,20	18,095
0,252	0,78	0,929	0,386	0	4,236	0,005		0,028		0,036		0,041		0,045		0,046		0,047	15,60	18,571
0,249	0,8	0,952	0,381	0	4,290	0,005		0,026		0,035		0,039		0,042		0,044		0,045	16,00	19,048
										Model Armour Layer Sw calculation/verification:										
0,483	0,21	0,252	0,740	0	2,208	0,070	5,358	0,377	6,997	0,492	7,922	0,557	8,597	0,605	8,881	0,624	9,109	0,643	4,24	5,047

Figure A.21 - Dynamic design calculation (Test 1b).

Table A.20 - Static design calculation (Test 1b - 1 of 5).

Prototype				
D67.5 (m)	Dn50 (m)	D50 (m)	τcrit (θcrit=0.056) (kPa)	τcrit (θcrit=0.035) (kPa)
0.028	0.02	0.024	21.83	16.31
0.057	0.04	0.048	43.66	32.61
0.085	0.06	0.071	65.49	48.92
0.114	0.08	0.095	87.32	65.22
0.142	0.10	0.119	109.15	81.53
0.171	0.12	0.143	130.98	97.84
0.199	0.14	0.167	152.81	114.14
0.212	0.1487	0.177	162.31	121.24
0.228	0.16	0.190	174.64	130.45
0.242	0.17	0.202	185.56	138.60
0.256	0.18	0.214	196.47	146.76
0.285	0.20	0.238	218.31	163.06
0.313	0.22	0.262	240.14	179.37
0.341	0.24	0.286	261.97	195.67
0.370	0.26	0.310	283.80	211.98
0.398	0.28	0.333	305.63	228.29
0.427	0.30	0.357	327.46	244.59
0.455	0.32	0.381	349.29	260.90
0.484	0.34	0.405	371.12	277.20
0.512	0.36	0.429	392.95	293.51
0.541	0.38	0.452	414.78	309.82
0.569	0.40	0.476	436.61	326.12
0.598	0.42	0.500	458.44	342.43
0.626	0.44	0.524	480.27	358.74
0.654	0.46	0.548	502.10	375.04
0.683	0.48	0.571	523.93	391.35
0.711	0.50	0.595	545.76	407.65
0.740	0.52	0.619	567.59	423.96
0.768	0.54	0.643	589.42	440.27
0.797	0.56	0.667	611.25	456.57
0.825	0.58	0.690	633.09	472.88
0.854	0.60	0.714	654.92	489.18
0.882	0.62	0.738	676.75	505.49
0.911	0.64	0.762	698.58	521.80
0.939	0.66	0.786	720.41	538.10
0.967	0.68	0.810	742.24	554.41
0.996	0.70	0.833	764.07	570.72
1.024	0.72	0.857	785.90	587.02
1.053	0.74	0.881	807.73	603.33
1.081	0.76	0.905	829.56	619.63
1.110	0.78	0.929	851.39	635.94
1.138	0.80	0.952	873.22	652.25

Table A.21 - Static design calculation (Test 1b - 2 of 5).

Prototype				
τc (kPa)	fc	ks (m)	z0_c	τw (kPa)
2.84	4.86E-03	0.060	1.98E-03	21.64
3.40	5.81E-03	0.119	3.97E-03	31.03
3.80	6.50E-03	0.179	5.95E-03	38.31
4.13	7.07E-03	0.238	7.94E-03	44.50
4.42	7.57E-03	0.298	9.92E-03	49.97
4.68	8.01E-03	0.357	1.19E-02	54.94
4.92	8.41E-03	0.417	1.39E-02	59.52
5.01	8.58E-03	0.443	1.48E-02	61.42
5.14	8.79E-03	0.476	1.59E-02	63.80
5.24	8.97E-03	0.506	1.69E-02	65.85
5.34	9.14E-03	0.536	1.79E-02	67.83
5.54	9.48E-03	0.595	1.98E-02	71.65
5.72	9.80E-03	0.655	2.18E-02	75.30
5.90	1.01E-02	0.714	2.38E-02	78.78
6.07	1.04E-02	0.774	2.58E-02	82.13
6.24	1.07E-02	0.833	2.78E-02	85.36
6.40	1.10E-02	0.893	2.98E-02	88.47
6.56	1.12E-02	0.952	3.17E-02	91.49
6.71	1.15E-02	1.012	3.37E-02	94.42
6.85	1.17E-02	1.071	3.57E-02	97.27
7.00	1.20E-02	1.131	3.77E-02	100.05
7.14	1.22E-02	1.190	3.97E-02	102.75
7.28	1.25E-02	1.250	4.17E-02	105.39
7.41	1.27E-02	1.310	4.37E-02	107.97
7.55	1.29E-02	1.369	4.56E-02	110.50
7.68	1.31E-02	1.429	4.76E-02	112.97
7.81	1.34E-02	1.488	4.96E-02	115.39
7.93	1.36E-02	1.548	5.16E-02	117.77
8.06	1.38E-02	1.607	5.36E-02	120.10
8.18	1.40E-02	1.667	5.56E-02	122.40
8.30	1.42E-02	1.726	5.75E-02	124.65
8.42	1.44E-02	1.786	5.95E-02	126.87
8.54	1.46E-02	1.845	6.15E-02	129.05
8.66	1.48E-02	1.905	6.35E-02	131.20
8.77	1.50E-02	1.964	6.55E-02	133.31
8.89	1.52E-02	2.024	6.75E-02	135.40
9.00	1.54E-02	2.083	6.94E-02	137.45
9.11	1.56E-02	2.143	7.14E-02	139.48
9.22	1.58E-02	2.202	7.34E-02	141.48
9.33	1.60E-02	2.262	7.54E-02	143.46
9.44	1.62E-02	2.321	7.74E-02	145.41
9.55	1.63E-02	2.381	7.94E-02	147.34

Table A.22 - Static design calculation (Test 1b - 3 of 5).

Prototype			
fw	z0_w	τcw_m (kPa)	τcw_max (kPa)
3.96E-02	1.98E-03	5.14	26.78
5.68E-02	3.97E-03	6.32	37.35
7.01E-02	5.95E-03	7.17	45.48
8.15E-02	7.94E-03	7.86	52.36
9.15E-02	9.92E-03	8.46	58.43
1.01E-01	1.19E-02	9.00	63.94
1.09E-01	1.39E-02	9.49	69.02
1.12E-01	1.48E-02	9.69	71.11
1.17E-01	1.59E-02	9.95	73.75
1.21E-01	1.69E-02	10.16	76.01
1.24E-01	1.79E-02	10.37	78.21
1.31E-01	1.98E-02	10.77	82.43
1.38E-01	2.18E-02	11.16	86.45
1.44E-01	2.38E-02	11.52	90.30
1.50E-01	2.58E-02	11.88	94.00
1.56E-01	2.78E-02	12.21	97.57
1.62E-01	2.98E-02	12.54	101.02
1.68E-01	3.17E-02	12.86	104.35
1.73E-01	3.37E-02	13.17	107.59
1.78E-01	3.57E-02	13.47	110.74
1.83E-01	3.77E-02	13.76	113.81
1.88E-01	3.97E-02	14.05	116.80
1.93E-01	4.17E-02	14.33	119.72
1.98E-01	4.37E-02	14.61	122.58
2.02E-01	4.56E-02	14.88	125.37
2.07E-01	4.76E-02	15.14	128.11
2.11E-01	4.96E-02	15.40	130.79
2.16E-01	5.16E-02	15.66	133.43
2.20E-01	5.36E-02	15.91	136.01
2.24E-01	5.56E-02	16.16	138.56
2.28E-01	5.75E-02	16.41	141.06
2.32E-01	5.95E-02	16.65	143.52
2.36E-01	6.15E-02	16.89	145.94
2.40E-01	6.35E-02	17.12	148.32
2.44E-01	6.55E-02	17.36	150.67
2.48E-01	6.75E-02	17.59	152.99
2.52E-01	6.94E-02	17.82	155.27
2.55E-01	7.14E-02	18.04	157.53
2.59E-01	7.34E-02	18.27	159.75
2.63E-01	7.54E-02	18.49	161.95
2.66E-01	7.74E-02	18.71	164.12
2.70E-01	7.94E-02	18.93	166.27

Table A.23 - Static design calculation (Test 1b - 4 of 5).

Prototype					
α4	α3	α2	α4·τcw_max (kPa)	α3·τcw_max (kPa)	α2·τcw_max (kPa)
4.00	3.00	2.00	107.11	80.33	53.55
			149.40	112.05	74.70
			181.93	136.45	90.96
			209.44	157.08	104.72
			233.74	175.30	116.87
			255.76	191.82	127.88
			276.07	207.05	138.03
			284.46	213.34	142.23
			295.00	221.25	147.50
			304.04	228.03	152.02
			312.83	234.62	156.41
			329.72	247.29	164.86
			345.81	259.36	172.91
			361.22	270.91	180.61
			376.02	282.01	188.01
			390.28	292.71	195.14
			404.06	303.05	202.03
			417.41	313.06	208.71
			430.37	322.78	215.18
			442.97	332.22	221.48
			455.23	341.43	227.62
			467.20	350.40	233.60
			478.88	359.16	239.44
			490.31	367.73	245.15
			501.49	376.11	250.74
			512.44	384.33	256.22
			523.18	392.38	261.59
			533.71	400.28	266.86
			544.06	408.04	272.03
			554.23	415.67	277.11
			564.22	423.17	282.11
			574.06	430.55	287.03
			583.75	437.81	291.87
			593.28	444.96	296.64
			602.68	452.01	301.34
			611.95	458.96	305.97
			621.09	465.82	310.54
			630.11	472.58	315.05
			639.01	479.26	319.51
			647.80	485.85	323.90
			656.48	492.36	328.24
			665.06	498.80	332.53

Table A.24 - Static design calculation (Test 1b - 5 of 5).

Prototype			
Φ (◦)	θmax	θcrit (Shields)	θcrit (De Vos)
	0.069		
	0.048		
	0.039		
	0.034		
	0.030		
	0.027		
	0.025		
	0.025		
	0.024		
	0.023		
	0.022		
	0.021		
	0.020		
	0.019		
	0.019		
	0.018		
	0.017		
	0.017		
	0.016		
	0.016		
	0.015		
0	0.015	0.056	0.035
	0.015		
	0.014		
	0.014		
	0.014		
	0.013		
	0.013		
	0.013		
	0.013		
	0.012		
	0.012		
	0.012		
	0.012		
	0.012		
	0.012		
	0.011		
	0.011		
	0.011		
	0.011		
	0.011		
	0.011		

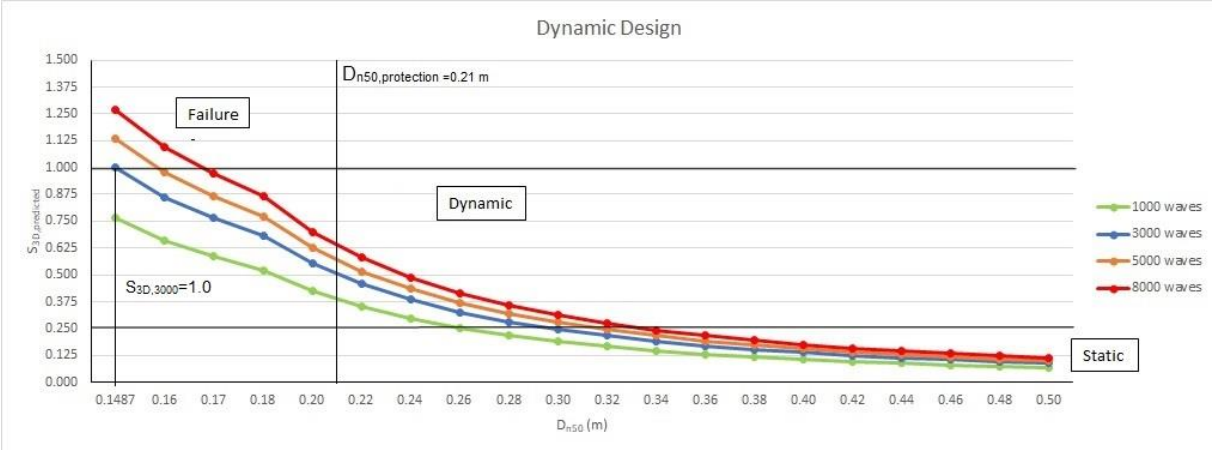

Figure A.22 - D_{n50} for S_{3D}=1.0 (Test 1b).

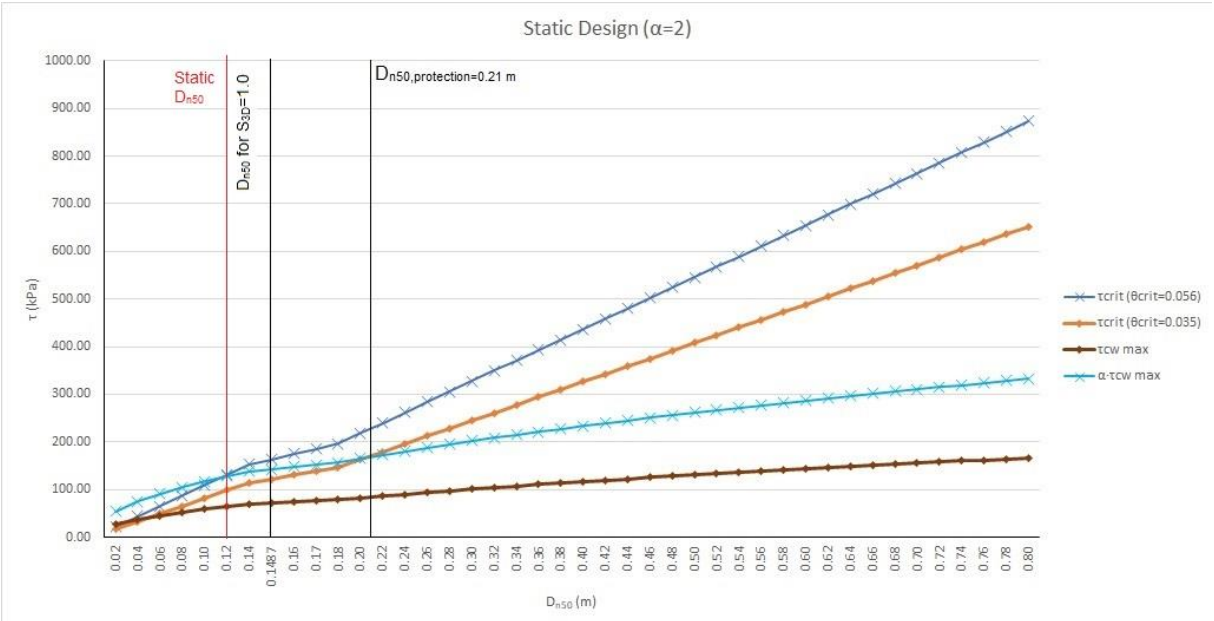

Figure A.23 - Static design α=2 (Test 1b).

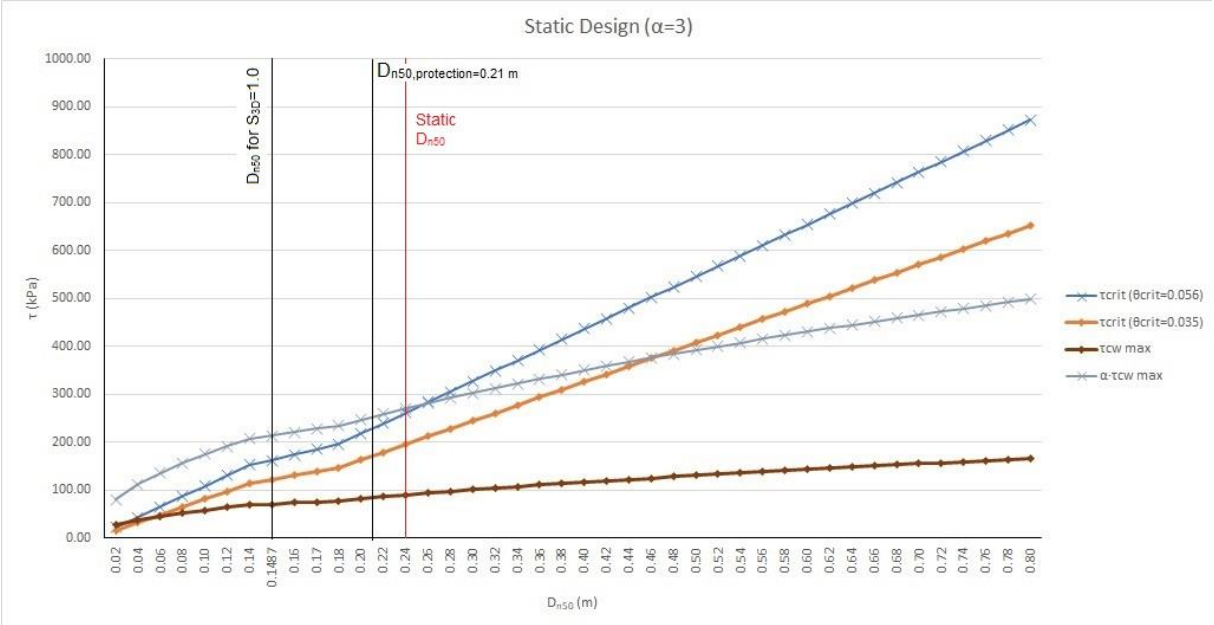

Figure A.24 - Static design α=3 (Test 1b).

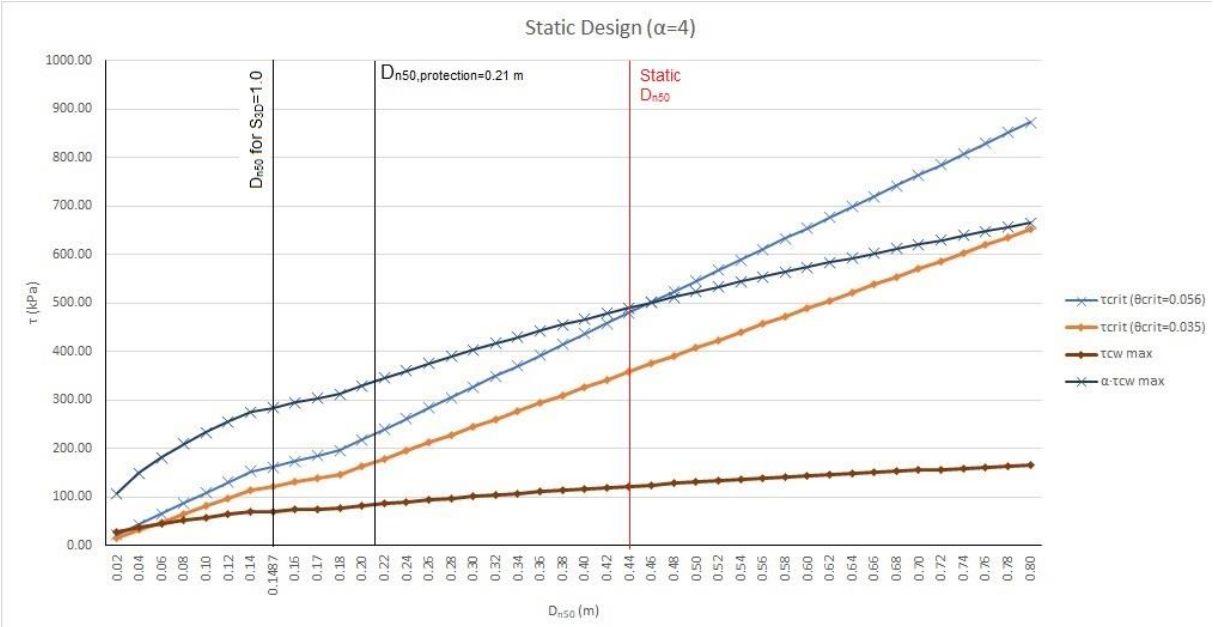

Figure A.25 - Static design α=4 (Test 1b).

A.6: TEST 2

Table A.25 - Prototype and model inputs (Test 2).

Prototype Target Conditions			
H_{m0} (m)	T_p (s)	d (m)	U_c (m/s)
5.3	11.22	18	1.068
MATLAB:	U_m (m/s)	1.025	

Model Target Conditions			
H_{m0} (m)	T_p (s)	d (m)	U_c (m/s)
0.106	1.59	0.36	0.151
MATLAB:	U_m (m/s)	0.15	

Scale (Froude)	
Scale λ_L:	0.020
Scale λ_T:	0.141
Scale λ_V:	0.141

Prototype (Other Parameters)					
ρ_w (kg/m^3):	1025	s	delta	g	σ_U
ρ_s (kg/m^3):	2694	2.628	1.628	9.81	2.04
A (m):	1.831				

a0	a2	a3	a4	b0	Tm-10	Um	rate(g*d)	(z-1)^3/2	rate(d)
0.00076	-0.022	0.0079	1	0.243	10.14	1.0253	16.28634075	2.017775911	4.242640687

	Prototype								N		N		N		N		N		Model	
									1000		3000		5000		7000		8000		3000		
Ucrlve	Dss (m)	Dss (m)	Ui,k / (gD$_{ss}$)	a1	w$_s$ (m/s)	$Sa/(N^b0)	N^b0	Sa0	N^b0	Sa0	N^b0	Sa0	N^b0	Sa0	N^b0	Sa0	N^b0	Sa0	Dn50 (mm)	D50 (mm)
1.574	0.02	0.024	2.411	1	0.678	20.710	5.358	110.362	6.397	144.315	7.322	164.067	8.537	178.046	8.881	183.318	9.159	183.258	0.40	0.476
1.113	0.04	0.048	1.705	1	0.359	4.201		22.503		29.396		33.281		36.117		37.308		38.331	0.80	0.952
0.909	0.06	0.071	1.392	1	1.175	1.666		8.926		11.657		13.198		14.322		14.794		15.224	1.20	1.429
0.787	0.08	0.095	1.205	1	1.357	0.864		4.630		6.046		6.845		7.428		7.673		7.896	1.60	1.905
0.704	0.10	0.119	1.078	1	1.517	0.517		2.772		3.620		4.099		4.448		4.595		4.728	2.00	2.381
0.643	0.12	0.143	0.984	1	1.662	0.338		1.813		2.368		2.681		2.909		3.005		3.092	2.40	2.857
0.595	0.14	0.167	0.911	0	1.795	0.156		0.833		1.088		1.232		1.337		1.381		1.422	2.80	3.333
0.562	0.14605	0.174	0.892	0	1.833	0.143		0.766		1.000		1.132		1.229		1.269		1.306	2.92	3.477
0.556	0.16	0.190	0.852	0	1.919	0.119		0.638		0.833		0.943		1.024		1.058		1.088	3.20	3.810
0.540	0.17	0.202	0.827	0	1.978	0.105		0.565		0.738		0.836		0.907		0.937		0.964	3.40	4.048
0.525	0.18	0.214	0.804	0	2.035	0.094		0.504		0.658		0.745		0.809		0.836		0.860	3.60	4.286
0.498	0.20	0.238	0.762	0	2.145	0.076		0.408		0.533		0.604		0.655		0.677		0.697	4.00	4.762
0.475	0.22	0.262	0.727	0	2.250	0.063		0.338		0.441		0.499		0.542		0.559		0.576	4.40	5.238
0.454	0.24	0.286	0.696	0	2.350	0.053		0.284		0.370		0.419		0.455		0.470		0.484	4.80	5.714
0.437	0.26	0.310	0.669	0	2.446	0.045		0.242		0.316		0.357		0.388		0.401		0.412	5.20	6.190
0.421	0.28	0.333	0.644	0	2.538	0.039		0.208		0.272		0.308		0.334		0.345		0.355	5.60	6.667
0.406	0.30	0.357	0.622	0	2.627	0.034		0.182		0.237		0.268		0.291		0.301		0.310	6.00	7.143
0.393	0.32	0.381	0.603	0	2.713	0.030		0.160		0.208		0.236		0.256		0.264		0.272	6.40	7.619
0.382	0.34	0.405	0.585	0	2.797	0.026		0.141		0.185		0.209		0.227		0.234		0.241	6.80	8.095
0.371	0.36	0.429	0.568	0	2.878	0.024		0.126		0.165		0.186		0.202		0.209		0.215	7.20	8.571
0.361	0.38	0.452	0.553	0	2.957	0.021		0.113		0.148		0.167		0.182		0.188		0.193	7.60	9.048
0.352	0.40	0.476	0.539	0	3.034	0.019		0.102		0.133		0.151		0.164		0.169		0.174	8.00	9.524
0.343	0.42	0.500	0.526	0	3.109	0.017		0.093		0.121		0.137		0.149		0.153		0.158	8.40	10.000
0.336	0.44	0.524	0.514	0	3.182	0.016		0.084		0.110		0.125		0.135		0.140		0.144	8.80	10.476
0.328	0.46	0.548	0.503	0	3.253	0.014		0.077		0.101		0.114		0.124		0.128		0.132	9.20	10.952
0.321	0.48	0.571	0.492	0	3.323	0.013		0.071		0.093		0.105		0.114		0.118		0.121	9.60	11.429
0.315	0.50	0.595	0.482	0	3.392	0.012		0.065		0.085		0.097		0.105		0.108		0.111	10.00	11.905
0.309	0.52	0.619	0.473	0	3.459	0.011		0.060		0.079		0.089		0.097		0.100		0.103	10.40	12.381
0.303	0.54	0.643	0.464	0	3.525	0.010		0.056		0.073		0.083		0.090		0.093		0.096	10.80	12.857
0.297	0.56	0.667	0.456	0	3.590	0.010		0.052		0.068		0.077		0.084		0.086		0.089	11.20	13.333
0.292	0.58	0.690	0.448	0	3.653	0.009		0.049		0.063		0.072		0.078		0.080		0.083	11.60	13.810
0.287	0.6	0.714	0.440	0	3.716	0.008		0.045		0.059		0.067		0.073		0.075		0.077	12.00	14.286
0.283	0.62	0.738	0.433	0	3.777	0.008		0.042		0.055		0.063		0.068		0.070		0.072	12.40	14.762
0.278	0.64	0.762	0.426	0	3.837	0.007		0.040		0.052		0.059		0.064		0.066		0.068	12.80	15.238
0.274	0.66	0.786	0.420	0	3.897	0.007		0.038		0.049		0.055		0.060		0.062		0.064	13.20	15.714
0.270	0.68	0.810	0.413	0	3.956	0.007		0.035		0.046		0.052		0.057		0.059		0.060	13.60	16.190
0.266	0.70	0.833	0.407	0	4.013	0.006		0.033		0.044		0.049		0.053		0.055		0.057	14.00	16.667
0.262	0.72	0.857	0.402	0	4.070	0.006		0.032		0.041		0.047		0.051		0.052		0.054	14.40	17.143
0.259	0.74	0.881	0.396	0	4.126	0.006		0.030		0.039		0.044		0.048		0.049		0.051	14.80	17.619
0.255	0.76	0.905	0.391	0	4.182	0.005		0.028		0.037		0.042		0.045		0.047		0.048	15.20	18.095
0.252	0.78	0.929	0.386	0	4.236	0.005		0.027		0.035		0.040		0.043		0.045		0.046	15.60	18.571
0.249	0.8	0.952	0.381	0	4.290	0.005		0.026		0.033		0.038		0.041		0.042		0.044	16.00	19.048
													Model Armour Layer Sop calculation/verification:							
0.483	0.21	0.252	0.740	0	2.208	0.068	5.358	0.364	6.397	0.475	7.322	0.598	8.537	0.583	8.881	0.603	9.159	0.620	4.24	5.047

Figure A.26 - Dynamic design calculation (Test 2).

Table A.26 - Static design calculation (Test 2 – 1 of 5).

Prototype					
D67.5 (m)	Dn50 (m)	D50 (m)	τcrit (θcrit=0.056) (kPa)	τcrit (θcrit=0.035) (kPa)	τc (kPa)
0.028	0.02	0.024	21.83	16.31	2.84
0.057	0.04	0.048	43.66	32.61	3.40
0.085	0.06	0.071	65.49	48.92	3.80
0.114	0.08	0.095	87.32	65.22	4.13
0.142	0.10	0.119	109.15	81.53	4.42
0.171	0.12	0.143	130.98	97.84	4.68
0.199	0.14	0.167	152.81	114.14	4.92
0.208	0.14605	0.174	159.42	119.08	4.98
0.228	0.16	0.190	174.64	130.45	5.14
0.242	0.17	0.202	185.56	138.60	5.24
0.256	0.18	0.214	196.47	146.76	5.34
0.285	0.20	0.238	218.31	163.06	5.54
0.313	0.22	0.262	240.14	179.37	5.72
0.341	0.24	0.286	261.97	195.67	5.90
0.370	0.26	0.310	283.80	211.98	6.07
0.398	0.28	0.333	305.63	228.29	6.24
0.427	0.30	0.357	327.46	244.59	6.40
0.455	0.32	0.381	349.29	260.90	6.56
0.484	0.34	0.405	371.12	277.20	6.71
0.512	0.36	0.429	392.95	293.51	6.85
0.541	0.38	0.452	414.78	309.82	7.00
0.569	0.40	0.476	436.61	326.12	7.14
0.598	0.42	0.500	458.44	342.43	7.28
0.626	0.44	0.524	480.27	358.74	7.41
0.654	0.46	0.548	502.10	375.04	7.55
0.683	0.48	0.571	523.93	391.35	7.68
0.711	0.50	0.595	545.76	407.65	7.81
0.740	0.52	0.619	567.59	423.96	7.93
0.768	0.54	0.643	589.42	440.27	8.06
0.797	0.56	0.667	611.25	456.57	8.18
0.825	0.58	0.690	633.09	472.88	8.30
0.854	0.60	0.714	654.92	489.18	8.42
0.882	0.62	0.738	676.75	505.49	8.54
0.911	0.64	0.762	698.58	521.80	8.66
0.939	0.66	0.786	720.41	538.10	8.77
0.967	0.68	0.810	742.24	554.41	8.89
0.996	0.70	0.833	764.07	570.72	9.00
1.024	0.72	0.857	785.90	587.02	9.11
1.053	0.74	0.881	807.73	603.33	9.22
1.081	0.76	0.905	829.56	619.63	9.33
1.110	0.78	0.929	851.39	635.94	9.44
1.138	0.80	0.952	873.22	652.25	9.55

Table A.27 - Static design calculation (Test 2 - 2 of 5).

Prototype				
fc	ks (m)	z0_c	τw (kPa)	fw
4.86E-03	0.060	1.98E-03	21.50	3.99E-02
5.81E-03	0.119	3.97E-03	30.84	5.72E-02
6.50E-03	0.179	5.95E-03	38.07	7.07E-02
7.07E-03	0.238	7.94E-03	44.22	8.21E-02
7.57E-03	0.298	9.92E-03	49.66	9.22E-02
8.01E-03	0.357	1.19E-02	54.60	1.01E-01
8.41E-03	0.417	1.39E-02	59.15	1.10E-01
8.53E-03	0.435	1.45E-02	60.47	1.12E-01
8.79E-03	0.476	1.59E-02	63.41	1.18E-01
8.97E-03	0.506	1.69E-02	65.44	1.21E-01
9.14E-03	0.536	1.79E-02	67.41	1.25E-01
9.48E-03	0.595	1.98E-02	71.21	1.32E-01
9.80E-03	0.655	2.18E-02	74.83	1.39E-01
1.01E-02	0.714	2.38E-02	78.29	1.45E-01
1.04E-02	0.774	2.58E-02	81.62	1.51E-01
1.07E-02	0.833	2.78E-02	84.82	1.57E-01
1.10E-02	0.893	2.98E-02	87.92	1.63E-01
1.12E-02	0.952	3.17E-02	90.92	1.69E-01
1.15E-02	1.012	3.37E-02	93.83	1.74E-01
1.17E-02	1.071	3.57E-02	96.67	1.79E-01
1.20E-02	1.131	3.77E-02	99.42	1.85E-01
1.22E-02	1.190	3.97E-02	102.11	1.90E-01
1.25E-02	1.250	4.17E-02	104.73	1.94E-01
1.27E-02	1.310	4.37E-02	107.30	1.99E-01
1.29E-02	1.369	4.56E-02	109.81	2.04E-01
1.31E-02	1.429	4.76E-02	112.26	2.08E-01
1.34E-02	1.488	4.96E-02	114.67	2.13E-01
1.36E-02	1.548	5.16E-02	117.03	2.17E-01
1.38E-02	1.607	5.36E-02	119.35	2.22E-01
1.40E-02	1.667	5.56E-02	121.63	2.26E-01
1.42E-02	1.726	5.75E-02	123.87	2.30E-01
1.44E-02	1.786	5.95E-02	126.08	2.34E-01
1.46E-02	1.845	6.15E-02	128.24	2.38E-01
1.48E-02	1.905	6.35E-02	130.38	2.42E-01
1.50E-02	1.964	6.55E-02	132.48	2.46E-01
1.52E-02	2.024	6.75E-02	134.55	2.50E-01
1.54E-02	2.083	6.94E-02	136.60	2.54E-01
1.56E-02	2.143	7.14E-02	138.61	2.57E-01
1.58E-02	2.202	7.34E-02	140.60	2.61E-01
1.60E-02	2.262	7.54E-02	142.57	2.65E-01
1.62E-02	2.321	7.74E-02	144.50	2.68E-01
1.63E-02	2.381	7.94E-02	146.42	2.72E-01

Table A.28 - Static design calculation (Test 2 - 3 of 5).

Prototype					
z0_w	τcw_m (kPa)	τcw_max (kPa)	α4	α3	α2
1.98E-03	5.13	26.64			
3.97E-03	6.31	37.15			
5.95E-03	7.16	45.24			
7.94E-03	7.86	52.08			
9.92E-03	8.46	58.12			
1.19E-02	8.99	63.59			
1.39E-02	9.49	68.64			
1.45E-02	9.63	70.09			
1.59E-02	9.94	73.35			
1.69E-02	10.16	75.59			
1.79E-02	10.36	77.78			
1.98E-02	10.77	81.98			
2.18E-02	11.15	85.98			
2.38E-02	11.52	89.80			
2.58E-02	11.87	93.48			
2.78E-02	12.21	97.03			
2.98E-02	12.53	100.46			
3.17E-02	12.85	103.77			
3.37E-02	13.16	106.99			
3.57E-02	13.46	110.13			
3.77E-02	13.75	113.18	4.00	3.00	2.00
3.97E-02	14.04	116.15			
4.17E-02	14.32	119.05			
4.37E-02	14.60	121.89			
4.56E-02	14.87	124.67			
4.76E-02	15.13	127.40			
4.96E-02	15.39	130.06			
5.16E-02	15.65	132.68			
5.36E-02	15.90	135.26			
5.56E-02	16.15	137.78			
5.75E-02	16.40	140.27			
5.95E-02	16.64	142.71			
6.15E-02	16.88	145.12			
6.35E-02	17.11	147.49			
6.55E-02	17.35	149.83			
6.75E-02	17.58	152.13			
6.94E-02	17.81	154.40			
7.14E-02	18.03	156.65			
7.34E-02	18.26	158.86			
7.54E-02	18.48	161.04			
7.74E-02	18.70	163.20			
7.94E-02	18.92	165.34			

Table A.29 - Static design calculation (Test 2 - 4 of 5).

Prototype		
α4·τcw_max (kPa)	α3·τcw_max (kPa)	α2·τcw_max (kPa)
106.55	79.91	53.27
148.60	111.45	74.30
180.95	135.71	90.47
208.30	156.23	104.15
232.47	174.35	116.23
254.37	190.77	127.18
274.55	205.92	137.28
280.38	210.28	140.19
293.38	220.04	146.69
302.37	226.78	151.19
311.11	233.33	155.55
327.90	245.93	163.95
343.90	257.93	171.95
359.22	269.41	179.61
373.93	280.45	186.97
388.12	291.09	194.06
401.82	301.37	200.91
415.09	311.32	207.55
427.98	320.98	213.99
440.50	330.38	220.25
452.70	339.53	226.35
464.60	348.45	232.30
476.22	357.16	238.11
487.58	365.68	243.79
498.69	374.02	249.35
509.58	382.19	254.79
520.26	390.19	260.13
530.74	398.05	265.37
541.02	405.77	270.51
551.13	413.35	275.57
561.07	420.81	280.54
570.86	428.14	285.43
580.49	435.36	290.24
589.97	442.48	294.98
599.32	449.49	299.66
608.53	456.40	304.26
617.62	463.21	308.81
626.59	469.94	313.29
635.44	476.58	317.72
644.18	483.13	322.09
652.81	489.61	326.41
661.34	496.01	330.67

Table A.30 - Static design calculation (Test 2 - 5 of 5).

Prototype			
Φ (◦)	θmax	θcrit (Shields)	θcrit (De Vos)
	0.068		
	0.048		
	0.039		
	0.033		
	0.030		
	0.027		
	0.025		
	0.025		
	0.024		
	0.023		
	0.022		
	0.021		
	0.020		
	0.019		
	0.018		
	0.018		
	0.017		
	0.017		
	0.016		
	0.016		
	0.015		
0	0.015	0.056	0.035
	0.015		
	0.014		
	0.014		
	0.014		
	0.013		
	0.013		
	0.013		
	0.013		
	0.012		
	0.012		
	0.012		
	0.012		
	0.012		
	0.011		
	0.011		
	0.011		
	0.011		
	0.011		
	0.011		
	0.011		

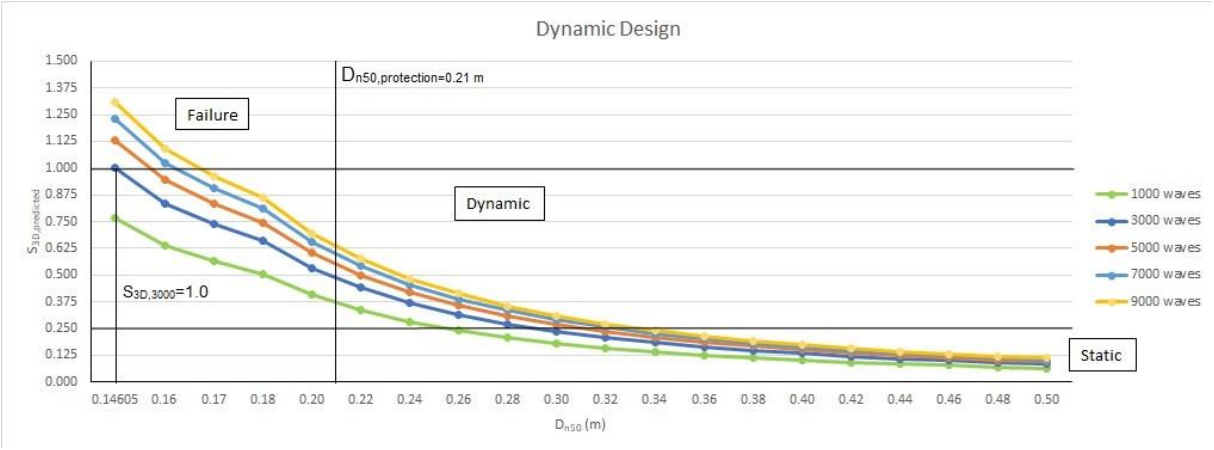

Figure A.27 - D_{n50} for S_{3D}=1.0 (Test 2).

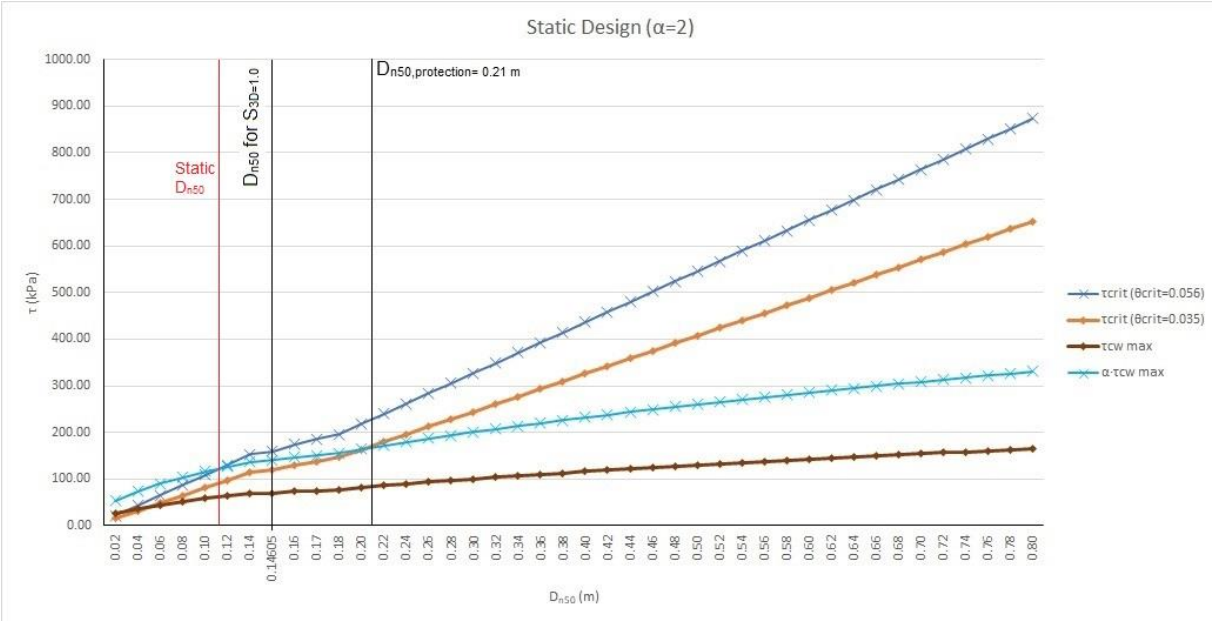

Figure A.28 - Static design α=2 (Test 2).

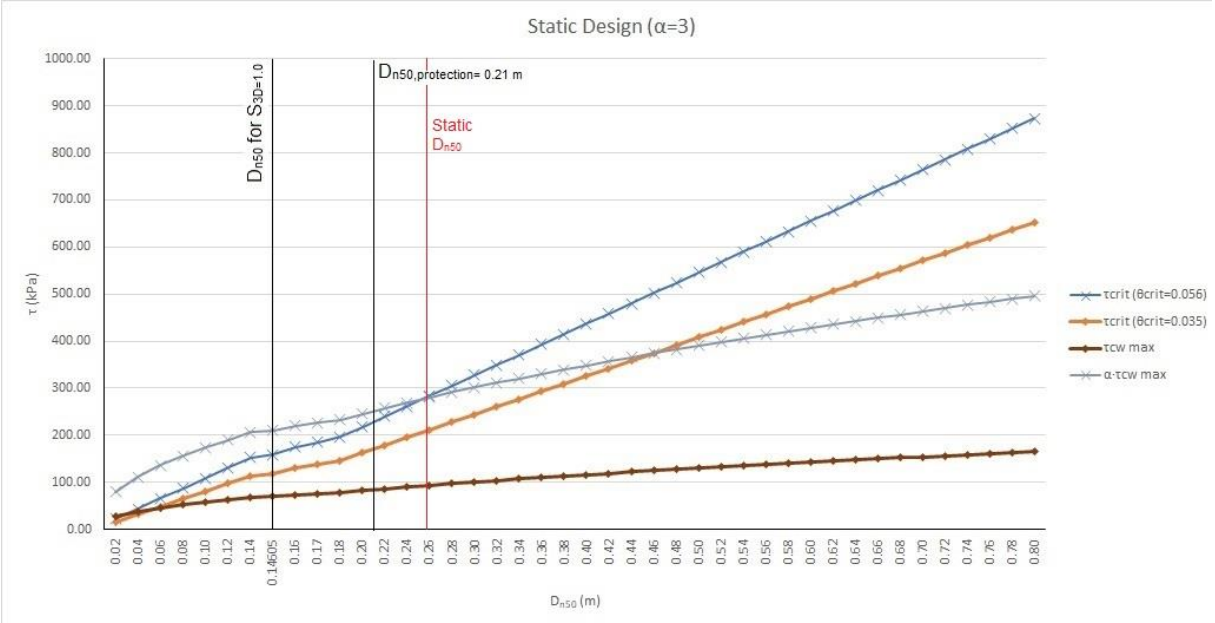

Figure A.29 - Static design α=3 (Test 2).

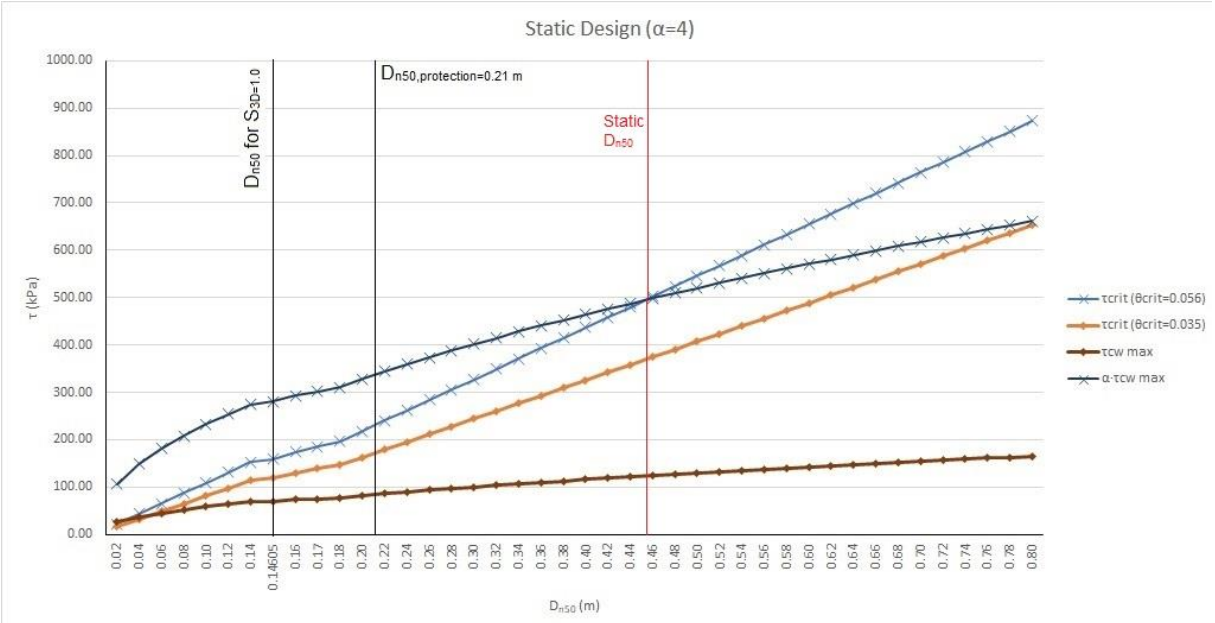

Figure A.30 - Static design α=4 (Test 2).

A.7: INDIVIDUAL WAVE TRAIN CONDITIONS

Table A.31 - Model test results.

Model			
H_{m0} (m)	T_p (s)	U_c (m/s)	U_m (m/s)
0.108	1.540	0.104	0.144
0.095	1.547	0.099	0.127
0.111	1.497	0.103	0.146
0.106	1.608	0.143	0.146
0.108	1.543	0.158	0.145
0.107	1.614	0.158	0.147
0.105	1.623	0.144	0.145
0.109	1.622	0.150	0.150
0.105	1.569	0.150	0.142
0.105	1.569	0.150	0.142
0.107	1.569	0.152	0.145
0.105	1.623	0.150	0.145
0.104	1.526	0.102	0.139
0.106	1.599	0.151	0.146
0.106	1.587	0.151	0.145

Table A.32 – Other model parameters.

Model					
d (m)	σ_U	ρ_w (kg/m3):	ρ_s (kg/m3):	A (m):	s
				0.035	
				0.031	
				0.035	
				0.037	
				0.036	
				0.038	
				0.037	
0.36	2.04	1000	2630	0.039	2.63
				0.035	
				0.035	
				0.036	
				0.037	
				0.034	
				0.037	
				0.037	

			a0	a2	a3	a4	
			0.00076	-0.022	0.0079	1	
		b0	Tm-1,0	Um	raiz(g*d)	(s-1)^3/2	raiz(d)
		0.243	10.14	1.025304833	1.879255172	2.08104469	0.6
		Model					
Uc/ws	Test (Reference)	D_{n50} (mm)	D_{50} (mm)	$U_c/\sqrt{(gD_{n50})}$	a1	w_s (m/s)	$S_{3D}/(N^{b0})$
0.083	O_03a_1000			0.510	0		0.062
0.079	O_04_2000_3000			0.485	0		0.043
0.082	O_04II_2000_5000			0.505	0		0.062
0.115	O_05_1000_1000			0.702	0		0.071
0.127	O_05II_2000_3000			0.777	0		0.064
0.126	O_05III_2000_5000			0.772	0		0.073
0.115	O_05IV_3000_8000			0.705	0		0.071
0.120	O_06_1000_1000	4.239	5.046	0.735	0	1.250	0.078
0.120	O_06II_2000_3000			0.735	0		0.062
0.120	O_06III_2000_5000			0.736	0		0.062
0.122	O_06IV_2000_7000			0.746	0		0.066
0.120	O_06V_2000_9000			0.738	0		0.071
0.082	Test 1a			0.500	0		0.055
0.121	Test 1b			0.739	0		0.070
0.120	Test 2			0.738	0		0.067
		N		N		N	
		1000		3000		5000	
Uc/ws	Test (Reference)	N^b0	S_{3D}	N^b0	S_{3D}	N^b0	S_{3D}
0.083	O_03a_1000		0.335		0.437		0.495
0.079	O_04_2000_3000		0.232		0.303		0.343
0.082	O_04II_2000_5000		0.330		0.431		0.488
0.115	O_05_1000_1000		0.381		0.497		0.563
0.127	O_05II_2000_3000		0.343		0.448		0.507
0.126	O_05III_2000_5000		0.391		0.511		0.579
0.115	O_05IV_3000_8000		0.380		0.496		0.561
0.120	O_06_1000_1000	5.358	0.420	6.997	0.548	7.922	0.621
0.120	O_06II_2000_3000		0.333		0.435		0.493
0.120	O_06III_2000_5000		0.333		0.435		0.493
0.122	O_06IV_2000_7000		0.355		0.463		0.525
0.120	O_06V_2000_9000		0.380		0.496		0.561
0.082	Test 1a		0.296		0.386		0.437
0.121	Test 1b		0.374		0.489		0.553
0.120	Test 2		0.362		0.472		0.535
		N		N		N	
		7000		8000		9000	
Uc/ws	Test (Reference)	N^b0	S_{3D}	N^b0	S_{3D}	N^b0	S_{3D}
0.083	O_03a_1000		0.537		0.555		0.571
0.079	O_04_2000_3000		0.372		0.384		0.395
0.082	O_04II_2000_5000		0.529		0.547		0.562
0.115	O_05_1000_1000		0.611		0.631		0.649
0.127	O_05II_2000_3000		0.551		0.569		0.585
0.126	O_05III_2000_5000		0.628		0.649		0.667
0.115	O_05IV_3000_8000		0.609		0.629		0.648
0.120	O_06_1000_1000	8.597	0.674	8.881	0.696	9.139	0.716
0.120	O_06II_2000_3000		0.535		0.552		0.568
0.120	O_06III_2000_5000		0.535		0.552		0.568
0.122	O_06IV_2000_7000		0.569		0.588		0.605
0.120	O_06V_2000_9000		0.609		0.629		0.648
0.082	Test 1a		0.474		0.490		0.504
0.121	Test 1b		0.601		0.620		0.638
0.120	Test 2		0.580		0.599		0.617

Figure A.31 - Dynamic design calculation for the test results.

	Model											
	D67.5 (mm)	D_{n50} (mm)	D50 (mm)	τcrit (θcrit=0.056) (kPa)	τcrit (θcrit=0.035) (kPa)	τ_c (kPa)	f_c	ks (m)	z_{0_c}	τ_w (kPa)	f_w	z_{0_w}
O_03a_1000	6.031	4.239	5.046	4.52	3.38	0.05	0.010	0.013	4.21E-04	1.44	0.139	4.21E-04
O_04_2000_3000				4.52	3.38	0.05	0.010	0.013	4.21E-04	1.19	0.148	4.21E-04
O_04II_2000_5000				4.52	3.38	0.05	0.010	0.013	4.21E-04	1.49	0.140	4.21E-04
O_05_1000_1000				4.52	3.38	0.10	0.010	0.013	4.21E-04	1.44	0.135	4.21E-04
O_05II_2000_3000				4.52	3.38	0.12	0.010	0.013	4.21E-04	1.45	0.138	4.21E-04
O_05III_2000_5000				4.52	3.38	0.12	0.010	0.013	4.21E-04	1.45	0.134	4.21E-04
O_05IV_3000_8000				4.52	3.38	0.10	0.010	0.013	4.21E-04	1.42	0.135	4.21E-04
O_06_1000_1000				4.52	3.38	0.11	0.010	0.013	4.21E-04	1.49	0.132	4.21E-04
O_06II_2000_3000				4.52	3.38	0.11	0.010	0.013	4.21E-04	1.40	0.139	4.21E-04
O_06III_2000_5000				4.52	3.38	0.11	0.010	0.013	4.21E-04	1.40	0.139	4.21E-04
O_06IV_2000_7000				4.52	3.38	0.11	0.010	0.013	4.21E-04	1.44	0.137	4.21E-04
O_06V_2000_9000				4.52	3.38	0.11	0.010	0.013	4.21E-04	1.42	0.135	4.21E-04
Test 1a	6.031	4.239	5.046	4.52	3.38	0.05	0.010	0.013	4.21E-04	1.37	0.142	4.21E-04
Test 1b				4.52	3.38	0.11	0.010	0.013	4.21E-04	1.44	0.135	4.21E-04
Test 2				4.52	3.38	0.11	0.010	0.013	4.21E-04	1.43	0.136	4.21E-04
	τ_{cw_m} (kPa)	τ_{cw_max} (kPa)	α4	α3	α2	α4·τ_{cw_max} (kPa)	α3·τ_{cw_max} (kPa)	α2·τ_{cw_max} (kPa)	Φ (°)	θ_{max}	$\theta_{crit\ (Shields)}$	$\theta_{crit\ (De\ Vos)}$
O_03a_1000	0.11	1.55	4.00	3.00	2.00	6.19	4.64	3.10	0	0.020	0.056	0.035
O_04_2000_3000	0.10	1.29				5.16	3.87	2.58		0.017		
O_04II_2000_5000	0.11	1.60				6.39	4.79	3.20		0.021		
O_05_1000_1000	0.20	1.63				6.53	4.90	3.26		0.021		
O_05II_2000_3000	0.23	1.69				6.75	5.06	3.37		0.022		
O_05III_2000_5000	0.23	1.68				6.72	5.04	3.36		0.022		
O_05IV_3000_8000	0.20	1.61				6.45	4.83	3.22		0.021		
O_06_1000_1000	0.21	1.70				6.81	5.10	3.40		0.022		
O_06II_2000_3000	0.21	1.61				6.43	4.82	3.22		0.021		
O_06III_2000_5000	0.21	1.61				6.43	4.83	3.22		0.021		
O_06IV_2000_7000	0.22	1.66				6.63	4.97	3.32		0.021		
O_06V_2000_9000	0.21	1.63				6.51	4.88	3.26		0.021		
Test 1a	0.10	1.48	4.00	3.00	2.00	5.91	4.43	2.95	0.00	0.019	0.056	0.035
Test 1b	0.21	1.65				6.61	4.95	3.30		0.021		
Test 2	0.21	1.64				6.57	4.93	3.28		0.021		

Figure A.32 – Static design calculation for the test results.

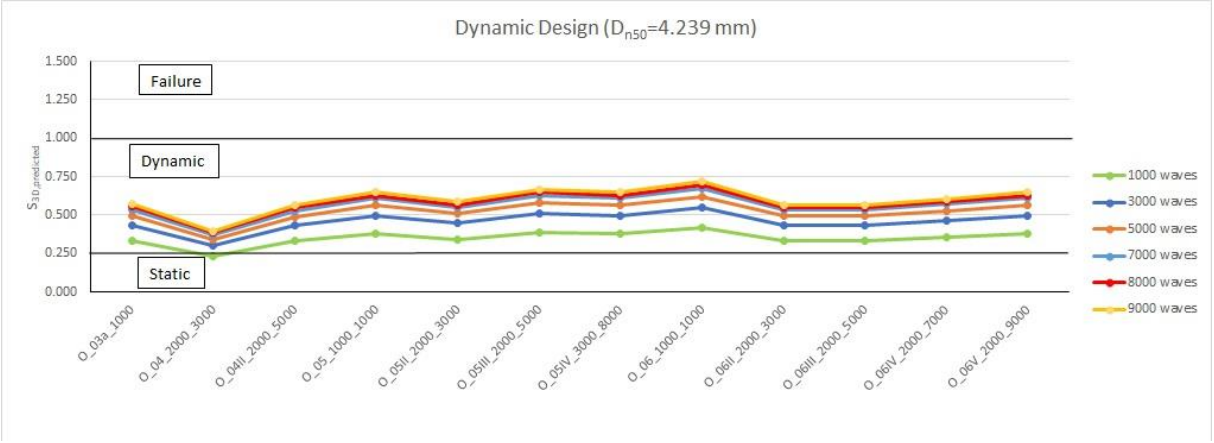

Figure A.33 - Evolution of the $S_{3D,predicted}$ for the test results.

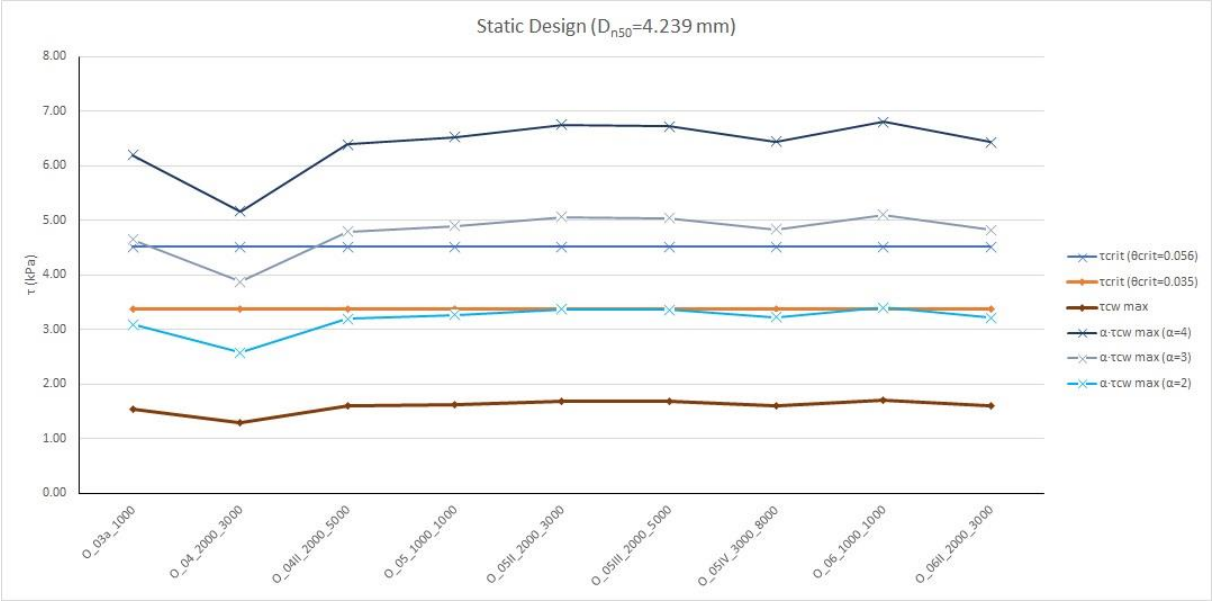

Figure A.34 – Static Design for the test results.